Synthetic Aperture Vector Flow Imaging

Oddershede, Niels

Publication date:
2008

Document Version
Publisher's PDF, also known as Version of record

Synthetic aperture vector flow imaging

Niels Oddershede

December, 2007

Center for Fast Ultrasound Imaging
Ørsted·DTU
Technical University of Denmark
2800 Kgs. Lyngby
Denmark

SUBMITTED IN PARTIAL FULFILLMENT OF THE
REQUIREMENTS FOR THE DEGREE OF
DOCTOR OF PHILOSOPHY
AT
THE TECHNICAL UNIVERSITY OF DENMARK
DECEMBER 2007

_____

Signature of Author

Contents

Contents i

Preface v

Acknowledgments vii

Abstract ix

1 Introduction 1

2 Blood flow estimation using ultrasound - history and present 5
2.1 History and basic principle . . . 5
2.2 Display modes . . . 7
2.3 Estimating blood flow velocity vectors . . . 9

3 Synthetic aperture imaging - from B-mode to vector flow 13
3.1 Synthetic aperture imaging . . . 13
3.1.1 Mono-static approach . . . 13
3.1.2 Synthetic receive aperture imaging . . . 13
3.1.3 Synthetic transmit aperture imaging . . . 14
3.1.4 Virtual sources . . . 16
3.1.5 Coding . . . 17
3.1.6 Recursive imaging . . . 17
3.1.7 Tissue motion . . . 17
3.1.8 Clinical results . . . 18
3.2 Synthetic aperture flow . . . 18
3.2.1 Synthetic aperture velocity estimation . . . 18
3.2.2 Finding the flow direction . . . 20

4 Analysis of the method 23
4.1 Focusing effects related to virtual sources . . . 23
4.2 Motion effects in synthetic aperture vector flow imaging . . . 27
4.2.1 The Doppler effect . . . 28
4.2.2 Motion between low resolution images . . . 28
4.2.3 Change in point spread function due to movement . . . 32
4.2.4 Motion compensated beamforming . . . 32
4.3 Separating the blood signal from unwanted clutter . . . 34
4.3.1 Modelling the slow-time signal . . . 34

4.3.2 Slow-time spectrum in realistic situation . . . 37
4.3.3 Possible refinements of filtering approach . . . 38

5 In-vivo investigations using synthetic aperture vector flow imaging 39
5.1 Previous in-vivo results of synthetic aperture flow imaging . . . 39
5.2 The common carotid artery . . . 40
5.3 The femoral artery and vein . . . 40
5.4 The carotid bifurcation . . . 42
5.5 The common carotid artery, revisited . . . 42

6 Multi-frequency encoding for fast color flow and quadroplex imaging 49
6.1 Purpose . . . 49
6.2 Encoding method for CFM and Quadroplex imaging . . . 50
6.3 Papers on the method . . . 52

7 Multi-dimensional spectrum analysis for 2-D vector flow imaging 53
7.1 Axial blood velocity estimation using 2-D Fourier transform . . . 53
7.2 Vector velocity estimation using 3-D Fourier transform . . . 55
7.3 Practical considerations regarding the setup . . . 56
7.4 Papers on the method . . . 57

8 Conclusion 59

Bibliography 61

A Appendix 71
A.1 Jensen, J. A. and **Oddershede, N.** ,
Estimation of velocity vectors in synthetic aperture ultrasound imaging, *IEEE Transactions on Medical Imaging, vol. 25, no. 12, December 2006, pp 1637-44.* . . . 71
A.2 **Oddershede, N.** and Jensen, J. A.,
Effects influencing focusing in synthetic aperture vector flow imaging, *IEEE Transactions on Ultrasonic, Ferroelectrics, and Frequency Control, vol. 54, no. 9, September 2007, pp 1811-25.* . . . 81
A.3 **Oddershede, N.** and Gran, F. and Jensen, J. A.,
Multi-frequency encoding for fast color flow or quadroplex imaging, *IEEE Transactions on Ultrasonic, Ferroelectrics, and Frequency Control, accepted for publication, December 2007.* . . . 99
A.4 **Oddershede, N.** and Løvstakken, L. and Torp, H. and Jensen, J. A.,
Estimating 2-D vector velocities using multi-dimensional spectrum analysis, *IEEE Transactions on Ultrasonic, Ferroelectrics, and Frequency Control, submitted for publication, November 2007.* . . . 109
A.5 **Oddershede, N.** and Jensen, J. A.,
Experimental investigation of synthetic aperture flow angle estimation, *Proceedings of SPIE Medical Imaging 2005, volume 5750, pp. 417-26.* . . . 121
A.6 **Oddershede, N.** and Jensen, J. A.,
Synthetic aperture flow angle estimation on in-vivo data from the common carotid, *Proceedings of IEEE Ultrasonics Symposium 2005, pp. 1331-34.* 133
A.7 **Oddershede, N.** and Jensen, J. A.,
Motion compensated beamforming in synthetic aperture vector flow imaging, *Proceedings of IEEE Ultrasonics Symposium 2006, pp. 2027-31.* . . . 139

A.8 **Oddershede, N.** and Hansen, K. L. and Nielsen, M. B. and Jensen, J. A., In-vivo examples of synthetic aperture vector flow imaging, *Proceedings of SPIE Medical Imaging 2007, volume 6513.* 147
A.9 **Oddershede, N.** and Gran, F. and Jensen, J. A., Multi-frequency encoding for rapid color flow and quadroplex imaging, *Proceedings of IEEE Ultrasonics Symposium 2007, accepted for publication.* . . 159
A.10 **Oddershede, N.** and Løvstakken, L. and Torp, H. and Jensen, J. A., Multi-dimensional spectrum analysis for 2-D vector velocity estimation, *Proceedings of IEEE Ultrasonics Symposium 2007, accepted for publication.* . . 165

Preface

In 1985, Wells and Skidmore wrote about ultrasonic blood flow estimation [1]: ”(...) what can be done now clinically is limited by the capabilities of the present technology and (...) there are still great opportunities for advancement.” Since then, 22 years have passed, and research has brought diagnostic ultrasound to a new level. But still today, the statement is very much true. This is one of the fascinating things about ultrasound research. Even after all these years of research, there are still a lot of thing we don't know, and a lot of problems which remain unsolved.

Although my three years of ultrasound research might not be considered significant to the greater ultrasound community, to me the significance is huge. I have laughed and cursed as successes and failures were unveiled. There have been times when I loved it and times when I hated it, but the curiosity to learn more has always been there. I am very grateful for having been granted the opportunity to work within this area and with my colleagues at the Center for Fast Ultrasound Imaging.

Niels Oddershede
Kgs. Lyngby
December 2007

Acknowledgments

First and foremost I would like to thank my supervisor and mentor Prof. Jørgen Arendt Jensen for his help and support throughout the years, and for making this project possible. His knowledge and guidance was vital for this project. It has been an honor and a privilege to work in a research group internationally respected for years of good research.

I would like to thank the pioneer of synthetic aperture flow imaging, Dr. Svetoslav Nikolov, for fruitful discussions on synthetic aperture and more. I wish to acknowledge Dr. Fredrik Gran for his great knowledge of signal processing and ultrasound and his fantastic ability to find the solution to any problem. Not only is he a brilliant researcher and a good friend, to me he is a role model.

I shared an office with Dr. Jesper Udesen for two and a half years. Although only moderately skilled as a chess player, Jesper is truly a good friend, a talented scientist, and a pedagogic genius with the ability to conceptualize and visualize the hardest physic problem so that even I could understand it. Thank you.

Furthermore, I would like to thank my colleague and friend Klaus Scheldrup Andersen for help and support in the everyday work and for late nights at the bar, discussing everything but ultrasound. I wish to thank Dr. Borislav Tomov for his efforts on keeping the hardware running, Henrik Laursen for help on computer and network related issues, and Elna Sørensen for her assistance on matters related to linguistics and administration. Also, I would like to thank my other colleagues at the Center for Fast Ultrasound Imaging (CFU) Jacob Kortbek, Iben Holfort, David Bæk, and Henrik Andresen for providing a comfortable and fruitful atmosphere.

A special thank you goes to the external collaborators who have contributed to this project. Of these, the most important is MD Kristoffer Lindskov Hansen from Rigshospitalet, without whom none of the *in-vivo* scans would have been possible. Thank you for putting up with us engineers, reminding us of the clinical reality, and for being a good friend. Also, prof. Michael Bachmann Nielsen and the rest of the group at the Section of Ultrasound, Department of Radiology at Rigshospitalet are thanked for the collaboration. Thank you also to the Department of Circulation and Medical Imaging at the Norwegian University of Science and Technology at Trondheim, Norway, for welcoming me at my two month stay in Trondheim. Especially prof. Hans Torp and Dr. Lasse Løvstakken are thanked for our collaboration, while also Dr. Svein Erik Måsøy and the rest of the Norwegian group are thanked for also entertaining me after working hours.

Last but not least I want to thank my wonderful wife Susanne Ellemose Oddershede for her love and support and for sometimes listening to my boring stories of the wonderful

world of ultrasound.

Abstract

Current ultrasonic blood flow velocity measurement systems are subject to a number of limitations, including limited frame rate, aliasing artifacts, and that only the velocity component along the ultrasound beam is estimated. This dissertation aims at solving some of these problems. The main part of the thesis considers a method for estimating the two-dimensional velocity vector within the image plane. This method, called synthetic aperture vector flow imaging, is first shortly reviewed. The main contribution of this work is partly an analysis of the method with respect to focusing effects, motion effects, and clutter rejection, and partly within *in-vivo* applications of the method, showing examples from various arteries and veins. Furthermore, two additional projects are described and tested. The first is an encoding method for simultaneously acquiring multiple lines for conventional velocity estimation. The method can be used for increasing the frame rate of color flow maps or alternatively for a new imaging modality entitled quadroplex imaging, featuring a color flow map and two independent spectrograms at a high frame rate. The second is an alternative method for ultrasonic vector velocity estimation. Two different velocity estimators were derived for finding both the axial and lateral velocity components through a multi-dimensional spectrum analysis. The work resulted in four journal papers and six conference papers, which are appended to the dissertation.

CHAPTER

ONE

Introduction

The public health care sector in Denmark is under a lot of pressure these days. Political initiatives and the lack of qualified labor put great demands on efficiency and make rapid and precise diagnostics increasingly important, while limited budgets enforce strict control on expenses. These facts favor ultrasound imaging which features low equipment cost, fast examinations, and rapid diagnosis, as opposed to the high equipment cost and the slower data acquisition of MRI and the use of ionizing radiation in CT.

Especially in areas of cardiovascular disease, where the real-time imaging of physiological parameters like blood flow velocity is of great importance, ultrasound imaging is the dominating imaging modality. Different modes are used for visualization. A color coded indication of flow velocity, called color flow mapping or color Doppler, is used mainly for guidance and overview, while single point measurements of the velocity over time, called spectrograms or spectral Doppler, are acquired when quantitative measures are needed.

Nevertheless, current commercial systems have significant limitations. The blood flow velocities measured are not the true velocities, which are three-dimensional by nature (or four-dimensional including time), but merely the component of the velocity towards or away from the transducer. The resulting estimate is only a fraction of the true velocity, where this fraction is dependent on the angle between the flow direction and the direction of the emitted beam. In some cases this angle can be determined visually from anatomy by the operator, and compensated for, but often the vessel geometry and the cardiac contraction cause quite complex flow patterns at arterial bifurcations and venous confluences, especially in patients with severe cardiovascular disease.

The work presented in this thesis addresses the problems in current ultrasonic blood flow velocity estimation, and offers potential solutions to these problems. The main focus is on synthetic aperture vector flow imaging, a method where not only the velocity along the beam direction is found but where the velocity within the image plane is estimated. This is the first step towards estimating the full three-dimensional velocity vector over time. The thesis describes the automation of the method, combining estimation of the velocity magnitude with estimation of the flow direction. Also, the combination of a short flow sequence with high temporal resolution and a long B-mode sequence with high spatial resolution is considered. Both sequences are needed to display both the anatomy and the velocity vectors at sufficient quality. An analysis of the method is performed, looking at both motion effects and effects related to clutter filtering. A method for compensating the motion effects in the receive beamforming is described and tested, showing the potential for increasing the performance of the estimator on the expense of increased computational complexity. Multiple *in-vivo* examples of synthetic aperture vector flow imaging

are presented, showing vector flow images from both straight arteries and more complex structures like arterial bifurcations and venous confluences.

Two additional projects were carried out during the 3 years at CFU. One was an encoding method for lowering the data acquisition time and/or increasing flexibility of conventional ultrasonic velocity estimation, while the other was an alternative method for estimating blood flow vector velocities in ultrasound. These are also described in this dissertation.

This dissertation is divided into eight chapters where the first is this introduction. The following chapters are

Chapter Two: *Blood flow estimation using ultrasound - history and present* This chapter gives a short overview of existing ultrasonic methods for estimation of blood flow velocities. The evolution of the technique is shortly reviewed, leading to the commercially available equipment and the current research within the topic. The chapter attempts to put the research presented in this thesis in the right context.

Chapter Three: *Synthetic aperture imaging - from B-mode to vector flow* The concept of synthetic aperture imaging is presented, and the method for vector velocity estimation using synthetic aperture imaging is explained, leading up to where this project was initiated.

Chapter Four: *Analysis of the method* This chapter gives an in-depth analysis of the synthetic aperture vector flow imaging method. Various assumptions are challenged, and the effects influencing the method are quantitatively tested. The chapter analyzes the opening angle of virtual sources from a signal-to-noise ratio point of view and compares it to geometrical considerations normally used. Various effects linked to the motion of the blood during investigation are considered, including the Doppler effect, summation of incoherent data, and changes in the point spread function. Finally, the clutter filtering is investigated through a simplified model of the data, showing some challenges yet to be met.

Chapter Five: *In-vivo investigations using synthetic aperture vector flow imaging.* A number of *in-vivo* examples of synthetic aperture vector flow imaging are presented in this chapter. These have been performed throughout the project. The examples include scans of the common carotid artery and the femoral artery and by more complex geometries like the carotid bifurcation and the confluence of the femoral and the saphenous veins. The common carotid artery of eleven healthy volunteers were scanned using synthetic aperture vector flow imaging and the stroke volumes were compared to MR phase contrast data.

Chapter Six: *Multi-frequency encoding for fast color flow and quadroplex imaging* As often happens in research, other ideas were conceived and pursued during the research project, one of which is presented in this chapter. The purpose of this work was to decrease the time used for data acquisition for conventional color flow mapping by simultaneously acquiring data for multiple lines in the color flow map using different frequency bands. The received data are separated by filters matched to the emitted signals. An

interesting application which results from this approach is Quadroplex imaging, which features a color flow map and two independent spectrograms at the same frame rate as a normal color flow map. The chapter gives a short introduction to the method.

Chapter Seven: *Multi-dimensional spectrum analysis for 2-D vector flow imaging* This chapter describes another idea pursued during the project. The work includes a theoretical formulation of the expected three-dimensional power spectrum of axial-lateral-temporal data when a constant velocity linear movement occurs. From this formulation, two estimators are derived for finding vector velocities within the axial-lateral plane. An application for ultrasound is given, showing how these estimators can find the vector velocity for both phantom and *in-vivo* data.

Chapter Eight: *Conclusion* This chapter summarizes the findings in this dissertation and tries to give some suggestions to future directions of research.

Appendix: *Papers* The research summarized in the previous chapters resulted in publication of a number of papers. These are all appended to the thesis, and throughout the thesis the reader is often referred to the papers for in-depth derivation of theory, various parameters, descriptions of measurement setups, or additional results.

The papers on synthetic aperture vector flow imaging are listed below. They include two journal papers, one of which is merely co-authored, and four conference papers:

- **Estimation of Velocity Vectors in Synthetic Aperture Ultrasound Imaging.**
  Jørgen Arendt Jensen and Niels Oddershede
  Published in IEEE Transactions on Medical Imaging, vol. 25, no. 12, December 2006, pp 1637-1644

- **Effects Influencing Focusing in Synthetic Aperture Vector Flow Imaging.**
  Niels Oddershede and Jørgen Arendt Jensen
  Published in IEEE Transactions on Ultrasonics, Ferroelectrics and Frequency Control, vol. 54, no. 9, September 2007, pp 1811-1825

- **Experimental Investigation of Synthetic Aperture Flow Angle Estimation.**
  Niels Oddershede and Jørgen Arendt Jensen
  Published in Proceedings of SPIE Medical Imaging meeting, Ultrasonic Imaging and Signal Processing, February 2005

- **Synthetic Aperture Flow Angle Estimation on In-vivo Data from the Carotid Artery.**
  Niels Oddershede and Jørgen Arendt Jensen
  Published in Proceedings of IEEE Ultrasonics Symposium, October 2005, pp 1331-1334

- **Motion Compensated Beamforming in Synthetic Aperture Vector Flow Imaging.**
  Niels Oddershede and Jørgen Arendt Jensen
  Published in Proceedings of IEEE Ultrasonics Symposium, October 2006, pp 2027-2031

- **In-vivo Examples of Synthetic Aperture Vector Flow Imaging.**
  Niels Oddershede, Kristoffer Lindskov Hansen, Michael Bachmann Nielsen and

Jørgen Arendt Jensen
Published in Proceedings of SPIE Medical Imaging meeting, Ultrasonic Imaging and Signal Processing, February 2007

The multi-frequency encoding project resulted in two papers, one journal paper for the IEEE Transactions on Ultrasonics, Ferroelectric, and Frequency Control and one conference paper for the IEEE Ultrasonics Symposium 2007:

- **Multi-Frequency Encoding for Fast Color Flow or Quadroplex imaging.**
  Niels Oddershede, Fredrik Gran and Jørgen Arendt Jensen
  Accepted for publication in IEEE Transactions on Ultrasonics, Ferroelectrics and Frequency Control, 2007
- **Multi-Frequency Encoding for Rapid Color Flow and Quadroplex imaging.**
  Niels Oddershede, Fredrik Gran and Jørgen Arendt Jensen
  Accepted for publication in Proceedings of IEEE Ultrasonics Symposium, October 2007

Likewise, the multi-dimensional spectrum analysis estimator project resulted in two papers, one journal paper and one conference paper, both co-authored by the collaborators at the Department of Circulation and Medical Imaging, Norwegian University of Science and Technology in Trondheim, Norway. The journal paper was submitted to the IEEE Transactions on Ultrasonics, Ferroelectrics, and Frequency Control in November 2007 and is now undergoing the reviewing process, while the conference paper was presented at the 2007 IEEE Ultrasonics Symposium:

- **Estimating 2-D vector velocities using multi-dimensional spectrum analysis.**
  Niels Oddershede, Lasse Løvstakken, Hans Torp and Jørgen Arendt Jensen
  Submitted for publication in IEEE Transactions on Ultrasonics, Ferroelectrics and Frequency Control, 2007
- **Multi-Dimensional Spectrum Analysis for 2-D Vector Velocity Estimation.**
  Niels Oddershede, Lasse Løvstakken, Hans Torp and Jørgen Arendt Jensen
  Accepted for publication in Proceedings of IEEE Ultrasonics Symposium, October 2007

CHAPTER

TWO

Blood flow estimation using ultrasound - history and present

This chapter attempts to put the current research in the right context by shortly reviewing the history of ultrasonic imaging and blood flow estimation. This is followed by a short discussion of the current state of commercial ultrasound devices and the research currently being conducted world-wide in the field of blood flow velocity estimation using ultrasound. For a more comprehensive historic overview, the reader is referred to [1, 2] or Chapter 1 of [3].

2.1 History and basic principle

The first research of ultrasound for medical applications dates back to the early 1950s. The principle of ultrasound imaging of human tissue is quite simple. A focused ultrasonic pulse is emitted from a piezoelectric transducer, and changes in density and propagation speed of sound in the interrogated tissue will cause partial scattering and reflection. The backscattered signal is received by the same transducer and the amplitude of the backscattering is displayed on a logarithmic scale [3].

The first ultrasonic system for blood flow estimation was presented by Satomura in 1957 [4]. This system emitted a continuous wave (CW), a single frequency sinusoid, and attempted to measure the Doppler shift of the received echo traces. The Doppler shift comes from the interaction between the ultrasonic pulse and the moving blood (mainly the red blood cells [3], and since these are much smaller than the wavelength commonly used for ultrasound imaging, Rayleigh scattering from blood is often assumed). The Doppler shift of the received echo trace is given by

$$f_d = \frac{2v_z f_0}{c + v_z} \approx \frac{2v_z f_0}{c}, \tag{2.1}$$

where f_0 is the center frequency of the emitted waveform, usually in the low MHz range, c is the propagation speed of sound within the human body, v_z is the blood flow velocity along the direction of the emitted ultrasound beam (denoted as the z-axis), and the approximation is made assuming $v_z \ll c$. This assumption is usually valid since the propagation speed of sound within the human body is around $c \approx 1540$ m/s, dependent on the type of tissue, whereas even the highest velocities of blood flow within the human body, even in severely diseased patients, are a few m/s. The signal from stationary tissue (often with amplitudes 20-60 dB above that of blood) can be removed by demodulating the received signal by f_0 and high-pass filtering. The blood flow velocity along the beam

direction is found by estimating the Doppler shift caused by the moving blood and using (2.1) to convert to velocity.

Since a CW system emits continuously, no information of the distance to the blood vessel (called range or depth, z) is readily available. In cases where multiple vessels are within the interrogated area, the estimated velocity will be biased.

This problem was solved by emitting pulsed waves, where an ultrasonic pulse is emitted, the echoes are received, and a new pulse is emitted, etc. This was done by [5–7] among others. Such a system is called a pulsed wave (PW) system, and through the known propagation speed of sound, the elapsed time from pulse emission relates directly to depth. Since the emitted signal is limited in time, the spectral bandwidth will increase, and the Doppler shift on the order of a few kHz can no longer be determined directly by a spectral analysis of a single received signal [3]. But by sampling the signal at a certain depth z over a number of pulse repetitions, a signal, were the center frequency scales with axial velocity at this depth $v_z(z)$ as given by (2.1), is seen. So by performing a spectral analysis over pulse repetitions (often denoted slow-time), or finding the number of zero-crossings of the signal (a method extensively used in the 1970s), the blood flow velocity at this depth can be found. Signal components from stationary tissue were often removed by a delay-line canceler [8], subtracting consecutive pulses prior to estimation.

For some years, the computational load was a problem, and real-time imaging of the blood flow velocities was cumbersome. Also, the need for mapping the axial velocities over a two-dimensional area and relating this information to the anatomy became apparent, further increasing the problem [2]. Through the 1970s and 1980s, color flow mapping was developed, where the axial velocity component is estimated along a number of directions spanning the image plane and combined with B-mode images showing the anatomic structures. Still processing time was an issue [1].

But with the introduction of the autocorrelation estimator by Kasai and coworkers in 1985 [9] this problem was solved. The autocorrelation estimator is essentially a time-domain formulation of finding the mean frequency of the slow-time signal (the signal across pulse repetitions at a certain depth). This is achieved through the first lag of the autocorrelation of the slow-time signal, which explains the name. The method has been further refined, for instance by Loupas who suggested to average the autocorrelation estimate over a number of range samples, thus achieving a better estimate of the blood flow velocity [10]. The autocorrelation method is a narrow-band method, indicating that the estimator performance increases as the bandwidth of the emitted signal is decreased, and relatively long pulses are therefore often employed, yielding good signal-to-noise ratio but lowered spatial resolution.

Numerous other estimators have been proposed for finding the axial velocity component, many of which are broad-band methods, yielding better spatial resolution and potentially better velocity estimates. Bonnefous and Pesque proposed to cross-correlate consecutive echo traces to find the spatial shift between two consecutive transmissions [11]. Ferrara and Algazi proposed a maximum likelihood estimator [12, 13], essentially using both the envelope information and the phase information for finding the axial velocity. Wilson [14] and later Torp and Kristoffersen [15] proposed to use the two-dimensional Fourier transform of the range / slow-time data to find the axial velocity component. This is possible since a single velocity component will be concentrated along a line in the two-dimensional power spectral plane. A similar approach, implemented in the time domain, was proposed by Alam and Parker [16]. It was named the Butterfly Search Technique because of the geometry of the search. Allam and coworkers [17, 18] proposed a

method for re-sampling the received echoes from broad-band emissions in the Fourier domain to employ narrow-band estimators, with high spectral resolution, known from radar applications. These are only a few examples, but a full list of ultrasonic blood flow estimators is considered outside the scope of this section.

In spite of this vast amount of estimators proposed by researchers throughout the years, almost all commercial ultrasound scanners today use the autocorrelation estimator [9] for finding the blood flow velocity. The reason for this is the easy implementation, the robustness, and the low computational load. But the estimator suffers from a few shortcomings.

1. Since the autocorrelation estimator is simply a time-domain formulation of finding the mean frequency of the signal along slow-time, the velocity range is limited by the sampling rate, the pulse repetition frequency f_{prf}, through the Nyquist limit. The pulse repetition frequency, in turn, is limited by the travel time of the ultrasonic pulse, which becomes longer as deeper lying structures are interrogated.

2. The autocorrelation estimator is used to find the blood flow velocity along a single line at a time, and multiple pulses (often around 8-16) are needed along this line to form the velocity estimates. To map the blood flow velocities within an area of interest, the procedure must be repeated a number of times. Remembering, that the pulse repetition frequency is limited by the travel time of the ultrasonic pulse, this sets a limit on the achievable frame-rate, which depends on the depth in the tissue.

3. The autocorrelation estimator, as well as all of the above mentioned estimators, gives only an estimate of the axial velocity component v_z which will be an unknown fraction of the true velocity, since

$$v_z = |\vec{v}| \cos(\theta), \tag{2.2}$$

   where $|\vec{v}|$ is the true velocity magnitude, and θ is the angle between the direction of the emitted ultrasound beam and the direction of flow. To find the true velocity magnitude within the imaging plane, the direction of flow θ must be known. Especially in areas of complex flow pattern, this might not be possible.

Nevertheless, almost all commercial ultrasound scanners today use the autocorrelation estimator for finding the blood flow velocity.

2.2 Display modes

This section aims at summarizing the functionality of the commercial ultrasound scanners currently available. Not all scanners are of course the same, and some have additional features. But basically all scanners have the following modalities:

- **B-mode Imaging.** B-mode images show the amplitude of scattering from the investigated tissue on a logarithmic gray-scale. A two-dimensional area, either rectangular or sector, is swept by stepping over a linear array or electronically steering the beam at different angles. The B-mode image is used to visualize anatomy and discriminate between different types of tissue.

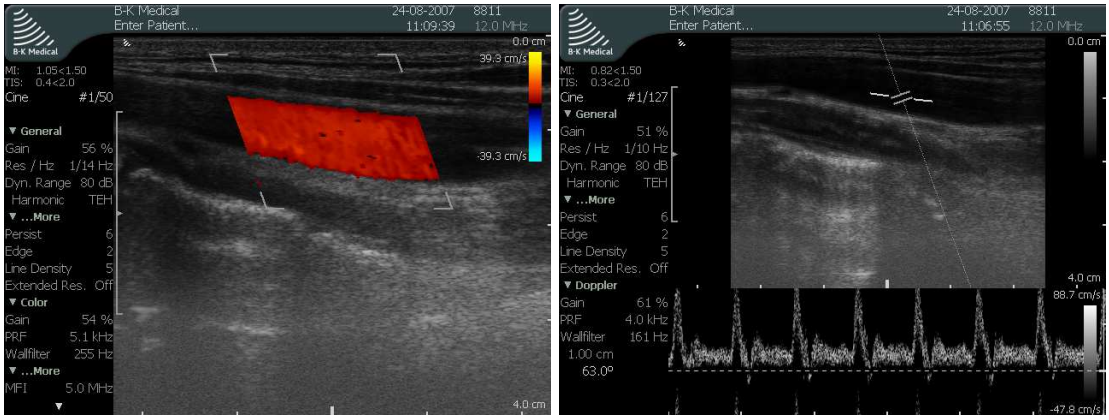

Figure 2.1: Display modes. Color flow mapping (left) and Duplex imaging (right)

- **Color Flow Mapping.** A color flow map combines a gray-scale B-mode image with color-coded information of axial velocity. The blood flow velocities are typically estimated using the autocorrelation estimator and only found within a window smaller than the size of the B-mode image. An example of a color flow map of the common carotid artery is shown in Fig. 2.1 (left). Different colors (red and blue) are used to distinguish between flow toward or away from the transducer.

- **Duplex Imaging.** A duplex image combines a B-mode image with a spectrogram, displaying the spectral distribution of the slow-time signal as a function of time. The spectrum is usually estimated using Welch's method [19] on the slow-time signal with highly overlapping segments. Through (2.1), the spectrum is often converted from frequency f_d to axial velocity v_z, and if the expected flow direction is supplied by the sonographer, the axial velocity is further converted to an expected velocity magnitude (see Section 2.3 for further on this approach). An example of a Duplex image from the common carotid artery is given in Fig. 2.1 (right).

- **Triplex Imaging.** A triplex image combines a color flow map with a spectrogram. To achieve all three measurements dynamically, the data acquisition time must in some way be divided between the modalities. This causes the frame rate of triplex imaging to be quite low, especially when interrogating deeper lying anatomic structures. An example of a triplex image of the common carotid artery is given in Fig. 2.2 (left).

- **Power Doppler.** A power Doppler image combines a gray-scale B-mode image with an area of color coding of residual power after the stationary signals have been removed. Hereby areas of flow will light up, but no measure of blood flow velocity is maintained. An example of a Power Doppler image of the common carotid artery is shown in Fig. 2.2 (right).

Some high-end scanners (high-end also means high-priced) have an additional feature called B-flow. In B-flow imaging, the blood speckle pattern is found, enhanced, and added to a B-mode image. B-flow imaging gives a qualitative visualization of the blood flow, but no quantitative measure of velocity is available.

Three-dimensional ultrasound imaging is at present an area of growth, and some high-end scanners have the ability of making three-dimensional B-mode images using two-dimensional transducer arrays. Some are even capable of making color flow maps of

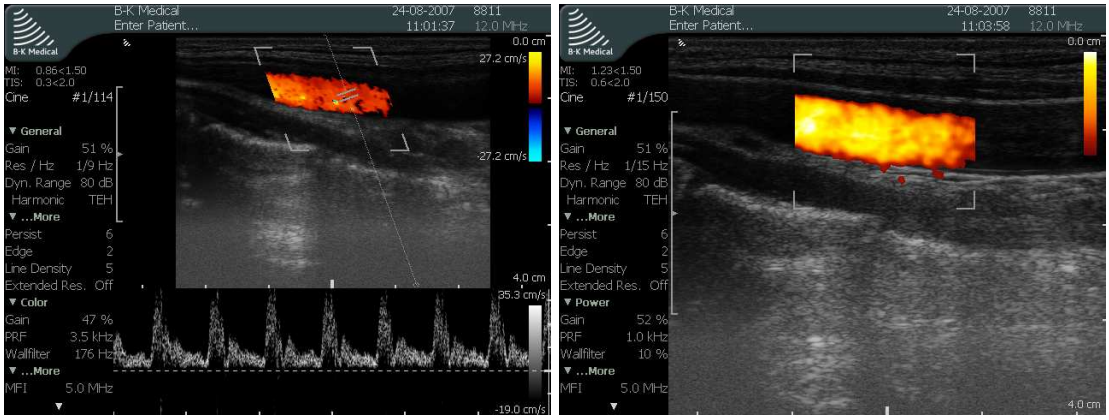

Figure 2.2: Display modes. Triplex imaging (left) and Power Doppler (right)

three-dimensional sectors, which is achieved through ECG-gating. The modality is therefore strictly speaking not real-time, since data covering a cardiac cycle is stitched together from multiple cardiac cycles.

To summarize, although most commercially available scanners today have multiple modalities for visualizing the blood flow velocity in the human cardiovascular system, none of them find the actual velocity magnitude and direction. Clinically, color flow mapping and power Doppler imaging is mostly used for finding areas of flow and recognizing areas of interest, while quantitative measures are found point-by-point using a spectrogram and compensating for the expected flow angle visually determined by the sonographer.

2.3 Estimating blood flow velocity vectors

As mentioned in the previous sections, almost all commercially available ultrasound scanners today can only estimate the axial component of the blood flow velocity. In most clinical situations, this will be sufficient for yielding a qualitative measure of blood flow. In clinical situations were a quantitative measure of blood flow is needed, a spectrogram is created at the point of interest, and the sonographer manually supplies the expected angle of flow, whereafter (2.2) is used to find an estimate of the true velocity magnitude. Nevertheless, only a small error in flow angle can lead to a significant error in the estimated velocity magnitude [20]. And in areas of complex flow, as is the case for instance in the carotid bifurcation, the direction of flow might change during the cardiac cycle [21]. This shows the motivation for estimating not only the axial velocity component, but the entire vector velocity, including both direction and magnitude.

In principle, the velocity vector is three-dimensional. It has an axial component v_z, a lateral component v_x, and a component in the elevation direction v_y. Nevertheless, as long as a one-dimensional transducer array is used, it is not possible to measure position along the elevation direction. The following is therefore restricted to discuss vector velocity estimation within the axial-lateral plane (the image plane), and the velocity component along the elevation direction is disregarded.

Almost since the introduction of ultrasonic blood flow velocity estimation, the estimation of velocity vectors has been an area of interest to researchers. The first approaches mainly concentrated on doing multiple one-dimensional velocity measurements along different

directions and combining these to form a two- or three-dimensional estimate of the velocity vector. A couple of these were [22, 23], but for a complete overview the reader is referred to [24], where similarities and differences of the systems proposed by different groups are considered. Common for these methods is the limited spatial area where the vector velocity estimate can be acquired, at least without significantly affecting the frame rate, and also the accuracy is dependent on the angle between the two beams. This limits the depth at which acceptably accurate measurements can be acquired. Both General Electric and Siemens have filed patents on derivatives of this technique [24].

Newhouse and coworkers [25] presented a method for estimating the lateral blood velocity component by finding the spectral bandwidth of the slow-time spectrum. This bandwidth has been shown to be proportional to the velocity normal to the ultrasound beam. But since the spectrum is stochastic of nature, the estimation of the bandwidth is far from trivial, and also, the method assumes all scatterers within the sample volume move at the same velocity.

The research group at Duke University, Durham NC, presented a vector velocity estimation method called speckle tracking [26], which is a two-dimensional cross-correlation method for finding the spatial shift of the speckle pattern. To use this method, a two-dimensional image of the region of interest must be created at a quite high frame rate. A few years earlier this problem had been solved by the same group in their Explososcan project, where multiple lines were beamformed simultaneously by using a broad transmit beam and multiple receive beamformers working in parallel [27]. This method is, although relatively computationally expensive, a simple and effective solution to the problem.

A method for finding both the axial and lateral velocity components called transverse oscillations was proposed by Munk and Jensen, and the work was later continued by Udesen and Jensen [28–34]. A similar approach entitled spatial quadrature was proposed by Anderson [35,36]. The idea is to create an oscillation transverse to the emitted ultrasound beam by manipulating the receive apodization. This is possible since a Fourier relationship exists between the apodization and the beam pattern. An estimator for finding the axial and lateral velocity components from the double-oscillating slow-time signal was derived in [31] and is essentially an extension of the autocorrelation estimator, while the efficiency of the method *in-vivo* was demonstrated in [34]. This method puts quite low computational demands on the system and is shown to have a standard deviation and bias of the lateral velocity estimate around 10% of the peak velocity [33] down to an angle of $\theta = 60°$.

Jensen also proposed emitting normally focused beams and beamforming lines along the direction of flow. The velocity magnitude was then found using a cross-correlation estimator [37, 38]. The method assumes the direction of flow is known, a problem later solved in [39, 40].

Recently, Wang and coworkers presented a blood vector velocity estimator [41], where an autocorrelation estimator was applied to the individual channel data prior to beamforming. A linear regression was applied to the individual estimates, yielding an estimate of both the axial and lateral velocities. The method was tested for a plug-flow (all scatterers moving at the same velocity), but due to the lack of focusing, the existence of a velocity distribution could potentially be a problem. The method is yet to be demonstrated *in-vivo*.

These are only some of the methods presented in literature throughout the last 40 years,

all of which have their advantages and disadvantages in terms of precision, implementation, computational load, etc. It might seem like quite an enigma, why none of these methods have become great commercial successes. One explanation is conservatism among the established ultrasound companies or among sonographers, although the introduction of many new features in ultrasound equipment (such as harmonic imaging, B-flow, 3-D color flow mapping, etc.) throughout the years indicates otherwise. Another explanation could be lack of clinical relevance. But as indicated in [20], the clinical velocity measurements performed using spectrograms are subject to quite a large inaccuracy, especially in areas of complex flow, where visually determining the flow direction is far from trivial. Also, the introduction of better methods of measurement could potentially feed new methods of diagnosis. A third explanation is price, which in commerce is often the most important. The development cost of vector velocity estimation methods might exceed the potential economic gain, at least while the area is still maturing.

The research presented in this thesis could be seen as yet another attempt to solve a problem of academic interest, but it is important to keep in mind the potential clinical relevance of solving this problem. As the area of blood flow vector velocity estimation matures, through academic research creating and distributing knowledge, the cost of development will drop, and eventually the technology will be available in clinical environments. This will enable more precise measurements of blood flow, potentially aiding diagnostics and help save lives.

CHAPTER

THREE

Synthetic aperture imaging - from B-mode to vector flow

3.1 Synthetic aperture imaging

Synthetic aperture techniques were originally conceived for radar systems in the 1950s and were initially implemented on digital computers in the late 1970s, and more advanced techniques were introduced in the late 1980s [42, 43]. The idea behind synthetic aperture techniques is to synthesize the effect of having a larger aperture than the one physically available, thus increasing resolution beyond that readily available with the current aperture. Typically, this is achieved in radar and sonar systems by placing the physical aperture on a moving platform, and in some clever way combining the image information gathered from different positions.

Synthetic aperture techniques have been investigated for ultrasound imaging since the late 1960s [44]. While at first the research was mostly concerned with nondestructive testing, only a few researchers considered synthetic aperture methods for medical ultrasound applications [45, 46] before the 1990s, where the area really grew. To the author's knowledge, no book on synthetic aperture ultrasound imaging exists, but the closest thing is the 2001 PhD thesis by Dr. Nikolov [47], to which the reader is referred for an in-depth tutorial on synthetic aperture ultrasound imaging.

3.1.1 Mono-static approach

There are multiple ways of implementing synthetic aperture techniques in medical ultrasound. The first, called the mono-static approach [48], is a more or less direct implementation of synthetic aperture, as it is known from synthetic aperture radar (SAR). A single transmitter/receiver emits a pulse and receives the echoes. The transmitter/receiver is moved, and another pulse is emitted. This process is continued, and the image is reconstructed from the acquired data. The principle is shown in Fig. 3.1, where the top row indicates the transmitting aperture, and the bottom row the receiving.

3.1.2 Synthetic receive aperture imaging

Alternatively, if only the receiving aperture is changed from emission to emission, while the transmitting aperture stays the same, the technique is entitled synthetic receive aperture (SRA) imaging [47, 49]. An example is shown in Fig. 3.2. Nock and Trahey used a

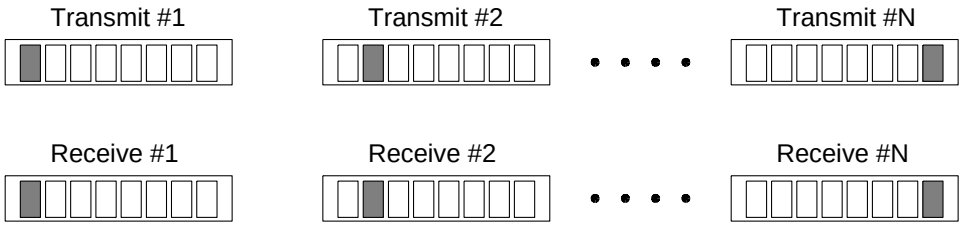

Figure 3.1: Mono-static synthetic aperture ultrasound imaging. The same single transducer element is used while transmitting and receiving, and after each emission the active element is slid.

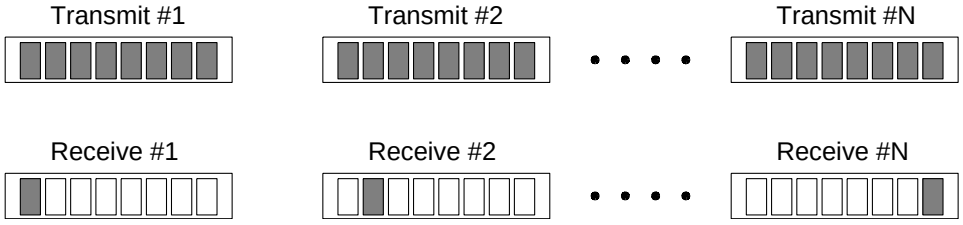

Figure 3.2: Synthetic receive aperture (SRA) imaging. Only the receiving element is changed from emission to emission, while the transmitting aperture stays the same.

SRA imaging approach in [50,51] to reduce hardware complexity, which has mainly been the reason for using SRA [47].

3.1.3 Synthetic transmit aperture imaging

If, in turn, the receiving aperture is kept unchanged from emission to emission, while the transmitting aperture is changed, the technique is entitled synthetic transmit aperture (STA) imaging [47,49], and an example is shown in Fig. 3.3.

The single element in transmit will create an almost cylindrical wave (circular within the image plane) emanating from the center of the transmitting transducer element. At emission m, the echoes $s_{m,n}(t)$ are received on all $n = 1, .., N$ elements, and the data are beamformed using delay-and-sum beamforming

$$\mathbf{L}_m(\vec{r}_p) = \sum_{n=1}^{N} w_n \cdot s_{m,n}(t - \tau_p), \tag{3.1}$$

where $\vec{r}_p$ is the position of the beamformed point, w_n is the apodization in the receiving

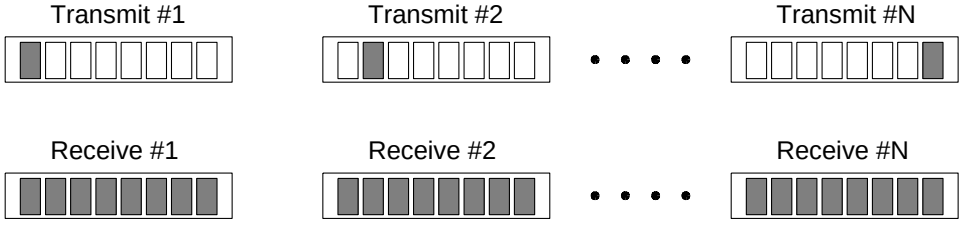

Figure 3.3: Synthetic transmit aperture (STA) imaging. Only the transmitting element is changed from emission to emission, while the receiving aperture stays the same.

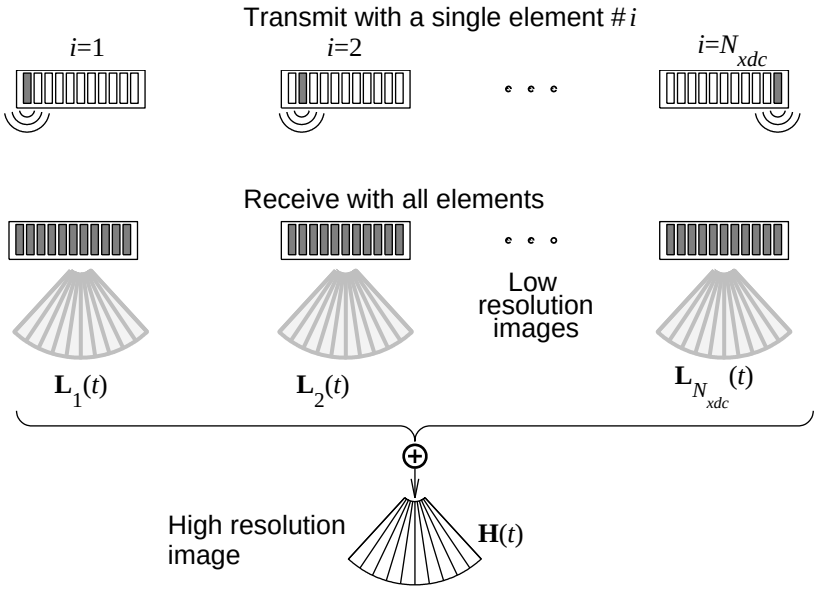

Figure 3.4: The concept of synthetic transmit aperture imaging. A single transducer element (or a collection of elements) emits an approximately spherical wave. Echoes from the tissue are received by all transducer elements, and a low resolution image is created by dynamic receive beamforming. The transmission is repeated a number of times, each time creating a new low resolution image by emitting from different spatial positions. The low resolution images are then summed to create a high resolution image, dynamically focused in both transmit and receive. Figure from [52].

stage, and τ_p is the travel time from the point of emission at the m'th emission down to the point $\vec{r}_p$ and back to the n'th receiver. This is written as

$$\tau_p = \frac{|\vec{r}_p - \vec{r}_m| + |\vec{r}_n - \vec{r}_p|}{c}, \tag{3.2}$$

where $\vec{r}_m$ is the position of the transmitting element at emission m, and $\vec{r}_n$ is the position of the n'th receiving element. The image $\mathbf{L}_m(\vec{r}_p)$ has quite low resolution due to the image being focused in receive only, and thus the image is referred to as a low resolution image (LRI). The emission is repeated using a new position of the transmitting element $\vec{r}_m$, and a new LRI is created. After M transmissions, M different LRIs are created. By summing these LRIs, an image of high resolution is created

$$\mathbf{H}_m(\vec{r}_p) = \sum_{m'=m-M+1}^{m} w_{m'} \mathbf{L}_{m'}(\vec{r}_p), \tag{3.3}$$

which is dynamically focused in both transmit and receive. Fig. 3.4 shows how the imaging is performed. This way of imaging has a number of advantages compared to the conventional way of imaging with focused beams. Using synthetic transmit aperture imaging, the image is dynamically focused in both transmit and receive, meaning that each point has the resolution it would have if data were beamformed in the conventional way, with focus in the point. Furthermore, the points imaged $\vec{r}_p$ are not restricted to any pre-specified geometry, for instance rectangular or fan. Also, it is possible to design sparse sequences, skipping some of the elements in transmit so that $M < N$. This has been investigated by Lockwood and colleagues with primary focus on 3-D imaging

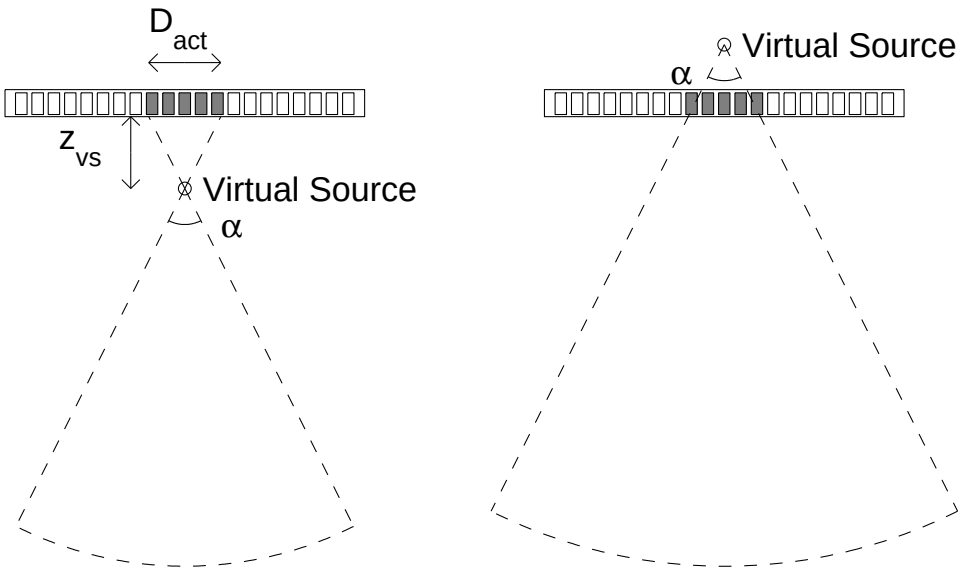

Figure 3.5: The concept of virtual sources. The left part of the figure shows a virtual source in front of the aperture. This is essentially just a fixed focus in transmit quite close to the aperture, at a low F-number. The emitted wave can then be treated as a spherical wave emanating from the virtual source. The right part shows a virtual source behind the aperture, where the electronic delays emulate emitting a spherical wave from the virtual source. Figure from [56].

application [53, 54]. Lockwood and Foster also introduced the effective aperture [55], defined as a spatial convolution between the transmitting $a_t(\vec{x})$ and the receiving $a_r(\vec{x})$ aperture functions

$$a_{t/r}(\vec{x}) = a_t(\vec{x}) \star a_r(\vec{x}) \tag{3.4}$$

Using the Fourier relationship between an aperture and its radiation pattern, the lateral part of the point spread function of the system resembles the Fourier transform of the effective aperture [47]. Since the imaging is considered a linear process, using multiple transmissions in forming the image corresponds to simply summing the effective apertures for each emission. This of course assumes the target has not moved. Using sparse sequences will typically affect the contrast (of course dependent on the effective aperture), often giving increased side-lobes, while the frame-rate can be increased significantly.

3.1.4 Virtual sources

But the synthetic transmit aperture imaging sequence in Fig. 3.4 has a problem. At each emission, only one element emits. The energy of the emitted waveform will therefore be much lower than that of a conventionally focused sequence, and so will therefore the signal-to-noise ratio (SNR) of the received echo traces. In 1992, O'Donnell and Thomas presented a method for intravascular imaging based on synthetic aperture imaging, using a circular aperture [57]. Here they emitted from multiple elements simultaneously. Since the aperture was circular, so was the emitted waveform almost, at least within a limited angular extent. Later, the application of multi-element subarrays in synthetic aperture imaging was investigated by multiple researchers [53, 54, 58, 59], and the delays were typically chosen to emulate emission from a point in front of or behind the transducer

[59]. This point is entitled a virtual source, since the focusing emulates emission from a source located here.

The concept of virtual sources is visualized in Fig. 3.5, where the left part shows a virtual source in front of the aperture, while the right part shows a virtual source behind the aperture. The angle α at which the emitted wave is assumed spherical is called the opening angle [59], while D_{act} is the size of the active aperture, and z_{vs} is the depth of the virtual source. According to [59], the opening angle α of the virtual source can be approximated by geometrical considerations

$$\alpha = 2 \arctan \frac{D_{act}}{2|z_{vs}|}. \tag{3.5}$$

This approximation will be considered further in Section 4.1, which takes a closer look at both amplitude drop of and phase misalignments of the approximately spherical wave.

3.1.5 Coding

Another way of addressing the signal-to-noise ratio problem in STA is by using coded excitations. The goal is to emit more energy without increasing the amplitude or lowering the bandwidth of the emitted signal. One way of coding is to use linear frequency modulated signals [60–64], also known as linear chirps, or non-linear frequency modulated signals [65, 66], known as non-linear chirps. Alternatively, Barker codes combined with an inverse filter for decoding [67, 68] or complementary code sequences [69, 70] can be used.

Multiple ways of coding for simultaneous emission from multiple virtual sources have been proposed. Among these are Hadamard coding [49], Golay coding [69], chirps with disjoint spectral support [66, 71, 72], and pseudo-random codes [73]. An overview of coding methods in synthetic transmit aperture imaging is given in [74].

3.1.6 Recursive imaging

Nikolov and colleagues presented the concept of recursive imaging [47, 75]. The idea is, that once a high resolution image $\mathbf{H}_m(\vec{r}_p)$ is created, a new HRI can be created by simply adding a new LRI and subtracting the oldest

$$\mathbf{H}_m(\vec{r}_p) = \mathbf{H}_{m-1}(\vec{r}_p) + \mathbf{L}_m(\vec{r}_p) - \mathbf{L}_{m-M}(\vec{r}_p). \tag{3.6}$$

Therefore it is possible to create a new HRI after each emission.

3.1.7 Tissue motion

Many researchers have addressed the problem of motion in synthetic aperture ultrasound imaging [51, 76–81]. The beamforming described assumes the target is stationary, and motion between LRIs will cause some sort of misalignment. It is commonly reported that axial motion is the dominant factor, causing image quality degradation due to significantly higher spatial frequencies in this dimensions [43]. Many of these papers propose a one-dimensional motion estimation and compensation to correct for this misalignment, and in [80], a two-dimensional compensation method is presented. Nevertheless, impressive results have been obtain using no motion compensation.

3.1.8 Clinical results

In [82], Pedersen and coworkers presented an in-vivo study, where synthetic transmit aperture imaging, using virtual sources and linear chirps, was compared to conventional imaging. Conventional and STA images were acquired interleaved, and seven volunteers were scanned abdominally. The images were compared and scored by three medical doctors using randomized blinded presentation. The results showed slightly but significant increase in penetration depth and a highly significant increase in image quality, when using STA. These results indicate quite a potential in using synthetic transmit aperture imaging in B-mode ultrasound.

3.2 Synthetic aperture flow

For many years, synthetic aperture ultrasound was investigated for B-mode imaging only. It was widely accepted that due to the summation of data from multiple emissions, using synthetic aperture methods for blood flow estimation made no sense. Nevertheless, the concept of recursive imaging [75] made synthetic aperture imaging possible at a very high frame-rate, and opened the possibility for blood flow estimation. The first attempt to estimate blood flow velocities with synthetic aperture ultrasound was published in 2000 [83], where the Hadamard encoding from [49] was combined with the recursive imaging approach from [75] and a cross-correlation estimator was used along axial lines to find the axial velocity component. Later [47, 52, 84], it was realized that although the recursive imaging gave a new high resolution image after every emission, only the high resolution images M emissions apart were made in the same way and therefore were subject to the same smearing due to motion. The axial velocity component was therefore estimated by cross-correlating axial lines M emissions apart, finding the spatial movement, and dividing by elapsed time. Still, the velocity estimator was subject to the same limitations as the conventional estimator; it only estimated the axial component of the velocity magnitude.

But as Nikolov indicated in his 2001 PhD thesis [47], synthetic aperture methods can be used to find not only the axial component, but the true velocity magnitude. Nikolov proposed using either speckle tracking methods [26], or beamforming along the flow direction [37,38,85,86], which is a refinement of the transverse beamforming first proposed by Bonnefous [87]. Synthetic aperture velocity estimation with beamforming along the flow direction was presented in [88,89]. The following subsection will take a look at how this works.

3.2.1 Synthetic aperture velocity estimation

Since synthetic transmit aperture imaging features dynamic focusing in both transmit and receive, it is possible to beamform arbitrary points within the image plane. If the direction of flow θ (defined as the angle between the axial direction z and the flow direction as shown in Fig. 3.6) in a point $\vec{r}_p$ is known, it is possible to beamform a line

$$\vec{p}_p(i) = \vec{r}_p + \Delta r[\sin\theta, 0, \cos\theta](i - \frac{N_i}{2}), \tag{3.7}$$

through this point. Notice that all points $\vec{p}_p(i)$ are coordinates in a right-hand cartesian coordinate system, where the x-axis follows the lateral direction, the y-axis follows the

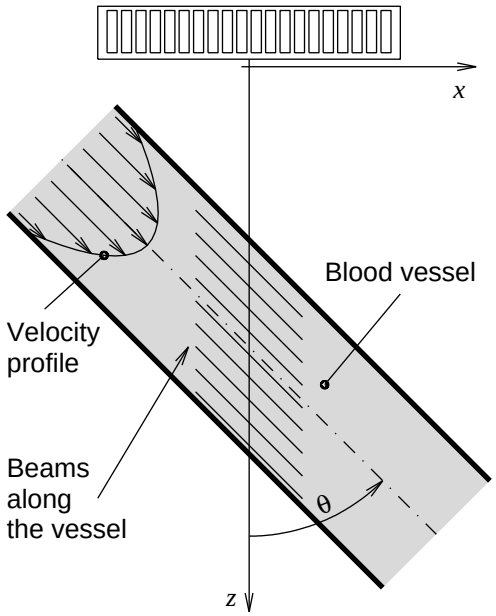

Figure 3.6: Beamforming along the vessel. Data can be beamformed within any desired grid since synthetic transmit aperture imaging features full flexibility of the geometry. Therefore it is possible to beamform points along lines following the blood vessel, assuming this direction is known in advance. Figure from [89].

elevation direction, and the z-axis follows depth as defined in Fig. 3.6. In (3.7), $\vec{r}_p$ is the center point of the line, Δr is the spatial sampling interval, θ is the angle between the z-axis and the flow direction, and $i = 0, ..., N_i$ is a sample index. This line will have length $N_i \Delta r$.

The received data are beamformed along the lines defined in (3.7), yielding high resolution lines

$$h_m(i) = \mathbf{H}_m(\vec{p}_p(i)), \tag{3.8}$$

where the beamforming is done as in (3.1) and (3.3). Assuming the blood flows during time MT_{prf} with a constant velocity $|\vec{v}|$ along the direction θ, the scatterers of the blood move the distance

$$d_M = |\vec{v}| M T_{prf}. \tag{3.9}$$

This correspond to a sample index of $k_s = d_M / \Delta r$. Neglecting any change in spatial impulse response due to the blood movement, we will approximately have

$$h_{m+M}(i) = h_m(i - k_s), \tag{3.10}$$

or in other words, the high resolution line acquired M emissions later will simply be a translated version of the original high resolution line. The translation, which scales with the velocity $|\vec{v}|$, is given by

$$k_s = \frac{|\vec{v}| T_{prf} M}{\Delta r}. \tag{3.11}$$

By cross-correlating two high resolution lines M emissions apart, we get

$$\begin{aligned} R_{12}(l) &= \frac{1}{N_i+1}\sum_{i=-N_i/2}^{N_i/2} h_m(i)h_{m+M}(i+l) \\ &= \frac{1}{N_i+1}\sum_{i=-N_i/2}^{N_i/2} h_m(i)h_m(i+l-k_s) \\ &= R_{11}(l-k_s), \end{aligned} \tag{3.12}$$

where $R_{12}(l)$ is the cross-correlation between the two lines and $R_{11}(l)$ is the autocorrelation of the first line. Since the autocorrelation $R_{11}(l)$ per definition peaks at $l = 0$, $R_{12}(l)$ must peak at $l = k_s$. Therefore, by cross-correlating two high resolution lines beamformed along the flow direction and finding the peak, we have a discrete estimate k_d of k_s

$$k_d = \arg\max_l R_{12}(l). \tag{3.13}$$

Since the cross-correlation function $R_{12}(l)$ is discretely sampled, of course only a discrete estimate of k_s is found. This estimate can be further refined by interpolating the discrete estimate by parabolic interpolation [90,91]

$$\widehat{k}_s = k_d - \frac{R_{12}(k_d+1) - R_{12}(k_d-1)}{2(R_{12}(k_d+1) - 2R_{12}(k_d) + R_{12}(k_d-1))}. \tag{3.14}$$

This interpolation essentially fits a parabola to the maximum of $R_{12}(k_d)$ and the two surrounding points and finds the position of the parabola's peak. A discussion of the limitations of parabolic interpolation is given in [92], where alternative approaches are also considered.

From $\widehat{k}_s$, we can use (3.11) to find an estimate of the flow velocity magnitude

$$\hat{v} = \frac{\widehat{k}_s \Delta r}{T_{prf} M}. \tag{3.15}$$

The method of course assumes that we know the direction of flow θ, which enables us to beamform the lines $\vec{p}_p(i)$. In [88,89], the flow direction was determined visually from the B-mode images and supplied to the estimator. This approach has the same limitations as when the sonographer visually determines the expected flow angle in conventional methods; the flow is not necessarily parallel to the vessel border, and in areas of complex flow, the flow direction might change during the cardiac cycle. The error due to angle inaccuracies in synthetic aperture velocity estimation is quantified in [89].

3.2.2 Finding the flow direction

The problem of finding the flow direction for directional beamforming was solved by Jensen in 2004 [39]. The basic idea is to beamform lines along multiple directions

$$\vec{p}_p(i,\theta) = \vec{r}_p + \Delta r[\sin\theta, 0, \cos\theta](i - \frac{N_i}{2}), \tag{3.16}$$

where $\theta = [0°, \Delta\theta, 2\Delta\theta, ..., 180°]$, yielding the beamformed lines

$$h_m(i,\theta) = \mathbf{H}_m(\vec{p}_p(i,\theta)). \tag{3.17}$$

Lines along the same direction θ but M emissions apart are cross-correlated as before. This is done at all angles

$$R_{12}(l,\theta) = \frac{1}{N_i+1} \sum_{i=-N_i/2}^{N_i/2} h_m(i,\theta) h_{m+M}(i+l,\theta). \tag{3.18}$$

The cross-correlation functions are normalized by the energy of the individual high resolution lines

$$\rho_{12}(l,\theta) = \frac{R_{12}(l,\theta)}{\sqrt{R_{11}(0,\theta)R_{22}(0,\theta)}}. \tag{3.19}$$

Notice that through definition $\rho_{11}(0,\theta) = \rho_{22}(0,\theta) = 1$. The normalized cross-correlation function $\rho_{12}(l,\theta)$ now holds the normalized cross-correlation function, when correlating lines at different angles θ.

The method suggested by [39] assumes that when θ differs from the true direction of flow, de-correlation due to scatterers not following the lines will cause a drop in normalized correlation. Therefore, it is assumed that the direction of flow will give the largest normalized cross-correlation, and that $\rho_{12}(l,\theta)$ will peak at the true flow direction θ and the lag k_s corresponding to the true velocity magnitude $|\vec{v}|$. The maximum correlation at each angle θ is found by

$$\rho(\theta) = \max(\rho_{12}(l,\theta)), \tag{3.20}$$

and the angle giving the highest correlation is where $\rho(\theta)$ has its maximum

$$\theta_d = \arg\max_{\theta} \rho(\theta). \tag{3.21}$$

The angle estimate θ_d is discrete, and the precision of the estimate is limited by the angular sampling $\Delta\theta$. In order to get a better estimate, the discrete angle estimate is interpolated using parabolic interpolation [90, 91]

$$\widehat{\theta} = \theta_d - \frac{\rho(\theta_d+\Delta\theta) - \rho(\theta_d-\Delta\theta)}{2(\rho(\theta_d+\Delta\theta) - 2\rho(\theta_d) + \rho(\theta_d-\Delta\theta))}\Delta\theta, \tag{3.22}$$

as was the case for finding the velocity magnitude (3.14). Once the flow direction has been found, the data can be beamformed along the direction $\widehat{\theta}$, and the velocity magnitude can be found as described in Section 3.2.1.

The angle determination method presented in [39] and reviewed here can be used both for directional beamforming in conventional focused imaging [40] and for synthetic aperture vector flow imaging [93], which is of course the focus here.

CHAPTER

FOUR

Analysis of the method

This chapter will present an analysis of synthetic aperture vector flow imaging, mainly built on the journal paper [56], which is found in the Appendix. Various effects will be considered, and an attempt is made to quantify the different effects in order to separate those of minor importance from those significantly affecting the performance of the method.

In Section 4.1, focusing effects related to virtual sources are considered. Section 4.2 will focus on motion effects, and will further separate these effects into three subcategories, those effects related to the Doppler effect, those related to motion between low resolution images, and those related to change in the point spread function. The final part of Section 4.2 tests the 2-D tissue motion compensation method from [80] for synthetic aperture vector flow imaging. These results have previously been published in [56, 94] which are both found in the Appendix. Section 4.3 considers the effects related to separating the signal from the moving blood from the unwanted signals from tissue, noise, etc.

4.1 Focusing effects related to virtual sources

The concept of using virtual sources for synthetic transmit aperture imaging was shortly reviewed in Section 3.1.4. Instead of using a single transducer element to create an approximately spherical wave, a collection of elements can be used [53, 54, 57, 58]. This is achieved by either using a fixed transmit focus in front of the transducer and treating this focus point as the source of a spherical wave, or by setting the transmit delays as if a spherical wave is emitted from a point behind the aperture. This corresponds to creating a virtual source in front of, or behind the transducer, respectively. Fig. 4.1, which is a repetition of Fig. 3.5, shows the concept of virtual sources in front of the aperture (left) or behind the aperture (right).

In [59], the opening angle α, the angle at which the emitted wave can be assumed spherical, was found by the simple geometrical consideration

$$\alpha = 2 \arctan \frac{D_{act}}{2|z_{vs}|}, \tag{4.1}$$

where D_{act} is the size of the active aperture, and z_{vs} is the depth of the virtual source. This depth z_{vs} is defined so that if $z_{vs} < 0$, the virtual source is placed behind the aperture. Since the F-number is defined as $F_{\#} = |z_{vs}|/D_{act}$, the geometrically determined opening angle from (4.1) can be written as

$$\alpha = 2 \arctan \frac{1}{2F_{\#}}. \tag{4.2}$$

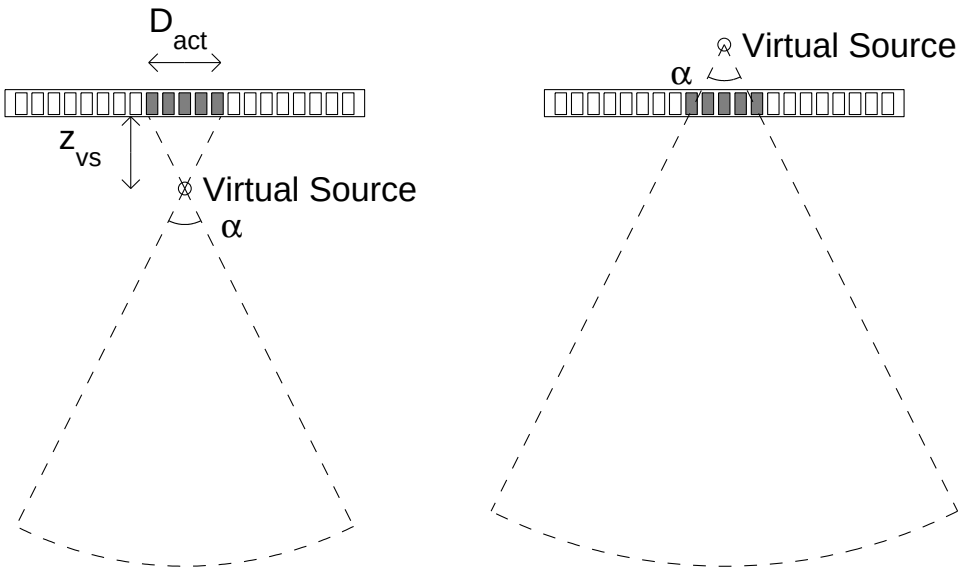

Figure 4.1: The concept of virtual sources. The left part of the figure shows a virtual source in front of the aperture. This is essentially just a fixed focus in transmit quite close to the aperture, at a low F-number. The emitted wave can then be treated as a spherical wave emanating from the virtual source. The left part shows a virtual source behind the aperture, where the electronic delays emulate emitting a spherical wave from the virtual source.

Although it has previously been shown qualitatively that (4.2) gives a fairly good approximation to the opening angle [47,59], this was addressed more quantitatively in [56]. The idea is to model two consecutive emissions from different virtual sources. Preferably the signal-to-noise ratio (SNR) should increase when adding the low resolution images created using these two virtual sources. If this is not the case, due to amplitude drop or phase misalignment, the summation is worthless and might even deteriorate the image. The modelled SNR for one emission is compared to that obtained by adding the signals from the two virtual sources. The acceptance angle is then defined a the angle for which the virtual source is still valuable in the SNR sense.

In [56], the pressure field from the n'th virtual source at a point on the created sphere was modelled as

$$p_n(t) = s_n(t) + \eta_n(t), \tag{4.3}$$

where $s_n(t)$ is the pressure field including the electrical impulse response from the transducer and measurement system, and $\eta_n(t)$ is uncorrelated white noise with zero mean and noise power σ_n^2. The signals from two consecutive virtual source emissions are modelled as damped and phase-shifted versions of each other

$$s_2(t) = ks_1(t - \frac{\Delta\phi}{2\pi f_0}), \tag{4.4}$$

where $0 < k \leq 1$ is the damping factor, and $\Delta\phi$ is the phase difference between signals $s_1(t)$ and $s_2(t)$. The criteria for finding the opening angle is, as mentioned, that the SNR must increase by adding a second virtual source which means that the low resolution image created from emission $n = 2$ should only be used if

$$SNR_1 \leq SNR_{1+2} \tag{4.5}$$

where SNR_1 is the SNR for emission 1, and SNR_{1+2} is the SNR of the sum of signals 1 and 2. If the emitted signal is assumed to be a monochromatic continuous wave signal

$$s_n(t) = A_n \cos(2\pi f_0 t + \phi_n), \tag{4.6}$$

and we define $A_2 = kA_1$ and $\Delta\phi = \phi_1 - \phi_2$ to obey (4.4), the criteria in (4.5) gives

$$\frac{1-k^2}{2k} \leq \cos\Delta\phi. \tag{4.7}$$

For a derivation, the reader is referred to [56] in the Appendix. The criteria in (4.7) states that when the amplitudes of the signals are the same $k = 1$, we have $\Delta\phi \leq \pi/2$, and the phase misalignment must be less than a quarter of a period. Likewise, when the phases are perfectly aligned $\Delta\phi = 0$, we have $k \geq \sqrt{2} - 1$.

If instead an m-cycle pulsed wave is emitted, so that

$$s_n(t) = w_n(t) A_n \cos(2\pi f_0 t + \phi_n), \tag{4.8}$$

where the rectangular windowing function $w_n(t)$ is given by

$$w_n(t) = \begin{cases} 1, & 0 < t < \frac{m}{f_0}, \\ 0, & \text{else}, \end{cases}$$

the inequality of (4.5) is in [56] derived to be

$$\frac{1-k^2}{2k} \leq \left(1 - \frac{\Delta\phi}{2\pi m}\right)\cos(\Delta\phi) - \frac{1}{2\pi m}\sin(\Delta\phi). \tag{4.9}$$

The additional terms in (4.9) compared to (4.7) simply accounts for the decrease in envelope overlap. As $m \to \infty$, meaning that the temporal length of the emitted waveform is increased towards the continuous wave case, (4.9) will approach (4.7).

Lines describing equality in the continuous wave criteria (4.7) and the pulsed wave criteria (4.9) for $m = 1$ and $m = 4$ are plotted in Fig. 4.2. Here it is clear that the pulsed wave case approaches the continuous wave case as the pulse length is increased.

In [56], the derived criteria are then used to find the opening angle α in a number of simulation performed in Field II [95, 96]. The wavefront from a virtual source emission is simulated, where the emitted waveform is a $m = 1$ cycle sinusoid at $f_0 = 5.5$ MHz. The simulation is repeated for $F_\# = [0.5, 0.75, 1, 1.5]$ and for the virtual source both in front of and behind the transducer. The amplitude drop k and phase misalignment $\Delta\phi$ are found along an arc around the virtual source in all simulations. The opening angle is then defined as the angle within which the criterion (4.9) is not violated. Fig. 4.3 (left) shows the results from this simulation, and compares to the geometric opening angle found from (4.2). For additional information on the simulation setup and parameters used, the reader is referred to [56] in the Appendix.

Fig. 4.3 (left) reveals a $\sim 10\%$ overestimation when using the geometrical consideration (4.2) compared to that found using the SNR approach. Nevertheless, the F-number in [56] is defined as

$$F_\# = \frac{|z_{vs}|}{2D_{act}} = \frac{|z_{vs}|}{2N_{act}d_x}, \tag{4.10}$$

where N_{act} is the number of active element in the virtual source emission, and d_x is the transducer pitch. By defining the F-number as

$$F_\# = \frac{|z_{vs}|}{2D_{act}} = \frac{|z_{vs}|}{2(N_{act}-1)d_x}, \tag{4.11}$$

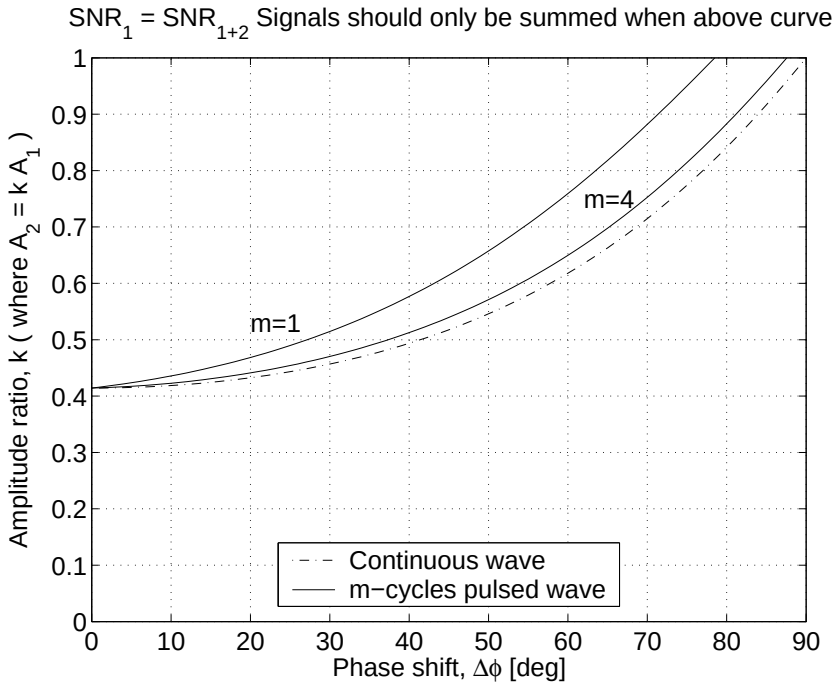

Figure 4.2: The figure shows the borderline between cases where the SNR is increased or decreased when summing signals from two virtual sources. The border is plotted for the continuous wave case and for the pulsed wave case emitting either an $m = 1$ or $m = 4$ cycles sinusoidal pulse. Figure from [56].

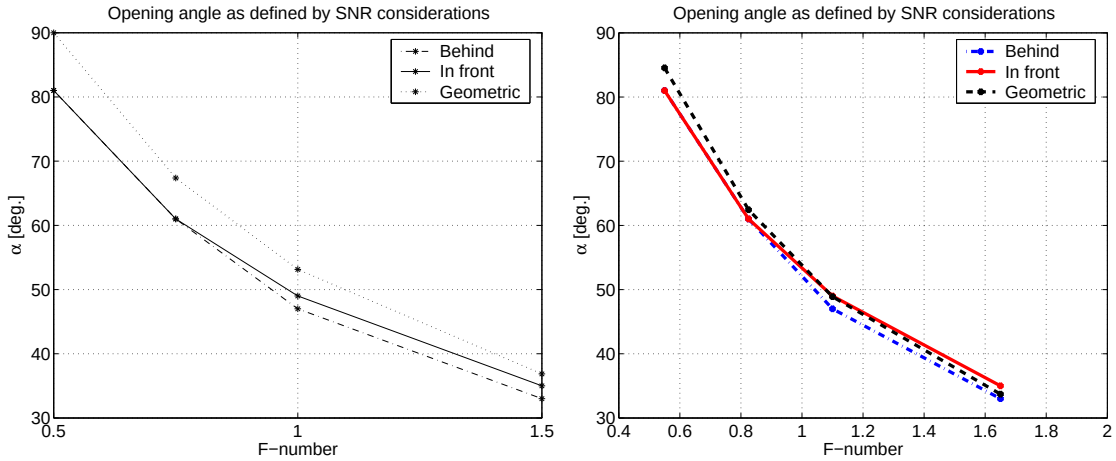

Figure 4.3: The opening angle of a virtual source for different F-numbers and for the virtual source placed either in front of or behind the transducer. The figures compare results from the geometrically calculated opening angle and that found from the SNR approach. The leftmost plot (from [56]) uses aperture size $D_{act} = N_{act}d_x$ while the rightmost plot uses $D_{act} = (N_{act} - 1)d_x$.

considering the size of the active aperture D_{act} as the distance from the center of the two outermost elements, we get the results in Fig. 4.3 (right). Here the geometric approximation fits very good. In conclusion, the opening angle found through the geometric consideration (4.2) fits the opening angle found through the SNR approach, when the F-number is defined as in (4.11).

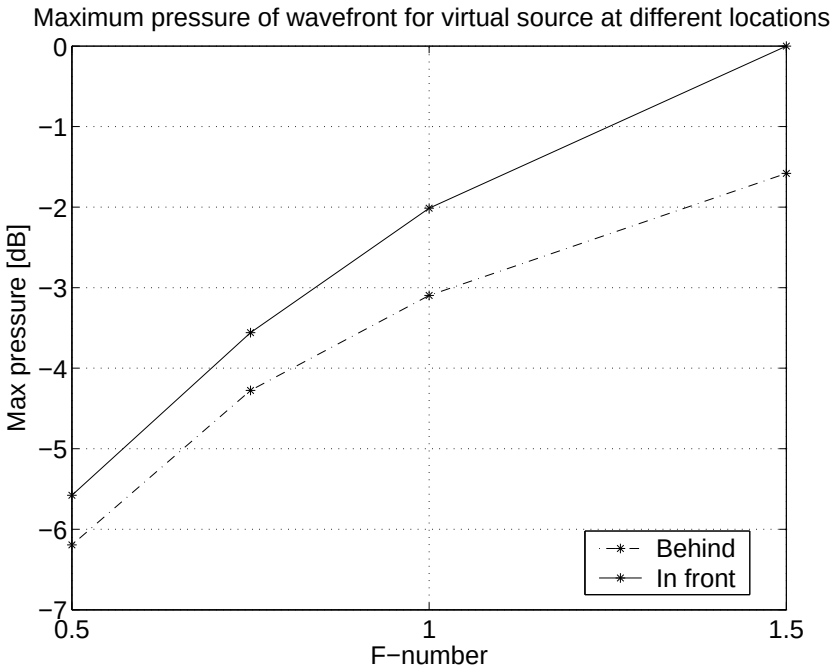

Figure 4.4: The maximum pressure of the spherical wavefront at depth 30 mm below the transducer surface for different position of the virtual source. Notice that these results assume $D_{act} = N_{act} d_x$. Figure from [56].

The wavefront simulations in [56] were also used to extract the maximum pressure of the wavefront for different virtual source placement. These are plotted in Fig. 4.4. From these results and the geometry involved (see Fig. 4.1) it was concluded that the optimal virtual source placement depends heavily on the depth of interest. If shallow structures are to be scanned, it is advisable to place the virtual source behind the aperture in order for each virtual source to be able to illuminate the area of interest. If deeper structures are to be imaged, the virtual sources are preferably placed in front of the aperture to avoid large energy leakage and attain an acceptable SNR.

4.2 Motion effects in synthetic aperture vector flow imaging

As described in Chapter 3, a high resolution image (or high resolution line) is created by summing a number of consecutive low resolution images (or lines), thus requiring multiple emissions. As previously pointed out by numerous authors [51, 76–79, 81], motion between these emissions might introduce incoherence in the data. Basically there are three effects that influence the focusing and potentially deteriorate the image

1. The Doppler effect
2. Motion between LRIs
3. Change in the point spread function

In [56], these three effects were investigated separately, and the same approach will be taken here.

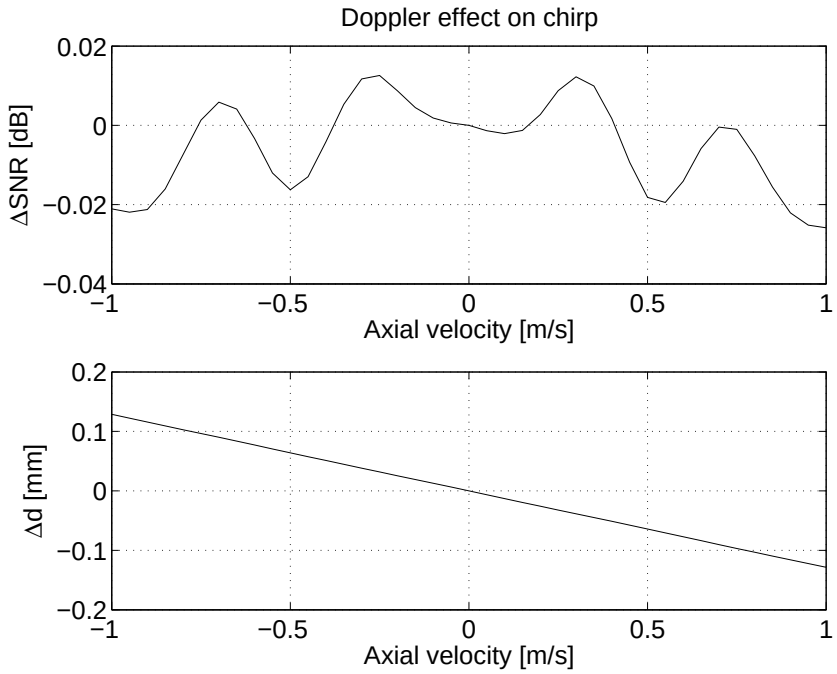

Figure 4.5: The Doppler effect causes both a change in the energy of the compressed chirp and a shift of the envelope peak. The top plot shows the change in SNR due to the Doppler effect at different axial velocities, whereas the bottom plot shows the shift in the peak of the compressed chirp due to the Doppler effect. Figure from [56].

4.2.1 The Doppler effect

The Doppler effect occurs when a sound receiver receives a signal from a sound source while there is a relative movement between the two. In ultrasound imaging, this occurs when the transducer is moved, or - more often - when the interrogated target moves. When imaging blood this is very much the case. Nevertheless, as already considered in Chapter 2, the speed of sound in human tissue $c \approx 1540$ m/s is orders of magnitude larger than even the highest blood flow velocities in the human body.

In [56], the Doppler effect was considered when using a linear chirp. The change in SNR, ΔSNR, and shift in envelope peak, Δd, due to the Doppler effect was quantified for axial velocities up to ± 1 m/s, and are shown in Fig. 4.5. As expected, this effect causes an insignificant change in signal-to-noise ratio, whereas a slight shift in the peak of the compressed chirp is seen. It should be noted that this shift will be constant for a constant velocity, and that this effect is not exclusive for synthetic aperture imaging, but will in fact also occur in conventional imaging using the same linear chirp.

4.2.2 Motion between low resolution images

Since a HRI is created by summing a number of LRIs, motion between the acquisition of these LRIs might cause degradation of the HRI. The synthetic aperture focusing technique described in Chapter 3 assumes the target is stationary, and multiple authors have considered these motion effects [51,76–79,81], mainly looking at contrast and resolution degradations. The approach taken in [56] is slightly different. Although the contrast is also considered, the degradation due to motion between LRIs is mainly analyzed with

respect to the change in SNR. The motivation for this is the assumption that the SNR is one of the key parameters affecting the performance of a blood flow estimator. Especially since the blood scattering amplitude is orders of magnitude lower than that of tissue, and often quite close to the noise floor. A slight degradation of the SNR around 0 dB might cause significant degradations on the performance of a cross-correlation estimator [97,98].

The change in SNR due to movement between LRIs is first considered from an analytical point of view. A simple one-dimensional linear model is assumed for the received signal $r(t)$ after one emission

$$r(t) = g(t) \star x(t) + \eta(t), \tag{4.12}$$

where $g(t)$ is the emitted waveform including the two-way electromechanical impulse response of the measurement system, $x(t)$ is a target function modelled as uncorrelated, white, Gaussian noise with power σ_x^2, $\star$ denotes convolution, and $\eta(t)$ is the signal noise assumed uncorrelated, white, and Gaussian distributed with noise power σ_η^2.

In [56], the SNR of a single LRI is in this model shown to be

$$SNR_{LRI} = \frac{\sigma_x^2 R_g(0)}{\sigma_\eta^2}, \tag{4.13}$$

where $R_g(\tau)$ is the autocorrelation of the function $g(t)$. Assuming $g(t)$ has finite energy, $R_g(0)$ is the total energy of the signal $g(t)$. The SNR of a HRI when the target is stationary is within this model shown to be [56]

$$SNR_{stat} = N\frac{\sigma_x^2 R_g(0)}{\sigma_\eta^2}, \tag{4.14}$$

where N is the number of LRIs used to create the HRI. If a time shift Δt of the target signal $x(t)$ occurs between the acquisition of each LRI, the SNR of a HRI created by summing these incoherent LRIs is shown in [56] to be

$$SNR_{mov} = \frac{\sigma_x^2 \left(N R_g(0) + 2\sum_{n=1}^{N-1}(N-n)R_g(n\Delta t)\right)}{N\sigma_\eta^2}, \tag{4.15}$$

which for $\Delta t = 0$ reduces to (4.14), since for all finite N

$$N + 2\sum_{n=1}^{N-1}(N-n) = N^2. \tag{4.16}$$

To investigate the degradation in SNR due to motion between LRIs in the model, the change in SNR between the stationary case SNR_{stat} and the case where movement occurs SNR_{mov} is considered. This is given by

$$\begin{aligned} \Delta SNR &= 10\log_{10}\left(\frac{SNR_{mov}}{SNR_{stat}}\right) \\ &= 10\log_{10}\left(\frac{1}{N} + \frac{2}{N^2 R_g(0)}\sum_{n=1}^{N-1}(N-n)R_g(n\Delta t)\right). \end{aligned} \tag{4.17}$$

In Fig. 4.6, the change in SNR as calculated by (4.17) is plotted for an m-cycle pulse with a rectangular envelope as a function of the movement between LRIs. Plots are made for various choices of pulse length m, and the number of LRIs summed when forming a

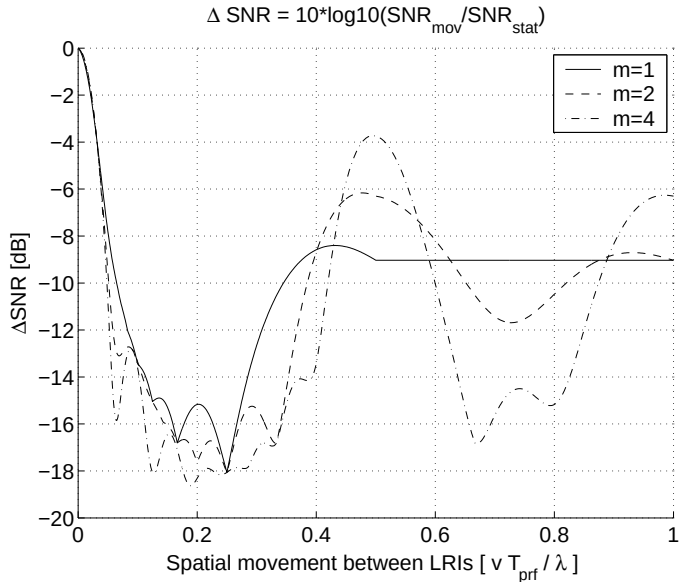

Figure 4.6: The change in SNR due to axial motion for different pulse lengths. ΔSNR is calculated from a simple one-dimensional model where both the target and the noise are modelled as uncorrelated white Gaussian processes with zero mean. The signal envelope is assumed rectangular.

HRI is assumed to be $N = 8$. The spatial inter-LRI movement is normalized to units of wavelength $\lambda = c/f_0$, making the result independent of center frequency f_0.

When no motion is present, $\Delta SNR = 0$ as expected, whereas the largest drop in SNR occurs approximately when the scatterers move $\lambda/4$ between LRIs. Here $\Delta SNR = 10\log_{10}(1/N^2)$, indicating as mentioned in [51], that motion effects increase when using longer sequences. When $N = 8$, the model predicts a 18 dB drop in SNR, effectively making velocity estimation impossible when an axial movement of $\sim \lambda/4$ occurs between LRIs. Furthermore, ΔSNR seams to drop rapidly with increased axial movement, even when the axial movement is only small fractions of λ.

The simple one-dimensional model in (4.12) is of course a crude approximation. To test a more realistic situation, a simulation was made, and the change in SNR ΔSNR was found as the difference in energy of the 2-D point spread function in the stationary $E_{v=0}$ and the moving $E_{v=v'}$ case

$$\Delta SNR = 10\log_{10}\left(\frac{E_{v=v'}}{E_{v=0}}\right) \tag{4.18}$$

In this simulation a 11.25 μs nonlinear chirp, designed using the method described in [65, 99], was used instead of a pulse with a rectangular window, so the results does not directly compare to Fig. 4.6. The SNR change was found for inter-LRI movement of 0 to 0.68λ, and both for axial and lateral movement. Fig. 4.7 shows the change in SNR as a function of inter-LRI movement both for axial (solid) and lateral (dashed) motion. Clearly, the change in SNR for axial motion in the simulation has great similarities to that found from the simple one-dimensional model. Nevertheless, it seams the SNR drop is not quite as dramatic as expected from the model. At an axial inter-LRI movement of $\sim \lambda/4$, then SNR drops around 10 dB. This is a very significant drop in SNR, and will in most practical cases ruin the velocity estimation.

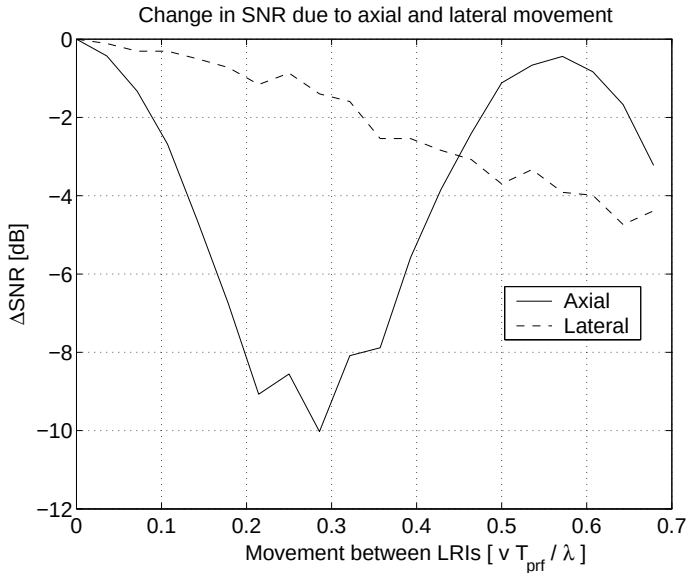

Figure 4.7: The change in SNR due to axial (solid) and lateral (dashed) motion, found by simulation.

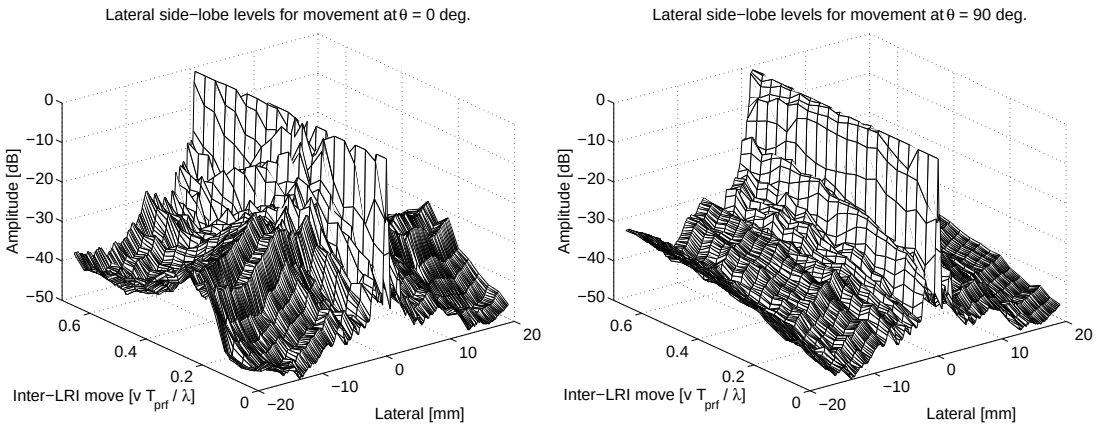

Figure 4.8: Lateral side-lobe structure at different degrees of movement. The side-lobes are shown for purely axial (left) and purely lateral (right) movement. Clearly, the side-lobes are severely affected at an axial movement of $\sim \lambda/4$ between LRIs.

Fig. 4.7 reveals that the SNR also drops as the target moves laterally. Nevertheless, the SNR drop is not as pronounced, and at movements below $\lambda/2$ between LRIs, the SNR drops less than 4 dB.

From the same simulated data, the lateral contrast at different velocities was extracted. The maxima at different lateral positions of the point spread function were extracted for different degrees of movement. Fig. 4.8 shows the lateral side-lobes as a function of inter-LRI movement for both a purely axial movement (left) and a purely lateral movement (right). Clearly the axial movement affects the contrast the most, as is the consensus in literature. At an axial inter-LRI movement of $\sim \lambda/4$, the lateral side-lobes are up almost 20 dB compared to the stationary case. In the case of lateral movement, a slight increase in side-lobe level as a function of movement is seen, but the effect is clearly much less than for axial movement.

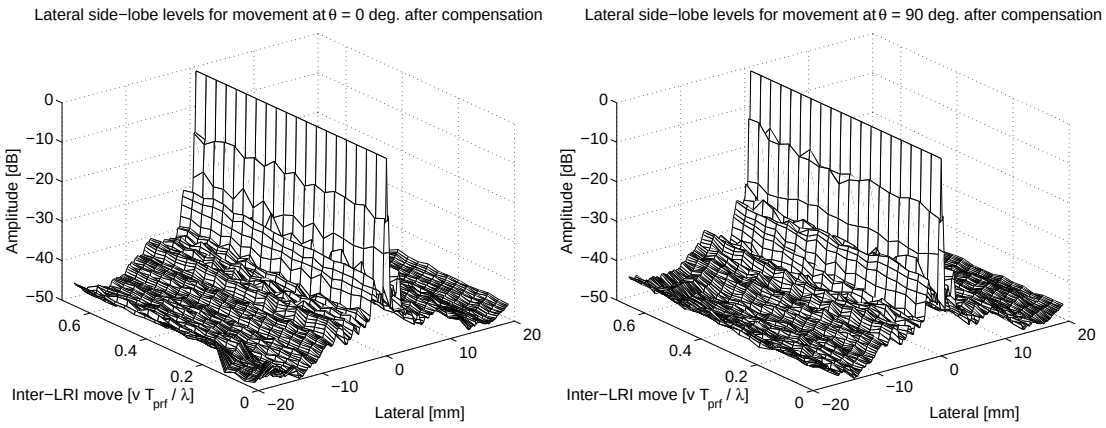

Figure 4.9: Lateral side-lobe structure at different degrees of movement after a compensation has been applied using the true velocity magnitude and direction. The side-lobes are shown for purely axial (left) and purely lateral (right) movement after compensation. Almost no change in side-lobes is seen as a function of movement after the compensation has been applied.

4.2.3 Change in point spread function due to movement

Since the individual scatterers move between LRI acquisitions when the blood flows, the point spread function will change slightly, compared to the stationary case, since it is space dependent. In [56], an attempt is made to quantify this effect. The model from [81] is used to argue, that although a slight change in the point spread function might occur, the effect is minimal, or at least negligible compared to effect 2). It must be stressed, that this effect can in most cases hardly be separated from effect 2), since the change in point spread function is caused by motion between LRIs. Furthermore, the simulation results shown in Fig. 4.7 and Fig. 4.8 include both effect 2) and 3).

One might argue that looking at the two effects separately makes no sense, but with the introduction of motion compensation, as will be described shortly, the separation of the two effects becomes clearer. The reason is that the compensation method compensates effect 2) but not effect 3). From the results of the compensation, it will therefore be clear that effect 3) is insignificant compared to effect 2).

4.2.4 Motion compensated beamforming

Motion compensation methods for synthetic aperture ultrasound have been considered by a number of researchers, among these [51, 77, 79], considering axial motion only. A 2-D motion compensation method for synthetic aperture B-mode imaging was presented in [80], where two different STA sequences were interleaved, one for making the B-mode image and one for estimating the tissue movement within the image plane. Both the magnitude and direction of movement (within the image plane) were therefore found. The B-mode image was then compensated using the estimated tissue movement.

To illustrate the significance of motion compensation, the simulated data from Fig. 4.8 was compensated using the known direction and magnitude of the movement. The

beamforming was performed as

$$h_m(i,\theta) = \sum_{m'=m-M+1}^{m} \mathbf{L}_{m'} \left(\vec{p_p}(i,\theta) + m' \vec{v}_{known} / f_{prf} \right), \tag{4.19}$$

effectively compensating effect 2) described previously. Still, effects 1) and 3) will affect the compensated result. Fig. 4.9 shows the lateral side-lobe structure after the compensated beamforming for purely axial (left) and purely lateral (right) movement. Comparing Fig. 4.9 to Fig. 4.8, it is clear that after compensation, the side-lobes are almost unaffected by the motion. This again confirms that the most important motion effect in synthetic aperture by far is the incoherence due to movement between LRIs. This also shows the huge potential for compensated beamforming in synthetic aperture, whether for B-mode or flow applications. All compensation methods however rely on accurate estimates of the movement.

In both the journal paper [56] and the conference paper [94], both found in the Appendix, the motion compensated beamforming method from [80] was implemented for synthetic aperture vector flow imaging. Here the case is slightly different from that of [80], where B-mode images are motion compensated. In synthetic aperture vector flow imaging, the goal is to estimate the vector velocities, but to do this better we would like to compensate for the vector velocities. This seems to be a paradox.

In [56, 94], the previous vector velocity estimate was used when beamforming data for the next vector velocity estimate, so that

$$h_m(i,\theta) = \sum_{m'=m-M+1}^{m} \mathbf{L}_{m'} \left(\vec{p_p}(i,\theta) + m' \vec{v}_{est} / f_{prf} \right), \tag{4.20}$$

where $\vec{v}_{est}$ is the previously estimated vector velocity within the image plane, including both direction and magnitude. Hereby, the estimator worked in an adaptive fashion which could potentially increase the estimator accuracy. The method was tested on measured data from a flow rig phantom at different flow directions and pulse repetition frequencies. The flow velocity was constant over time. A significant improvement in estimator performance was seen in one out of four examples, whereas the three other examples hardly were affected.

The method of adaptively compensating the beamforming in synthetic aperture vector flow imaging as presented in [56, 94] has numerous shortcomings. The most significant is probably that no stability is insured in the adaption, and the compensation could potentially decrease the estimator performance. Nevertheless, an adapting compensation scheme could potentially yield great improvements in estimator performance, but the problem of stability must be addressed in future work.

An alternative way of including the motion compensation is by essentially compensating by each vector velocity while probing for it. Thus, instead of performing the regular cross-correlation as described in Section 3.2.1, each lag of the cross-correlation function is calculated by compensating for the vector velocity corresponding to that lag along the current direction. Although extremely computationally expensive, this method might significantly increase performance of synthetic aperture vector flow imaging.

4.3 Separating the blood signal from unwanted clutter

The amplitude of ultrasonic scattering from the surrounding tissue is typically orders of magnitude higher than that of the red blood cells. Some attempt to remove the signal from the quasi-stationary tissue must therefore be made prior to velocity estimation, or the stationary component will dominate. In conventional ultrasonic blood flow estimation, this is usually accomplished by a simple high-pass filtering operation over pulse repetitions, removing low frequency components, which through (2.1) corresponds to a low axial velocity.

Since both the performance of the autocorrelation estimator [9] and the cross-correlation estimator [11] at some velocities will be dependent on the clutter filter used [100], numerous authors have addressed the problem of clutter filtering or stationary echo cancelling. Originally, the delay-line cancellers known from MTI radar applications [8] were often used. This is essentially a FIR filter with impulse response $h(n) = [1, -1]$ applied along pulse repetitions. Designing longer FIR high-pass filters is also widely used, although using a K-tap filter means discarding $K - 1$ echo traces prior to estimation. Initialized IIR filters [101, 102] and regression filters [103] have been proposed, and during the last decade numerous researchers have worked on adaptive clutter filtering, which mainly is accomplished through decomposition onto for instance the eigenvector space [104–108].

When estimating only the axial velocity component, (2.1) applies, and although sometimes partly overlapping, the tissue and blood component can usually be separated adequately for velocity estimation. In vector velocity estimation, the problem is significantly more complex [107, 109]. To further address this issue, a simplified model of the slow time signal must be derived.

4.3.1 Modelling the slow-time signal

A simplified model of the slow-time signal is derived through considering the point spread function (PSF). The two-dimensional PSF is modelled as separable in axial and lateral space

$$psf(z, x) = f(z)g(x). \tag{4.21}$$

The axial spatial signal $f(z)$ depends only on the emitted waveform $p(t)$ which in the following includes the two-way electromechanical impulse response of the imaging system, so that $f(z) = p(2z/c)$. The lateral spatial signal in turn depends on the effective aperture and the aperture smoothing function. In the following we will restrict the discussion to concern the focus point only, which is a natural restriction, since synthetic aperture imaging feature dynamic focus in both transmit and receive. Furthermore, we will disregard all motion effects described in the previous section. The aperture smoothing function in the focus point is given by [110]

$$W(\vec{k}) = \int_{-\infty}^{\infty} a_{t/r}(\vec{x}) e^{j\vec{k}\cdot\vec{x}} d\vec{x}, \tag{4.22}$$

where $a_{t/r}(\vec{x})$ is the effective aperture and $\vec{k}$ is the k-vector of spatial frequencies in the x-, y-, and z-directions. Assuming the effective aperture is a linear array of $2N_m + 1$ omnidirectional point sources, equally spaced at distance d, the effective aperture can be written as a discrete function $a(m) = a_{t/r}([md, 0, 0])$, where $m = [-N_m, ..., N_m]$, and the

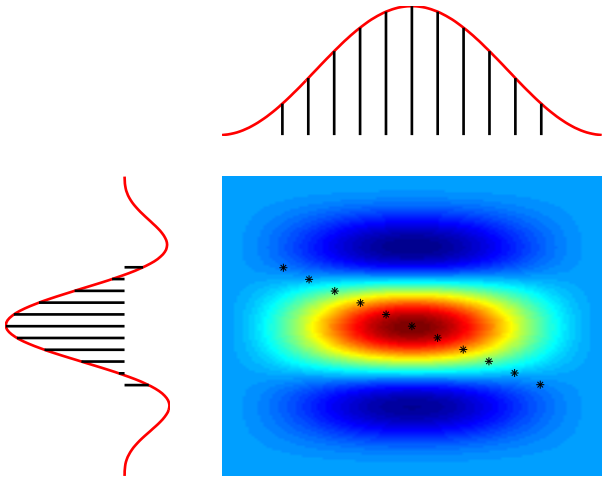

Figure 4.10: The PSF is assumed separable in an axial function $f(z)$ (left, red) and a lateral function $g(x)$ (top, red). The slow-time signal is modelled as a spatial sampling in the PSF, corresponding to sampling $f(z)$ and $g(x)$ as shown (black).

aperture smoothing function in the focus point reduces to

$$W(\vec{k}) = \sum_{m=-N_m}^{N_m} a(m) e^{jk_x md}. \tag{4.23}$$

Here the spatial frequency along the x-direction, in units of radians per meter, is

$$k_x = -\frac{\omega_0}{c}\sin(\alpha) = -\frac{2\pi f_0}{c}\frac{x}{r} \approx -\frac{2\pi}{\lambda z}x, \tag{4.24}$$

where α is the angle from the aperture center axis to the point (x, z), $r = \sqrt{x^2 + z^2}$ is the distance from the aperture center to (x, z), and the approximation $r \approx z$ is made assuming a small angle α. The function $g(x)$ is therefore modelled as

$$g(x) = \sum_{m=-N_m}^{N_m} a(m) e^{-j\frac{2\pi md}{\lambda z}x}, \tag{4.25}$$

which is the Fourier transform of the effective aperture.

When a scatterer moves while being imaged, this approximately corresponds to sampling the PSF of this point spatially. As a first approximation we can therefore sample $psf(z, x)$ spatially to model a slow time signal at a given vector velocity. When the blood moves at velocity magnitude v in the direction θ with respect to the z-axis, the spatial translation between pulses along axial and lateral space will be

$$\begin{aligned} \Delta z &= v\cos(\theta)T \\ \Delta x &= v\sin(\theta)T, \end{aligned} \tag{4.26}$$

where T is the time between samples. The slow-time signal can thus be modelled as

$$s(n) = f(n\Delta z)g(n\Delta x) \tag{4.27}$$

The signal $s(n)$ is a sampled version of the continuous signal $s_c(t)$, where the sampling is performed at a sampling frequency of f_{prf}/M. M is again the number of LRIs summed

to create a HRI, and as described in Chapter 3, only HRIs M emissions apart are created in the same way. Notice also that $T = MT_{prf}$. The continuous signal $s_c(t)$ which is given by

$$s_c(t) = f(vt\cos\theta)g(vt\sin\theta), \tag{4.28}$$

has the spectrum

$$S_c(f) = \mathcal{F}\{s_c(t)\} = \mathcal{F}\{f(vt\cos\theta)\} \star \mathcal{F}\{g(vt\sin\theta)\}, \tag{4.29}$$

where $\mathcal{F}\{\cdot\}$ denotes the Fourier transform with respect to time. In the axial direction we have

$$\begin{aligned} \mathcal{F}\{f(vt\cos\theta)\} &= \mathcal{F}\left\{p\left(\frac{2v\cos\theta}{c}t\right)\right\} \\ &= \frac{c}{2|v\cos\theta|}P\left(\frac{c}{2v\cos\theta}f\right). \end{aligned} \tag{4.30}$$

This correspond to the spectrum of the emitted signal $p(t)$, where the frequency axis is scaled according to (2.1). The axis scales linearly with $v_z = v\sin\theta$. In the lateral direction we have

$$\begin{aligned} \mathcal{F}\{g(vt\sin\theta)\} &= \mathcal{F}\left\{\sum_{m=-N_m}^{N_m} a(m)e^{-j\frac{2\pi md}{\lambda z}(vt\sin\theta)}\right\} \\ &= \int_{-\infty}^{\infty}\left[\sum_{m=-N_m}^{N_m} a(m)e^{-j\frac{2\pi md}{\lambda z}(vt\sin\theta)}\right]e^{j2\pi ft}dt \\ &= \sum_{m=-N_m}^{N_m} a(m)\int_{-\infty}^{\infty} e^{j2\pi(f-\frac{mdv\sin\theta}{\lambda z})t}dt \\ &= \sum_{m=-N_m}^{N_m} a(m)\delta(f-\frac{mdv\sin\theta}{\lambda z}). \end{aligned} \tag{4.31}$$

This spectrum has the shape of the effective aperture, where the frequency axis is scaled by the lateral velocity component $v_x = v\sin\theta$. From this we can see that if the flow is purely axial $\theta = 0°$, $\mathcal{F}\{g(vt\sin\theta)\}$ reduces to a δ-function at $f = 0$ and $S_c(f)$ will resemble the spectrum of the emitted signal. Likewise, when the flow direction approaches the lateral direction $\theta \to 90°$, $\mathcal{F}\{f(vt\cos\theta)\}$ approaches a δ-function at $f = 0$, and $S_c(f)$ will resemble the effective aperture. At all intermediate angles, the spectrum $S_c(f)$ will be a convolution of the two, effectively smearing the spectral content.

As a slight parenthesis, notice that this broadening of the axial spectrum through the convolution in (4.29) is what is used for estimating the lateral velocity component in [25]. The model also qualitatively correspond to the findings in Section 3.3 of [32], where the slow-time spectrum of Transverse Oscillations data was shown to have four peaks.

Since the signal $s(n)$ is a sampled version of $s_c(t)$, its spectrum will be repeated at all multiples of the sampling frequency f_{prf}/M

$$S(f) = \frac{f_{prf}}{M}\sum_{k=-\infty}^{\infty} S_c\left(f + k\frac{f_{prf}}{M}\right). \tag{4.32}$$

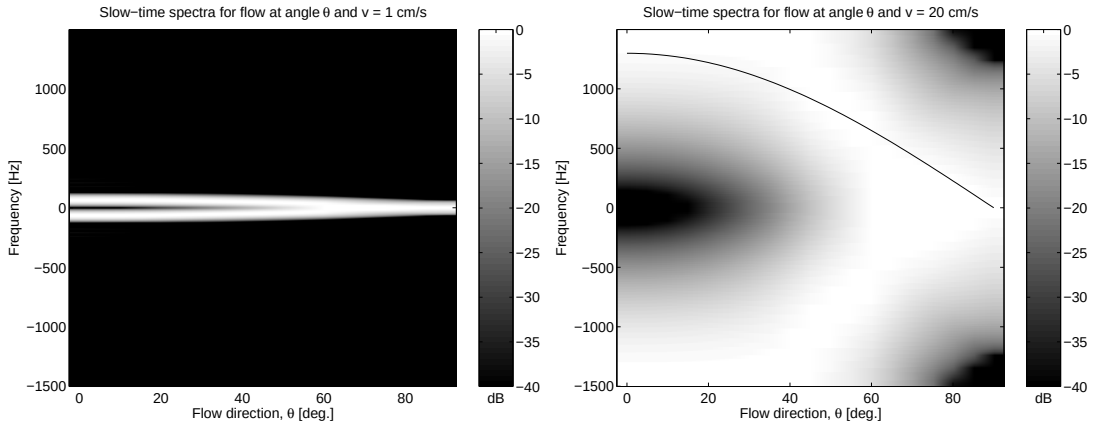

Figure 4.11: The modelled slow-time spectra at different flow directions θ assuming a flow velocity of $v = 1$ cm/s (left), corresponding to a typical tissue component during systole, or a velocity of $v = 20$ cm/s (right), corresponding to a typical flow velocity in a large artery during diastole, or in a large vein.

4.3.2 Slow-time spectrum in realistic situation

The model is visualized by defining a number of parameters close to a realistic situation. The parameter choice reflects scanning a carotid artery at depth $z = 20$ mm, using a pulse repetition frequency of $f_{prf} = 24$ kHz, an emission sequence of $M = 8$ emissions, and a center frequency of $f_0 = 5$ MHz.

Table 4.1: Parameters for model.

Speed of sound, c	1540 m/s
Center frequency, f_0	5 MHz
Effective pulse repetition frequency, f_{prf}/M	3 kHz
Depth in tissue, z	20 mm

The emitted waveform $p(t)$ was set as two cycles of a sinusoidal function at f_0 tapered by a Hamming window, whereas the effective aperture $a(n)$ was set as a triangular function of width 76.5 mm, corresponding to the convolution of two 128 element arrays with pitch $d = 0.3$ mm. The model just derived was used to find the slow time spectra at different velocities and different flow directions.

Fig. 4.11 shows the modelled slow-time spectra at different flow angles for a velocity of $v = 1$ cm/s (left), a realistic velocity for the wall of the common carotid during systole [111], and for a velocity of $v = 20$ cm/s (right), a velocity close to what is normally seen during diastole in for instance the common carotid. For the tissue example (left), the slow-time spectrum has no components above ~ 100 Hz, regardless of the direction of movement θ. For the $v = 20$ cm/s example (right), the modelled slow-time spectra are much broader. The spectra peak at frequencies close to that predicted from (2.1), which is marked by a black solid line, but seam to alias at flow directions of $\theta < 80°$. Furthermore, the spectra have components at $f = 0$ for $\theta > 20°$. For a velocity of $v = 1$ m/s (not shown), the spectra are flat regardless of flow direction.

In other words, according to the derived model, the slow-time spectra of tissue components will be concentrated around $f = 0$, and even at realistic peak velocities of the carotid wall of $v = 1$ cm/s [111] the slow-time spectra will be below $f \sim 100$ Hz, even

when $\theta = 0°$. The slow-time spectrum of a flow component, even at a velocity of $v = 20$ cm/s often seen in the diastole of large arteries or in many veins, will be largely spread out, essentially covering the entire range of frequencies. Also, even at this relatively low velocity, aliasing occurs at directions not close to the transverse. At $v = 1$ m/s, a high degree of aliasing causes the spectra to be almost flat, regardless of the flow direction.

The model shows how the clutter filtering in synthetic aperture vector flow imaging is possible, but also how it might affect the velocity estimates. A tissue component can easily be removed by the use of a high-pass filter designed to remove the component in Fig. 4.11, left. Hereby the tissue component will be completely removed. Nevertheless, the filter will simultaneously have removed some of the blood flow signal around $f = 0$, essentially changing the flow signal prior to applying the cross-correlation estimator. This is a problem presently not completely understood or solved.

4.3.3 Possible refinements of filtering approach

Since the flow signal and the unwanted clutter signal overlap in the frequency domain, no filter that separates according to frequency content will ever be able to completely remove the clutter component without affecting the flow signal. This is true even though the continuous data flow in synthetic aperture vector flow imaging enables using very long clutter filters with very short transition bands.

To refine the filtering approach, the blood signal and the unwanted clutter signal might have to be separated in another way than through filtering. One approach could also be to estimate the blood signal within the presence of the dominating clutter signal, thereby not trying to remove the clutter but incorporating it in the estimation model. This approach was considered for conventional velocity estimation systems in [112]. Alternatively, the filters could be adapted to the signal at hand, and at least only the smallest possible part of the flow signal is removed while suppressing the clutter. The paper [106] gives a good overview of some of the possibilities previously tested for conventional systems, including clutter filtering through eigenvector decomposition.

A few preliminary tests of the adaptive filtering approaches described in [106] for synthetic aperture flow have been performed during this project, but without any conclusive results. For the eigenvector decomposition methods, the clutter signal and the flow signal seemed not to separate well into different eigenvectors. This work was therefore abandoned for other projects.

To conclude the discussion of separating the blood signal from unwanted clutter; this is a problem still to be solved. The *in-vivo* results presented in Chapter 5 are all made using conventional high-pass FIR filters of various lengths, but great improvement of the results might be expected if the separation problem is solved.

CHAPTER

FIVE

In-vivo investigations using synthetic aperture vector flow imaging

Diagnostic ultrasound equipment is designed to non-invasively image parts of the human anatomy or physiology, as for instance visualizing the blood flow velocity in some vessel over the cardiac cycle. Fortunately, most people have beating hearts and draw their breath, creating motion that is distributed to parts of the body. But this motion might create some problems as seen in Section 4.3. When performing *in-vivo* scans, a number of regulations set by the FDA [113] must be obeyed, in order to keep the intensity of the emitted acoustic waves below certain thresholds. This limits the amplitude of the acoustic waveform. Furthermore, in the human body, frequency dependent attenuation occurs, lowering the SNR of the received signals and challenging the estimators. Also, since the true blood flow velocity in a vessel at each time instance is not known, the results cannot be readily validated. So when performing *in-vivo* scans, many things are therefore different from phantom experiments where everything can be controlled and a reference is readily available. Nevertheless, since these applications are essentially what diagnostic ultrasound equipment is designed for, new methods must be tested in *in-vivo* situations.

5.1 Previous in-vivo results of synthetic aperture flow imaging

Prior to this PhD project, no *in-vivo* synthetic aperture vector flow imaging examples had been published, where both the flow direction and magnitude were found automatically. Still some examples had been published where either only the axial component of the velocity was found or the flow direction was provided by the user.

The first *in-vivo* synthetic aperture flow image was presented in [52], where the common carotid artery of a healthy 29-year male volunteer was scanned. In this paper, only the axial component of the velocity was found. In [88, 89], another example of synthetic aperture flow imaging was shown. Both the common carotid artery and the jugular vein were captured within the image plane. In this example, the data were beamformed along the flow direction as shown in Fig. 3.6, yielding the velocity magnitude along the flow direction. This of course assumes the flow direction is known, and in this example it was provided by the user. This example was performed at quite low pulse repetition frequency of $f_{prf} = 3$ kHz and possibly therefore worked best at low velocities [88].

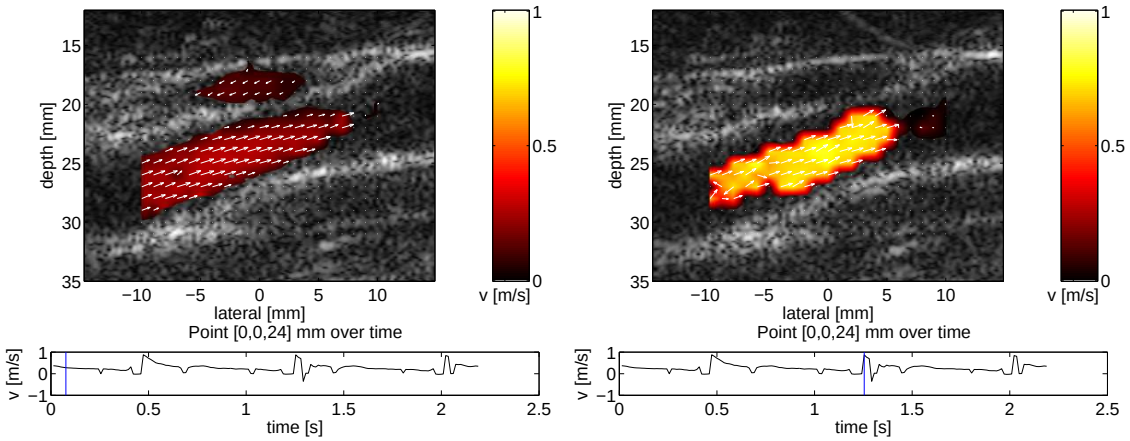

Figure 5.1: Synthetic aperture vector flow imaging of the common carotid artery. The left figure shows a frame during diastole, while the right figure show a frame during systole. The graphs beneath the figures show the velocity at $(x, z) = (0, 24)$ mm over time. Figures from [93, 114].

5.2 The common carotid artery

Throughout the project, a number of *in-vivo* scans have been performed to test and validate synthetic aperture vector flow imaging under *in-vivo* conditions. Some of these have been published [93, 114, 115], and one of these is shown in Fig. 5.1. This scan shows the common carotid artery of a healthy 32-year-old male volunteer, and above that a cross-section of the jugular vein. The left figure is from diastole, while the right figure is from the systolic phase. The color coding indicates the velocity magnitude, and the arrows indicate the direction of flow. The graphs below the frames show the velocity magnitude estimated in point $(x, z) = (0, 24)$ mm over time, and a vertical bar indicates where the individual frames are acquired. The frame rate was approximately 78 frames/second.

For this scan, the same parameters as in [89] were used, except the pulse repetition frequency was increased to $f_{prf} = 10$ kHz. Thereby the hope was to avoid the breakdown at systole described in [89]. As it is seen in Fig. 5.1 (right), this is partly achieved, although the vessel is not completely filled. The discrimination between tissue and blood flow was done by comparing the energy before and after clutter filtering and thresholding the value [93]. But the largest difference between the example in Fig. 5.1 and that of [89] is that here the flow direction is not supplied by the user, but is estimated locally by the method described in Section 3.2.2.

The B-mode images in Fig. 5.1 were made from the flow sequence, where only $M = 8$ virtual sources were used. Therefore, the quality of the B-mode images is quite poor, even at the dynamic range of 30 dB used in Fig. 5.1. This shows the need for interleaving a second sequence for creating B-mode images of a sufficient quality.

5.3 The femoral artery and vein

The next example is from the femoral triangle, showing the femoral artery and the confluence of the femoral vein and the saphenous vein. It has previously been published in the conference paper [115] which can be found in the Appendix. The three images in

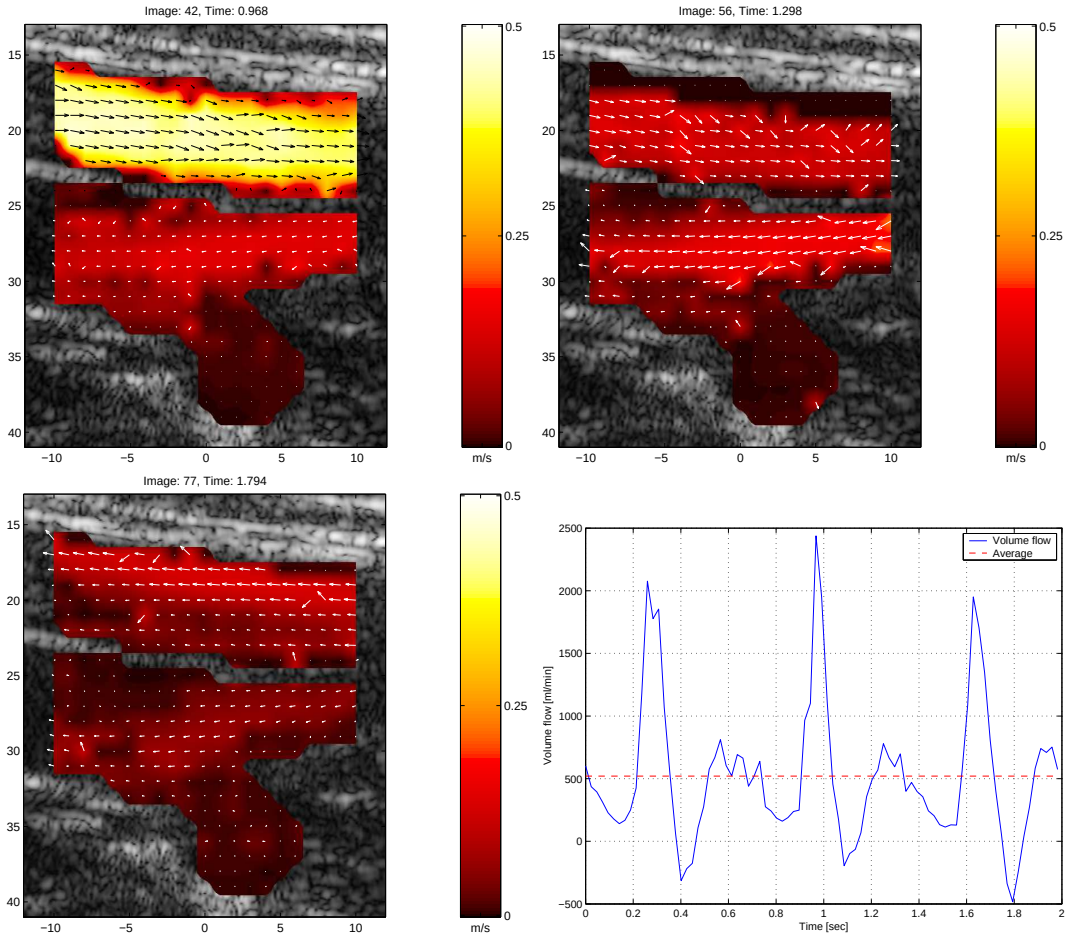

Figure 5.2: Synthetic aperture vector flow images of the femoral artery and the confluence of the femoral vein and the saphenous vein. The three images are from different time instances during the cardiac cycle. This includes the systole (top, left), the diastole (top right), and the time of reverse flow in the femoral vein (bottom, left). Notice, that the scaling and coloring of the arrows is different in the top left image. The bottom right figure shows the estimated volume flow in the femoral artery as a function of time. Figures from [115].

Fig. 5.2 show this example during different instances of time, including the systole (top, left), the diastole (top, right), and the time of reverse flow (bottom, left). In all three images, the femoral artery is seen at the top, the femoral vein enters from the right, while a cross-section of the saphenous vein is seen at the bottom center.

The B-mode images are here created from a different sequence, using 118 emissions covering all possible positions of 11 consecutive elements on a 128 element linear array transducer. This B-mode sequence has been interleaved 1-to-1 with the flow sequence, which means that every even emission is a B-mode emission, while every odd emission is a flow emission. Thereby, the effective pulse repetition frequency of the flow sequence is halved compared to normally $f_{eff} = f_{prf}/(2M)$, but the quality of the B-mode images, here shown in 40 dB dynamic range, could potentially be better than in Fig. 5.1. The reason why no large improvement in B-mode image quality is seen in this example is an error in the multiplexor setup slightly degrading the focus in the B-mode sequence. This error was later found and is not present in the following examples.

The discrimination between tissue and blood flow in Fig. 5.2 is not done automatically, as in the previous example. The reason for this is that the discrimination using the energy before and after clutter filtering removed a lot of valid estimates, while the B-mode images did not have sufficient quality to support an automatic discrimination procedure.

The volume flow in the femoral artery was found from the vector velocity estimates. The estimates were re-sampled to fit a 8 mm long grid following the artery, and the projection of the estimates onto the visually determined flow direction was found. A rotationally symmetric vessel geometry was assumed, and the estimates were averaged along the 8 mm. In Fig. 5.2 (bottom, right) the estimated volume flow is shown as a function of time. The average over the two seconds is just above 500 ml/min. A magnetic resonance imaging study found in literature showed an average volume flow in the 411 ml/min for 25 healthy male subjects between 26 and 80 years of age. A statistically significant tendency to decreased volume flow as a function of age was found in the study. Thus, the estimated volume flow just above 500 ml/min for the 26-year-old volunteer seems plausible.

5.4 The carotid bifurcation

The conference paper [115] presented another example of synthetic aperture vector flow imaging. The carotid bifurcation of a healthy 32-year-old male volunteer was scanned for approximately 2 seconds, and an image from the late systolic phase is shown in Fig. 5.3. The common carotid enters from the right and splits into the internal carotid (top) and the external carotid (bottom). In this example the flow sequence and the B-mode sequence are interleaved M-to-1, meaning that after every M flow emissions, one B-mode emission is carried out. This results in an effective pulse repetition frequency of $f_{eff} = f_{prf}/(M+1)$ but lowers the frame rate of the B-mode images to just below 20 frames/second for the current setup.

The image in Fig. 5.3 reveals some interesting aspects which are not readily visible using conventional ultrasonics color flow mapping, where only the axial velocity component is shown. In Fig. 5.3 a high velocity of almost 1 m/s is seen in the common carotid artery (right) and close to the separating wall in both the internal (top) and external (bottom) carotid. In the carotid bulb, it seems like a vortex is building up. This is not an unknown phenomenon. It agrees with both MRI measurements and numerical simulations of flow in the carotid bifurcation geometry [21], and with ultrasound vector flow measurements of the carotid bifurcation using Transverse Oscillation [32, 34].

Discrimination between the B-mode image and the color-coded flow visualization is made from the B-mode image data. The B-mode image is created and both a median filtering and a low-pass filtering is performed before a threshold is set. If the filtered B-mode image is below this value, flow information is shown and vice-versa. This discrimination approach works well for large vessels, but will probably not work for small vessels. Also, it should be noted that the multiplexor error described in the previous section was corrected prior to this measurement.

5.5 The common carotid artery, revisited

A small in-vivo study of synthetic aperture vector flow imaging was carried out as a collaboration between colleagues at CFU and medical doctors from the Department of

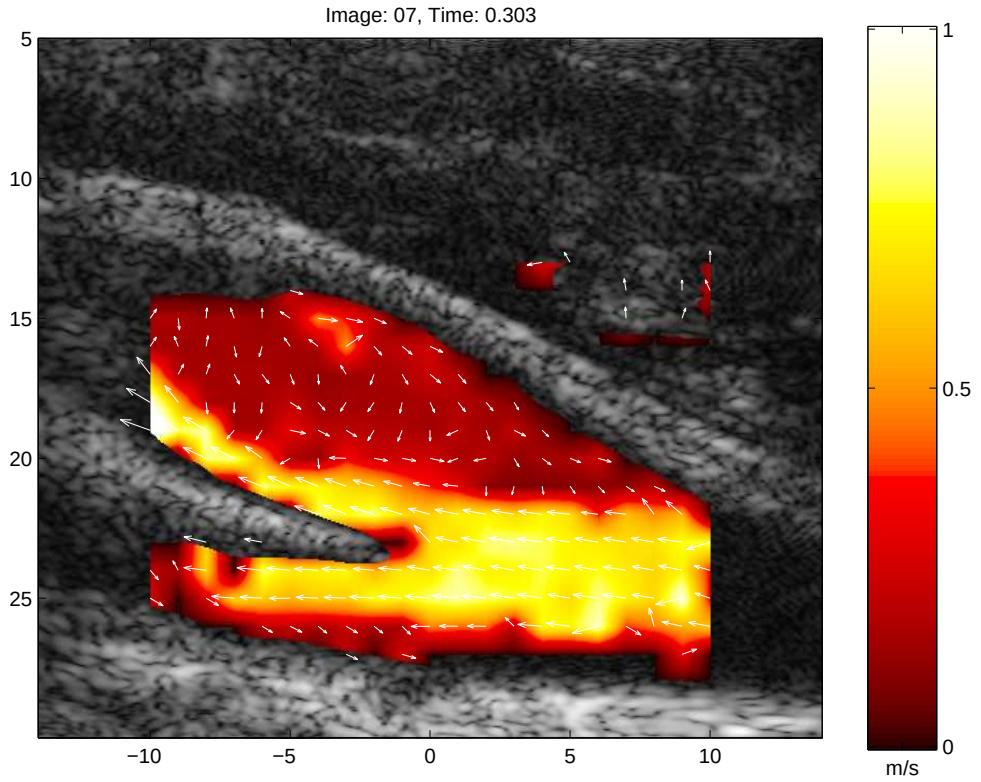

Figure 5.3: The carotid bifurcation of a healthy 32-year-old male volunteer in late systole. Figure from [115].

Radiology at University Hospital of Copenhagen, Rigshospitalet. Eleven healthy volunteers (seven males and four females, mean age 32 years, range 24 - 44 years) were scanned using three different ultrasonic vector flow methods and MR phase contrast imaging, and the stroke volume in the right common carotid artery was found using the three ultrasound methods and MR. Each volunteer was, thus, scanned four times on four different days. Thereby, each ultrasound method could be compared to MR phase contrast imaging which was used as a reference. The ultrasonic vector flow methods include Transverse Oscillation [34], directional beamforming [40] with a few twists [116], and synthetic aperture vector flow imaging. The results of this study are to be published in [117].

Part of the study was scanning the right side common carotid artery of 11 healthy volunteers with synthetic aperture vector flow imaging. The same setup as the carotid bifurcation scan [115] was used, so for the parameters, the reader is referred to [115] in the Appendix. The only difference is the clutter filter. In the present *in-vivo* study, a 65 tap high-pass FIR clutter filter designed using the Parks-McClellan method [118] was used. The transfer function of this filter is show in Fig. 5.4.

The filter in Fig. 5.4 is shown on a frequency scale which is scaled according to the effective pulse repetition frequency $f_{eff} = f_{prf}/(M+1)$. All frequencies below $f_p = 0.05 f_{eff} = 0.05 f_{prf}/(M+1)$ are attenuated at least -80 dB. This frequency corresponds to an axial velocity of

$$v_z = \frac{c f_p}{2 f_0} = \frac{c f_{prf}}{40(M+1) f_0} = \frac{1540\,\mathrm{m/s} \cdot 21\,\mathrm{kHz}}{40 \cdot (8+1) \cdot 6.2\,\mathrm{MHz}} = 1.45\,\mathrm{cm/s} \tag{5.1}$$

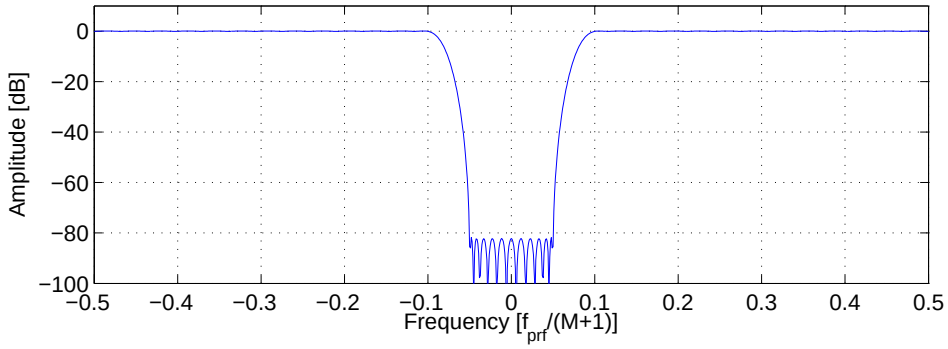

Figure 5.4: Clutter filter used for all eleven volunteers in the in-vivo study. The horizontal frequency axis is scaled by the effective pulse repetition frequency.

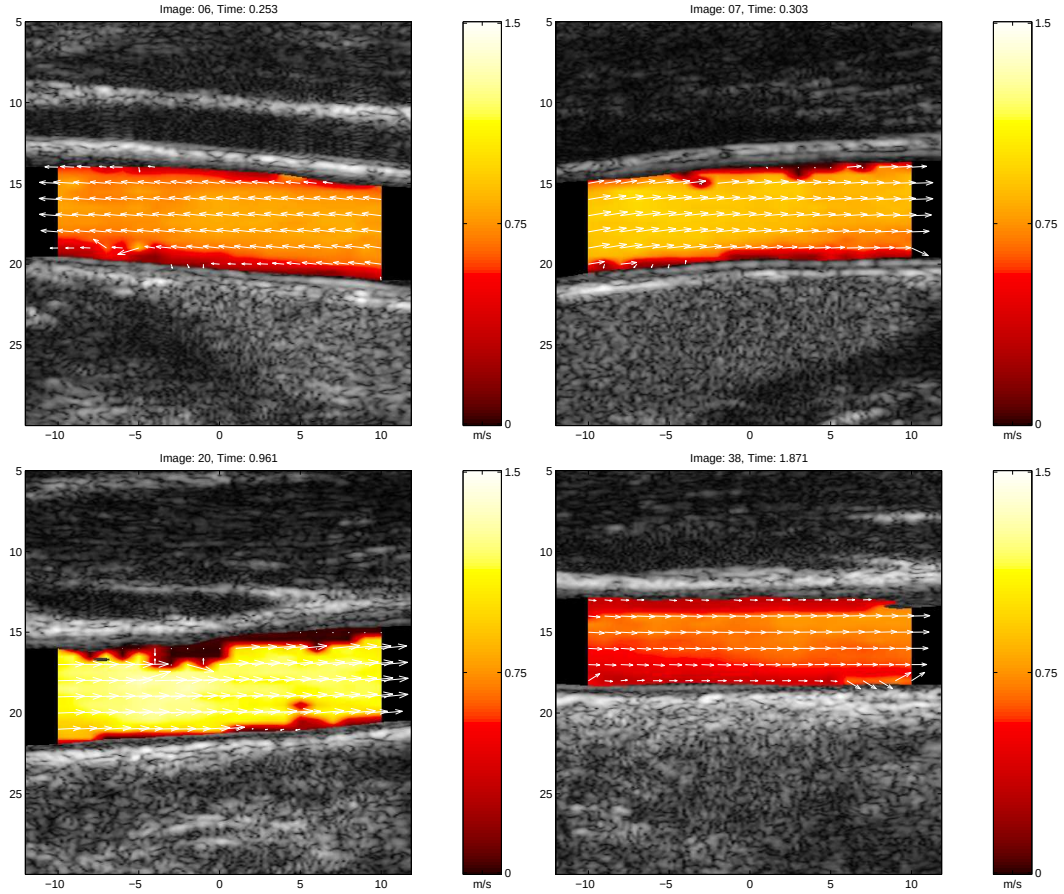

Figure 5.5: The common carotid artery of four healthy volunteers during systole. From the top left the volunteers are number 4, 2, 6, and 9.

at the center frequency of the transducer $f_0 = 6.2$ MHz. All frequencies above $f_p = 0.1 f_{eff}$, corresponding to $v_z = 2.9$ cm/s at f_0, are passed unaltered. Comparing this to the findings of Section 4.3, this filter should remove all of the clutter signal but will also in most cases remove some of the flow signal.

Synthetic aperture vector flow movies were created for all 11 volunteers and frames from some of these are shown here. Fig. 5.5 shows the right side common carotid artery during systole for four different volunteers. These are volunteer number 4 (top left), number 2

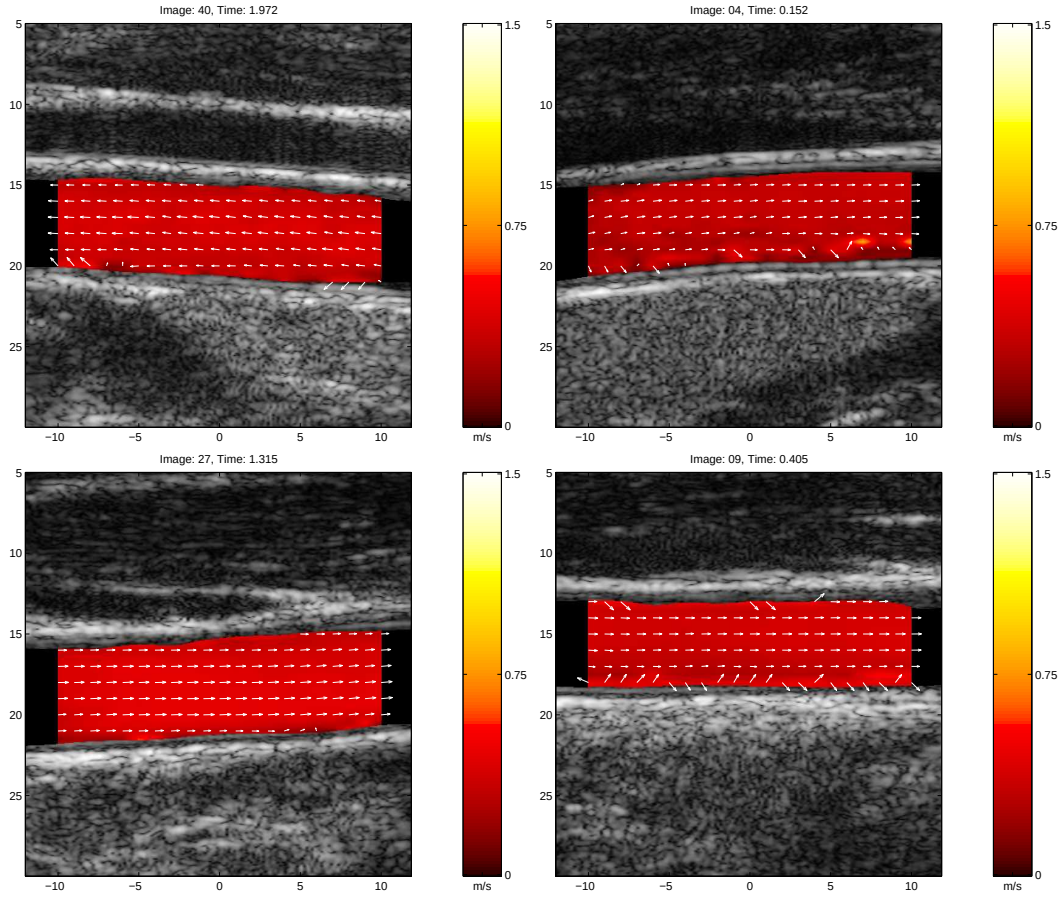

Figure 5.6: The common carotid artery of four healthy volunteers during diastole. From the top left the volunteers are number 4, 2, 6, and 9.

(top right), number 6 (bottom left), and number 9 (bottom right). A few false estimates are seen as holes in the colored areas, especially for volunteer number 6, and some arrows at the vessel edge, mainly for volunteer number 9, do not follow the vessel edge. While the systolic peak velocity for volunteer 6 seems to be close to 1.5 m/s, the peak velocity for volunteer 9 is only half of that.

Fig. 5.6 shows frames from the diastolic phase for the same four volunteers. Here the velocities are much lower, but still the arrows showing the flow direction seem to follow the vessel edges and the velocities seem to fall off close to the edge. One exception is volunteer 9 (lower right part of Fig. 5.6). Here the estimated flow direction close to the border seems almost random and the velocity estimates are higher close to the edge than in the vessel center. More on this later.

The volume flow over time in the right common carotid artery of the 11 volunteers was found from the vector velocity estimates. This was found by an automatic procedure developed at CFU and described in [119]. Basically, the vessel borders are found, from that the vessel center axis is approximated by a polynomium, and the projection of the vector velocity estimates along the direction of the center axis is found. By assuming a rotationally symmetric vessel, the volume flow is found at multiple cross-sections of the vessel, and these volume flow estimates are averaged along the vessel. Likewise, the volume flow in the right common carotid artery of all volunteers is found from the MR phase contrast data. An automatic procedure, which is further described in [119], was

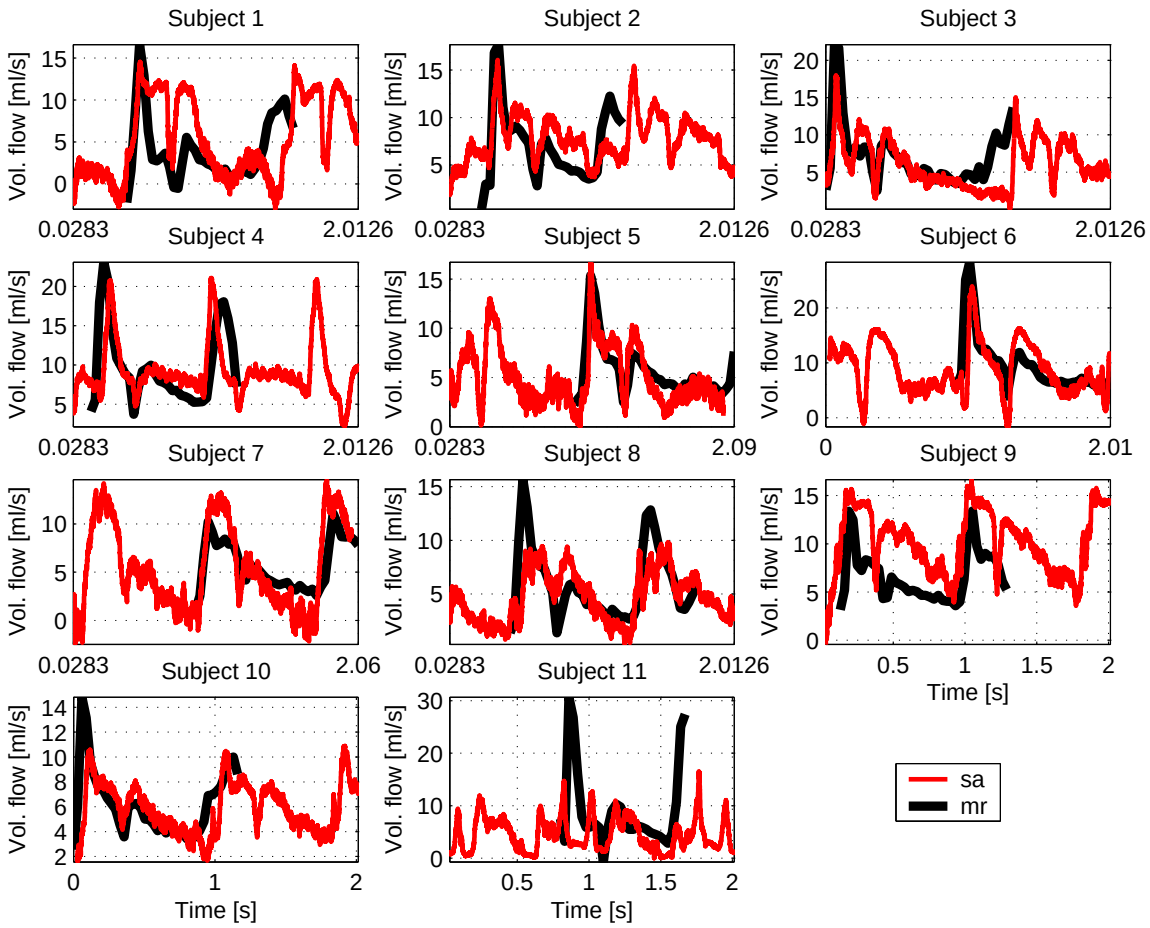

Figure 5.7: Volume flow over time for the 11 volunteer, found using MR angiography (black) and synthetic aperture vector flow imaging (red).

also developed for this. For each volunteer, the synthetic aperture volume flow estimates can then be compared to those found from MR phase contrast imaging.

Fig. 5.7 shows the volume flow found using synthetic aperture vector flow imaging (red) and the volume flow found using MR phase contrast imaging (black). The two curves are aligned temporally to aid visual comparison. It is hard to draw conclusions across all volunteers, but a tendency is seen in a slight underestimation of the systolic volume flow and a slight overestimation in the diastolic phase. Also, there is a clear overestimation of the volume flow for volunteers 1 and 9, and a fall-out of the systole for volunteer 11. Nevertheless, the curves are generally well aligned and show the same tendencies.

Synthetic aperture vector flow imaging was compared to MR phase contrast imaging through stroke volume, since this measure is less heart rate dependent and therefore a more reliable parameter, when comparing measurements obtained at two different occasions [119,120]. Fig. 5.8 shows the stroke volume of the 11 volunteers estimated from the synthetic aperture velocity estimates and from MR phase contrast imaging. The correlation between the ultrasound method and MRI was $R = 0.71$ ($p < 0.05$; 95% CI: 0.19 to 0.92) [117], which is a quite weak correlation. The dashed line gives the line of perfect fit, whereas the solid line gives the linear regression line. The stroke volume seems to be overestimated by the synthetic aperture method for 3 of the volunteers, volunteer 1, 2, and 9, all seen beneath the solid line.

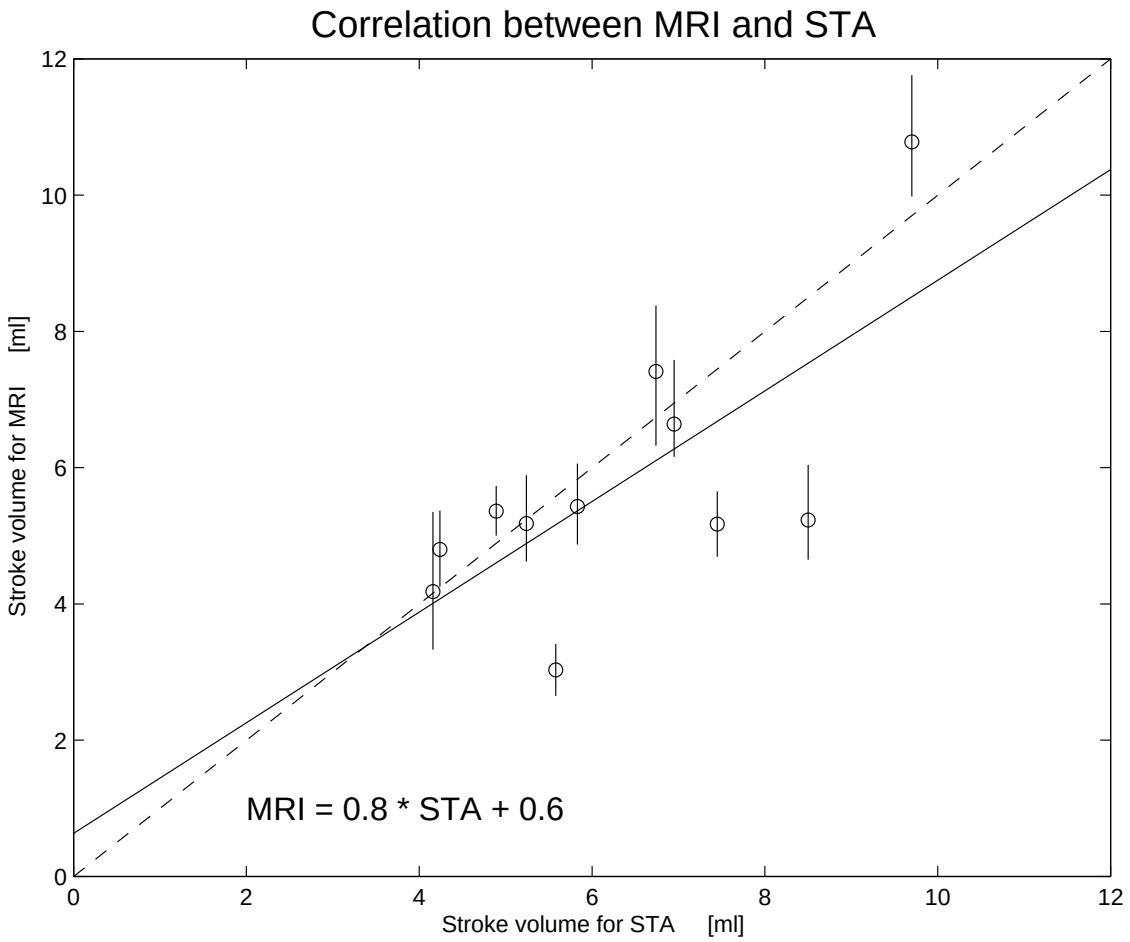

Figure 5.8: The stroke volume of the 11 volunteers estimated from the synthetic aperture vector flow estimates and the MR phase contrast imaging. The dashed line is the line of perfect fit, whereas the solid line is the linear regression line. The stroke volume seems to be overestimated by the synthetic aperture method for 3 of the volunteers. The vertical lines at each estimates indicates the range of MRI stroke volume when enforcing the restriction of circular symmetry. Figure from [117].

One of the volunteers, where the stroke volume is overestimated is volunteer number 9. Looking at Fig. 5.7, a clear overestimation of the volume flow is seen in the diastole, whereas the peak systolic flow is only slightly overestimated. Vector flow frames for volunteer 9 are seen in the bottom right corner of Fig. 5.5 and Fig. 5.6 for systole and diastole, respectively. In Fig. 5.5, bottom right, a few velocity estimates at wrong directions and increased velocity are seen at the bottom right vessel edge. In Fig. 5.6, bottom right, increased velocity estimates at wrong directions are seen along the entire vessel border. Although these errors might seem insignificant visually, the circular assumption while computing the volume flow weights these errors quite high since the outermost circular sections have much larger area than the innermost.

Fig. 5.7 indicates a drop-out of synthetic aperture vector flow imaging during systole for volunteer 11. The tissue movement for this volunteer was far larger than for the other volunteers. Therefore, the filter in Fig. 5.4 did not suppress the tissue signal sufficiently at the peak systole, and mainly the tissue component was found by the estimator causing a significant bias during systole.

It is extremely difficult to draw significant conclusions from a study of only 11 subjects, but the data can definitely be used for studying tendencies and for development purposes. One indication supported by the data is the lack of a constant clutter filter which works across all volunteers throughout the cardiac cycle. The filter shown in Fig. 5.4 does not remove the clutter component sufficiently for volunteer 11, while it removes the flow signal close to the vessel borders at diastole for volunteer 1, 2, and 9. This supports the indication of Section 4.3, that the clutter filtering is presently the Achilles heal of synthetic aperture vector flow imaging.

CHAPTER

SIX

Multi-frequency encoding for fast color flow and quadroplex imaging

The following chapter describes another research project carried out as part of the PhD project. In principle it has no direct connection to synthetic aperture vector flow imaging, but it aims at solving one of the problems in conventional CFM systems; the frame rate problem. The method is described in a journal paper [121] submitted for the IEEE Transactions on Ultrasonics, Ferroelectrics, and Frequency Control, and a conference paper [122] presented at the IEEE Ultrasonics Symposium 2007 in New York. Both papers are found in the Appendix.

6.1 Purpose

The purpose of this work is to increase the frame rate of CFM systems by simultaneously acquiring data along multiple lines in the image plane. This is as such not a new idea. Simultaneous acquisition of multiple parallel beams (the so-called multi-line acquisition) is a concept used for decades [27], where a broad transmit beam is emitted, and a number of parallel lines are beamformed at the receiver. The method has also been used for conventional blood flow estimation [123] and for vector flow imaging using speckle tracking [26]. But for this method to work, the transmit beam must be broad, potentially reducing the SNR and the lateral resolution, and a number of artifacts might appear due to the misalignment of the transmitter and the receiver [124]. Furthermore, the receive beams must be placed inside the broad transmit beam, limiting the geometric flexibility when designing the imaging sequence.

To acquire multiple lines simultaneously, a multi-frequency encoding method is used, emitting multiple signals simultaneously and separating them in the receiver. A similar encoding method has previously been used for frequency division in synthetic aperture imaging, where a broad-band pulse was synthesized using multiple narrow-band signals [71] and for directional velocity estimation in synthetic transmit aperture ultrasound [72]. The significant difference is that in this work, no broad-band synthesis is performed, but the narrow-band signals are merely used directly for velocity estimation. The present work is conducted in collaboration with the authors of [71,72].

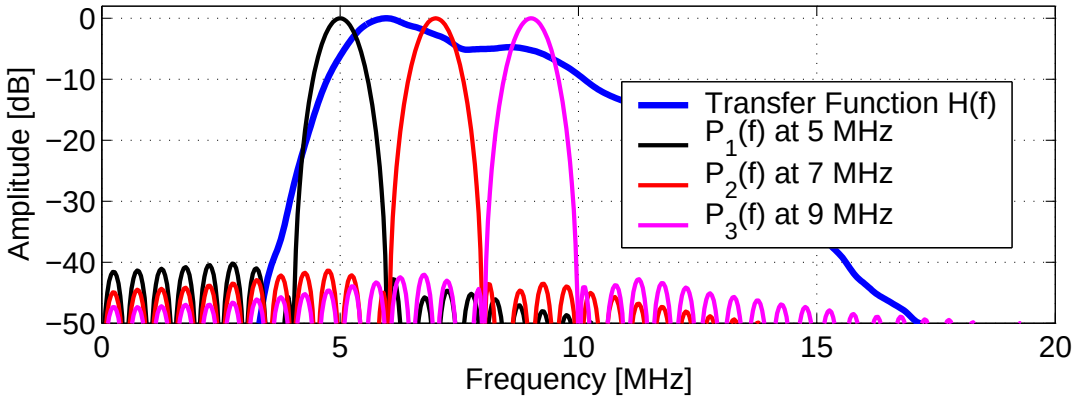

Figure 6.1: Two-way system transfer function (blue) and the amplitude spectra of the three signals used for encoding. Notice that the cross-talk between the signals is below -40 dB.

6.2 Encoding method for CFM and Quadroplex imaging

The method presented here and described in the papers [121, 122] uses the fact that the autocorrelation method [9] is a narrow-band method but works across a wide range of frequencies. Therefore multiple lines for a CFM can be acquired using different narrow-band signals with disjoint spectral support at different spatial locations. An example of such signals is shown in Fig. 6.1. Here 3 narrow band signals are shown which are sinusoidal signals of length $T = 2$ μs with a Hamming tapering at center frequencies of $f_0 = 5$, 7, and 9 MHz. The transfer function of the transducer and measurement system used [125] is shown in blue. Notice how all three bands experience a minimum of attenuation by the transducer and measurement system, and how the spectral cross-talk between signals is below -40 dB.

The multiple signals can be emitted simultaneously and be separated in the receiver by filters matched to the emitted waveforms. The lines can then be beamformed as usual, and the autocorrelation method is applied as is normally done. The method is summarized in Fig. 6.2 which shows the difference between the normal pulsing strategy and the proposed. By using M different signals, the data for a color flow map is acquired using only $1/M$ times the time normally spent, and the frame rate can thus be increased by a factor of M. Ultimately, this method could be combined with the multi-line acquisition method from [27], yielding a frame rate increase of M times the number of parallel lines. This could potentially enable real-time CFM of three-dimensional volumes at an acceptable frame rate. Today 3-D CFMs are made using ECG-gating and are principally not real-time.

The proposed method has another and maybe more interesting application. Since the lines can be acquired simultaneously and totally independent, they can be placed wherever it is convenient. This yields the possibility of using one signal for acquiring the CFM while two others are used to create two independent spectrograms. This was also implemented and tested, and an example from the common carotid artery of a healthy male volunteer is shown in Fig. 6.3. Here the 5 MHz band was used for creating the CFM, while the 7 MHz and the 9 MHz bands were used to create the left and right spectrograms, respectively. We have named this method Multi-Frequency Quadroplex imaging (MFQ), since it is essentially triplex imaging (as shown in Fig. 2.2, left) with an additional

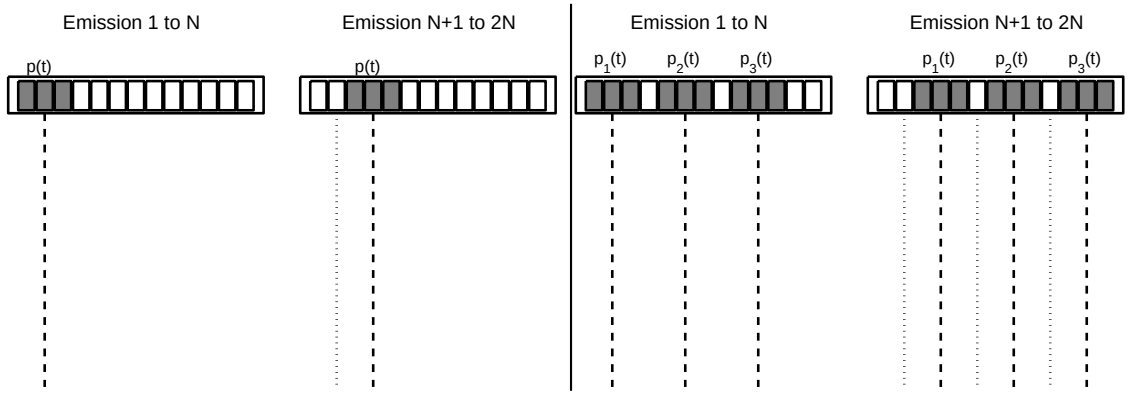

Figure 6.2: The principle of the method. The left figure shows how the acquisition of data for CFM is usually done using a linear array. N pulses are emitted along one direction, the sub-aperture is slid, and N new pulses are emitted, etc. The right figure shows how three lines are acquired simultaneously by emitting N pulses along three lines at the same time. The three pulses are different and can be separated in the receiver. Following this, the sub-apertures are slid, and the pulsing is repeated. The frame rate will be increase by a factor of three.

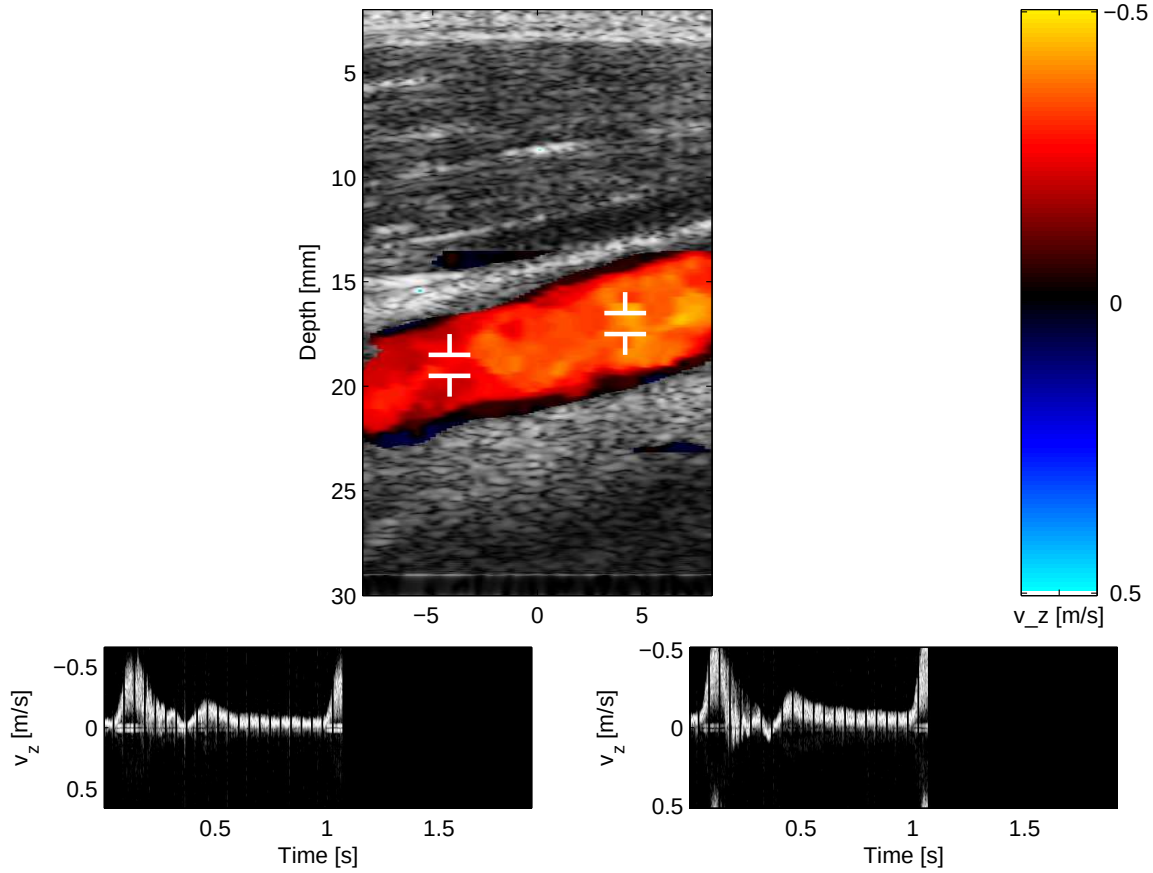

Figure 6.3: Multi-Frequency Quadroplex image of the common carotid artery during systole. The upper image shows the color flow map made using the 5 MHz band, the leftmost spectrogram is made using the 7 MHz band and the rightmost using the 9 MHz band. The gaps in the spectrograms are caused by the lack of spectral data during acquisition of B-mode data.

spectrogram. Using this mode will enable the medical doctor to for instance study the flow velocity over the cardiac cycle at both sides of a stenosis at the same time, while maintaining the CFM for guidance. Potentially, measures of the degree of a stenosis could be derived from these two spectrogram, where the timing is the same. Notice that the frame rate for MFQ imaging will equal that of a normal CFM, since the spectrogram data are acquired simultaneously with the CFM data.

In Fig. 6.3, a number of gaps are seen in both spectrograms. These are caused by the imaging sequence, where data for the B-mode image is collected in blocks. The B-mode data are of course collected using a broad-band pulse to maximize resolution, and spectrogram data are therefore not available during this time. There are various ways to avoid these gaps, either but interleaving the two sequences at the expense of a lowered velocity range [3], by creating synthetic data to fill the gaps [126], or by finding the power spectrum through the autocorrelation of sparse sequences [127]. These gaps are thus not inherent to this method, but are simply a product of the imaging sequence chosen.

6.3 Papers on the method

The conference paper on this encoding method [122] is basically just a short version of the journal paper [121]. For implementation issues, the reader is therefore referred to the journal paper [121]. The paper reviews the conventional flow techniques, presents the encoding method, considers the design of signals and filters for the method, and discusses some side-effects mainly related to using different center frequencies. These include the range of measurable velocities, the expected estimator variance, and frequency dependent attenuation. The encoding method is tested both for fast color flow mapping and for Quadroplex imaging, both in a controlled phantom environment and *in-vivo*. The paper is ended by a discussion of the perspectives of the method. Both papers [121,122] are found in the Appendix.

CHAPTER

SEVEN

Multi-dimensional spectrum analysis for 2-D vector flow imaging

The following chapter describes another project carried out as part of the PhD project. The method presented here is also described in the journal paper [128] submitted for the IEEE Transactions on Ultrasonics, Ferroelectrics, and Frequency Control in November 2007, and in the conference paper [129] which was presented at the IEEE Ultrasonics Symposium 2007. The work has been performed as a collaboration between the author and professor Jørgen Arendt Jensen from CFU and post doc Lasse Løvstakken and professor Hans Torp from the Department of Circulation and Medical Imaging at Norwegian University of Technology and Science in Trondheim, Norway. The purpose of this work is to derive a new 2-D vector flow estimator in the spectral domain based on the wideband 1-D estimator for axial velocities previously presented by Wilson [14] and Torp and Kristoffersen [15].

7.1 Axial blood velocity estimation using 2-D Fourier transform

Wilson's 1991 paper [14] and the paper by Torp and Kristoffersen [15] describe a method for estimation of the axial blood flow velocity through the use of the two-dimensional Fourier transform. If N repeated focused transmissions are made along the same line, a matrix $s(z,t)$ can be formed, where z is the depth along the beamformed line, and t is the time of pulse emission. The matrix is discrete along both dimensions since the data are sampled axially, and pulses are only emitted at certain times. First, it is assumed that $s(z,t)$ is continuous in both dimensions, and that the observation time and space are infinitely long. The two-dimensional Fourier transform of the matrix $s(z,t)$ is then given by

$$S(\zeta, f_d) = \int_{-\infty}^{\infty} \int_{-\infty}^{\infty} s(z,t) e^{-j2\pi\zeta z} e^{-j2\pi f_d t} dz dt, \tag{7.1}$$

where f_d is the frequency along the temporal dimension, and ζ is the spatial frequency along depth in units of meter^{-1}. Assuming everything within the (infinitely large) observation space and time moves at a constant velocity v_z along the z-direction, $s(z,t)$ can be regarded as a one-dimensional function $s_0(z)$ changing over time

$$s(z,t) = s_0(z - v_z t). \tag{7.2}$$

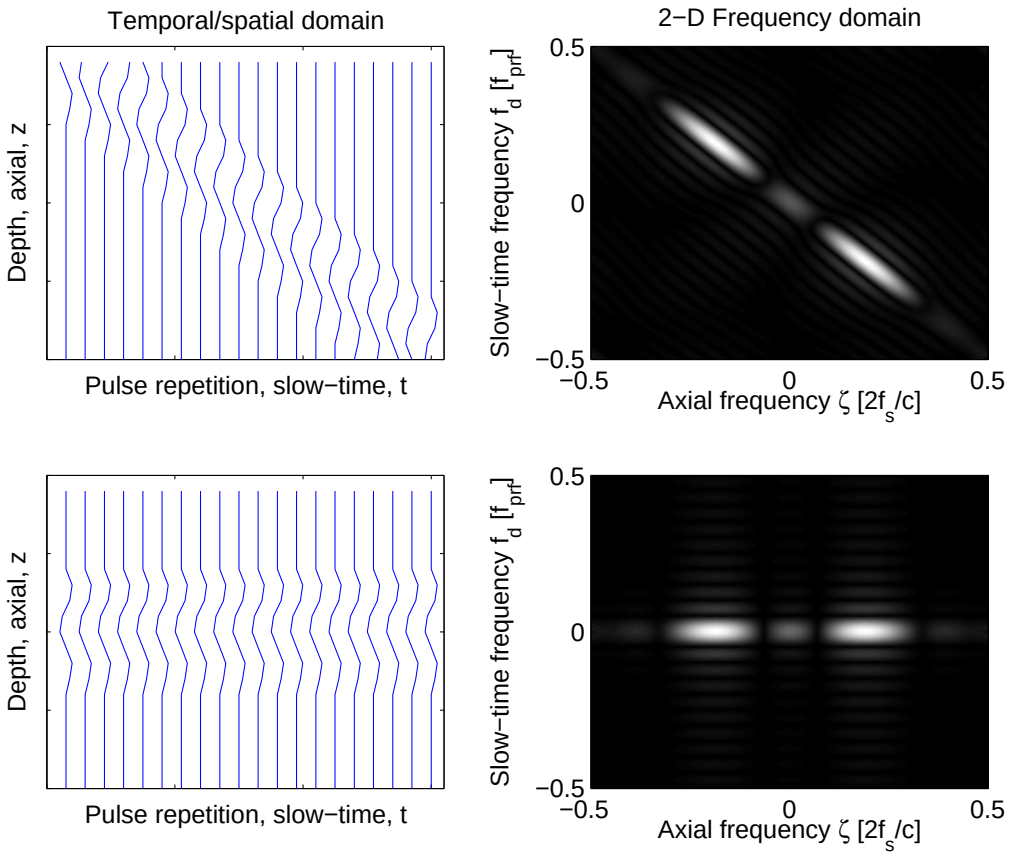

Figure 7.1: Sketch showing the principle of broad-band axial velocity estimation through use of the 2-D Fourier transform. The left plots show beamformed lines in the spatiotemporal domain and the left plots show their corresponding spectra. The top example shows $v_z > 0$ while the bottom example shows $v_z = 0$.

In this case, the Fourier transform of $s(z,t)$ will be given by

$$\begin{aligned}
S(\zeta, f_d) &= \int_{-\infty}^{\infty}\int_{-\infty}^{\infty} s_0(z - v_z t) e^{-j2\pi\zeta z} e^{-j2\pi f_d t} dz dt \\
&= \int_{-\infty}^{\infty}\left[\int_{-\infty}^{\infty} s_0(z - v_z t) e^{-j2\pi\zeta z} dz\right] e^{-j2\pi f_d t} dt \\
&= \int_{-\infty}^{\infty}\left[S_0(\zeta) e^{-j2\pi\zeta v_z t}\right] e^{-j2\pi f_d t} dt \\
&= \int_{-\infty}^{\infty} S_0(\zeta) e^{-j2\pi(f_d + \zeta v_z)t} dt \\
&= S_0(\zeta)\int_{-\infty}^{\infty} e^{-j2\pi(f_d + \zeta v_z)t} dt \\
&= S_0(\zeta)\delta(f_d + \zeta v_z), \qquad (7.3)
\end{aligned}$$

where $S_0(\zeta)$ is the Fourier transform of $s_0(z)$. According to (7.3), the spectral content of $s(z,t)$ will be concentrated along a line in the two-dimensional Fourier space. This line is described by

$$f_d = -\zeta v_z, \qquad (7.4)$$

and is called an iso-velocity line in [15] for obvious reasons. At the axial spatial center frequency $\zeta_0 = 2f_0/c$, this reduces to (2.1). Notice that the sign difference between (7.4) and (2.1) is due to different definitions of the z-axis. The line in (7.4) intercepts $(\zeta, f_d) = (0, 0)$ and has the axial velocity as slope. Fig. 7.1 sketches two examples at different velocities. The left plots show the beamformed lines in the spatiotemporal domain, while the right plots show the corresponding 2-D amplitude spectra. In the top row, a positive axial velocity v_z is seen which result in a negative slope in the 2-D spectral domain. In the lower row, the velocity is $v_z = 0$, resulting in a slope of 0 in the spectral domain.

In the ζ direction (horizontal in Fig. 7.1 right), the spectrum is limited by $S_0(\zeta)$ which corresponds to the spatial spectrum of the emitted waveform, including the system transfer function. Since the observation space and time are finite, spectral broadening will occur, and the spectral side-lobes seen in Fig. 7.1 will be present. Also, since the data are sampled in both space and time, spectral repetitions will be present at all multiples of the sampling frequency. Nevertheless, the spectral content is still concentrated along the line given by (7.4).

The axial velocity can be estimated by finding the slope of the line in the spectral domain. Both [14] and [15] proposed to integrate the power spectrum along lines of different slopes and choosing the slope corresponding to maximum power. This slope then corresponds to the axial velocity estimate.

7.2 Vector velocity estimation using 3-D Fourier transform

If the sampling is done both axially and laterally over time, a three-dimensional data matrix $s(x, z, t)$ can be formed, where x is the lateral coordinate. A constant velocity within the image plane is assumed, so that $s(x, z, t) = s_0(x - v_x t, z - v_z t)$, where $s_0(x, z)$ is a spatial two-dimensional function resembling the speckle pattern, and v_x and v_z are the velocities along the lateral and axial directions, respectively. The three-dimensional Fourier transform of this function, making the same assumptions as before, is

$$\begin{aligned}
F(\chi, \zeta, f_d) &= \int_{-\infty}^{\infty}\int_{-\infty}^{\infty}\int_{-\infty}^{\infty} s(x, z, t) e^{-j2\pi\chi x} e^{-j2\pi\zeta z} e^{-j2\pi f_d t} dx dz dt \\
&= \int_{-\infty}^{\infty}\left[\int_{-\infty}^{\infty}\int_{-\infty}^{\infty} s_0(x - v_x t, z - v_z t) e^{-j2\pi\chi x} e^{-j2\pi\zeta z} dx dz\right] e^{-j2\pi f_d t} dt \\
&= \int_{-\infty}^{\infty}\left[S_0(\chi, \zeta) e^{-j2\pi\chi v_x t} e^{-j2\pi\zeta v_z t}\right] e^{-j2\pi f_d t} dt \\
&= S_0(\chi, \zeta)\int_{-\infty}^{\infty} e^{-j2\pi(f_d + v_x\chi + v_z\zeta)t} dt \\
&= S_0(\chi, \zeta)\delta(f_d + v_x\chi + v_z\zeta), \qquad (7.5)
\end{aligned}$$

where $S_0(\chi, \zeta)$ is the two-dimensional Fourier transform of $s_0(x, z)$, and χ is the spatial frequency along the lateral direction. This means that where a single axial velocity in Section 7.1 was concentrated along a line in the 2-D Fourier plane, a single velocity is now concentrated along a plane in the 3-D Fourier space. This plane is given by

$$f_d = -v_x\chi - v_z\zeta. \qquad (7.6)$$

Similar to the former case, the limited observation time and space cause spectral broadening and side-lobes, and the sampling causes spectral repetitions. Two different estimators are derived for finding the velocity within the image plane. They both search for

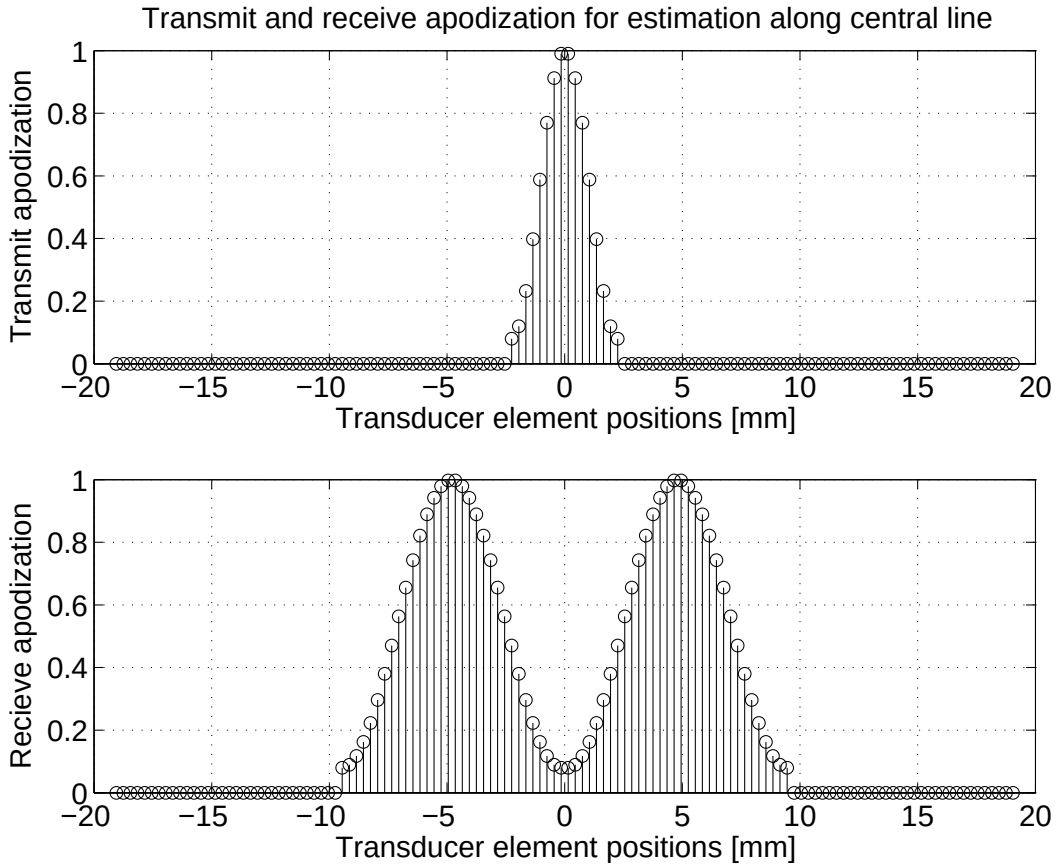

Figure 7.2: Transmit (top) and receive (bottom) apodization.

the plane where the summed power spectral components are maximized. One estimator uses the Fourier transform for finding the power spectral estimates while the other uses a minimum variance approach [110, 130]. The estimators are derived and tested in the journal paper [128] and the conference paper [129], both found in the Appendix.

7.3 Practical considerations regarding the setup

The iso-velocity plane given by (7.6) is limited by the function $S_0(\chi, \zeta)$ through (7.5). This function can be approximated as a separable function $S_0(\chi, \zeta) = S_x(\chi)S_z(\zeta)$, where $S_z(\zeta)$ is the spectrum of the emitted waveform, including the system transfer function, and $S_x(\chi)$ is a scaled version of the effective aperture [128]. These considerations are similar to those used in Section 4.3. Using transmit and receive apertures shown in Fig. 7.2, will give an effective aperture with two peaks and cause the function $S_0(\chi, \zeta)$ to have four maxima. Hereby four clouds in the power spectral domain will characterize the iso-velocity plane. This will also cause a slight oscillation in the lateral direction of the point spread function, a fact that has previously been used for vector velocity estimation by other researchers [28, 30–36]. The narrow transmit apodization will create a broad transmit beam and enable beamforming of multiple parallel lines [27], supplying multiple samples along the lateral direction. Hereby the matrix $s(x, z, t)$ can be created.

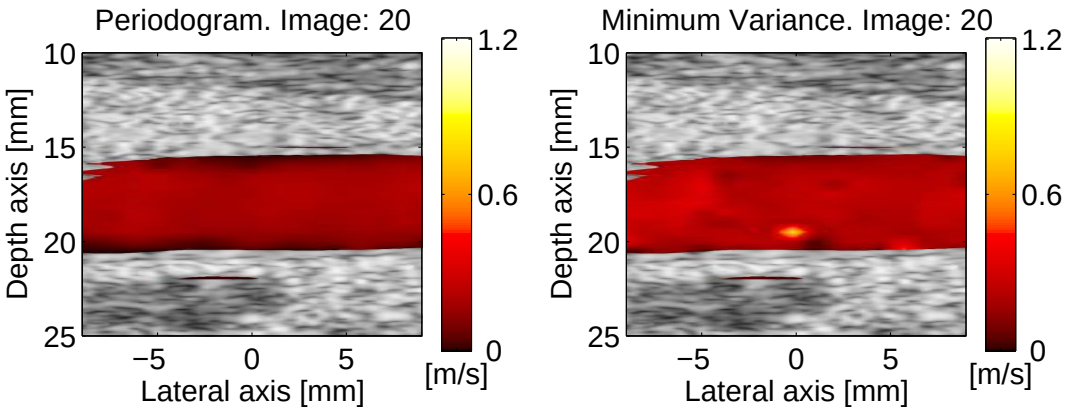

Figure 7.3: Color flow map of the common carotid artery of a healthy male volunteer during diastole. The leftmost part shows the magnitude of the velocity estimates found using one estimator, while the rightmost shows that using the other. Image from [129].

7.4 Papers on the method

The conference paper on this blood vector velocity estimation method [129] is basically just a short version of the journal paper [128]. First, the data model as given by Section 7.2 is derived, showing how the iso-velocity plane can give information of the lateral and axial velocity components. Two estimator for finding the velocity components are then derived. Results from a number of phantom measurement at different beam-to-flow angle are presented, showing that the lateral velocity estimates have larger standard deviation than the axial. Also, the estimator performance increased as the beam-to-flow angle approached $\theta = 90°$. An *in-vivo* measurement of the common carotid artery of a healthy male volunteer was performed, and color flow maps are shown. An example can be seen in Fig. 7.3. Both papers [128, 129] are found in the Appendix.

CHAPTER

EIGHT

Conclusion

Current blood flow velocity estimation systems are subject to a number of limitations including limited frame rate, aliasing artifacts, and maybe the most severe that only the velocity component along the beam direction is estimated. The PhD project described in this thesis has aimed to solve some of these problems.

The main focus has been on synthetic aperture vector flow imaging, a method for finding the vector velocity within the imaging plane by the use of synthetic aperture techniques known mainly from radar and sonar applications. The technique has been shortly reviewed. The contribution of this work is mainly within two areas; an analysis of the method including effects related to focusing, motion, and clutter filtering, and the application of the method for *in-vivo* scans.

It was shown that a geometric approximation to the opening angle of a virtual source corresponds well to the opening angle found through signal-to-noise ratio considerations. Also, it was shown that the Doppler effect causes negligible changes in the signal-to-noise ratio for synthetic aperture vector flow imaging. Movement between the acquisition of low resolution images was shown to seriously affect the signal-to-noise ratio of the system. Especially axial movement around a quarter of a wavelength between low resolution images should be avoided since this will cause the SNR to drop around 10 dB, essentially making velocity estimation impossible. A method for compensating for this motion in the beamformation was presented, showing that motion compensation might increase the signal-to-noise ratio and contrast and thus the estimator performance. The issue of stability must be considered in future work.

The problem of separating the blood flow signal from unwanted clutter, which has amplitudes orders of magnitude higher, is illustrated through the use of a simplified model. At present, the clutter cannot be removed without removing some of the flow signal since the signals are overlapping spectrally, at least for some flow directions and velocities. This problem is yet to be solved and is presently a serious limitation of synthetic aperture vector flow imaging, and most other vector flow methods for that matter.

Synthetic aperture vector flow images of various *in-vivo* situations were presented, including the common carotid artery, the carotid bifurcation, the femoral artery, and the confluence of the femoral and saphenous vein. Furthermore, results of a small *in-vivo* study were presented, where the common carotid artery of eleven healthy volunteers were scanned. The stroke volume was found from the synthetic aperture vector flow images by assuming the vessel was rotationally symmetric. This stroke volume was compared to the stroke volume of the same patients found through MR phase contrast angiography. A quite weak correlation of $R = 0.71$ was found, mainly because of three outliers where the stroke volume was overestimated by the ultrasound method. The

reason for this overestimation was found in the clutter filter creating false high-velocity estimates close to the vessel border during diastole.

Future work on synthetic aperture vector flow imaging should include solving the problem of clutter filtering, either by separating the signals in another way than simply filtering or by estimating the flow velocity within the presence of clutter. If this problem could be solved, synthetic aperture vector flow imaging has great potential for clinical applications.

Two additional research projects have been carried out as part of the project. The first aims at increasing the frame rate of conventional blood flow estimation by acquiring multiple lines for a color flow map simultaneously. This was achieved through the use of a frequency encoding, acquiring each line using different signals with approximately disjoint spectral support. In the receiver, the signals were filtered out by filters matched to the emitted signals, creating multiple lines simultaneously at different center frequencies. Thereby, the frame rate could be increased by a factor of M, where M is the number of lines acquired simultaneously. Alternatively, the method could be used for acquiring a color flow map in one band, while the other $M - 1$ bands were used for creating independent spectrograms. Using $M = 3$ frequency bands, the method was entitled quadroplex imaging, featuring a color flow map and two independent spectrograms at the same frame rate as a normal color flow map. The encoding method was tested both in phantoms and *in-vivo*, for both fast color flow mapping and quadroplex imaging.

The second project was the derivation and test of an alternative vector velocity estimator, where the velocity estimation was performed by a multi-dimensional spectral estimation. The method requires beamforming of multiple parallel lines at each transmission and the creation of a lateral oscillation of the point spread function by manipulation of the receive apodization. The method was tested in a phantom at various flow angles, including transverse flow, showing approximately 10 times higher standard deviations of the velocity component across the beam direction than the component along the beam direction. Furthermore, the method was tested *in-vivo*, showing potential for future applications. The method is in an early state of development, and future work should include a parameter study, unveiling how performance depends on acquisition parameters like the receive apodization, the spatial and temporal sampling, the emitted waveform, and spatial and temporal sample sizes.

The research presented in this thesis resulted in four journal papers, two of which are published [56, 93], one is accepted for publication [121], and one is now undergoing the review process [128]. Furthermore, the work resulted in six conference papers which have all been published [94, 114, 115, 122, 129, 131]. These ten papers can all be found in the Appendix.

Bibliography

[1] P. N. T. Wells and R. Skidmore, "Doppler developments in the last quinquennium," *Ultrasound Med. Biol.*, vol. 11, pp. 613–623, 1985.

[2] B. Sigel, "A Brief History of Doppler Ultrasound in the Diagnosis of Pheriferal Vascular Disease," *Ultrasound Med. Biol.*, vol. 24, no. 2, pp. 169–176, 1998.

[3] J. A. Jensen, *Estimation of Blood Velocities Using Ultrasound: A Signal Processing Approach*, Cambridge University Press, New York, 1996.

[4] Shigeo Satomura, "Ultrasonic Doppler method for the inspection of cardiac functions," *J. Acoust. Soc. Am.*, vol. 29, pp. 1181–1185, 1957.

[5] D. W. Baker, "Pulsed ultrasonic Doppler blood-flow sensing," *IEEE Trans. Son. Ultrason.*, vol. SU-17, pp. 170–185, 1970.

[6] P. N. T. Wells, "A range gated ultrasonic Doppler system," *Med. Biol. Eng.*, vol. 7, pp. 641–652, 1969.

[7] M. Brandestini, "Topoflow - a digital full range Doppler velocity meter," *IEEE Trans. Son. Ultrason.*, vol. SU-25, pp. 287–293, 1978.

[8] M.I. Skolnik, *Introduction to Radar Systems*, McGraw-Hill, New York, 1980.

[9] C. Kasai, K. Namekawa, A. Koyano, and R. Omoto, "Real-time two-dimensional blood flow imaging using an autocorrelation technique," *IEEE Trans. Son. Ultrason.*, vol. 32, pp. 458–463, 1985.

[10] T. Loupas, J. T. Powers, and R. W. Gill, "An axial velocity estimator for ultrasound blood flow imaging, based on a full evaluation of the Doppler equation by means of a two-dimensional autocorrelation approach," *IEEE Trans. Ultrason., Ferroelec., Freq. Contr.*, vol. 42, pp. 672–688, 1995.

[11] O. Bonnefous and P. Pesqué, "Time domain formulation of pulse-Doppler ultrasound and blood velocity estimation by cross correlation," *Ultrason. Imaging*, vol. 8, pp. 73–85, 1986.

[12] K. W. Ferrara and V. R. Algazi, "A new wideband spread target maximum likelihood estimator for blood velocity estimation – Part I: Theory," *IEEE Trans. Ultrason., Ferroelec., Freq. Contr.*, vol. 38, pp. 1–16, 1991a.

[13] K. W. Ferrara and V. R. Algazi, "A new wideband spread target maximum likelihood estimator for blood velocity estimation – Part II: Evaluation of estimators with experimental data," *IEEE Trans. Ultrason., Ferroelec., Freq. Contr.*, vol. 38, pp. 17–26, 1991b.

[14] L. S. Wilson, "Description of broad-band pulsed Doppler ultrasound processing using the two-dimensional Fourier transform," *Ultrason. Imaging*, vol. 13, pp. 301–315, 1991.

[15] H. Torp and K. Kristoffersen, "Velocity matched spectrum analysis: A new method for suppressing velocity ambiguity in pulsed-wave doppler," *Ultrasound Med. Biol.*, vol. 21, no. 7, pp. 937–944, 1995.

[16] S. K. Alam and K. J. Parker, "The butterfly search technique for estimation of blood velocity," *Ultrasound Med. Biol.*, vol. 21, no. 5, pp. 657–670, 1995.

[17] M. E. Allam and J. F. Greenleaf, "Isomorphism between pulsed-wave doppler ultrasound and direction-of-arrival estimation - part i: Basic principles," *IEEE Trans. Ultrason., Ferroelec., Freq. Contr.*, vol. 43, pp. 911–922, 1996.

[18] M. E. Allam, R. R. Kinnick, and J. F. Greenleaf, "Isomorphism between pulsed-wave doppler ultrasound and direction-of-arrival estimation - part ii: Experimental results," *IEEE Trans. Ultrason., Ferroelec., Freq. Contr.*, vol. 43, pp. 923–935, 1996.

[19] Peter D. Welch, "The use of fast Fourier transform for the estimation of power spectra: A method based on time averaging over short, modified periodograms," *IEEE Trans. Au. Electroacous.*, vol. AU-15, pp. 70–73, 1967.

[20] D. J. Phillips, K. W. Beach, J. Primozich, and D. E. Strandness, "Should results of ultrasound Doppler studies be reported in units of frequency or velocity?," *Ultrasound Med. Biol.*, vol. 15, pp. 205–212, 1989.

[21] R. Botnar, G. Rappitsch, M. B. Scheidegger, D. Liepsch, K. Perktold, and P. Boesiger, "Hemodynamics in the carotid artery bifurcation: a comparison between numerical simulations and in vitro MRI measurements," *J. Biomech.*, vol. 33, pp. 137–144, 2000.

[22] M. D. Fox, "Multiple crossed-beam ultrasound Doppler velocimetry," *IEEE Trans. Son. Ultrason.*, vol. SU-25, pp. 281–286, 1978.

[23] John R. Overbeck, Kirk W. Beach, and D. Eugene Strandness, "Vector Doppler: Accurate measurement of blood velocity in two dimensions," *Ultrasound Med. Biol.*, vol. 18, pp. 19–31, 1992.

[24] B. Dunmire and K. W. Beach, "A Brief History of Vector Doppler," in *Med. Imag. V Symp.*, Feb. 2001, vol. 4325, pp. 200–214.

[25] V. L. Newhouse, D. Censor, T. Vontz, J. A. Cisneros, and B. B. Goldberg, "Ultrasound Doppler probing of flows transverse with respect to beam axis," *IEEE Trans. Biomed. Eng.*, vol. BME-34, pp. 779–788, 1987.

[26] G. E. Trahey, J. W. Allison, and O. T. von Ramm, "Angle independent ultrasonic detection of blood flow," *IEEE Trans. Biomed. Eng.*, vol. BME-34, pp. 965–967, 1987.

[27] D. P. Shattuck, M. D. Weinshenker, S. W. Smith, and O. T. von Ramm, "Explososcan: A parallel processing technique for high speed ultrasound imaging with linear phased arrays," *J. Acoust. Soc. Am.*, vol. 75, pp. 1273–1282, 1984.

[28] P. Munk, "Estimation of the 2-D flow vector in ultrasonic imaging: a new approach," M.S. thesis, Department of Information Technology, Technical University of Denmark, 1996.

[29] J. A. Jensen, "Apparatus and method for determining movements and velocities of moving objects, International patent PCT/DK97/00287," Priority date: 1996, Granted 1998.

[30] J. A. Jensen and P. Munk, "A new method for estimation of velocity vectors," *IEEE Trans. Ultrason., Ferroelec., Freq. Contr.*, vol. 45, pp. 837–851, 1998.

[31] J. A. Jensen, "A new estimator for vector velocity estimation," *IEEE Trans. Ultrason., Ferroelec., Freq. Contr.*, vol. 48, no. 4, pp. 886–894, 2001.

[32] J. Udesen, *2-D blood vector velocity estimation using a phase shift estimator.*, Ph.D. thesis, Ørsted•DTU, Technical University of Denmark, 2800, Lyngby, Denmark, 2005.

[33] J. Udesen and J. A. Jensen, "Investigation of transverse oscillation method," *IEEE Trans. Ultrason., Ferroelec., Freq. Contr.*, vol. 53, pp. 959–971, 2006.

[34] J. Udesen, M. B. Nielsen, K. R. Nielsen, and J. A. Jensen, "Examples of in-vivo blood vector velocity estimation," *Ultrasound Med. Biol.*, vol. 33, no. 4, pp. 541–548, 2007.

[35] M. E. Anderson, "Spatial quadrature: a novel technique for multi-dimensional velocity estimation," in *Proc. IEEE Ultrason. Symp.*, 1997, vol. 45, pp. 1233–1238.

[36] M. E. Anderson, "A heterodyning demodulation technique for spatial quadrature," in *Proc. SPIE - med. imag.*, 2000, pp. 1487–1490.

[37] J. A. Jensen, "Directional velocity estimation using focusing along the flow direction: I: Theory and simulation," *IEEE Trans. Ultrason., Ferroelec., Freq. Contr.*, pp. 857–872, 2003.

[38] J. A. Jensen and R. Bjerngaard, "Directional velocity estimation using focusing along the flow direction: II: Experimental investigation," *IEEE Trans. Ultrason., Ferroelec., Freq. Contr.*, pp. 873–880, 2003.

[39] J. A. Jensen, "Velocity vector estimation in synthetic aperture flow and B-mode imaging," in *IEEE International Symposium on Biomedical imaging from nano to macro*, 2004, pp. 32–35.

[40] J. Kortbek and J. A. Jensen, "Estimation of velocity vector angles using the directional cross-correlation method," *IEEE Trans. Ultrason., Ferroelec., Freq. Contr.*, vol. 53, pp. 2036–2049, 2006.

[41] S.-L. Wang and M.-L. Li, "Estimating the Blood Velocity Vector Using Aperture Domain Data," *IEEE Trans. Ultrason., Ferroelec., Freq. Contr.*, vol. 54, no. 1, pp. 70–78, January 2007.

[42] M. Soumekh, *Synthetic aperture radar. Signal processing with MATLAB algorithms*, John Wiley & Sons, Inc., New York, 1999.

[43] J. A. Jensen, S. Nikolov, K. Løkke Gammelmark, and M. Høgholm Pedersen, "Synthetic aperture ultrasound imaging," *Ultrasonics*, vol. 44, pp. e5–e15, 2006.

[44] J. J. Flaherty, K. R. Erikson, and V. M. Lund, "Synthetic aperture ultrasound imaging systems," United States Patent, US 3,548,642, 1967.

[45] C. B. Burckhardt, P-A. Grandchamp, and H. Hoffmann, "An experimental 2 MHz synthetic aperture sonar system intended for medical use," *IEEE Trans. Son. Ultrason.*, vol. 21, no. 1, pp. 1–6, January 1974.

[46] K. Nagai, "A new synthetic-aperture focusing method for ultrasonic *B*-scan imaging by the fourier transform," *IEEE Trans. Son. Ultrason.*, vol. SU-32, no. 4, pp. 531–536, 1985.

[47] S. I. Nikolov, *Synthetic aperture tissue and flow ultrasound imaging*, Ph.D. thesis, Ørsted•DTU, Technical University of Denmark, 2800, Lyngby, Denmark, 2001.

[48] J. T. Ylitalo and H. Ermert, "Ultrasound synthetic aperture imaging: monostatic approach," *IEEE Trans. Ultrason., Ferroelec., Freq. Contr.*, vol. 41, pp. 333–339, 1994.

[49] R. Y. Chiao, L. J. Thomas, and S. D. Silverstein, "Sparse array imaging with spatially-encoded transmits," in *Proc. IEEE Ultrason. Symp.*, 1997, pp. 1679–1682.

[50] L. F. Nock and G. E. Trahey, "Synthetic receive aperture imaging with phase correction for motion and for tissue inhomogenities - part I: basic principles," *IEEE Trans. Ultrason., Ferroelec., Freq. Contr.*, vol. 39, pp. 489–495, 1992.

[51] G. E. Trahey and L. F. Nock, "Synthetic receive aperture imaging with phase correction for motion and for tissue inhomogenities - part II: effects of and correction for motion," *IEEE Trans. Ultrason., Ferroelec., Freq. Contr.*, vol. 39, pp. 496–501, 1992.

[52] S. I. Nikolov and J. A. Jensen, "In-vivo synthetic aperture flow imaging in medical ultrasound," *IEEE Trans. Ultrason., Ferroelec., Freq. Contr.*, pp. 848–856, 2003.

[53] G. R. Lockwood and F.S. Foster, "Design of sparse array imaging systems," in *Proc. IEEE Ultrason. Symp.*, 1995, pp. 1237–1243.

[54] G. R. Lockwood, J. R. Talman, and S. S. Brunke, "Real-time 3-D ultrasound imaging using sparse synthetic aperture beamforming," *IEEE Trans. Ultrason., Ferroelec., Freq. Contr.*, vol. 45, pp. 980–988, 1998.

[55] G. R. Lockwood and F. S. Foster, "Optimizing sparse two-dimensional arrays using an effective aperture approach," in *Proc. IEEE Ultrason. Symp.*, 1994, pp. 1497–1501.

[56] N. Oddershede and J. A. Jensen, "Effects influencing focusing in synthetic aperture vector flow imaging," *IEEE Trans. Ultrason., Ferroelec., Freq. Contr.*, vol. 54, no. 9, pp. 1811–1825, September 2007.

[57] M. O'Donnell and L. J. Thomas, "Efficient synthetic aperture imaging from a circular aperture with possible application to catheter-based imaging," *IEEE Trans. Ultrason., Ferroelec., Freq. Contr.*, vol. 39, pp. 366–380, 1992.

[58] M. Karaman, P. C. Li, and M. O'Donnell, "Synthetic aperture imaging for small scale systems," *IEEE Trans. Ultrason., Ferroelec., Freq. Contr.*, vol. 42, pp. 429–442, 1995.

[59] S. I. Nikolov and J. A. Jensen, "Virtual ultrasound sources in high-resolution ultrasound imaging," in *Proc. SPIE - Progress in biomedical optics and imaging*, 2002, vol. 3, pp. 395–405.

[60] M. O'Donnell, "Coded excitation system for improving the penetration of real-time phased-array imaging systems," *IEEE Trans. Ultrason., Ferroelec., Freq. Contr.*, vol. 39, pp. 341–351, 1992.

[61] T. Misaridis, *Ultrasound imaging using coded signals*, Ph.D. thesis, Ørsted•DTU, Technical University of Denmark, Lyngby, Denmark, 2001.

[62] T. Misaridis and J. A. Jensen, "Use of modulated excitation signals in ultrasound, Part I: Basic concepts and expected benefits," *IEEE Trans. Ultrason., Ferroelec., Freq. Contr.*, pp. 192–207, 2005.

[63] T. Misaridis and J. A. Jensen, "Use of modulated excitation signals in ultrasound, Part II: Design and performance for medical imaging applications," *IEEE Trans. Ultrason., Ferroelec., Freq. Contr.*, pp. 208–219, 2005.

[64] T. Misaridis and J. A. Jensen, "Use of modulated excitation signals in ultrasound, Part III: High frame rate imaging," *IEEE Trans. Ultrason., Ferroelec., Freq. Contr.*, pp. 220–230, 2005.

[65] F. Gran and J. A. Jensen, "Designing non-linear frequency modulated signals for medical ultrasound imaging," in *Proc. IEEE Ultrason. Symp.*, 2006, pp. 1714–1717.

[66] F. Gran and J. A. Jensen, "Designing waveforms for temporal encoding using a frequency sampling method," *IEEE Trans. Ultrason., Ferroelec., Freq. Contr.*, vol. 54(10), pp. 2070–2081, 2007.

[67] H. Zhao, L. Y. L. Mo, and S. Gao, "Barker-coded ultrasound color flow imaging: theoretical and practical design considerations," vol. 54, no. 2, pp. 319–331, February 2007.

[68] F. Gran, J. Udesen, and J. A. Jensen, "Coded ultrasound for blood flow estimation using subband processing," in *Proc. SPIE - Progress in biomedical optics and imaging*, 2007, p. Accepted.

[69] R. Y. Chiao and L. J. Thomas, "Synthetic transmit aperture using orthogonal Golay coded excitation," in *Proc. IEEE Ultrason. Symp.*, 2000, pp. 1469–1472.

[70] R. Y. Chiao and X. Hao, "Coded excitation for diagnostic ultrasound: A system developer's perspective," *IEEE Trans. Ultrason., Ferroelec., Freq. Contr.*, vol. 52, pp. 160–170, 2005.

[71] F. Gran and J. A. Jensen, "Frequency division transmission and synthetic aperture reconstruction," *IEEE Trans. Ultrason., Ferroelec., Freq. Contr.*, vol. 53(5), pp. 900–911, 2006.

[72] F. Gran and J. A. Jensen, "Directional velocity estimation using a spatio-temporal encoding technique based on frequency division for synthetic transmit aperture ultrasound," *IEEE Trans. Ultrason., Ferroelec., Freq. Contr.*, vol. 53(7), pp. 1289–1299, 2006.

[73] F. Gran and J. A. Jensen, "Spatial encoding using code division for fast ultrasound imaging," *IEEE Trans. Ultrason., Ferroelec., Freq. Contr.*, vol. Accepted for publication, 2008.

[74] F. Gran, *Spatio-temporal encoding in medical ultrasound imaging*, Ph.D. thesis, Ørsted•DTU, Technical University of Denmark, Lyngby, Denmark, 2005.

[75] S. I. Nikolov, K. Gammelmark, and J. A. Jensen, "Recursive ultrasound imaging," in *Proc. IEEE Ultrason. Symp.*, 1999, vol. 2, pp. 1621–1625.

[76] H. Ş. Bilge, M. Karaman, and M. O'Donnell, "Motion estimation using common spatial frequencies in synthetic aperture imaging," in *Proc. IEEE Ultrason. Symp.*, 1996, pp. 1551–1554.

[77] M. Karaman, H. Ş. Bilge, and M. O'Donnell, "Adaptive multi-element synthetic aperture imaging with motion and phase aberation correction," *IEEE Trans. Ultrason., Ferroelec., Freq. Contr.*, vol. 42, pp. 1077–1087, 1998.

[78] C. R. Hazard and G. R. Lockwood, "Theoretical assessment of a synthetic aperture beamformer for real-time 3-D imaging," *IEEE Trans. Ultrason., Ferroelec., Freq. Contr.*, vol. 46, pp. 972–980, 1999.

[79] J. S. Jeong, J. S. Hwang, M. H. Bae, and T. K. Song, "Effects and limitations of motion compensation in synthetic aperture techniques," in *Proc. IEEE Ultrason. Symp.*, 2000, pp. 1759 –1762.

[80] K. L. Gammelmark and J. A. Jensen, "Duplex synthetic aperture imaging with tissue motion compensation," in *Proc. IEEE Ultrason. Symp.*, 2003, pp. 1569–1573.

[81] S. I. Nikolov and J. A. Jensen, "K-space model of motion artifacts in synthetic transmit aperture ultrasound imaging," in *Proc. IEEE Ultrason. Symp.*, 2003, pp. 1824–1828.

[82] M. H. Pedersen, K. L. Gammelmark, and J. A. Jensen, "In-vivo evaluation of convex array synthetic aperture imaging," *Ultrasound Med. Biol.*, vol. 33, pp. 37–47, 2006.

[83] S. I. Nikolov, K. Gammelmark, and J. A. Jensen, "Velocity estimation using recursive ultrasound imaging and spatially encoded signals," in *Proc. IEEE Ultrason. Symp.*, 2000, vol. 2, pp. 1473–1477.

[84] S. I. Nikolov and J. A. Jensen, "Velocity estimation using synthetic aperture imaging," in *Proc. IEEE Ultrason. Symp.*, 2001, pp. 1409–1412.

[85] J. A. Jensen and I. R. Lacasa, "Estimation of blood velocity vectors using transverse ultrasound beam focusing and cross-correlation," in *Proc. IEEE Ultrason. Symp.*, 1999, pp. 1493–1497.

[86] I. R. Lacasa, "Estimation of blood velocities with ultrasound," M.S. thesis, Department of Information Technology, Technical University of Denmark, 1999.

[87] O. Bonnefous, "Measurement of the complete (3D) velocity vector of blood flows," in *Proc. IEEE Ultrason. Symp.*, 1988, pp. 795–799.

[88] J. A. Jensen and S. I. Nikolov, "Transverse flow imaging using synthetic aperture directional beamforming," in *Proc. IEEE Ultrason. Symp.*, 2002, pp. 1488–1492.

[89] J. A. Jensen and S. I. Nikolov, "Directional synthetic aperture flow imaging," *IEEE Trans. Ultrason., Ferroelec., Freq. Contr.*, pp. 1107–1118, 2004.

[90] S. G. Foster, *A pulsed ultrasonic flowmeter employing time domain methods*, Ph.D. thesis, Dept. Elec. Eng., University of Illinois, Urbana, Ill., 1985.

[91] S. G. Foster, P. M. Embree, and W. D. O'Brien, "Flow velocity profile via time-domain correlation: Error analysis and computer simulation," *IEEE Trans. Ultrason., Ferroelec., Freq. Contr.*, vol. 37, pp. 164–175, 1990.

[92] X. Lai and H. Torp, "Interpolation methods for time-delay estimation using cross-correlation method for blood velocity measurement," *IEEE Trans. Ultrason., Ferroelec., Freq. Contr.*, vol. 46, no. 2, pp. 277–290, March 1999.

[93] J. A. Jensen and N. Oddershede, "Estimation of velocity vectors in synthetic aperture ultrasound imaging.," *IEEE Trans. Med. Imag.*, pp. 1637–1644, 2006.

[94] N. Oddershede and J. A. Jensen, "Motion compensated beamforming in synthetic aperture vector flow imaging," in *Proc. IEEE Ultrason. Symp.*, 2006, pp. 2027–2031.

[95] J. A. Jensen and N. B. Svendsen, "Calculation of pressure fields from arbitrarily shaped, apodized, and excited ultrasound transducers," *IEEE Trans. Ultrason., Ferroelec., Freq. Contr.*, vol. 39, pp. 262–267, 1992.

[96] J. A. Jensen, "Field: A program for simulating ultrasound systems," *Med. Biol. Eng. Comp.*, vol. 10th Nordic-Baltic Conference on Biomedical Imaging, Vol. 4, Supplement 1, Part 1, pp. 351–353, 1996b.

[97] W. F. Walker and G. E. Trahey, "A fundamental limit on delay estimation using partially correlated speckle signals," *IEEE Trans. Ultrason., Ferroelec., Freq. Contr.*, vol. 42, no. 2, pp. 301–308, March 1995.

[98] E. Weinstein and A. J. Weiss, "Fundamental limitation in passive time-delay estimation - part 2: Wide-band systems," *IEEE transactions on acoustics, speech, and signal processing*, vol. 32, pp. 1064–1078, 1984.

[99] F. Gran and J. A. Jensen, "Designing waveforms for temporal encoding using a frequency sampling method," *IEEE Trans. Ultrason., Ferroelec., Freq. Contr.*, vol. 54, no. 10, pp. 2070–2081, October 2007.

[100] H. Torp, "Clutter Rejection Filters in Color Flow Imaging: A Theoretical Approach," *IEEE Trans. Ultrason., Ferroelec., Freq. Contr.*, vol. 44, no. 2, pp. 417–424, 1997.

[101] M. A. Shariati, J. H. Dripps, and W. N. McDicken, "Deadbeat IIR Based MTI Filtering for Color Flow Imaging Systems," in *Proc. IEEE Ultrason. Symp.*, 1993, pp. 1059–1063.

[102] A. P. Kadi and T. Loupas, "On the performance of regression ans step-initialized IIR clutter filters for color Doppler systems in diagnostic medical ultrasound," *IEEE Trans. Ultrason., Ferroelec., Freq. Contr.*, vol. 42, pp. 927–937, 1995.

[103] A. P. G Hoeks, J. J. W. van de Vorst, A. Dabekaussen, P. J. Brands, and R. S. Reneman, "An efficient algorithm to remove low frequency Doppler signal in digital Doppler systems," *Ultrason. Imaging*, vol. 13, pp. 135–145, 1991a.

[104] L. A. F. Ledoux, P. J. Brands, and A. P. G. Hoeks, "Reduction of the clutter component in doppler ultrasound signals based on singular value decomposition: a simulation study," *Ultrason. Imaging*, pp. 1–18, 1997.

[105] S. Bjaerum and H. Torp, "Optimal adaptive clutter filtering in color flow imaging," in *Proc. IEEE Ultrason. Symp.*, 1997, pp. 1223–1226.

[106] S. Bjærum, H. Torp, and K. Kristoffersen, "Clutter filters adapted to tissue motion in ultrasound color flow imaging," *IEEE Trans. Ultrason., Ferroelec., Freq. Contr.*, vol. 49, no. 6, pp. 693–704, June 2002.

[107] C. M. Gallippi and G. E. Trahey, "Adaptive Clutter Filtering via Blind Source Separation for Lateral Blood Velocity Measurement," in *Proc. IEEE Ultrason. Symp.*, 2002, pp. 1517–1521.

[108] L. Løvstakken, S. Bjærum, K. Kristoffersen, R. Haaverstad, and H. Torp, "Real-time adaptive clutter rejection filtering in color flow imaging using power method iterations," *IEEE Trans. Ultrason., Ferroelec., Freq. Contr.*, vol. 53, no. 9, pp. 1597–1608, September 2006.

[109] B. H. Friemel, L. N. Bohs, K. R. Nightingale, and G. E. Trahey, "Wall filtering challenges in two-dimensional vector velocity estimation," *Proc. IEEE Ultrason. Symp.*, vol. 2, pp. 1031–1034, 1993.

[110] D. H. Johnson and D. E. Dudgeon, *Array signal processing. Concepts and techniques.*, Prentice-Hall., Englewood Cliffs, New Jersey, 1993.

[111] A. Schmidt-Trucksass, D. Grathwohl, A. Schmid, R. Boragk, C. Upmeier, J. Keul, and M. Huonker, "Assesment of Carotid Wall Motion and Stiffness with Tissue Doppler Imaging," *Ultrasound Med. Biol.*, vol. 24, no. 5, pp. 639–646, May 1998.

[112] L. Løvstakken, S. Bjærum, and H. Torp, "Optimal velocity estimation in ultrasound color flow imaging in presence of clutter," *IEEE Trans. Ultrason., Ferroelec., Freq. Contr.*, vol. 54, no. 3, pp. 539–549, March 2007.

[113] FDA, "Information for manufacturers seeking marketing clearance of diagnostic ultrasound systems and transducers," Tech. Rep., Center for Devices and Radiological Health, United States Food and Drug Administration, 1997.

[114] N. Oddershede and J. A. Jensen, "Synthetic aperture flow angle estimation on in-vivo data from the carotid artery," in *Proc. IEEE Ultrason. Symp.*, 2005, pp. 1331–1334.

[115] N. Oddershede, K. L. Hansen, M. B. Nielsen, and J. A. Jensen, "In-vivo examples of synthetic aperture vector flow imaging," in *Proc. SPIE - Medical Imaging 2007: Ultrasound Imaging and Signal Processing*, 2007, vol. 6513.

[116] L. Henze, I. K. Holfort, J. Kortbek, K. L. Hansen, and J. A. Jensen, "In Vivo Vector Flow Imaging Using Improved Directional Beamforming," in *Proc. IEEE Ultrason. Symp.*, Oct. 2007 (Accepted).

[117] K. L. Hansen, J. Udesen, N. Oddershede, L. Henze, C. Thomsen, J. A. Jensen, and M. B. Nielsen, "In-vivo study of directional beamforming, synthetic transmit aperture flow imaging and transverse oscillation compared with mr phase contrast angiography," *Ultrasound Med. Biol.*, p. To be submitted, 2007.

[118] J. H. McClellan and T. W. Parksand L. R. Rabiner, "A computer program for designing optimum fir linear phase digital filters," *IEEE Transactions on Audio and Electroacoustics*, vol. AU-21, no. 6, pp. 506–526, 1973.

[119] K. L. Hansen, J. Udesen, C. Thomsen, J. A. Jensen, and M. B. Nielsen, "In-vivo validation of transverse oscillation vector velocity estimation with MR angiography," *Ultrasound Med. Biol.*, p. Submitted, 2007.

[120] M. B. Higginbotham, K. G. Morris, R. S. Williams, P. A. McHale, R. E. Coleman, and F. R. Cobb, "Regulation of Stroke Volume during Submaximal and Maximal Upright Exercise in Normal Man," *Circulation Research*, vol. 58, pp. 281–291, 1986.

[121] N. Oddershede, F. Gran, and J. A. Jensen, "Multi-frequency encoding for fast color flow or quadroplex imaging," *IEEE Trans. Ultrason., Ferroelec., Freq. Contr.*, p. accepted, 2007.

[122] N. Oddershede, F. Gran, and J. A. Jensen, "Multi-frequency encoding for rapid color flow or quadroplex imaging," in *Proc. IEEE Ultrason. Symp.*, 2007, p. Accepted.

[123] J. W. Allison, *Parallel Doppler processing in ultrasonic flow imaging.*, Ph.D. thesis, Duke University, Durham, NC, 1987.

[124] T. Hergum, T. Bjåstad, K. Kristoffersen, and H. Torp, "Parallel Beamforming Using Synthetic Transmit Beams," *IEEE Trans. Ultrason., Ferroelec., Freq. Contr.*, vol. 54, no. 2, pp. 271–280, February 2007.

[125] J. A. Jensen, O. Holm, L. J. Jensen, H. Bendsen, S. I. Nikolov, B. G. Tomov, P. Munk, M. Hansen, K. Salomonsen, J. Hansen, K. Gormsen, H. M. Pedersen, and K. L. Gammelmark, "Ultrasound research scanner for real-time synthetic aperture image acquisition," *IEEE Trans. Ultrason., Ferroelec., Freq. Contr.*, vol. 52 (5), pp. 881–891, May 2005.

[126] K. Kristoffersen and B. A. J. Angelsen, "A time-shared ultrasound Doppler measurement and 2-D imaging system," *IEEE Trans. Biomed. Eng.*, vol. BME-35, pp. 285–295, 1988.

[127] J. A. Jensen, "Spectral velocity estimation in ultrasound using sparse data sets," *J. Acoust. Soc. Am.*, vol. vol 120(1), pp. 211–220, 2006.

[128] N. Oddershede, L. Løvstakken, H. Torp, and J. A. Jensen, "Estimating 2-d vector velocities using multi-dimensional spectrum analysis," *IEEE Trans. Ultrason., Ferroelec., Freq. Contr.*, p. Submitted, 2007.

[129] N. Oddershede, L. Løvstakken, H. Torp, and J. A. Jensen, "Multi-dimensional spectrum analysis for 2-d vector velocity estimation," in *Proc. IEEE Ultrason. Symp.*, 2007, p. Accepted.

[130] J. Capon, "High-Resolution Frequency-Wavenumber Spectrum Analysis," *Proc. IEEE*, vol. 57, no. 8, pp. 1408–1418, August 1969.

[131] N. Oddershede and J. A. Jensen, "Experimental investigation of synthetic aperture flow angle estimation," in *Proc. SPIE - Medical imaging 2005: Ultrasonic Imaging and Signal Processing*, 2005, vol. 5750, pp. 417–426.

APPENDIX

A

Appendix

A.1 Jensen, J. A. and Oddershede, N. ,
Estimation of velocity vectors in synthetic aperture ultrasound imaging, *IEEE Transactions on Medical Imaging, vol. 25, no. 12, December 2006, pp 1637-44.*

Estimation of Velocity Vectors in Synthetic Aperture Ultrasound Imaging

Jørgen Arendt Jensen* and Niels Oddershede

***Abstract*—A method for determining both velocity magnitude and angle in a synthetic aperture ultrasound system is described. The approach uses directional beamforming along the flow direction and cross correlation to determine velocity magnitude. The angle of the flow is determined from the maximum normalized correlation calculated as a function of angle. This assumes the flow direction is within the imaging plane. Simulations of the angle estimation method show both biases and standard deviations of the flow angle estimates below 3° for flow angles from 20° to 90° (transverse flow). The method is also investigated using data measured by an experimental ultrasound scanner from a flow rig. A commercial 128 element 7-MHz linear array transducer is used, and data are measured for flow angles of 60° and 90°. Data are acquired using the RASMUS experimental ultrasound scanner, which samples 64 channels simultaneously. A 20-μs chirp was used during emission and eight virtual transmit sources were created behind the transducer using 11 transmitting elements. Data from the eight transmissions are beamformed and coherently summed to create high-resolution lines at different angles for a set of points within the region of flow. The velocity magnitude is determined with a precision of 0.36% (60°) and 1.2% (90°), respectively. The 60° angle is estimated with a bias of 0.54° and a standard deviation of 2.1°. For 90° the bias is 0.0003° and standard deviation 1.32°. A parameter study with regard to correlation length and number of emissions is performed to reveal the accuracy of the method. Real time data covering 2.2 s of the carotid artery of a healthy 30-year-old male volunteer is acquired and then processed offline using a computer cluster. The direction of flow is estimated using the above mentioned method. It is compared to the flow angle of 106° with respect to the axial direction, determined visually from the B-mode image. For a point in the center of the common carotid artery, 76% of the flow angle estimates over the 2.2 s were within 10° of the visually determined flow angle. The standard deviation of these estimates was below 2.7°. Full color flow maps from different parts of the cardiac cycle are presented, including vector arrows indicating both estimated flow direction and velocity magnitude.**

***Index Terms*—Angle determination, medical ultrasound, synthetic aperture, vector velocity estimation.**

I. Introduction

CURRENT ultrasound velocity estimation systems only estimate the blood velocity projected onto the direction of the steered ultrasound beam [1], [2]. The velocities are, thus, only found in one direction in the image, and velocities in the direction perpendicular to the beam cannot be estimated. Neither the correct velocity magnitude nor the velocity angle are, thus, estimated.

A two-dimensional (2-D) velocity estimation system should be able to give both velocity magnitude and direction [3]–[5]. A directional beamforming approach was suggested for conventional ultrasound imaging in [6] and for synthetic aperture (SA) flow imaging in [7] and [8]. Here, the received echoes are dynamically focused in points along a line following the direction of the flow. A cross-correlation estimator is then used to find the velocity magnitude along the flow direction. In these papers, the angle for the beam processing is, however, manually determined from the B-mode image before beamforming.

This paper presents a method for also estimating the velocity angle in a SA flow system as originally suggested in [9]. The procedure determines both velocity magnitude and angle using cross correlation of the received signals, and it can be employed for estimation of both blood velocity and tissue motion. This paper will described the method in details and give data for its performance for simulated data, measured data from a flow rig, and *in vivo* data. The basic principle of directional synthetic aperture flow imaging is described in Section II and the angle determination procedure is detailed in Section III. In Section IV, simulations of the angle determination method is presented for a wide range of flow angles. The performance of the approach is determined in Section V from data measured using an experimental ultrasound scanner and a flow rig, and a parameter study is given in Section VI. Finally, examples of vector velocity images are presented in Section VII for flow rig data and for *in vivo* data from the carotid artery in Section VIII.

II. Method for SA Flow Imaging

SA ultrasound images are acquired by emitting a spherical wave with one or a collection of transducer elements [10], [11]. The scattered signals are then received by all transducer elements, and a low-resolution image is generated by focusing the received signal in all points of the image. The process is repeated for other sets of transmitting elements and new low-resolution images are formed. Combining all low-resolution images will give a high-resolution image, that is dynamically focused in both transmit and receive, thus, yielding a higher resolution than traditional images, if a sufficient number of transmissions N_t are used [12]. A new high-resolution image can be formed after each transmission, if the transmission sequence is repeated. The oldest transmission event is then replaced by the newest, and the imaging can therefore be done recursively [13].

SA images can also be used for flow estimation, if the data collection is repeated. Data from two high-resolution images

Manuscript received June 15, 2006; revised July 20, 2006. This work was supported by the Danish Science Foundation under Grant 26-04-0024 and in part by B-K Medical Aps, Herlev, Denmark. *Asterisk indicates corresponding author.*

*J. A. Jensen is with the Center for Fast Ultrasound Imaging, Technical University of Denmark, DK-2800 Lyngby, Denmark.

N. Oddershede with the Center for Fast Ultrasound Imaging, Technical University of Denmark, DK-2800 Lyngby, Denmark.

Digital Object Identifier 10.1109/TMI.2006.883087

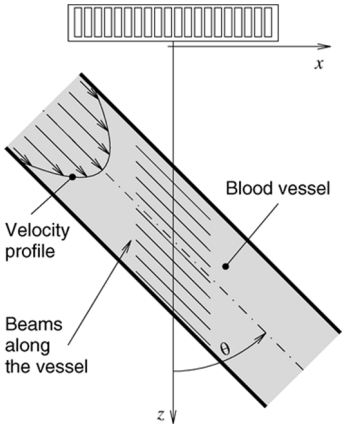

Fig. 1. Beamforming is made along the laminar flow. Figure from [8].

can be correlated to obtain the velocity of the blood or tissue [14]. It is here important that the two images are acquired in a short time interval, and that the emission sequence is exactly the same to maximize correlation. The recursive image formation can also be employed here and a new correlation function estimate formed after each emission. It is vital that the image formation sequence is exactly the same and high-resolution images N_t emissions apart should only be correlated. The correlation functions can, however, be averaged for all emissions, if the velocity is constant [14].

SA flow imaging has several advantages compared to traditional ultrasound flow imaging. The primary one is the continuously available data for all points in the image. The velocity estimation can, therefore, take place continuously, the initialization of stationary echo canceling filters becomes trivial, and the number of samples for velocity estimation are only restricted by the time for which the flow can be assumed quasi-stationary.

Another advantage of SA flow imaging is that data can be focused in any direction. It is, thus, possible to focus signals along the flow direction as suggested in [7] and shown in Fig. 1. Here, a three-dimensional (3-D) cartesian coordinate system with origo at the center of the transducer surface is used, where x follows the lateral direction, y the elevation direction, and z the axial direction. The high-resolution image data are then beamformed along the direction of the flow. The focusing points are given by $\vec{r}_p(k) = [\Delta r \cdot k \cdot \sin(\theta), 0, \Delta r \cdot k \cdot \cos(\theta) + z_{st}]$, where Δr is spatial sampling interval, k sample index, θ flow angle between the flow vector and z-axis, and z_{st} depth of the vessel. The data are focused for each emission and the final high-resolution directional signal is obtained by adding all N_t low-resolution images L_j

$$y_d^{(n)}(k) = \sum_{j=n-N_t+1}^{n} L_j(\vec{r}_p(k)). \tag{1}$$

The spatial movement between high-resolution images is $\vec{d}_s = \vec{v} T_{\mathrm{prf}} N_t$, where the blood velocity is $\vec{v} = |\vec{v}|[\sin\theta, 0, \cos\theta]$, and T_{prf} is the pulse repetition period. This distance corresponds to a sample index of

$$k_s = \frac{|\vec{v}| T_{prf} N_t}{\Delta r}. \tag{2}$$

Correlating two received signals over $N_k + 1$ samples from two high-resolution images gives

$$\begin{aligned} R_{12}(l) &= \frac{1}{N_k+1} \sum_{k=-N_k/2}^{N_k/2} y_d^{(n)}(k) y_d^{(n+N_t)}(k+l) \\ &= \frac{1}{N_k+1} \sum_{k=-N_k/2}^{N_k/2} y_d^{(n)}(k) y_d^{(n)}(k+l-k_s) \\ &= R_{11}(l-k_s) \end{aligned} \tag{3}$$

where $y_d^{(n)}(k)$ is the directional signal focused after emission n and $R_{11}(l)$ is its autocorrelation function.

A global maximum is found at $l = k_s$ and the velocity magnitude is estimated from

$$|\vec{v}| = \frac{k_s \Delta r}{T_{\mathrm{prf}} N_t}. \tag{4}$$

The spatial sampling interval Δr must be below $\lambda/4$ to obey the sampling criterion, where λ is the wavelength, but reducing Δr increases the amount of beamformation. Parabolic interpolation [15], [16] is used to increase the precision of the estimated velocity.

III. Determination of Velocity Angle

The velocity angle for beam formation has previously been determined manually from the B-mode image, and this section introduces an automatic approach for determining the angle.

The primary reason for decorrelation of traditional flow signals is the velocity distribution within the range gate. This makes part of the scatterers travel faster or slower than others, which decorrelates the received signal from emission to emission. Directional beamforming along the true flow direction avoids the decorrelation, since it tracks the scatterers in the correct direction and thereby maintains a high correlation. When beamforming along all other directions, the signals will again decorrelate. This observation is used to devise a method for automatic angle determination. The correlation peak found for the correct angle normalized by the power of the signal must, therefore, have the highest correlation values, since it has the least decorrelation due to a velocity distribution. This is stated as

$$R_{12n}(\theta_m) = \left(\frac{\max(R_{12}(l, \theta_m))}{R_{11}(0, \theta_m)} \right) \tag{5}$$

$$\theta = \underset{\theta_m}{\mathrm{Arg\ min}}\, R_{12n}(\theta_m) \tag{6}$$

where $\max(R_{12}(l, \theta_m))$ is the maximum value of the cross-correlation function for the angles θ_m and $R_{11}(0, \theta_m)$ is the corresponding power of the signal. The correct angle θ is found where the normalized correlation function as a function of angle $R_{12n}(\theta_m)$ has its peak value.

An example of the calculated normalized correlation is shown in Fig. 2 for a true angle of 90°. The data are from the measurements described in Section V. The correlation has been calculated for every 2°, and the global maximum coincides with the correct angle.

The resolution in angle determination is here equal to 2°, which is less accurate than desired. An interpolated value using

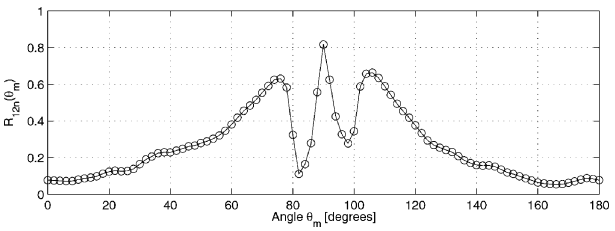

Fig. 2. Normalized maximum correlation as a function of beam formation angle. Circle show the values for the individual estimates.

a parabolic approximation of the peak is calculated for the angle as [15], [16]

$$\theta_{\text{int}} = \theta - \frac{R_{12n}(\theta+\Delta\theta) - R_{12n}(\theta-\Delta\theta)}{2(R_{12n}(\theta+\Delta\theta) - 2R_{12n}(\theta) + R_{12n}(\theta-\Delta\theta))}\Delta\theta \tag{7}$$

to avoid having to calculate the directional signals for too many directions. Here, $\Delta\theta$ is the angle sampling interval. The number of values can of course be narrowed down, if prior information can be used to determine a rough estimate. This could be from either temporal or spatial neighbors to the current estimate.

IV. Simulation

The angle determination method was tested along a wide range of flow angles using simulated data from the simulation program Field II [17], [18]. A parabolic flow was simulated inside a 10-mm-long cylinder with a radius of 2.5 mm, centered at $[x, y, z] = [0, 0, 37.5]$ mm. The cylinder was rotated to the angle θ, as shown in Fig. 1. For each volume of λ^3, where λ is the wavelength given in Table I, 10 scatterers were randomly distributed, and their amplitudes were generated from a Gaussian distribution with zero mean. At each emission, the scatterers were propagated according to their radial position

$$d_\theta = v_0 T_{prf}\left(1 - \left(\frac{r}{R}\right)^2\right), \quad r < R \tag{8}$$

where d_θ is the distance propagated along θ at each emission, v_0 is the peak velocity, r is the radial position of the scatterer, and R is the cylinder radius. As the scatterers reached the cylinder end, they were feed back to the beginning.

A 7-MHz commercial linear array transducer was simulated. The simulations have been performed by using eight emissions equally spread over the 128 element aperture, with each emission using 11 defocused elements to emulate a spherical wave emission [10]. A frequency encoded chirp is used in transmission, which in measurement situations will increase the signal-to-noise ratio (SNR) [19], [12]. The chirp has a duration of 20 μs and a bandwidth of 7 MHz centered around the transducer center frequency. Only 64 receiving elements are used at each reception, and they are multiplexed to be closest to the emitting center element, and all 128 receiving elements are hereby sampled. The transmission is repeated with a pulse repetition frequency of 3 kHz and 1280 individual emissions have been simulated by repeating the sequence 160 times. A summary of the parameters used for simulation and processing is shown in Table I.

The received radio frequency (RF) element signals are first matched filtered to compress the signals in the axial direction and increase the SNR [19]. The resulting signals are beamformed along every 5° covering a total of 180°. Hereby, low-resolution directional signals are formed, and high-resolution signals are made by adding the latest eight low-resolution signals. Stationary echo canceling is performed separately for each direction by finding the mean value of the focused lines and then subtracting this from the signals. The focused directional signals from the same image formation are subsequently cross-correlated and added to the other cross-correlation functions, and the velocity angle is found from the combined cross-correlation function, as described in Section III.

TABLE I
Parameters for Transducer and Parabolic Flow Simulation

Center frequency	f_0	7 MHz
Wavelength	$\lambda = c/f_0$	0.22 mm
Element pitch	w	0.208 mm
Element height	h_e	4.5 mm
Number of receive elements	N_r	128
Number of transmit events	N_t	8
Elevation focus	R_e	20 mm
Directional signals	N_e	128
Pulse repetition frequency	f_{prf}	3 kHz
RF sampling frequency	f_s	120 MHz
Distance between estimates	dz	0.25 mm
Sampling interval for lines	$\Delta r = \lambda/20$	0.011 mm
Correlation interval	$-10\lambda : 10\lambda$	-2.2:2.2 mm
Radius of vessel	R	2.5 mm
Distance to vessel center	z_{st}	37.5 mm
Peak velocity in flow	v_0	0.15 m/s
Simulated flow angles	θ	$0°, 10°, .., 90°$

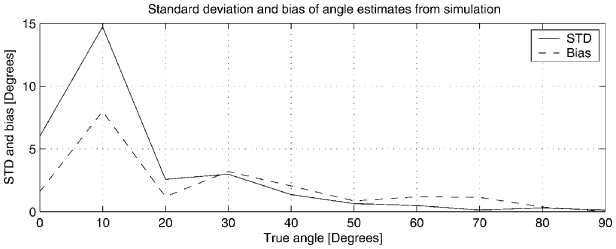

Fig. 3. Standard deviation and bias for 10 independent velocity angle estimates in the center of the simulated blood vessel. Simulation is repeated for angles $\theta = 0°, 10°, \ldots, 90°$. Dashed line shows the bias, and the solid line shows the standard deviation as a function of the true angle θ.

Ten simulations at flow angles θ equally spaced from 0° (axial flow) to 90° (lateral flow) have been performed. The velocity angle was found in the center of the cylinder from 16 sequences of eight emissions, each corresponding to a total of 128 emissions. Hereby, 10 independent estimates are made from the 1280 emissions. The bias and standard deviation of the angle estimates have been calculated and is plotted in Fig. 3 as a function of the true flow angle.

Both the bias and standard deviation of the angle estimates are below 3° for flow angles from $\theta = 20°$ to 90°. At flow angles of 0° (axial flow) and 10°, an unfortunate combination of the flow velocity and the pulse repetition frequency result in higher bias and standard deviation. Here, the propagation between shots at the vessel center coincide with a quarter of a wavelength $d_\theta \approx \lambda/4$, resulting in a reduction of the SNR and an increase in sidelobes levels [20]. A higher pulse repetition frequency than 3 kHz would solve this problem [20].

TABLE II
STANDARD PARAMETERS FOR TRANSDUCER AND PARABOLIC FLOW MEASUREMENT

Center frequency	f_0	7 MHz
Wavelength	$\lambda = c/f_0$	0.22 mm
Element pitch	w	0.208 mm
Element height	h_e	4.5 mm
Number of receive elements	N_r	128
Number of transmit events	N_t	8
Elevation focus	R_e	20 mm
Directional signals	N_e	128
Pulse repetition frequency	f_{prf}	3 kHz
RF sampling frequency	f_s	40 MHz
Distance between estimates	dz	0.25 mm
Sampling interval for lines	$\Delta r = \lambda/20$	0.011 mm
Correlation interval	$-10\lambda : 10\lambda$	-2.2:2.2 mm
Radius of vessel	R	8.5 mm
Distance to vessel center	z_{st}	37.5 mm
Peak velocity in flow	v_0	0.15 m/s

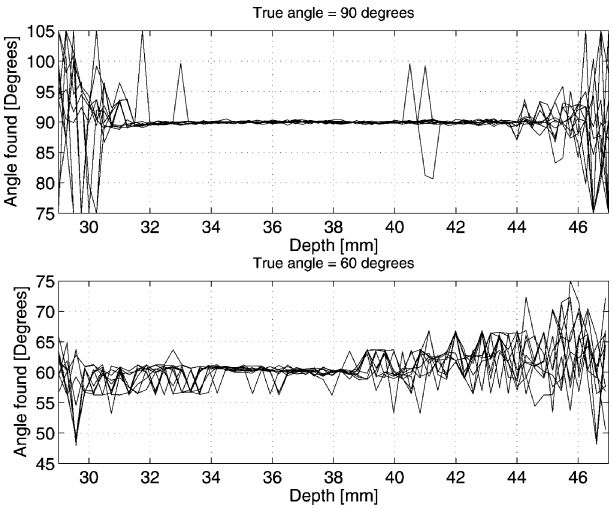

Fig. 4. Estimated velocity angles for a true velocity angle of 90° (top) and 60° (bottom).

V. MEASUREMENTS

The angle determination method was also investigated using a circulating flow rig. A Smedegaard EcoWatt 1 pump circulates a blood mimicking fluid made by Danish Phantom Service consisting of water, glycerol, orgasol, Trition x-100, NaBenzoat, and K_2EDTA diluted 10 to 1 with demineralised water. A reduction valve was used to control the velocity. The tubing consisted of a 1.2-m-long, 20-mm-diameter steel tube before the flow entered a 18-mm-diameter heat shrink tubing. The thickness of the heat shrink tubing was 0.5 mm giving an internal diameter of 17 mm. The flow was maintained with a peak velocity less than 0.15 m/s giving a Reynolds number of 1276 assuming a viscosity of 2 cP and a parabolic profile.

Measurements were performed using the RASMUS research scanner [21]. It can emit arbitrary signals in 128 individual channels and can simultaneously sample signals from 64 receive channels at 40 MHz with 12-bits precision. A two-to-one multiplexing makes it possible to cover all 128 transducer elements in twp emissions. Data are stored in the system's 16 GB of memory in real-time, and they are transferred to a Linux computer cluster with 100 CPUs for beam formation and velocity estimation.

The 7-MHz commercial linear array transducer previously simulated was also used in the experiments. It was mounted in a fixation device above the tube at a certain beam to flow angle and at a certain distance from the tube center. The transmission sequence was the same as for the simulations, again using a linear chirp and generating spherical waves from eight different locations each time using 11 defocused elements. A total of 3000 individual emissions was acquired by repeating the sequence 375 times. A summary of the parameters used for data acquisition and processing is shown in Table II. The data is the same as that used in [8] for investigating the velocity estimation.

Two experiments at flow angles θ of 60° and 90° (transverse velocity) were performed. The velocity along the flow direction was found from 16 sequences of eight emissions, each corresponding to a total of 128 emissions. This is the same number of emissions that is used in normal spectral velocity imaging [2] over which the flow normally can be considered quasi-stationary in the human body. The velocity could be estimated with a standard deviation over the whole profile of 0.36% relative to the peak velocity of the vessel for a velocity angle of 60°. The standard deviation was 1.2% for 90° [7].

The angle determination method has been applied on the data and the results are shown in the bottom part of Fig. 4 for a true velocity angle of 60°. One line is shown for each of the 10 independent velocity estimates, and the velocity has been found for 180° in steps of 5°. The vessel boundaries are between 30 and 46 mm. Here, the mean value of all estimates is 60.54° and the standard deviation is 2.1°. A slight increase in standard deviation as a function of depth is seen. This is probably due to the decrease in SNR as a function of depth.

The same experiment has been repeated for a true velocity angle of 90° and the result is shown in the top part of Fig. 4. Here, the mean value is 90.0003° and the standard deviation is 1.32°. The standard deviation rises sharply at the edges of the vessel. Here, the velocity is low and the echo canceling will remove most of the signal power. The SNR is, thus, low and the accuracy of the estimates is thereby low. The standard deviation and bias are, therefore, found using only data inside the vessel to avoid domination by these edge effects.

The velocity magnitude profiles after both angle and velocity estimation can be seen in Fig. 5. First, the angle has been determined and then the corresponding velocity for the angle has been used as the velocity magnitude. No interpolation between the 5° angle estimates have been performed, before the velocity magnitude was determined, and the velocity is just found at the angle with the peak normalized correlation given by (6). The top graph shows the ten profiles at 90° and the bottom at 60°. The standard deviation of data averaged over the profile at 60° is 0.0046 m/s or 2.9% relative to the peak velocity. At 90°it is 0.0034 m/s or 2.1397%. The standard deviation is, thus, somewhat increase compared to when no determination of angle is used.

VI. PARAMETER STUDY

A parameter study has been performed on the data described in the previous section. Here, the influence of a variation in the number of lines and the correlation length has been performed

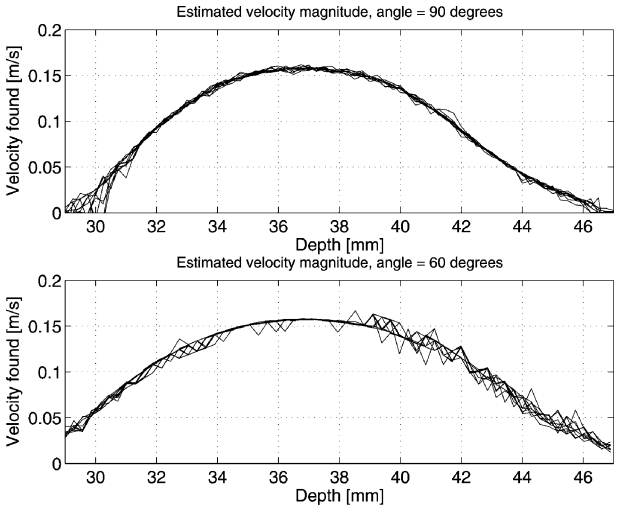

Fig. 5. Estimated velocity magnitude for a true velocity angle of 90° (top) and 60° (bottom).

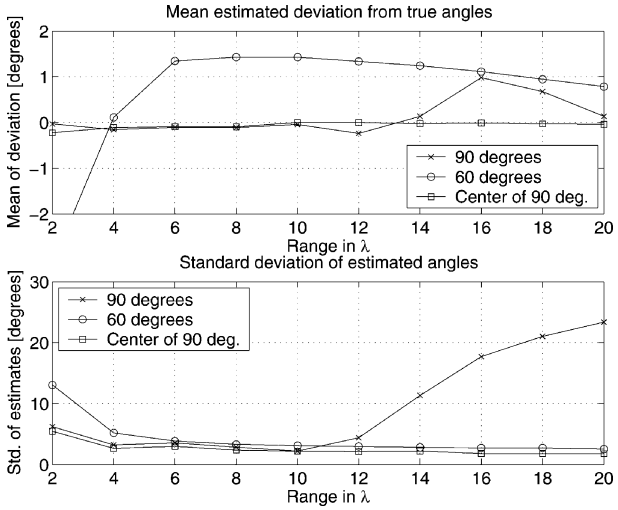

Fig. 6. Variation in correlation range in terms of the wavelength λ. Upper graph shows the bias of the angle estimates and the lower graph shows the standard deviation. Circled line is for the 60° experiment, the crossed line is for the 90° experiment, and the squared line is for the center part of the tube at 90°.

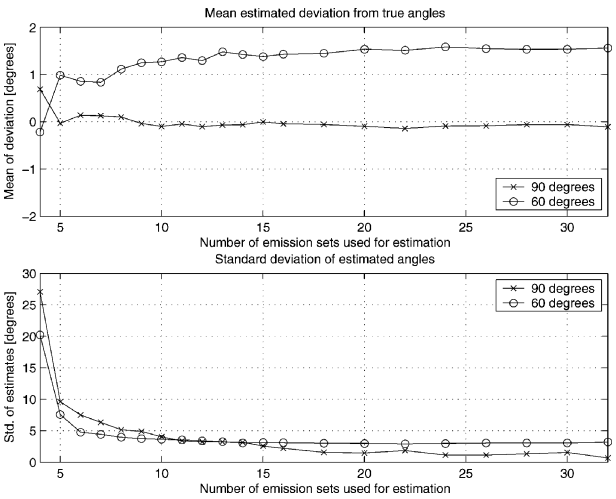

Fig. 7. Variation in number of lines used in the cross-correlation function. One set consists of eight emissions for creating a high-resolution image or line. Circles mark the 60° experiment, and the crosses mark the 90° experiment.

for the 60° and 90° data sets. The standard parameters shown in Table II are used for the processing.

In Fig. 6, the variation in the mean estimated deviation from the true angle is shown in the top graph as a function of correlation interval given as a multiple of the wavelength λ. The correlation is over an interval of $\pm$ the range given on the figures x axis. A value of 10, thus, indicates a correlation range of $-10\lambda : 10\lambda$. The bias and standard deviation have been found in the center of the vessel, which is from 31.8 to 44.1 mm at 90° and from 31.8 to 46.0 mm at 60°. Hereby the angle is only found in the center part of the vessel and the uncertain and less important estimates at the edges are excluded. The standard deviation is shown in the lower graph in Fig. 6. For all ranges above 4λ, the bias is below 2° at 60° and below 1° at 90° flow angles. The std. also drops for increasing range, since more data is available in the correlation for 60°. At 90°, the standard decreases until 10λ after which it increases. The standard drops in the middle of the vessel but rises at the edges, since the correlation range is so large, that directional lines reaches outside the vessel and this affects the angle estimator. The graph with the squares show the performance in the central core of the vessel at depths between 33.7 and 43 mm. Here, there are no edge effects and the standard deviation and bias decreases with increasing correlation range. It is, thus, not advisable to have too long directional lines in this case, and lower ranges are also an advantage, when nonlaminar flow patterns and turbulence are encountered.

Fig. 7 shows the performance as a function of number of high-resolution images employed in the estimation process. Each sets corresponds to eight emissions that makes up a high-resolution image. For this stationary flow measurement, it is an advantage to use more lines as both mean deviation (top) and standard deviation (bottom) is reduced for an increasing number of sets. For 60°, the bias does no decrease and this might be due to a misalignment of the vessel, so that the true angle is closer to 61.5° than 60°.

VII. Vector Velocity Image

The acquired data can be used to find both direction and velocity magnitude for a full image from the 128 emissions. Such a velocity vector image is shown in Fig. 8. The velocity vector is found for every 1 mm in the lateral and axial direction, and the velocity magnitude and direction are shown as arrows with a length proportional to velocity. The underlying velocity color map has been made from the estimates by interpolating the values by a factor of 10 in each direction and encode the color from the velocity magnitude. Only velocity estimates above a magnitude of 0.005 m/s are shown and else the underlying B-mode image is shown. The B-mode image has been made from eight emissions and a dynamic range of 40 dB is used. Most of the vessel is filled with color and the direction is found to be 90° at nearly all locations.

A similar image for 60° is shown in Fig. 9. The lower left corner shows erroneous velocity estimates, which is due to lack of signal. Only noise is present in this part and random velocity vectors are, thus, found. These could be removed by employing

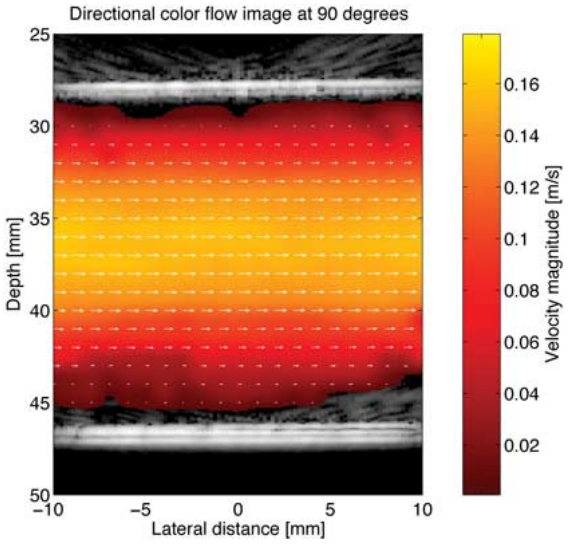

Fig. 8. Vector velocity image for a true velocity angle of 90°. Both magnitude and directions are estimated.

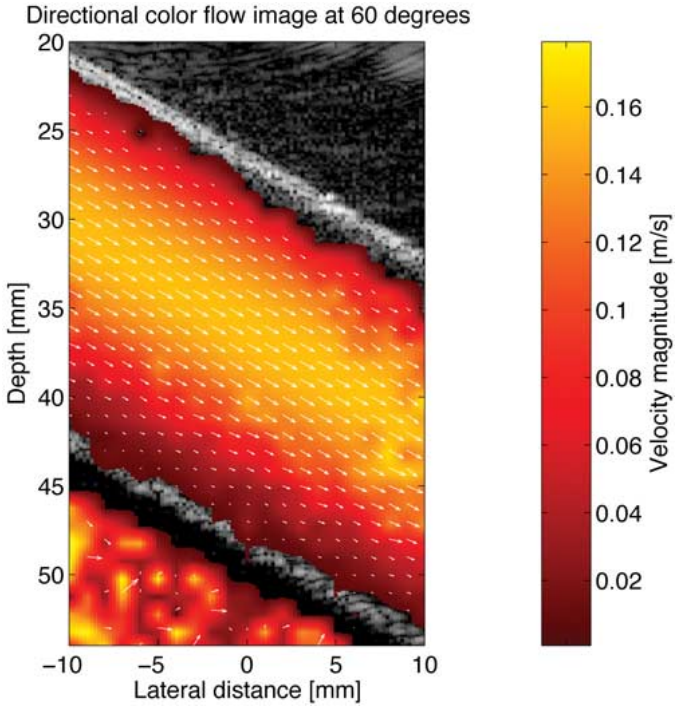

Fig. 9. Vector velocity image for a true velocity angle of 60°. Both magnitude and directions are estimated.

a discriminator using the energy of the signals and excluding estimates only based on noise. The energy is found as

$$E = \sum_{n=1}^{N_l} \sum_{k=-N_k/2}^{N_k/2} (y_d^{(n)}(k))^2 \tag{9}$$

where $N_k + 1$ is the number of samples in the directional lines and N_l is the number of directional signal used for a single velocity estimation. This could be compared to the expected noise energy of current setup.

TABLE III
PARAMETERS USED FOR THE EXPERIMENT

Transducer type	Linear array
Number of transducer elements	128
Transducer element pitch	0.3 mm
Transducer element kerf	0.035 mm
Transducer element height	5 mm
Elevation focus	20 mm
Center frequency, f_0	6.2 MHz
Wavelength, $\lambda = c/f_0$	0.25 mm
Excitation type	20 μs tapered chirp
Frequencies swept	$\sim$ 3 - 8 MHz
Number of emitting elements	11
Number of receiving elements	64, centered at em.
Number of emissions in sequence, N_t	8
Number of virtual sources, $(= N_t)$	8
Virtual source positions	[x, 0, -2.5] mm
Pulse repetition frequency, f_{prf}	10 kHz
Points in line, $N_k + 1$	401
Spatial sampling interval, Δr	$\lambda/20 = 12.5\mu$m
Line length	$20\lambda = 5$ mm
Angular sampling interval, $\Delta\theta$	5°
Stationary echo canceling method	Linear regression [23]
Number of correlations averaged, L	113
Velocity search range	-1.5 to 1.5 m/s

VIII. *In Vivo* MEASUREMENTS

This section shows examples for *in vivo* data. 2.2 s of real-time *in vivo* data of the common carotid artery of a healthy 30-year-old male volunteer was acquired using the RASMUS multichannel sampling system [21] and a 128 element linear array transducer. The scanning was done by an experienced sonographer. Data processing was performed offline on a 100 CPU computer cluster. The parameters used for data acquisition and processing are outlined in Table III.

Due to hardware limitations, only 64 elements of the full 128 element array was used at reception. The receiving subaperture was slid at each emission to be centered around the emitting subaperture. The excitation waveform was a 20-μs chirp linearly sweeping frequencies from 3 to 8 MHz, amplitude tapered by a 10% Tukey window. The received signals were compressed using a mismatch compression filter, which was the time-inverse chirp tapered by a Chebyshev window with 70% relative sidelobe attenuation [22].

Data were processed in blocks of 128 emissions corresponding to 12.8 ms of data. The flow angle was estimated for every data block, as described in Section III for a 1-mm grid of points ranging from 16 to 31 mm depth and -10 to 10 mm lateral. The velocity magnitude was estimated along the angle found for each individual point. The estimation process for each point was therefore mutually independent.

B-mode images were simply made by beamforming high-resolution lines along the axial direction followed by envelope detection and logarithmic compression. All B-mode images are shown in 30-dB dynamic range only. The reason for the low B-mode image quality compared to that of [24] is found in the sparse emission sequence used for flow estimation. A solution could be to make interleaved emission sequences of both B-mode and flow emissions.

Full 2-D vector flow images were made by combining B-mode images with both colors indicating velocity magnitude

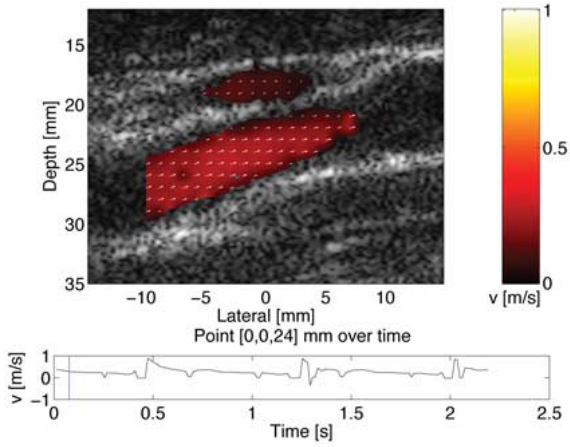

Fig. 10. Synthetic aperture vector flow image of the common carotid artery and jugular vein at middiastole. Vertical line in the bottom part marks the time of the image.

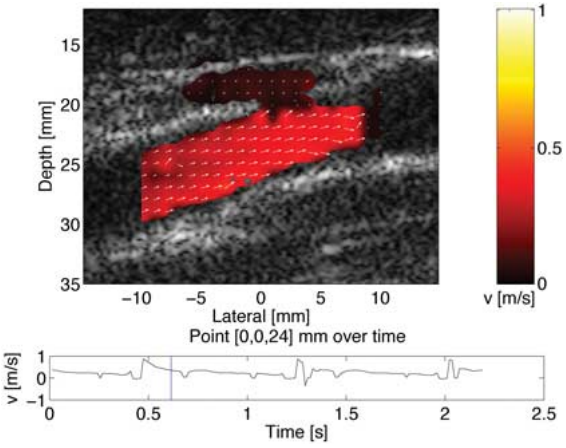

Fig. 11. Synthetic aperture vector flow image of the common carotid artery and jugular vein at end systole. Vertical line in the bottom part marks the time of the image.

and vector arrows showing the estimated flow direction and velocity magnitude. Velocity estimates were displayed when the energy of the directional signals after stationary echo canceling was above a certain fraction of the energy of the signals prior to echo canceling. This can be written as

$$\frac{\sum_{n=1}^{N_l}\sum_{k=-N_k/2}^{N_k/2}\mathrm{SEC}[(y_d^{(n)}(k))^2]}{\sum_{n=1}^{N_l}\sum_{k=-N_k/2}^{N_k/2}(y_d^{(n)}(k))^2} > E_f \qquad (10)$$

where $\mathrm{SEC}[\cdot]$ denotes the stationary echo canceling operation, N_k+1 is the number of samples in the directional lines, N_l is the number of directional signal used for a single velocity estimation, and E_f is the required energy fraction.

Fig. 10 shows a synthetic aperture vector flow image made at mid-diastole. Both the common carotid artery and a cross section of the jugular vein is seen. The base of each vector arrow shows the point of estimation, and the vector direction and length indicates the flow angle and magnitude, respectively. The bottom plot indicates the velocity at point [0,0,24] mm over the entire 2.2 s of data, and the vertical bar indicates the time of the current frame. The peak systoles occur around time $t = 0.5,\ 1.3,$ and 2.0 s.

A vector flow image made at end systole is shown in Fig. 11. The increased velocity is indicated both by a lighter color, and by the increased length of the vector arrows. A slight discrimination problem between tissue and blood is seen at the border between the carotid artery and the jugular vein.

Fig. 12 shows a vector flow image made at peak systole. Dark velocity vectors are used for better visualization. In the vessel center, the majority of the angle estimates are within the expected range, but close to the vessel border the performance is poor. This is mainly due to problems of suppressing the large vessel border movements during the systolic phase.

The top plot of Fig. 13 shows the estimated angles for a point in the center of the common carotid artery over time. The majority of the estimates are centered around $\theta = 106°$ which corresponds to the flow angle visually determined from the B-mode image (see Fig. 10). The bottom plot shows a histogram of the angle estimates, where 76% of the 171 estimates are within the

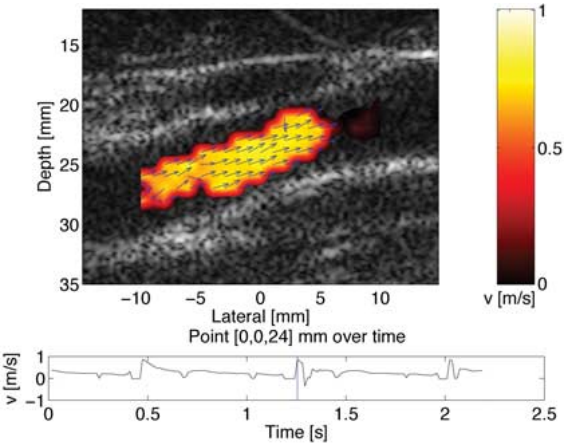

Fig. 12. Synthetic aperture vector flow image of the common carotid artery and jugular vein at peak systole. Vertical line in the bottom part marks the time of the image.

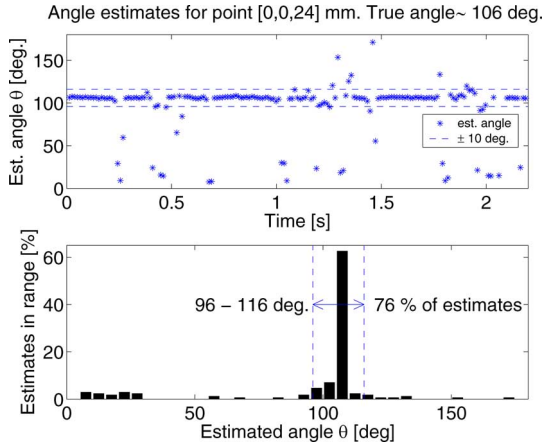

Fig. 13. Top plot show the individual angle estimates for a point in the center of the common carotid artery [0,0,24] mm over time. Bottom plot shows a histogram of the flow angle estimates, indicating that 76% of the estimates are within $\pm 10°$ of the flow angle of $106°$ visually determined from the B-mode image.

range of $106^\circ \pm 10^\circ$, which is considered adequate for finding the velocity magnitude. These estimates within the $\pm 10^\circ$ range have a standard deviation below 2.7°. 69% of the estimates are within the range of $106^\circ \pm 5^\circ$. There seems to be a tendency for an increasing number of false estimates around time $t = 0.5$, 1.3, and 2.0 s where the peak systoles are found. Furthermore, it is noticed that the majority of the erroneous estimates are close to perpendicular to the flow direction, indicating that the suppression of the high amplitude tissue signal by the stationary echo canceling filter is not optimal. This can potentially be solved by applying more advanced stationary echo canceling filters.

IX. Conclusion

An approach for determining both velocity magnitude and angle in a SA flow system has been presented. For data measured using an experimental ultrasound scanner and a flow rig, both magnitude and angle could be determined with a relative standard deviation of roughly 2% for flow angles of 60° and 90°. A parameter study showed the influence of the number of lines in an estimate and the correlation length.

The synthetic aperture 2-D vector velocity estimation method was applied to *in vivo* data from the human common carotid artery. Full color flow maps including 2-D vectors showing the flow direction were presented from both the diastolic and systolic phase. For a point in the vessel center, the flow angle is estimated over time and 76% of the estimates were within $\pm 10^\circ$ of the flow direction visually determined from the B-mode image.

Acknowledgment

The authors would like to thank M. B. Nielsen and K. R. Nielsen, both from the Department of Radiology, Section of Ultrasound, Rigshospitalet, Denmark, for performing the clinical scanning, and S. Nikolov for making the measurements in the flow rig.

References

[1] D. H. Evans, W. N. McDicken, R. Skidmore, and J. P. Woodcock, *Doppler Ultrasound, Physics, Instrumentation, and Clinical Applications*. New York: Wiley, 1989.

[2] J. A. Jensen, *Estimation of Blood Velocities using Ultrasound: A Signal Processing Approach*. New York: Cambridge Univ. Press, 1996.

[3] G. E. Trahey, J. W. Allison, and O. T. von Ramm, "Angle independent ultrasonic detection of blood flow," *IEEE Trans. Biomed. Eng.*, vol. BME-34, pp. 965–967, 1987.

[4] M. D. Fox, "Multiple crossed-beam ultrasound Doppler velocimetry," *IEEE Trans. Son. Ultrason.*, vol. SU-25, pp. 281–286, 1978.

[5] O. Bonnefous, "Statistical analysis and time processes applied to velocity measurement," in *Proc. IEEE Ultrason. Symp.*, 1989, pp. 887–892.

[6] J. A. Jensen and I. R. Lacasa, "Estimation of blood velocity vectors using transverse ultrasound beam focusing and cross-correlation," in *Proc. IEEE Ultrason. Symp.*, 1999, vol. 2, pp. 1493–1497.

[7] J. A. Jensen and S. I. Nikolov, "Transverse flow imaging using synthetic aperture directional beamforming," *Proc. IEEE Ultrason. Symp.*, vol. 2002, no. 2, pp. 1488–1492, 2002.

[8] ——, "Directional synthetic aperture flow imaging," in *IEEE Trans. Ultrason. Ferroelec. Freq. Contr.*, Sep. 2004, vol. 51, no. 9, pp. 1107–1118.

[9] J. A. Jensen, "Velocity vector estimation in synthetic aperture flow and B-mode imaging," in *IEEE Int. Symp. Biomed. Imag. Nano Macro*, Apr. 2004, vol. 1, pp. 32–35.

[10] M. Karaman, P. C. Li, and M. O'Donnell, "Synthetic aperture imaging for small scale systems," *IEEE Trans. Ultrason. Ferroelectr. Freq. Control*, vol. 42, no. 3, pp. 429–442, May 1995.

[11] G. R. Lockwood, J. R. Talman, and S. S. Brunke, "Real-time 3-D ultrasound imaging using sparse synthetic aperture beamforming," *IEEE Trans. Ultrason. Ferroelectr. Freq. Control*, vol. 45, no. 4, pp. 980–988, Jul. 1998.

[12] K. L. Gammelmark and J. A. Jensen, "Multielement synthetic transmit aperture imaging using temporal encoding," *IEEE Trans. Med. Imag.*, vol. 22, no. 4, pp. 552–563, Apr. 2003.

[13] S. I. Nikolov, K. Gammelmark, and J. A. Jensen, "Recursive ultrasound imaging," in *Proc. IEEE Ultrason. Symp.*, 1999, vol. 2, pp. 1621–1625.

[14] S. I. Nikolov and J. A. Jensen, "In-vivo synthetic aperture flow imaging in medical ultrasound," *IEEE Trans. Ultrason. Ferroelectr. Freq. Control*, vol. 50, no. 7, pp. 848–856, Jul. 2003.

[15] S. G. Foster, "A pulsed ultrasonic flowmeter employing time domain methods," Ph.D. dissertation, Dept. Elec. Eng., Univ. Illinois, Urbana, Il, 1985.

[16] S. G. Foster, P. M. Embree, and W. D. O'Brien, "Flow velocity profile via time-domain correlation: Error analysis and computer simulation," *IEEE Trans. Ultrason. Ferroelectr. Freq. Control*, vol. 37, no. 3, pp. 164–175, May 1990.

[17] J. A. Jensen, "Field: A program for simulating ultrasound systems," in *Med. Biol. Eng. Comp.*, 1996b, vol. 4, 10th Nordic-Baltic Conference on Biomedical Imaging, pp. 351–353.

[18] J. A. Jensen and N. B. Svendsen, "Calculation of pressure fields from arbitrarily shaped, apodized, and excited ultrasound transducers," *IEEE Trans. Ultrason. Ferroelectr, Freq. Control*, vol. 39, no. 2, pp. 262–267, Mar. 1992.

[19] T. X. Misaridis and J. A. Jensen, "An effective coded excitation scheme based on a predistorted FM signal and an optimized digital filter," in *Proc. IEEE Ultrason. Symp.*, Oct. 1999, vol. 2, pp. 1589–1593.

[20] N. Oddershede and J. A. Jensen, "Effects influencing focusing in synthetic aperture vector flow imaging," *IEEE Trans. Ultrason. Ferroelectr. Freq. Control*, 2006, submitted for publication.

[21] J. A. Jensen, O. Holm, L. J. Jensen, H. Bendsen, S. I. Nikolov, B. G. Tomov, P. Munk, M. Hansen, K. Salomonsen, J. Hansen, K. Gormsen, H. M. Pedersen, and K. L. Gammelmark, "Ultrasound research scanner for real-time synthetic aperture image acquisition," *IEEE Trans. Ultrason. Ferroelec. Freq. Control*, vol. 52, no. 5, pp. 881–891, May 2005.

[22] T. Misaridis, Ultrasound imaging using coded signals. Lyngby, Denmark, Technical University of Denmark (DTU), 2001, Ph.D. dissertation.

[23] A. P. G. Hoeks, J. J. W. van de Vorst, A. Dabekaussen, P. J. Brands, and R. S. Reneman, "An efficient algorithm to remove low frequency Doppler signal in digital Doppler systems," *Ultrason. Imag.*, vol. 13, pp. 135–145, 1991a.

[24] M. H. Pedersen, K. L. Gammelmark, and J. A. Jensen, "Preliminary in-vivo evaluation of convex array synthetic aperture imaging," *Proc. SPIE – Progress in Biomedical Optics and Imaging*, pp. 33–43, 2004.

A.2 Oddershede, N. and Jensen, J. A.,
Effects influencing focusing in synthetic aperture vector flow imaging, *IEEE Transactions on Ultrasonic, Ferroelectrics, and Frequency Control, vol. 54, no. 9, September 2007, pp 1811-25.*

Effects Influencing Focusing in Synthetic Aperture Vector Flow Imaging

Niels Oddershede, *Student Member, IEEE* and Jørgen Arendt Jensen, *Senior Member, IEEE*

***Abstract*—Previously, a synthetic aperture vector velocity estimation method was proposed. Data are beamformed at different directions through a point, where the velocity is estimated. The flow direction is estimated by a search for the direction where the normalized cross-correlation peaks and the velocity magnitude along this direction are found.**

In this paper, different effects that influence the focusing in this method are investigated. These include the effect of phase errors in the emitted spherical waves, motion effects, and the effect of various interpolation methods in beamforming.

A model based on amplitude drop and phase error for spherical waves created using the virtual source concept is derived. This model can be used to determine the opening angle of a virtual source. Simulations for different virtual source placements are made, and it is recommended that the virtual sources be placed behind the aperture when shallow structures are imaged, and when deeper-lying structures are imaged the virtual sources be placed in front of the aperture.

Synthetic aperture methods involve summation of data from numerous emissions. Motion between these emissions results in incoherence and affects resolution, contrast, and the signal-to-noise ratio. The effects of motion on the synthetic aperture vector velocity estimation method are investigated, and it is shown that for both axial and lateral motion, the contrast and signal-to-noise ratio can be seriously affected. A compensation method using the previous vector velocity estimate, when new data are beamformed, is implemented and tested. It is shown from a number of flow phantom experiments that a significant improvement with respect to bias and standard deviation of the velocity estimates can be obtained by using this compensation. Increased performance is gained at the expense of computation time.

Different interpolation methods can be used for beamforming the data. In this paper, the velocity estimation performance using various more complex interpolation schemes are compared to that using linear interpolation. No significant difference in the performance of the method is seen when other interpolation methods are used.

I. Introduction

The majority of ultrasound scanners that are commercially available at present time feature blood velocity estimation based on the autocorrelation method presented in [1]. The method is robust and fairly simple to implement, but the velocity found is not the true velocity magnitude, but simply the projection of the velocity magnitude onto the axial direction. Different attempts have been made to find the 2-D velocity vector, and one of the more promising, based on synthetic aperture techniques, was presented in [2], [3]. In the present paper, a number of effects that influence the performance of this method are investigated.

Synthetic transmit aperture (STA) imaging [4] is performed by emitting spherical waves from different parts of the aperture. After every transmission, a complete low resolution image (LRI) of the area under investigation can be created using dynamic receive beamforming. The LRIs from a number of emissions are summed to create a high resolution image (HRI), which is dynamically focused in both transmit and receive. The process is shown in Fig. 1, where the spherical wave is created by emitting from a single transducer element. Alternatively, more elements can be used to emulate a spherical wave as described in Section II. This is the concept of virtual sources, and Section II furthermore presents a signal-to-noise ratio (SNR) approach to determine the maximum opening angle of the virtual sources that can provide SNR enhancement. Different placements of the virtual sources are examined and the maximum opening angles calculated.

Due to the summation of a number of low resolution images created at different time instances, STA imaging is susceptible to motion artifacts resulting in incoherent summation and degradation of resolution, contrast, and SNR.

The effects of tissue motion in synthetic aperture ultrasound have been studied by various authors [6]–[10]. Trahey and Nock investigated motion effects in a synthetic receive aperture system in [6] and showed that motion along the axial direction has a far larger effect on the resolution than lateral movement. Also, it was argued that the problem increases with the length of the emission sequence and the center frequency. A motion compensation method based on axial cross-correlation of LRIs was proposed.

Hazard and Lockwood [8] tested motion effects in an STA system with three emissions in the emission sequence. They showed that axial movement on the order of 3% of the wavelength between emissions had only little effect on the resolution and virtually no effect on the contrast, whereas a 10 times larger movement resulted in both a slight shift and widening of the main lobe and a reduced contrast.

A method for blood flow velocity estimation using STA was presented in [3] based on cross-correlation of lines

Manuscript received February 23, 2006; accepted April 8, 2007. This work was supported by grant 26-04-0024 from the Danish Science Foundation and by B-K Medical A/S, Her-lev, Denmark.

The authors are with the Center for Fast Ultrasound Imaging, Ørsted•DTU, Technical University of Denmark, DK-2800 Lyngby, Denmark (e-mail: no@oersted.dtu.dk).

Digital Object Identifier 10.1109/TUFFC.2007.465

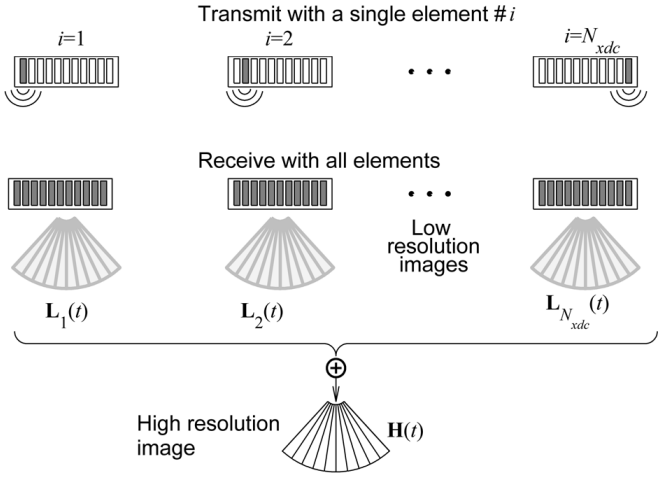

Fig. 1. Synthetic transmit aperture imaging. A single element i emits an approximately spherical wave. All elements receive the echo, and a low resolution image is created by using dynamic receive focusing. A number of low resolution images are summed to create a high resolution image. Figure from [5].

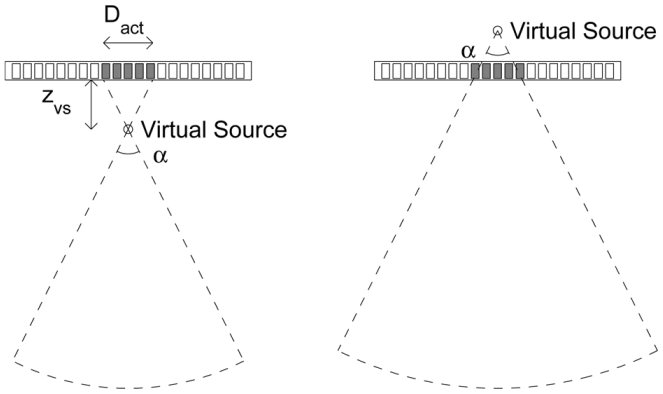

Fig. 2. Virtual sources can be placed either in front of the transducer (left) or behind the transducer (right). The emitted pressure waveform is assumed spherical within a limited angular extend, the opening angle α. The virtual source depth $z_{\rm vs}$ and the size of the active aperture $D_{\rm act}$ can be used to approximate the opening angle.

beamformed along the flow, assuming the direction of flow is known. A method for estimating the direction of flow was presented in [2] based on a search for the highest normalized cross-correlation as a function of angle. By finding both the in-plane flow direction and magnitude, 2-D velocity vectors can be displayed for, in principle, all image points. The synthetic aperture velocity estimation method as presented in [2] is shortly described in Section III. In [2] the resolution and contrast degradation due to motion of blood are neglected. Motion results in a smearing and a decrease in the SNR. The problem increases with the pulse repetition period and the number of emissions in the emission sequence. In Section IV the effects of motion in this system are evaluated with respect to both SNR and contrast.

In [11], a motion compensation method for STA B-mode imaging was presented. The method used an interleaved sequence consisting of both a long STA sequence for making high resolution B-mode images and a short STA sequence for motion estimation. The cross-correlation estimator of [2] was used on the short sequence to find the tissue motion in two dimensions, and a compensation was made from the estimated tissue motion, when beamforming the B-mode image from the long sequence.

In the present paper the motion compensation method presented in [11] is used in flow estimation. Here only a short sequence is used for both blood velocity estimation and motion compensation. The previous 2-D velocity vector estimate is used for compensating for the motion of the blood in the initial beamforming of the following high resolution lines. This method is described and tested in Section V.

In [12], the effect of using different interpolation methods during beamforming of STA data was investigated. It was shown that using more advanced interpolation methods than linear interpolation can significantly increase contrast. The effect of these interpolation methods on the performance of the STA vector velocity estimation method is tested in Section VI using some flow phantom data.

II. Position of Virtual Source

Using the emission sequence shown in Fig. 1, where only one transducer element emits at a time, results in a low emitted energy and, thus, a low SNR. A number of elements are therefore used to create a virtual source [13], [14] either behind or in front of the aperture, as shown in Fig. 2. The assumption is that the emitted pressure wave will propagate as a spherical wave from the position of the virtual source. This assumption is, of course, valid only within a limited angular extent determined by the transducer geometry and the spatial position of the virtual source. The angle for which the wave can be assumed spherical is called the opening angle α. By geometrical considerations, the opening angle can be approximated by

$$\alpha = 2 \arctan \frac{1}{2F_{\#}}, \tag{1}$$

where $F_{\#}$ is the F-number given by $F_{\#} = |z_{\rm vs}|/D_{\rm act}$, where $|z_{\rm vs}|$ is the distance from the virtual source to the transducer surface, and $D_{\rm act}$ is the size of the active aperture. In [15] it was shown that (1) gives a good approximation for virtual sources both behind and in front of the transducer. In order to quantitatively test this approximation, the pressure fields from two consecutive emissions from different virtual sources are modelled. Preferably, the SNR should increase when adding the LRIs acquired by these two virtual sources. If this is not the case, for instance, due to amplitude drop or phase misalignments, the summation is worthless and can even deteriorate the image. The modelled SNR for one emission is compared to that obtained by adding the signals from two virtual sources. The acceptance angle is then defined as the angle

for which the virtual source is still valuable in the SNR sense.

The pressure field from the n'th virtual source at a point on the created sphere is modelled as

$$p_n(t) = s_n(t) + \eta_n(t), \tag{2}$$

where $s_n(t)$ is the pressure field including the electrical impulse response from the scanner and the transducer, and $\eta_n(t)$ is uncorrelated white noise with zero mean and noise power σ_η^2. The SNR is defined as

$$\mathrm{SNR}_n = \frac{E[s_n^2(t)]}{E[\eta_n^2(t)]} = \frac{E[s_n^2(t)]}{\sigma_\eta^2}, \tag{3}$$

where $E[\cdot]$ denotes the expectation value. In the following sections, the continuous wave case and the pulsed wave case are treated separately.

A. Continuous Wave

Assuming the n'th virtual source emits a monochromatic continuous wave signal at frequency f_0, the signal on the sphere will be

$$s_n(t) = A_n \cos(2\pi f_0 t + \phi_n), \tag{4}$$

and the SNR is then given by (3). Assuming emission from two virtual sources, the responses from the two emissions should be summed only if this increases the SNR. In other words, the LRI created from emission $n = 2$ should be used only for creating the HRI if

$$\mathrm{SNR}_1 \leq \mathrm{SNR}_{1+2}, \tag{5}$$

where SNR_1 is the SNR for emission 1, and SNR_{1+2} is the SNR of the sum of signals 1 and 2. This combined SNR is given by

$$\begin{aligned}\mathrm{SNR}_{1+2} &= \frac{E[(s_1(t)+s_2(t))^2]}{E[(\eta_1(t)+\eta_2(t))^2]} \\ &= \frac{E[s_1^2(t)+s_2^2(t)+2s_1(t)s_2(t)]}{2\sigma_\eta^2} \\ &= \frac{E[s_1^2(t)]+E[s_2^2(t)]+E[2s_1(t)s_2(t)]}{2\sigma_\eta^2},\end{aligned} \tag{6}$$

assuming the noise is independent from measurement to measurement. If we assume the signal from the second virtual source is simply a damped and phase-shifted version of the signal from the first virtual source,

$$s_2(t) = k s_1\left(t - \frac{\Delta\phi}{2\pi f_0}\right), \tag{7}$$

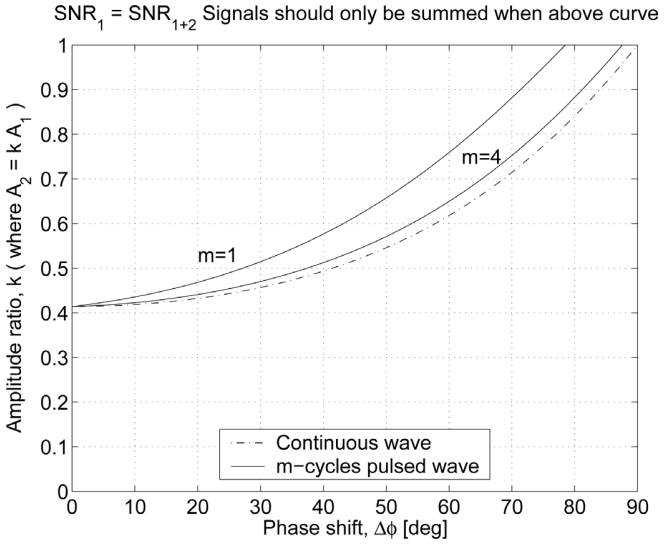

Fig. 3. The figure shows the border line between cases where the SNR increases, and where the SNR decreases when summing signals from two virtual sources. The border is plotted for both the continuous wave case and the pulsed wave case.

where $0 < k \leq 1$, and $\Delta\phi = \phi_1 - \phi_2$ is the phase difference, the last term in the numerator of (6) can be written as

$$\begin{aligned}&E[2s_1(t)s_2(t)] = 2R_{s_1s_2}(0) = 2kR_{s_1}\left(-\frac{\Delta\phi}{2\pi f_0}\right) \\ &= 2k\lim_{T\to\infty}\frac{1}{T}\int_T s_1\left(t+\frac{\Delta\phi}{4\pi f_0}\right)s_1\left(t-\frac{\Delta\phi}{4\pi f_0}\right)dt \\ &= 2kA_1^2\lim_{T\to\infty}\frac{1}{T}\int_T \cos\left(2\pi f_0 t+\frac{\Delta\phi}{2}\right)\cos\left(2\pi f_0 t-\frac{\Delta\phi}{2}\right)dt \\ &= kA_1^2\lim_{T\to\infty}\frac{1}{T}\int_T(\cos(4\pi f_0 t)+\cos(\Delta\phi))dt \\ &= kA_1^2\cos(\Delta\phi).\end{aligned} \tag{8}$$

Here $R_{s_1s_2}(\tau)$ denotes the cross-correlation of signals $s_1(t)$ and $s_2(t)$, and $R_{s_1}(\tau)$ is the auto-correlation of $s_1(t)$. The SNR of the combined signal is then given by

$$\mathrm{SNR}_{1+2} = \frac{A_1^2/2 + k^2A_1^2/2 + kA_1^2\cos(\Delta\phi)}{2\sigma_\eta^2}, \tag{9}$$

and the inequality of (5) can be written as

$$\begin{aligned}&\mathrm{SNR}_1 \leq \mathrm{SNR}_{1+2}, \\ &\frac{A_1^2/2}{\sigma_\eta^2} \leq \frac{A_1^2/2 + k^2\,A_1^2/2 + k\,A_1^2\cos(\Delta\phi)}{2\sigma_\eta^2}.\end{aligned}$$

Rearranging the terms gives

$$\frac{1-k^2}{2k} \leq \cos\,\Delta\phi. \tag{10}$$

In Fig. 3, the border line for inequality (10) is plotted as the dashed line. Notice that when the amplitude of the signals are the same $k = 1$, the phase difference $\Delta\phi$ should not exceed a quarter of a period, and that when the signals are in phase $\Delta\phi = 0$, the sum of amplitudes must exceed $A_1 + kA_1 = \sqrt{2}A_1$.

B. Pulsed Wave

In realistic applications only a pulsed wave is emitted from each virtual source. A m-cycle pulsed wave signal at center frequency f_0 is given by

$$s_n(t) = w_n(t) A_n \cos(2\pi f_0 t + \phi_n), \tag{11}$$

where the rectangular windowing function $w_n(t)$ is given by

$$w_n(t) = \begin{cases} 1, & 0 < t < \frac{m}{f_0}, \\ 0, & \text{else.} \end{cases} \tag{12}$$

The combined SNR can again be found as

$$\mathrm{SNR}_{1+2} = \frac{E[s_1^2(t)] + E[s_2^2(t)] + E[2s_1(t)s_2(t)]}{2E[\eta_1^2(t)]}. \tag{13}$$

Assuming as before that $s_2(t) = k\, s_1(t - (\Delta\phi / 2\pi f_0))$, the last term in the numerator equals

$$\begin{aligned} E[2s_1(t)s_2(t)] &= 2kR_{s_1}\left(-\frac{\Delta\phi}{2\pi f_0}\right) \\ &= 2kA_1^2 \int_{\frac{\Delta\phi}{4\pi f_0}}^{\frac{m}{f_0} - \frac{\Delta\phi}{4\pi f_0}} \cos\left(2\pi f_0 t + \frac{\Delta\phi}{2}\right) \cos\left(2\pi f_0 t - \frac{\Delta\phi}{2}\right) dt \\ &= kA_1^2 \int_{\frac{\Delta\phi}{4\pi f_0}}^{\frac{m}{f_0} - \frac{\Delta\phi}{4\pi f_0}} (\cos(4\pi f_0 t) + \cos(\Delta\phi)) dt \\ &= kA_1^2 \left[\frac{1}{4\pi f_0} \sin(4\pi f_0 t) + t\cos(\Delta\phi)\right]_{t=\frac{\Delta\phi}{4\pi f_0}}^{\frac{m}{f_0} - \frac{\Delta\phi}{4\pi f_0}} \\ &= kA_1^2 \frac{m}{f_0} \left(\left(1 - \frac{\Delta\phi}{2\pi m}\right)\cos(\Delta\phi) - \frac{1}{2\pi m}\sin(\Delta\phi)\right). \end{aligned} \tag{14}$$

The first two numerator terms of (13) are simply the energy of signals $s_1(t)$ and $s_2(t)$, respectively. Assuming m is an integer, the signal energy is the signal power $A_n^2/2$ multiplied by signal length m/f_0, and (13) can be written as

$$\mathrm{SNR}_{1+2} = \frac{\frac{A_1^2 m}{2f_0} + k^2 \frac{A_1^2 m}{2f_0} + 2kR_{s_1}\left(-\frac{\Delta\phi}{2\pi f_0}\right)}{2E[\eta_1^2(t)]}. \tag{15}$$

The inequality of (5) for an m-cycle pulsed wave signal with a rectangular envelope is then given by

$$\frac{1-k^2}{2k} \le \left(1 - \frac{\Delta\phi}{2\pi m}\right)\cos(\Delta\phi) - \frac{1}{2\pi m}\sin(\Delta\phi), \tag{16}$$

where the additional terms compared to (10) simply account for the decrease in envelope overlap. Equality in (10) and (16) is reached when the SNR of the single signal equals the SNR of the combined signal. The border lines for both inequalities are plotted in Fig. 3. Here lines are included for both $m = 1$ and $m = 4$, indicating that the pulsed wave case approaches the continuous wave case for longer pulses.

TABLE I
PARAMETERS USED FOR PRESSURE WAVEFRONT SIMULATION.

Transducer	
Transducer type	Linear array
Number of transducer elements	128
Transducer element pitch	0.3 mm
Transducer element kerf	0.035 mm
Transducer element height	5 mm
Elevation focus	20 mm
Center frequency, f_0	5.5 MHz
Wavelength, $\lambda = c/f_0$	0.28 mm
Transducer impulse response	$h(t) = \delta(t)$
STA transmission	
Excitation type	One-cycle sinus at f_0
Number of emitting elements	11
Size of active aperture, D_{act}	3.3 mm
Virtual source positions	$[2.5, 0, z_{\mathrm{vs}}]$ mm
Used F-numbers, $F_{\#}$	0.5, 0.75, 1, 1.5
Pressure field sampling	
Angular sampling interval	1°
Angular sampling range	−60° to 60°
Distance from transducer	30 mm

It can be noted that when another windowing function $w_n(t)$ is applied in the pulsed wave case, it will approach the continuous wave case slower with increasing pulse length. This effect is due to the faster roll-off of the tails of $R_{s_1}(\tau)$.

C. Simulations

A series of simulations was made in Field II [16], [17]. When specifying the transducer geometry, impulse response, and emission setup, the simulation program Field II can calculate the emitted pressure field at points specified by the user. For each simulation, the position of the virtual source was altered and the emitted pressure field was simulated. F-numbers of 0.5, 0.75, 1, and 1.5 were used for the virtual source both in front of and behind the transducer, resulting in a total of eight simulations. In all simulations, 11 elements of a linear array transducer with a pitch of 0.3 mm fired a one-cycle pulse at $f_0 = 5.5$ MHz. The transducer impulse response was assumed to be a delta function. The emitted pressure field was simulated along an arc at depth 30 mm below the transducer surface at 1° angular increments in a total of 120°. The arc was in each case centered at the position of the virtual source. The parameters for the simulation are given in Table I.

For each point on the arc, both the amplitude drop k with respect to maximum pressure on the arc and the phase shift $\Delta\phi$ with respect to the expected phase were estimated. The criterion in (16) was applied to determine the opening angle as the angle α where the criterion is not violated, e.g., both k and $\Delta\phi$ are within the allowed range.

Fig. 4 shows the opening angle for each simulation and, for comparison, the geometric opening angle as defined by (1) is plotted. Fig. 4 confirms that the opening angle is not significantly dependent on whether the virtual sources are placed in front of or behind the transducer. Further-

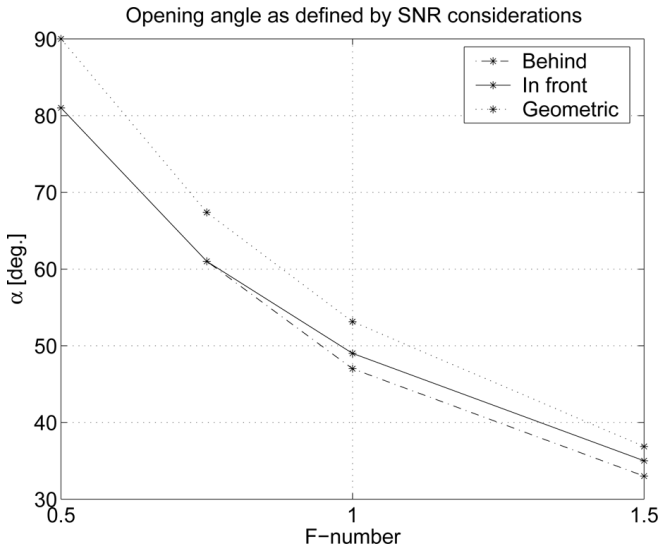

Fig. 4. Opening angle for different positions of the virtual source found using the criteria in (16). Only minor difference is seen between placing the virtual source in front of or behind the aperture. The simulations combined with the criteria in (16) yield opening angles ∼10% lower than the geometrical considerations in (1).

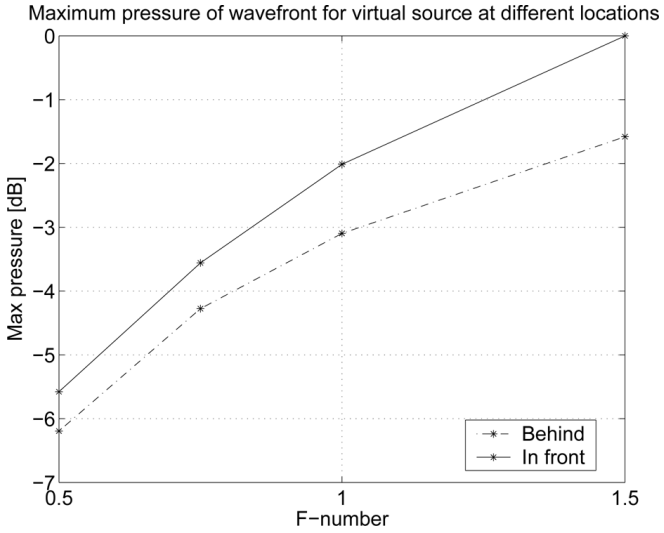

Fig. 5. Maximum pressure of wavefront for different positions of the virtual source.

more, the SNR approach indicates that the opening angle might be slightly less than the geometrically calculated. A difference of ∼10% is seen.

The maximum pressure at the arc for each simulation is plotted in Fig. 5. At larger F-numbers, the emitted energy is concentrated within a smaller angular extent which increases the peak pressure. Also, when the virtual source is placed in front of the aperture, the angular extend measured from the virtual source position corresponds to a smaller area, and therefore the peak pressure is larger.

The choice of virtual source position for a sparse STA sequence, as used for blood flow estimation, depends on the depth of interest. If shallow structures are to be scanned,

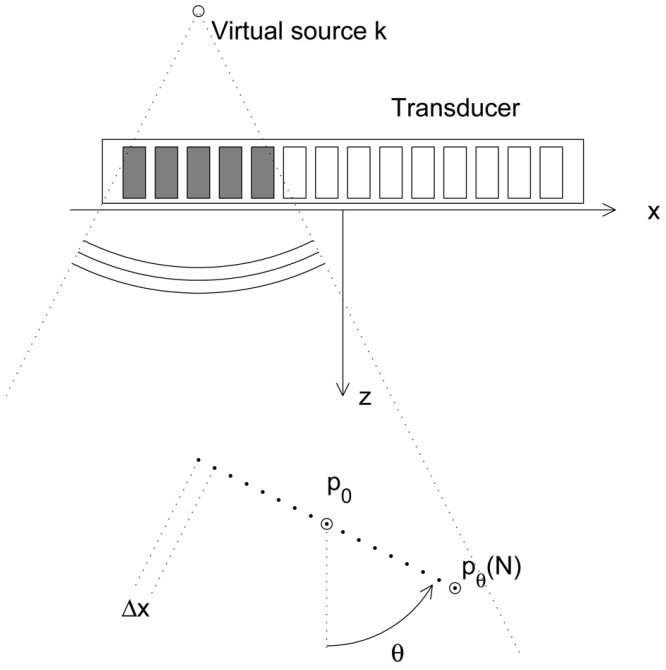

Fig. 6. A number of elements emit a wave which is approximately spherical within a limited angular extend as if it originated from virtual source k. One of the lines beamformed through $\vec{p_0}$ is indicated along with the angle θ and the spatial sampling interval Δx.

it is advisable to place the virtual sources behind the aperture in order for each virtual source to be able to illuminate the area of interest. Also, the spherical approximation of the wave travelling from the virtual source becomes better as the distance to the virtual source increases. If deeper structures are imaged, it is advisable to place the virtual sources in front of the aperture to avoid large energy leakage and attain an acceptable SNR.

III. Synthetic Aperture Velocity Estimation

This section describes how the STA velocity estimation method presented in [2] is performed. Due to the dynamic focusing in both transmit and receive, data can be beamformed in every point within the opening angle of the virtual source. This is used for determining the flow direction and velocity.

For every point p_0 where the velocity direction and magnitude is estimated, a number of lines $\vec{p_\theta}(n)$ are beamformed through the point at different angles:

$$\vec{p_\theta}(n) = \vec{p_0} + \Delta x[\sin\theta, 0, \cos\theta]\left(n - \frac{N}{2}\right), \tag{17}$$

where $n = [0, 1, \ldots, N]$ and $\theta = [0, \Delta\theta, 2\Delta\theta, \ldots, 180°]$ are the angles with respect to the beam axis z, and Δx is the spatial sampling distance. Fig. 6 shows one of the lines through $\vec{p_0}$. The lines are beamformed by delaying the received signals from each of the receiving elements according to the time of flight and summing over all Q

receiving elements and all K emissions in the emission sequence as

$$h_{l,\theta}(n) = \sum_{k=0}^{K-1} \sum_{q=0}^{Q-1} r_{l+k,q}\left(t_{(l+k) \bmod K,q}(\vec{p_\theta}(n))\right), \tag{18}$$

where $r_{l,q}(t)$ is the signal received at element q at emission l, $h_{l,\theta}(n)$ is the l-th high resolution line at angle θ, $(l+k) \bmod K$ is the integer remainder of dividing $(l+k)$ with K, and $t_{k,q}(\vec{p_\theta}(n))$ is the time of flight from the virtual source k to the point $\vec{p_\theta}(n)$ and back to receiving element q. The time of flight given by

$$t_{k,q}(\vec{p_\theta}(n)) = \frac{\|\vec{p_\theta}(n) - \vec{r}_{\mathrm{xmt},k}\| + \|\vec{r}_{\mathrm{rcv},q} - \vec{p_\theta}(n)\|}{c}, \tag{19}$$

where $\vec{r}_{\mathrm{xmt},k}$ is the position of virtual source k, $\vec{r}_{\mathrm{rcv},q}$ is the position of receiving element q, and c is the speed of sound. As described in Section II, the emitted wave can be assumed spherical only within a limited angular extent. When beamforming $h_{l,\theta}(n)$, only data where $\vec{p_0}$ is within this angular extent are used. For all other emissions, $r_{l,q}(t)$ is set to zero.

The flow direction is found by searching for the angle of maximum normalized cross-correlation [2]. The normalized cross-correlation between two high-resolution lines acquired using the same emission sequence is given by

$$p_l(m,\theta) = \frac{\sum_{n=0}^{N} hc_{l,\theta}(n) hc_{l+K,\theta}(n+m)}{\sqrt{\sum_{n=0}^{N} hc_{l,\theta}^2(n) \sum_{n=0}^{N} hc_{l+K,\theta}^2(n)}}, \tag{20}$$

where $hc_{l,\theta}(n)$ is the high-resolution line after stationary echo cancelling, and K is the number of emissions in the emission sequence. The stationary echo cancelling is done using a linear regression filter [18] over high resolution lines made using the same emission sequence. L cross-correlations are averaged:

$$\rho_{\mathrm{av}}(m,\theta) = \frac{1}{L} \sum_{l=0}^{L-1} \rho_l(m,\theta), \tag{21}$$

and the maximum cross-correlation at each angle is found:

$$\rho(\theta) = \max(\rho_{\mathrm{av}}(m,\theta)). \tag{22}$$

The flow direction is then found as the angle where ρ has its maximum:

$$\theta_d = \arg\max_\theta \rho(\theta). \tag{23}$$

The discrete angle estimate θ_d is interpolated using a parabolic approximation given by [19]

$$\hat{\theta} = \theta_d - \frac{\rho(\theta_d+1) - \rho(\theta_d-1)}{2\left(\rho(\theta_d+1) - 2\rho(\theta_d) + \rho(\theta_d-1)\right)} \Delta\theta, \tag{24}$$

where $\Delta\theta$ is the angular sampling interval. The flow velocity along the estimated direction is then found by repeating the beamforming along $\hat{\theta}$ and finding the lag of maximum correlation:

$$m_d = \arg\max_m \rho_{\mathrm{av}}(m,\hat{\theta}). \tag{25}$$

This lag can be interpolated using parabolic interpolation to yield $\hat{m}$. The velocity magnitude along $\hat{\theta}$ is then found by

$$\hat{v}_{\hat{\theta}} = \frac{\hat{m}\Delta x f_{\mathrm{prf}}}{K}, \tag{26}$$

where f_{prf} is the pulse repetition frequency. By applying prior knowledge of the expected velocity range, the search range can be limited by evaluating only the cross correlation function (20) in lags corresponding to the expected velocity range.

IV. Motion Effects on Synthetic Transmit Aperture Imaging

An STA image is focused by combining data from a number of emissions. Motion between these emissions will introduce incoherence in the data [6], [9], and this will distort the point spread function and lower the received signal amplitude. Three effects basically deteriorate the response from the scatterer:

- the Doppler effect,
- the spatial movement causing the low resolution images to sum out of phase,
- the change in the point spread function due to the spatial movement.

The three effects, although partly linked, will be investigated separately and for a single scatterer only. Assuming the imaging process is linear, this can easily be extended to a large number of scatterers.

A. The Doppler Effect

When a scatterer moves with an axial velocity v_z while interacting with an ultrasound pulse, the Doppler shift due to scatterer motion during interaction with the pulse is given by the well known Doppler equation:

$$f_d = \frac{2v_z f_0}{c}, \tag{27}$$

where f_0 is the center frequency, and c is the speed of sound. In synthetic aperture vector flow imaging, a chirp is often used to increase the SNR [3], [20]; thus, things get a little more complicated. A linear chirp is given by

$$g(t) = a(t)\sin(2\pi f_1 t + \pi S_0 t^2), \quad 0 < t < T, \tag{28}$$

where f_1 is the start frequency, T is the duration, $a(t) = A$ is a weighting function assumed constant for simplicity, and S_0 is the sweep rate given by $S_0 = (f_2 - f_1)/T$, where

f_2 is the end frequency at $t = T$. The received signal from a single stationary scatterer at depth d is

$$\begin{aligned} r_s(t) &= rg\left(t - \frac{2d}{c}\right) \\ &= rA\sin\left(2\pi f_1\left(t - \frac{2d}{c}\right) + \pi S_0\left(t - \frac{2d}{c}\right)^2\right), \end{aligned} \tag{29}$$

where r is the backscatter coefficient. The expression is valid for $(2d/c) < t < T + (2d/c)$. Due to the Doppler effect, the received signal from a single moving scatterer will experience a slight change in both frequency content and duration. The received signal is then given by [21]

$$\begin{aligned} r_m(t) &= r\sqrt{\beta}g\left(\beta\left(t - \frac{2d}{c + v_z}\right)\right) \\ &= r\sqrt{\beta}A\sin\left(2\pi\left(\beta f_1 - \frac{2d}{c + v_z}S_0\right)t + \pi\beta^2 S_0 t^2 + \varphi\right), \end{aligned} \tag{30}$$

where $\beta = (c + v_z)/(c - v_z)$ is the Doppler expansion/compression factor, and

$$\begin{aligned} \frac{2d}{c + v_z} < t < \frac{T}{\beta} + \frac{2d}{c + v_z}, \\ \varphi = -2\pi f_1 \frac{2d}{c - v_z} + \pi S_0\left(\frac{2d}{c - v_z}\right)^2. \end{aligned} \tag{31}$$

The change in SNR due to the Doppler effect is then found by

$$\Delta\text{SNR} = \frac{\text{SNR}_m}{\text{SNR}_s} = \frac{E[|r_m(t) * g(-t)|^2]}{E[|r_s(t) * g(-t)|^2]}. \tag{32}$$

This expression is evaluated in MATLAB (The MathWorks, Inc., Natick, MA) for different values of v_z and plotted in Fig. 7 (top). The investigated waveform is a $T = 20$ μs chirp with a rectangular amplitude tapering linearly, sweeping frequencies from 3 to 8 MHz. A speed of sound of $c = 1540$ m/s is assumed, and the signals are sampled at $f_s = 1$ GHz.

Fig. 7 shows that the changes of SNR due to the Doppler effect are within a few percent of a dB. The reason for achieving positive ΔSNR at certain velocities lies in the SNR definition used here. Note that the peak SNR is, of course, largest at $v_z = 0$, whereas the energy after filtering is not necessarily. The axial shift of the compressed peak is also investigated for different velocities and plotted in Fig. 7 (bottom). The shift is below a wavelength λ for all velocities below $v_z = 1$ m/s.

B. Low Resolution Images are Summed Out of Phase

When tissue motion or blood flow is present, the individual LRIs will not be summed in phase. To investigate the significance of this effect, a simple model is used for approximating the SNR at different velocities where only axial motion is considered. Later, simulations of both axial and lateral motion are used to test the model. Assuming the received signal $r(t)$ as a simple one-dimensional linear model, after one emission it is

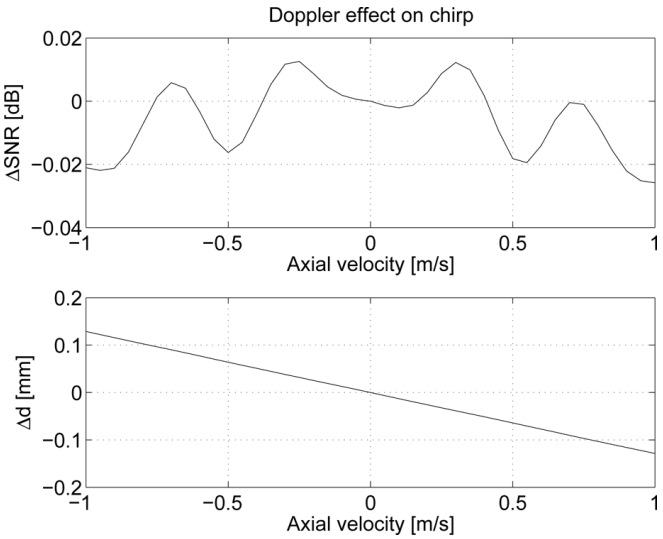

Fig. 7. The Doppler effect causes both a change in the energy of the compressed chirp and a shift of the envelope peak. The top plot shows the change in SNR due to the Doppler effect at different axial velocities, whereas the bottom plot shows the shift in the peak of the compressed chirp due to the Doppler effect.

$$r(t) = g(t) * x(t) + \eta(t), \tag{33}$$

where $g(t)$ is the emitted waveform including the two-way electromechanical impulse response of the system, $x(t)$ is the target function modelled as uncorrelated, white, gaussian noise with power σ_x^2, and $\eta(t)$ is the signal noise assumed uncorrelated, white, and gaussian distributed with power σ_η^2. The SNR of a single LRI is then given by

$$\begin{aligned} \text{SNR}_{\text{LRI}} &= \frac{E[(g(t) * x(t))^2]}{E[\eta^2(t)]} \\ &= \frac{\sigma_x^2 R_g(0)}{\sigma_\eta^2}, \end{aligned} \tag{34}$$

where $R_g(\tau)$ is the autocorrelation of $g(t)$. The SNR of the HRI created by summing N LRIs is

$$\begin{aligned} \text{SNR}_{\text{HRI}} &= \frac{E[(\sum_{n=0}^{N-1} g(t) * x(t + n\Delta t))^2]}{NE[\eta^2(t)]} \\ &= \frac{E[(x(t) * \sum_{n=0}^{N-1} g(t - n\Delta t))^2]}{N\sigma_\eta^2} \\ &= \frac{\sigma_x^2 E\left[(\sum_{n=0}^{N-1} g(t - n\Delta t))^2\right]}{N\sigma_\eta^2}, \end{aligned} \tag{35}$$

where Δt is the time shift between two LRIs due to the scatterer motion. When no motion is present, $\Delta t = 0$, the SNR of the HRI is

$$\text{SNR}_{\text{stat}} = \frac{\sigma_x^2 E[N^2 g^2(t)]}{N\sigma_\eta^2} = N\frac{\sigma_x^2 R_g(0)}{\sigma_\eta^2}, \tag{36}$$

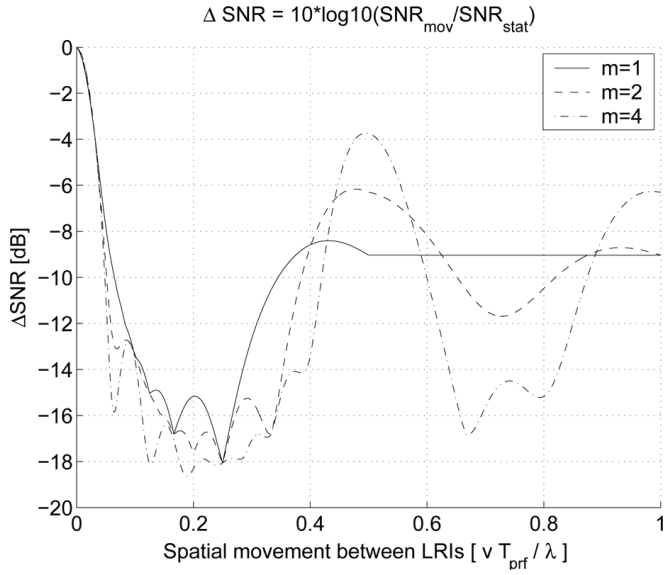

Fig. 8. The change in SNR due to axial motion for different pulse lengths. ΔSNR is calculated from a simple one-dimensional model where both the target and the noise are modelled as uncorrelated white gaussian processes with zero mean. The signal envelope is assumed rectangular.

TABLE II
PARAMETERS USED FOR THE SIMULATION OF INTER–LRI MOVEMENT.

Transducer	
Transducer type	Linear array
Number of transducer elements	128
Transducer element pitch	0.3 mm
Transducer element kerf	0.035 mm
Transducer element height	5 mm
Elevation focus	20 mm
Center frequency, f_0	5.5 MHz
Wavelength, $\lambda = c/f_0$	0.28 mm
STA transmission	
Excitation type	11.25 μs nonlinear chirp [22]
Frequencies swept	∼3.5–7.5 MHz
Number of emitting elements	11
Number of receiving elements, Q	64, centered at emission
Number of emissions in sequence, K	8
Number of virtual sources, $(= K)$	8
Virtual source positions	$[x_{\mathrm{vs}}, 0, -2.5]$ mm
Pulse repetition frequency, f_{prf}	5 kHz
Inter-LRI movement	
Velocities simulated, v'	$0, 5, 10, \ldots, 95$ cm/s
Corresponding inter-LRI movement	$0, \ldots, 0.68\lambda$

or N times the SNR of the individual LRIs. The expectation value in (35) is simply the auto-correlation of the sum of N signals consecutively delayed. As shown in the appendix, this can be rewritten as

$$E\left[\left(\sum_{n=0}^{N-1} g(t-n\Delta t)\right)^2\right] = NR_g(0) + 2\sum_{n=1}^{N-1}(N-n)R_g(n\Delta t),$$

where $R_g(\tau)$ is the autocorrelation of $g(t)$. The SNR of the HRI when movement is present is then given by

$$\mathrm{SNR}_{\mathrm{mov}} = \frac{\sigma_x^2\left(NR_g(0) + 2\sum_{n=1}^{N-1}(N-n)R_g(n\Delta t)\right)}{N\sigma_\eta^2}. \quad (37)$$

To investigate the difference between the SNR in the stationary case and when movement is present, the change in SNR due to movement is defined as

$$\Delta\mathrm{SNR} = 10\log_{10}\left(\frac{\mathrm{SNR}_{\mathrm{mov}}}{\mathrm{SNR}_{\mathrm{stat}}}\right). \quad (38)$$

By inserting (36) and (37) into (38) we get the modelled change in SNR due to movement:

$$\Delta\mathrm{SNR} = 10\log_{10}\left(\frac{1}{N} + \frac{2}{N^2R_g(0)}\sum_{n=1}^{N-1}(N-n)R_g(n\Delta t)\right), \quad (39)$$

which for $\Delta t = 0$ equals $\Delta\mathrm{SNR} = 0$, as expected. In Fig. 8, the change in SNR as calculated by (39) is plotted for an m-cycle pulse with a rectangular envelope as a function of axial movement between LRIs. Plots are made for various choices of pulse length m, and the number of LRIs summed to create a HRI is assumed to be $N = 8$. When no motion is present, $\Delta\mathrm{SNR} = 0$, whereas when the scatterer moves a quarter of a wavelength $\lambda/4$, $\Delta\mathrm{SNR} = 10\log_{10}(1/N^2)$, indicating, as mentioned in [6], that motion effects increase when using longer sequences. Fig. 8 clearly indicates that summing LRIs out of phase significantly deteriorates the SNR of the HRI.

A number of simulations were performed using Field II. Here a single scatterer, initially located at depth $z =$ 30 mm and below the aperture center $x = 0$ mm, is moving along the axial direction while $N = 8$ LRIs are acquired. The HRI is then created by summing the LRIs. The SNR of the HRI is then compared to the SNR of the HRI, assuming no motion. The simulation was repeated for velocities of $v' = 0, 5, 10, \ldots, 95$ cm/s, corresponding to movement of up to 0.68λ between LRIs, where $\lambda = c/f_0$ is the wavelength. The excitation waveform was an 11.25-μs nonlinear chirp designed using a frequency sampling method [22]. The parameters used in the simulation are given in Table II.

For each of the simulations, the change in SNR due to movement $\Delta\mathrm{SNR}$ is found as

$$\Delta\mathrm{SNR} = 10\log_{10}\left(\frac{E_{v=v'}}{E_{v=0}}\right), \quad (40)$$

where $E_{v=v'}$ is the total energy of the 2-D HRI point spread function when the point moves at velocity v'. This assumes that the noise power is the same in both cases. $\Delta\mathrm{SNR}$ is plotted in Fig. 9 as a function of the movement

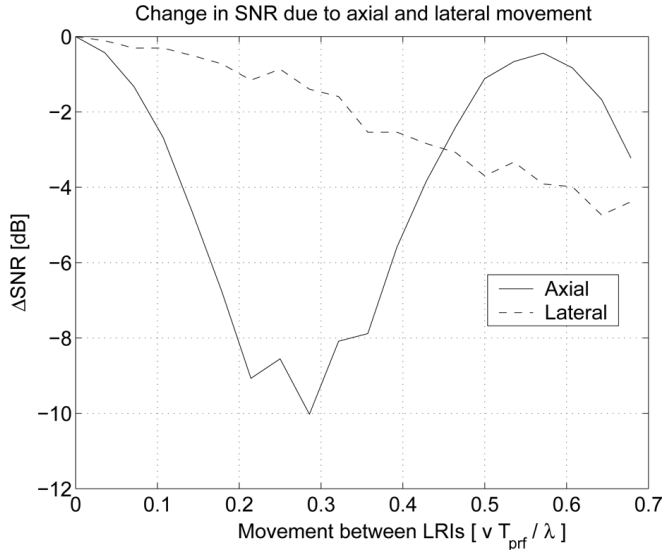

Fig. 9. The change in SNR due to axial and lateral motion, found by simulation using a nonlinear chirp sweeping frequencies from 3.7 to 7.3 MHz.

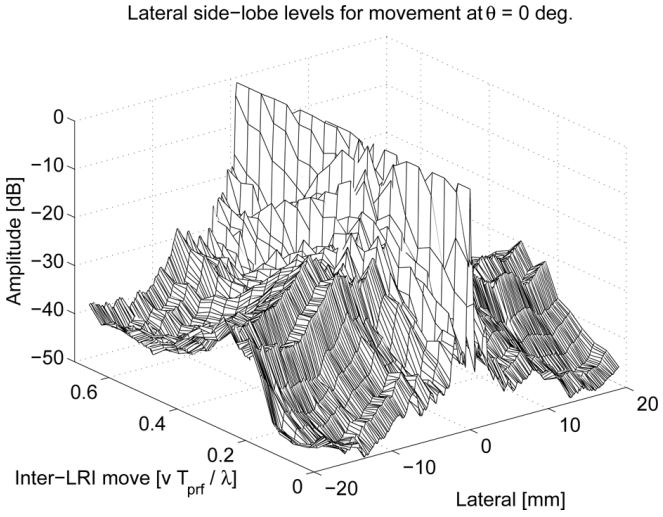

Fig. 10. Lateral sidelobe structure at different purely axial velocities. A ∼20-dB increase in sidelobes is seen around $v = 0.35$ m/s, corresponding to a movement of 0.25λ between LRIs.

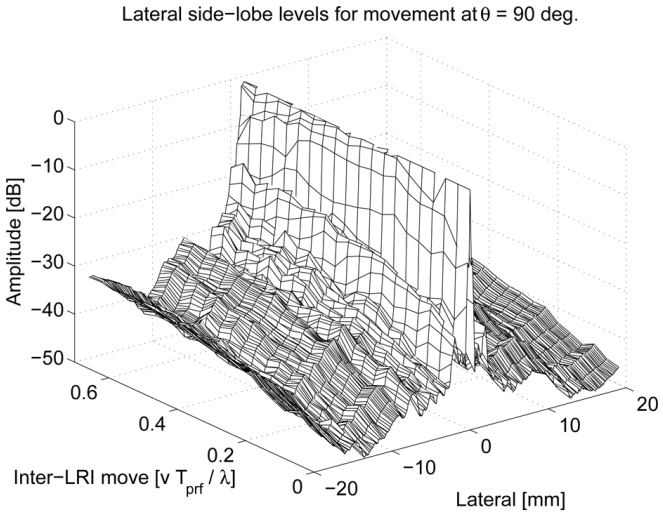

Fig. 11. Lateral sidelobe structure at different purely lateral velocities. A slight increase in sidelobe levels as a function of velocity is seen.

between LRIs given by $vT_{\mathrm{prf}}/\lambda$, where T_{prf} is the pulse repetition period. The same simulation is repeated for lateral movement at the same velocities. The resulting ΔSNR is plotted in Fig. 9.

The results of the simulation of axial movement shown in Fig. 9 basically show the same tendency as the model in Fig. 8. The SNR is significantly deteriorated at an inter-LRI movement of $\sim 0.25\lambda$, whereas the SNR at $\sim 0.5\lambda$ is comparable to that of a stationary scatterer. The deterioration seen in the simulation is, although significant, not as pronounced as for the model. It is therefore expected that the presented model exaggerates the motion effects on the SNR.

From these simulations, the lateral contrast at different velocities can also be extracted. This has been done, and the resulting plots are shown in Fig. 10 and Fig. 11 for purely axial and purely lateral motion, respectively.

For the axial motion of $v' = 0.35$ m/s in Fig. 10, corresponding to 0.25λ, the lateral sidelobes are up almost 20 dB compared to the stationary case. This is the worst case, where the received echoes are 180° out of phase, and also close to where the SNR is lowest (Fig. 9). At higher axial velocities, both contrast and SNR are better. In the case of lateral movement shown in Fig. 11, we see a tendency to a slightly increased sidelobe level at higher velocities, but the effect is not as large as for axial movement.

C. The Change of the Point Spread Function

In STA imaging, the point spread function of a single scatterer in a low resolution image will experience a rotation toward the point of emission [10], e.g., the virtual source. This rotation will have an angle of

$$\beta \approx \arcsin \frac{|x_p - x_{\mathrm{vs}}|}{|z_p - z_{\mathrm{vs}}|}, \tag{41}$$

where $[x_p, 0, z_p]$ is the position of the scatterer, and $[x_{\mathrm{vs}}, 0, z_{\mathrm{vs}}]$ is the position of the virtual source. When no motion is present in the summed image, these rotated point spread functions increase the lateral contrast. In the presence of motion, the scatterer has moved between emissions, and therefore the angle β will be affected as in (41), and the tilting of the point spread function will differ from the tilting experienced by a stationary scatterer. When $|x_p - x_{\mathrm{vs}}|$ is small compared to $|z_p - z_{\mathrm{vs}}|$, this effect will be negligible compared to that described in Section IV-B. Even for a lateral velocity of $|\vec{v}| = 1$ m/s at a pulse repetition frequency of $f_{\mathrm{prf}} = 5$ kHz with $N = 8$ emissions in the sequence, the point spread function at depth 30 mm will at maximum experience an angle change of $\Delta\beta \sim 2°$

due to motion. This simply corresponds to a slightly narrower/wider distribution of virtual sources.

This shows that the largest deterioration of the blood flow signal is due to the incoherent summation of low resolution images, as described in Section IV-B.

V. Velocity Estimation with Motion Compensation

To sum LRIs in phase, a compensation must be made for the current velocity. In a velocity estimation system the velocity is, of course, not known in advance, but by assuming a constant velocity, the velocity vector estimate from the latest time instance $\vec{v}_{\text{est}}$ can be used as a compensation for creating the next high resolution lines:

$$h_{l,\theta}(n) = \sum_{k=0}^{K-1} \sum_{q=0}^{Q-1} r_{l+k,q}\left(t_{k \bmod K,q}(\vec{p_\theta}(n) + k\vec{v}_{\text{est}}/f_{\text{prf}})\right), \tag{42}$$

where k is the emission number, $\vec{v}_{\text{est}} = \hat{v}_{\hat{\theta}}[\sin(\hat{\theta}), 0, \cos(\hat{\theta})]$ is the latest velocity vector estimate, and f_{prf} is the pulse repetition frequency. If $\vec{v}_{\text{est}}$ equals the true velocity, the effect B in Section IV will be fully compensated for, whereas effects A and C will still be present. Cross-correlating two high-resolution lines K emissions apart will still expectedly peak at the lag corresponding to the blood velocity. Even if an erroneous velocity estimate is used for the compensation, the point spread function of a single scatterer is simply smeared, which was already the case.

A. Simulations

To test the motion compensation method, compensation is done for the single point simulations previously described. Fig. 12 and Fig. 13 show the lateral sidelobe structure for the compensated simulations for purely axial motion and purely lateral motion, respectively. These can be compared to Fig. 10 and Fig. 11. After compensation, almost no increase in sidelobe levels due to the motion is seen. This again confirms that the incoherent summation of LRIs accounts for by far the most severe degradation due to motion. Also, this shows the potential for the motion compensation.

B. Phantom Experiments

A number of experiments were conducted on a flow rig phantom where blood mimicking fluid was circulated through tubes. A linear array transducer was fixed at a certain height z_0 above the tubing and at a certain angle θ with respect to the flow. The flow was constant over time, and the flow velocity profile was assumed parabolic. The velocity directly below the transducer center as a function of depth z is then

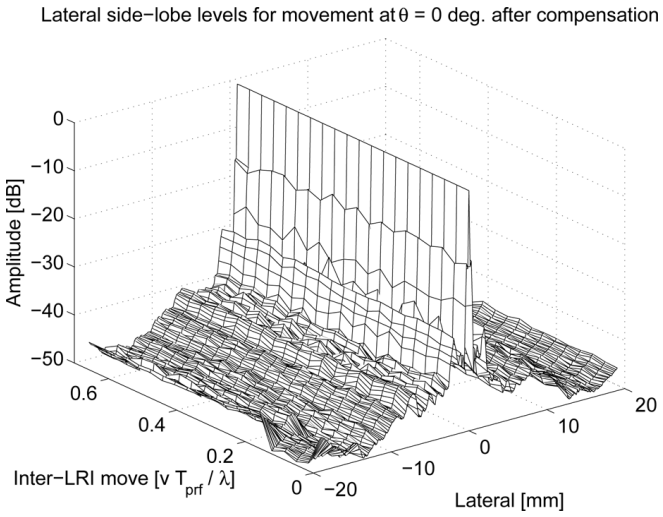

Fig. 12. Lateral sidelobe structure at different purely axial velocities when the motion is compensated in beamforming.

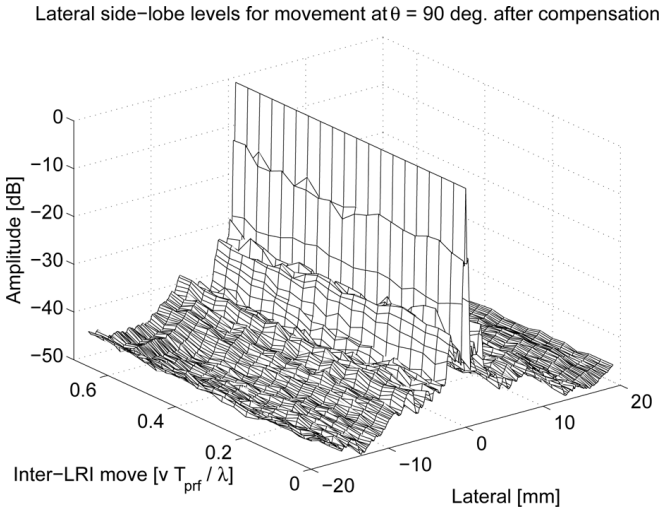

Fig. 13. Lateral sidelobe structure at different purely lateral velocities when the motion is compensated in beamforming.

$$v(z) = v_0\left(1 - \left(\frac{(z - z_0)\sin(\theta)}{R}\right)^2\right), \ |z - z_0| < \frac{R}{\sin(\theta)}, \tag{43}$$

where R is the vessel radius. Data were acquired using our RASMUS ultrasound multichannel sampling system [23] and processed as described in Section III. Various parameters for the data acquisition and processing are given in Table III. Measurements were made for flow angles of $\theta = 60°$ and $90°$ and for pulse repetition frequencies of $f_{\text{prf}} = 5$ kHz and 1 kHz. This corresponds to a peak movement of $\sim$7% and 35% of λ between emissions with the peak velocity $v_0 = 0.1$ m/s and $\lambda = 0.28$ mm. Lowering the f_{prf} is equivalent to increasing the velocity. Experiments where $v_0 = 0.1$ m/s and $f_{\text{prf}} = 1$ kHz, of course, correspond to a velocity of $v_0 = 1$ m/s at $f_{\text{prf}} = 10$ kHz.

TABLE III
PARAMETERS USED FOR THE PHANTOM EXPERIMENTS.

Transducer	
Transducer type	Linear array
Number of transducer elements	128
Transducer element pitch	0.3 mm
Transducer element kerf	0.035 mm
Transducer element height	5 mm
Elevation focus	20 mm
Center frequency, f_0	5.5 MHz
Wavelength, $\lambda = c/f_0$	0.28 mm
Flow rig setup	
Tube radius, R	6 mm
Flow angles, θ	60° and 90°
Depth of tube center, z_0	34.5 mm (60°), 39.5 mm (90°)
Peak velocity, v_0	0.1 m/s
STA transmission	
Excitation type	11.25 μs nonlinear chirp [22]
Frequencies swept	∼3.5–7.5 MHz
Number of emitting elements	11
Number of receiving elements, Q	64, centered at emission
Number of emissions in sequence, K	8
Number of virtual sources, $(= K)$	8
Virtual source positions	$[x_{\text{vs}}, 0, -2.5]$ mm
Pulse repetition frequency, f_{prf}	5 kHz and 1 kHz
STA processing	
Points in line, $N + 1$	401
Spatial sampling interval, Δx	12.5 μm
Line length	5 mm
Angular sampling interval, $\Delta\theta$	5°
Stationary echo cancelling method	Linear regression
Number of correlations averaged, L	113
Velocity search range	−1 to 1 m/s

Velocity direction and magnitude were estimated along a profile through the tube at 20 uncorrelated time instances, and the estimated velocities were compared to the expected velocity profile given by (43). The resulting angle and velocity estimates are shown in Fig. 14, which also show the average profiles ±3 times the standard deviation. The plots are ordered with angle estimates in the left column and velocity estimates in the right column. The first two rows are for the $\theta = 60°$ and $f_{\text{prf}} = 5$ kHz experiment. The following two are for $\theta = 60°$ and $f_{\text{prf}} = 1$ kHz. Finally, two rows are for $\theta = 90°$ and $f_{\text{prf}} = 5$ kHz, and two for $\theta = 90°$ and $f_{\text{prf}} = 1$ kHz. The performance of the estimator at $f_{\text{prf}} = 5$ kHz is quite good at both angles, but at $f_{\text{prf}} = 1$ kHz, the bias and standard deviation increase. This is most significant for $\theta = 90°$, where the method fails to estimate both the flow angle and velocity.

The compensation method given by (42) is applied to the data prior to velocity estimation. Here the previous estimate of the vector velocity is used to compensate for the inter-LRI movement while beamforming. The resulting profiles are plotted in Fig. 15, where the individual plots are ordered as in Fig. 14.

The average bias $\overline{B}_v$ and average standard deviation $\overline{\sigma}_v$ of the 20 estimated velocity profiles are used as a measure

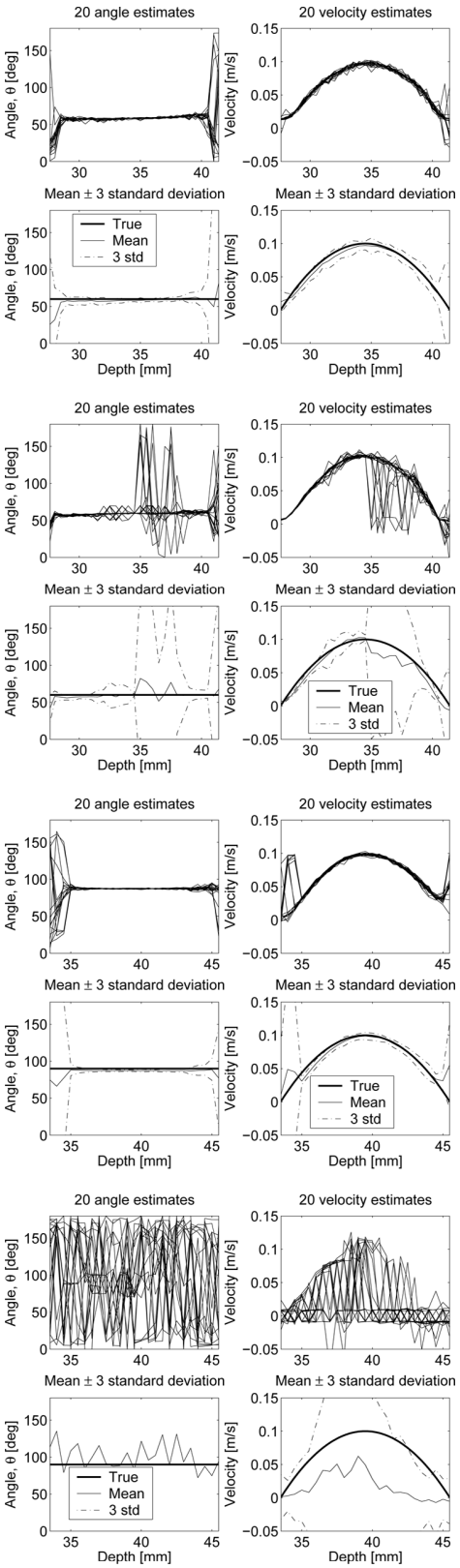

Fig. 14. Angle (left column) and velocity (right column) estimates for flow phantom experiments when no motion compensation is applied. The figure shows 20 independent estimates and the average and standard deviation compared to the true values. The two first rows are for $\theta = 60°$ and $f_{\text{prf}} = 5$ kHz, then $\theta = 60°$ and $f_{\text{prf}} = 1$ kHz, then $\theta = 90°$ and $f_{\text{prf}} = 5$ kHz, and finally $\theta = 90°$ and $f_{\text{prf}} = 1$ kHz.

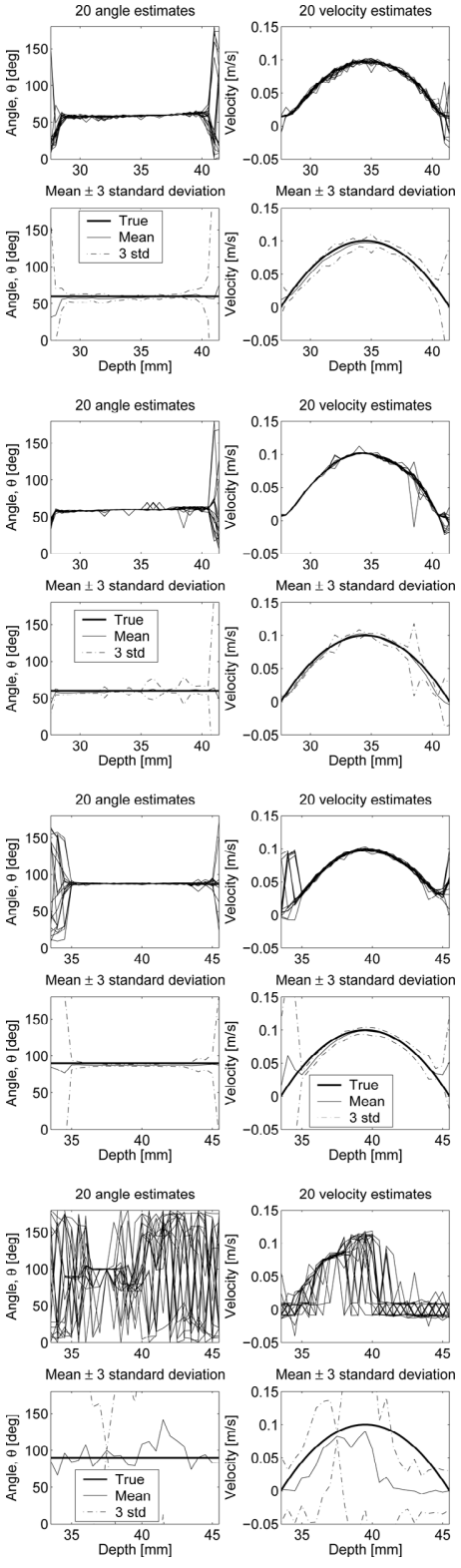

Fig. 15. Angle (left column) and velocity (right column) estimates for flow phantom experiments when the proposed motion compensation is applied. The figure shows 20 independent estimates and the average and standard deviation compared to the true values. The two first rows are for $\theta = 60°$ and $f_{\text{prf}} = 5$ kHz, then $\theta = 60°$ and $f_{\text{prf}} = 1$ kHz, then $\theta = 90°$ and $f_{\text{prf}} = 5$ kHz, and finally $\theta = 90°$ and $f_{\text{prf}} = 1$ kHz.

TABLE IV
AVERAGE BIAS AND STANDARD DEVIATION OF VECTOR VELOCITY ESTIMATES IN % OF PEAK VELOCITY v_0 FOR PROFILE MADE WITH AND WITHOUT COMPENSATION.

Angle	f_{prf}, kHz	Bias, %	SD, %	Bias, comp, %	SD, comp, %
60°	5	−3.1	3.7	−2.8	3.7
60°	1	−8.4	12.2	−3.6	2.8
90°	5	−0.1	5.6	0.5	5.6
90°	1	−50.8	30.1	−38.5	20.3

for the performance of the velocity estimation method. These are given by

$$\overline{B}_v = \frac{1}{v_0(z_2 - z_1)} \int_{z_1}^{z_2} (\overline{v}(z) - v(z))dz,$$

$$\overline{\sigma}_v = \frac{1}{v_0(z_2 - z_1)} \int_{z_1}^{z_2} \sqrt{\frac{1}{20} \sum_{i=1}^{20} (\hat{v}_i(z) - \overline{v}(z))^2} dz,$$

where $z_1 = z_0 - R/\sin\theta$ and $z_2 = z_0 + R/\sin\theta$ are the tube edges, $\hat{v}_i(z)$ is the i^{th} velocity estimate at depth z, $v(z)$ is the true velocity at depth z as defined by (43), and $\overline{v}(z) = \sum_{i=1}^{20} \hat{v}_i(z)/20$ is the average estimate at depth z. These quantities are calculated for the velocity profiles in Fig. 14 and Fig. 15 and are given in Table IV.

Table IV shows a significant decrease in both average bias and average standard deviation for the measurement at $\theta = 60°$ and $f_{\text{prf}} = 1$ kHz, whereas only small changes are seen for the other measurements. This indicates that the compensation method can decrease the number of false peaks when only a limited number of false peaks are present.

VI. Interpolation Method

In [12], different interpolation schemes in the dynamic receive beamforming were tested for synthetic aperture B-mode imaging. Linear interpolation, polynomial interpolation of orders 2 to 5, and combined upsampling and finite-impulse response (FIR) filtering were tested. An increased contrast was seen when interpolation schemes more complex than the linear interpolation were used.

Polynomial interpolation of 5^{th} order and interpolation by combined upsampling by a factor of 8 and filtering by a 48-tap lowpass FIR filter were tested on the flow phantom data. No motion compensation was applied in the beamforming. The average bias and average standard deviation of the velocity profiles are used as performance measures to compare the effects of the different interpolation schemes.

Table V shows the average bias of the velocity profiles for the four flow phantom experiments using the three different interpolation methods. The biases are given in % of the peak velocity v_0. In Table VI, the average standard deviations of the velocity profiles are shown for all three

TABLE V
AVERAGE BIAS OF VECTOR VELOCITY ESTIMATES IN % OF PEAK VELOCITY v_0 FOR DIFFERENT INTERPOLATION METHODS.

Angle	f_{prf}, kHz	Bias, linear, %	Bias, poly 5th, %	Bias, FIR,%
60°	5	−3.1	−3.1	−3.1
60°	1	−8.4	−9.1	−9.1
90°	5	−0.1	0.1	0.1
90°	1	−50.8	−51.1	−51.2

TABLE VI
AVERAGE STANDARD DEVIATION OF VECTOR VELOCITY ESTIMATES IN % OF PEAK VELOCITY v_0 FOR DIFFERENT INTERPOLATION METHODS.

Angle	f_{prf}, kHz	SD, linear, %	SD, poly 5th, %	SD, FIR, %
60°	5	3.7	3.7	3.7
60°	1	12.2	13.2	13.2
90°	5	5.6	5.6	5.6
90°	1	30.1	29.9	29.9

interpolation methods applied to the four flow phantom experiments. Average standard deviations are given in % of the peak velocity v_0.

Tables V and VI show no significant change in the performance of the synthetic aperture velocity estimation method when using more complex interpolation schemes than linear interpolation.

VII. DISCUSSION

Section II introduced an SNR approach for finding the opening angles for virtual sources placed at different positions. It was shown that the geometrical formula (1) from [15] gives a good approximation to the opening angle, and that the opening angle is not significantly dependent on whether the virtual sources are placed in front of or behind the aperture. Simulations showed that the peak pressure on the created sphere was largest when the virtual sources were placed in front of the aperture. It was, thus, recommended that the virtual sources be placed in front of the aperture when deeper lying structures are imaged. When shallower structures are imaged, it was recommended that the virtual sources be placed behind the aperture in order for each virtual source to illuminate the area of interest and for the spherical wave approximation to be valid.

In Section IV, the investigation of the different effects caused by motion of the scatterer was reported. The evaluation of analytical expressions for the Doppler effect showed that only a very small change in the SNR will be caused by the Doppler effect. Fig. 7 also showed that the Doppler effect would cause a slight shift of the peak of the compressed chirp. When the velocity is constant, this shift of $< \lambda$ will be constant, and will not affect the velocity estimation. Only in the case of a very large acceleration of the flow could this shift be of any importance. It can also be noted that this effect is not exclusive for synthetic aperture methods.

Also in Section IV, investigation of the effect of movement between the individual LRIs was reported. A simple one-dimensional model was used to illustrate the significance of this effect. The model showed a drop in SNR of $10\log_{10}(1/N^2)$ dB for an axial movement of $\lambda/4$ between LRIs, where N is the number of emissions in the emission sequence. Simulations showed that the model exaggerated the effect but confirmed the tendency. Axial motion of $\lambda/4$ between LRIs does in fact dramatically lower both the SNR, as seen in Fig. 9, and the contrast, as seen in Fig. 10. Simulations showed that lateral movement had a more moderate effect on both the SNR and the contrast, as seen in Fig. 9 and Fig. 11, respectively.

As long as the velocity is close to constant, the contrast degradation will be the same in the lines that are cross-correlated, and the lag can supposedly still be estimated. But when the SNR is low, ∼0 dB, as is often the case in blood flow estimation, even a moderate decrease in the SNR may significantly degrade the performance of the cross-correlation estimator [24], [25]. Therefore axial inter-LRI motion on the order of $\lambda/4$ should be avoided by either increasing the pulse repetition frequency f_{prf} or decreasing the number of emissions N or the center frequency f_0, or some compensation should be made.

Flow phantom experiments showed that although the SNR and contrast degradation is most severe for axial flow, the synthetic aperture velocity estimation method breaks down for lower velocities for purely lateral movement than for movement at $\theta = 60°$. The reason should probably be found in the lower center frequency (∼0 Hz) of the high resolution lines along the lateral direction. This widens the cross-correlation peaks and makes the estimator more susceptible to noise [24].

In Fig. 12 and Fig. 13 it was shown that if the inter-LRI motion is known, the motion effects can be compensated for in the beamforming. The flow phantom experiments showed that as long as the synthetic aperture vector velocity estimation method is only moderately challenged, the previous vector velocity estimate can be used to compensate in the beamforming of the following data. Hereby the performance of the method is improved. The velocity should, of course, not have changed too much between estimates.

In Section VI various interpolation methods were tried in the dynamic receive beamforming of the synthetic aperture velocity estimation method. Almost no changes in average bias and average standard deviation of the velocity estimates were seen as a function of interpolation method. It is therefore recommended that linear interpolation, which is the easiest to implement, be used.

Appendix A

Here a general expression for the autocorrelation of a finite sum of N mutually delayed signals is inferred using mathematical induction. A proof is given for

$$E\left[\left(\sum_{n=0}^{N-1} g(t-n\Delta t)\right)^2\right] = NR_g(0) + 2\sum_{n=1}^{N-1}(N-n)R_g(n\Delta t), \quad (44)$$

where $g(t)$ is a real finite energy signal, N is the number of signals, Δt is the delay, and $R_g(\tau)$ is the autocorrelation of the signal $g(t)$. Eq. (44) is first proven for $N = 2$.

$$\begin{aligned} E\left[\left(\sum_{n=0}^{2-1} g(t-n\Delta t)\right)^2\right] &= E\left[(g(t)+g(t-\Delta t))^2\right] \\ &= E[g^2(t)] + E[g^2(t-\Delta t)] + E[2g(t)g(t-\Delta t)] \\ &= 2R_g(0) + 2R_g(\Delta t) \\ &= 2R_g(0) + 2\sum_{n=1}^{2-1}(2-n)R_g(n\Delta t). \end{aligned} \quad (45)$$

Now, assuming (44) holds for $N = L$, the case $N = L + 1$ is tested by

$$\begin{aligned} &E\left[\left(\sum_{n=0}^{(L+1)-1} g(t-n\Delta t)\right)^2\right] \\ &= E\left[\left(g(t-L\Delta t) + \sum_{n=0}^{L-1} g(t-n\Delta t)\right)^2\right] \\ &= E\left[g^2(t-L\Delta t)\right] + E\left[\left(\sum_{n=0}^{L-1} g(t-n\Delta t)\right)^2\right] \\ &\quad + E\left[2g(t-L\Delta t)\sum_{n=0}^{L-1} g(t-n\Delta t)\right] \\ &= R_g(0) + E\left[\left(\sum_{n=0}^{L-1} g(t-n\Delta t)\right)^2\right] + 2\sum_{n=1}^{L} R_g(n\Delta t) \\ &= R_g(0) + LR_g(0) + 2\sum_{n=1}^{L-1}(L-n)R_g(n\Delta t) \\ &\quad + 2\sum_{n=1}^{L} R_g(n\Delta t) \\ &= (L+1)R_g(0) + 2\sum_{n=1}^{(L+1)-1}((L+1)-n)\,R_g(n\Delta t). \end{aligned} \quad (46)$$

It was shown in (45) that (44) holds for $N = 2$. In (46) it was shown that if (44) holds for $N = L$, it also holds for $N = L + 1$. Following the laws of mathematical induction, (44) then holds for all finite values of $N \geq 2$.

Acknowledgment

Jacob Kortbek and Henrik Andresen are acknowledged for their work on a beamformation toolbox [12], enabling the comparison of different interpolation schemes. Also, Fredrik Gran is thanked for designing the nonlinear chirp used for the measurements.

References

[1] C. Kasai, K. Namekawa, A. Koyano, and R. Omoto, "Real-time two-dimensional blood flow imaging using an autocorrelation technique," *IEEE Trans. Sonics Ultrason.*, vol. 32, pp. 458–463, 1985.

[2] J. A. Jensen, "Velocity vector estimation in synthetic aperture flow and B-mode imaging," in *Proc. IEEE Int. Symp. Biomed. Imag.*, 2004, pp. 32–35.

[3] J. A. Jensen and S. I. Nikolov, "Transverse flow imaging using synthetic aperture directional beamforming," in *Proc. IEEE Ultrason. Symp.*, 2002, pp. 1488–1492.

[4] R. Y. Chiao, L. J. Thomas, and S. D. Silverstein, "Sparse array imaging with spatially-encoded transmits," in *Proc. IEEE Ultrason. Symp.*, 1997, pp. 1679–1682.

[5] S. I. Nikolov and J. A. Jensen, "In-vivo synthetic aperture flow imaging in medical ultrasound," *IEEE Trans. Ultrason., Ferroelect., Freq. Contr.*, vol. 50, no. 7, pp. 848–856, 2003.

[6] G. E. Trahey and L. F. Nock, "Synthetic receive aperture imaging with phase correction for motion and for tissue inhomogenities—Part II: Effects of and correction for motion," *IEEE Trans. Ultrason., Ferroelect., Freq. Contr.*, vol. 39, pp. 496–501, 1992.

[7] M. Karaman, H. S. Bilge, and M. O'Donnell, "Adaptive multielement synthetic aperture imaging with motion and phase aberation correction," *IEEE Trans. Ultrason., Ferroelect., Freq. Contr.*, vol. 42, pp. 1077–1087, 1998.

[8] C. R. Hazard and G. R. Lockwood, "Effects of motion artifacts on a synthetic aperture beamformer for real-time 3D ultrasound," in *Proc. IEEE Ultrason. Symp.*, 1999, pp. 1221–1224.

[9] J. S. Jeong, J. S. Hwang, M. H. Bae, and T. K. Song, "Effects and limitations of motion compensation in synthetic aperture techniques," in *Proc. IEEE Ultrason. Symp.*, 2000, pp. 1759–1762.

[10] S. I. Nikolov and J. A. Jensen, "K-space model of motion artifacts in synthetic transmit aperture ultrasound imaging," in *Proc. IEEE Ultrason. Symp.*, 2003, pp. 1824–1828.

[11] K. L. Gammelmark and J. A. Jensen, "Duplex synthetic aperture imaging with tissue motion compensation," in *Proc. IEEE Ultrason. Symp.*, 2003, pp. 1569–1573.

[12] J. Kortbek, H. Andresen, S. Nikolov, and J. A. Jensen, "Comparing interpolation schemes in dynamic receive ultrasound beamforming," in *Proc. IEEE Ultrason. Symp.*, 2005, pp. 1972–1975.

[13] M. Karaman, P. C. Li, and M. O'Donnell, "Synthetic aperture imaging for small scale systems," *IEEE Trans. Ultrason., Ferroelect., Freq. Contr.*, vol. 42, pp. 429–442, 1995.

[14] G. R. Lockwood, J. R. Talman, and S. S. Brunke, "Real-time 3-D ultrasound imaging using sparse synthetic aperture beamforming," *IEEE Trans. Ultrason., Ferroelect., Freq. Contr.*, vol. 45, pp. 980–988, 1998.

[15] S. I. Nikolov and J. A. Jensen, "Virtual ultrasound sources in high-resolution ultrasound imaging," *Proc. SPIE—Progr. Biomed. Optics Imag.*, vol. 3, pp. 395–405, 2002.

[16] J. A. Jensen and N. B. Svendsen, "Calculation of pressure fields from arbitrarily shaped, apodized, and excited ultrasound transducers," *IEEE Trans. Ultrason., Ferroelect., Freq. Contr.*, vol. 39, pp. 262–267, 1992.

[17] J. A. Jensen, "Field: A program for simulating ultrasound systems," *Med. Biol. Eng. Comput.*, vol. 4, Suppl. 1, pt. 1, pp. 351–353, 1996.

[18] A. P. G. Hoeks, J. J. W. van de Vorst, A. Dabekaussen, P. J. Brands, and R. S. Reneman, "An efficient algorithm to remove low frequency Doppler signal in digital Doppler systems," *Ultrason. Imag.*, vol. 13, pp. 135–145, 1991.

[19] S. G. Foster, "A pulsed ultrasonic flowmeter employing time domain methods," Ph.D. thesis, Department of Electrical Engineering, University of Illinois, Urbana, IL, 1985.
[20] T. X. Misaridis and J. A. Jensen, "An effective coded excitation scheme based on a predistorted FM signal and an optimized digital filter," in *Proc. IEEE Ultrason. Symp.*, 1999, pp. 1589–1593.
[21] J. E. Wilhjelm, "Ultrasound FM Doppler systems for flow profiling with comparison to PW Doppler systems," Ph.D. thesis, Worcester Polytechnic Institute, Worcester, MA, 1991.
[22] F. Gran and J. A. Jensen, "Designing waveforms for temporal encoding using a frequency sampling method," in *Proc. IEEE Ultrason. Symp.*, 2006, pp. 1714–1717.
[23] J. A. Jensen, O. Holm, L. J. Jensen, H. Bendsen, S. I. Nikolov, B. G. Tomov, P. Munk, M. Hansen, K. Salomonsen, J. Hansen, K. Gormsen, H. M. Pedersen, and K. L. Gammelmark, "Ultrasound research scanner for real-time synthetic aperture image acquisition," *IEEE Trans. Ultrason., Ferroelect., Freq. Contr.*, vol. 52, no. 5, pp. 881–891, May 2005.
[24] W. F. Walker and G. E. Trahey, "A fundamental limit on delay estimation using partially correlated speckle signals," *IEEE Trans. Ultrason., Ferroelect., Freq. Contr.*, vol. 42, no. 2, pp. 301–308, Mar. 1995.
[25] E. Weinstein and A. J. Weiss, "Fundamental limitation in passive time-delay estimation—Part 2: Wide-band systems," *IEEE Trans. Acoust. Speech Signal Processing*, vol. 32, pp. 1064–1078, 1984.

Niels Oddershede was born in Thisted, Denmark, in 1979. He received the Master of Science degree in electronical engineering from the Technical University of Denmark in 2005. He is currently pursuing the Ph.D. degree at the Technical University of Denmark. He is a student member of the IEEE society. His research interests include signal processing with applications in medical ultrasound imaging.

Jørgen Arendt Jensen (M'93–SM'02) earned his M.S. degree in electrical engineering in 1985 and the Ph.D. degree in 1989, both from the Technical University of Denmark. He received the Dr.Techn. degree from the university in 1996. He has published more than 140 journal and conference papers on signal processing and medical ultrasound and the book, *Estimation of Blood Velocities Using Ultrasound*, Cambridge University Press, in 1996. He is also developer of the Field II simulation program. He has been a visiting scientist at Duke University, Stanford University, and the University of Illinois at Urbana-Champaign. He is currently full professor of Biomedical Signal Processing at the Technical University of Denmark at Ørsted•DTU and head of Center for Fast Ultrasound Imaging. He is also adjunct full professor at the Faculty of Health Sciences at the University of Copenhagen. He has given courses on blood velocity estimation at both Duke University and the University of Illinois and teaches biomedical signal processing and medical imaging at the Technical University of Denmark. He has given several short courses on simulation, synthetic aperture imaging, and flow estimation at international scientific conferences. He has received several awards for his research. He is also the co-organizer of a new biomedical engineering education program offered by the Technical University of Denmark and the University of Copenhagen. His research is centered around simulation of ultrasound imaging, synthetic aperture imaging and blood flow estimation, and constructing systems for such imaging.

A.3 Oddershede, N. and Gran, F. and Jensen, J. A.,
Multi-frequency encoding for fast color flow or quadroplex imaging, ***IEEE Transactions on Ultrasonic, Ferroelectrics, and Frequency Control, accepted for publication, December 2007.***

Multi-frequency encoding for fast color flow or quadroplex imaging

Niels Oddershede, Fredrik Gran, and Jørgen Arendt Jensen
Center for Fast Ultrasound Imaging, Ørsted•DTU, Build. 348,
Technical University of Denmark, DK-2800 Kgs. Lyngby, Denmark

***Abstract*— Ultrasonic color flow maps are made by estimating the velocities line by line over the region of interest. For each velocity estimate, multiple repetitions are needed. This sets a limit on the frame rate, which become increasingly severe when imaging deeper lying structures or when simultaneously acquiring spectrogram data for triplex imaging. This paper proposes a method for decreasing the data acquisition time by simultaneously sampling multiple lines for color flow maps, using narrow band signals with approximately disjoint spectral support. The signals are separated in the receiver by filters matched to the emitted waveforms, producing a number of data sets with different center frequencies. The autocorrelation estimator is then applied to each of the data sets. The method is presented, various side effects are considered, and the method is tested on data from a recirculating flow phantom. A mean standard deviation across the flow profile of 3.1%, 2.5%, and 2.1% of the peak velocity was found for bands at 5 MHz, 7 MHz, and 9 MHz, respectively. Alternatively, the method can be used for simultaneously sampling data for a color flow map and for multiple spectrograms using different spectral bands. Using three spectral bands, data for a color flow map and two independent spectrograms can be acquired at the time normally spent on acquiring data for a color flow map only. This yields an expansion of triplex imaging named multi-frequency quadroplex imaging, which enables studying the flow over an arterial stenosis by simultaneously acquiring spectrograms on both sides of the stenosis, while maintaining the color flow map. The method was tested *in-vivo* on data from the common carotid artery of a healthy male volunteer, both for fast color flow mapping and for multi-frequency quadroplex imaging.**

I. Introduction

Since the introduction of the autocorrelation estimator for ultrasonic blood flow imaging by Kasai et. al. [1] in the mid-eighties, it has been possible to create full color flow maps (CFM) in real time. The method is robust and fairly simple to implement. The velocities are estimated line by line over the region of interest, and for each line, repeated transmissions are needed. The performance of the estimator is closely linked to the number of repetitions used to form the estimate [2]. An inherent trade-off between frame rate and performance therefore exist. When imaging deep structures like the heart, this might severely affect either the performance or the frame rate. Also, in the triplex imaging mode where both CFM data and a spectrogram are shown, the time for data acquisition must be divided between multiple sets of data, increasing the significance of this problem even further.

The autocorrelation estimator essentially assumes a narrow-band signal, and the variance of the velocity estimates decreases as the bandwidth is decreased [2]. Therefore a long sinusoidal narrow-band pulse is used for CFM. Nevertheless, ultrasound transducers are often designed fairly wide-band to ensure a good resolution in B-mode images. Using only a narrow frequency band for collecting CFM data does not exploit the available bandwidth efficiently.

Numerous wide-band estimators have been proposed for ultrasonic blood velocity estimation including cross-correlation [3], maximum likelihood estimation [4], two-dimensional Fourier transformation methods [5], [6] among others. Common for all these methods are increased computational complexity, which is probably the reason why the autocorrelation approach is still the most used estimator in commercial equipment. It has also been proposed to use the wide band of the transducer for improving the velocity estimates in the autocorrelation approach by emitting a broad band pulse [7]. The received signals are then filtered into numerous narrow bands, and the velocity is estimated in each band. The velocity estimates can then be combined to form a better estimate [8] by for instance averaging. Still, none of these methods directly address the limitation set by the time needed for data acquisition.

Parallel receive beamforming has been proposed for decreasing the time spent on data acquisition for B-mode images [9]. Here a broadly focused transmit beam is emitted, and multiple receive beams are generated simultaneously by steering the beams in slightly different directions. This method has also been investigated for blood flow estimation applications [10].

This paper proposes a method for significantly decreasing the time spent on data collection for CFM by simultaneously sampling multiple lines using different frequency bands. The signals are then separated in the receiver by a simple filtering operation and the autocorrelation estimator is applied. The number of frequency bands used M depends on the available transducer bandwidth and the intensity limits set by the Food and Drug Administration [11]. The total time spent on CFM data acquisition will decrease by a factor of M, potentially increasing the frame rate with a factor of M. Alternatively, the proposed method can be used for simultaneously acquiring CFM data and spectrogram data for triplex imaging. This paper will demonstrate how data for an extension of triplex imaging, namely Multi-Frequency Quadroplex imaging (MFQ) featuring two independent spectrograms and a CFM, can be acquired during the time normally spent on acquiring a CFM.

While the parallel receive beamforming presented in [9] is limited to sample closely spaced lines within the transmitted beam, the proposed method provides a larger flexibility in

where data is sampled. Ultimately, the two methods could be combined, yielding either the possibility of a very high frame rate of CFMs, or introducing the possibility of making CFMs of 3D volumes at an acceptable frame rate.

Simultaneously transmitting multiple frequency bands in ultrasound imaging from different spatial locations and separating the signals in the receiver is not a new concept. It has previously been used for frequency division in synthetic transmit aperture imaging, where a broad-band pulse is synthesized using multiple narrow-band signals [12], and for directional velocity estimation in synthetic transmit aperture ultrasound [13]. In this paper, no broad band synthesis is performed, but the narrow-band signals are essentially used directly in the autocorrelation estimator and for spectral estimation.

The remainder of the paper is organized as follows. Section II gives a short review of the autocorrelation method and spectral velocity estimation and describes the proposed encoding method. In Section III the proposed method is tested quantitatively in a flow phantom, both for simultaneous sampling of multiple CFM lines and for MFQ imaging, and Section IV presents in-vivo results from the common carotid artery of a healthy male volunteer. The method is finally discussed in Section V.

II. Theory

A. Autocorrelation estimator

The autocorrelation method for ultrasonic blood flow imaging was first introduced by Kasai et. al. [1] Narrow-band pulses are repeatedly emitted along the same direction, and the received rf data are Hilbert transformed to give the in-phase and quadrature component. This results in a complex matrix $y(l,i)$, where i is the transmission number and l is the sample index along the rf line corresponding to depth $d_l = \frac{c}{2f_s}l$. The axial velocity at a given depth can be estimated as [1]

$$v_z = -\frac{cf_{prf}}{4\pi f_0}\arctan\left(\frac{\Im\{R(1)\}}{\Re\{R(1)\}}\right), \tag{1}$$

where c is the speed of sound, f_{prf} is the pulse repetition frequency, f_0 is the center frequency of the emitted narrow-band signal, and $R(1)$ is the complex auto-correlation function of $y(l,i)$ at lag 1, evaluated at a certain depth corresponding to $l = L_d$. This autocorrelation function can be estimated by

$$\hat{R}(1) = \frac{1}{(N-1)N_l}\sum_{l=0}^{N_l-1}\sum_{i=0}^{N-2} y(l+L_d,i)y^*(l+L_d,i+1), \tag{2}$$

which includes an averaging over N_l rf samples. This has been shown to lower the variance of the estimated autocorrelation function, and thereby increase the accuracy of the velocity estimate [14].

By demanding that a whole period of the signal must be observed to distinguish the flow signal from that of a stationary structure, the minimum detectable velocity of an autocorrelation estimator is given by [2]

$$v_{min} = \frac{c}{2}\frac{f_{prf}}{Nf_0}. \tag{3}$$

This is a quite conservative demand, and v_{min} is not considered a rigid limit. According to the Nyquist sampling theorem, the maximum detectable velocity of an autocorrelation estimator is [2]

$$v_{max} = \frac{c}{2}\frac{f_{prf}}{2f_0+B}, \tag{4}$$

where B is the bandwidth of the emitted signal. The variance of the velocity estimate assuming a constant velocity, and under the assumption that no noise is present, can be approximated by [2]

$$\sigma_v^2 = \frac{c}{4\pi^2 f_0^2}\frac{f_{prf}}{T}|v_z|, \tag{5}$$

where T is the duration of the emitted pulse.

B. Spectral velocity estimation

A spectrogram displays variation of the spectral content of the slow-time signal over time, thereby yielding a direct measure of the axial velocity of the moving blood. It can be estimated from the complex signal matrix $y(l,i)$ when the number of observations is sufficiently high. At a certain time instance $t = k/f_{prf}$, the power spectrum over pulse repetitions is estimated from N_s pulse repetitions and averaged over a number of rf samples N_l, which is known as the range gate. The segment size N_s is chosen low enough to capture the frequency variations over time and high enough to give an acceptable spectral resolution. A window $w(i)$ is often applied to the data prior to the Fourier transform. The estimated power spectral density is given by

$$\hat{P}_y(f_p,k) = \frac{1}{N_l}\frac{1}{N_s}\sum_{l=0}^{N_l-1}\left|\sum_{i=0}^{N_s-1} w(i)y(l+L_d,i+k)e^{-j2\pi f_p i/f_{prf}}\right|^2 \tag{6}$$

which for a certain depth corresponding to rf index L_d is a function of frequency f_p and time given by pulse repetition number k. Using a Hamming window given by

$$w(i) = 0.54 - 0.46\cos\left(\frac{2\pi i}{N-1}\right), \quad i = 0,1,...,N-1 \tag{7}$$

will lower the spectral side-lobes, coming from the limited observation time, to approximately -40 dB.

The estimated power spectrum is displayed as brightness on a logarithmic scale with the frequency axis vertically and the time axis horizontally. The frequency axis is often scaled to give the axial velocity estimate through

$$v_z = \frac{c}{2f_0}f_p, \tag{8}$$

visualizing the changes in the axial velocities within the range gate over time. A spatial velocity distribution within the range gate will result in a broadening of the power spectrum [1]. Due to the sampling of the slow-time signal with sampling frequency f_{prf}, the power spectrum $\hat{P}_y(f_p,k)$ has repetitions at all integer multiples of f_{prf}.

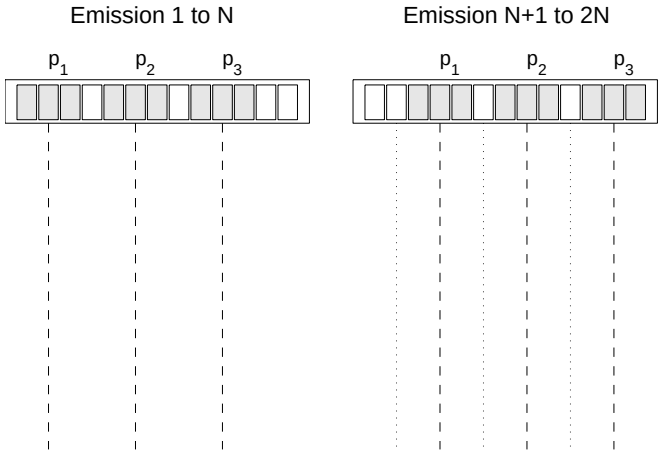

Fig. 1. The basic principle of the proposed method. Three different pulses $p_1(t)$, $p_2(t)$, and $p_3(t)$ are emitted N times and the received signals are separated in the receiver to simultaneously create three lines of the color flow map. The position of the transmitting sub-apertures are shifted and new lines are created.

C. Spatial encoding using frequency division

The proposed method aims at increasing the frame rate of color flow mapping by simultaneously sampling data for multiple lines in the CFM. Fig. 1 (left) shows a linear array transducer simultaneously emitting $M = 3$ different pulses $p_1(t)$, $p_2(t)$, and $p_3(t)$ using different sub-apertures. Assuming the signals can be separated in the receiver, three different lines can be beamformed after each emission. The emission is repeated N times at a given pulse repetition frequency f_{prf} and three lines in the CFM are created using the autocorrelation estimator [1]. The transmitting sub-apertures are slid and the emissions are repeated until data for the entire CFM is collected. The time used for collecting data will in this example only be a third of that normally used.

Alternatively, the CFM data can be acquired as is usually done, using one narrow band signal $p_1(t)$. Simultaneously, data for two spectrograms can be acquired using the signals $p_2(t)$ and $p_3(t)$. These signals are repeatedly emitted from the same sub-apertures, continuously sampling along the same lines. Thus, a CFM and two spectrograms are acquired simultaneously yielding an expansion of triplex imaging named Multi-Frequency Quadroplex imaging (MFQ). The data acquisition time will equal that normally spent on acquiring a CFM. At some point, a transducer element will be required to emit both a delayed version of $p_1(t)$ and for instance $p_2(t)$. To use the entire amplitude range while emitting each signal, $p_2(t)$ and $p_3(t)$ are delayed so that they are emitted later than $p_1(t)$.

The emitted signals $p_1(t)$, $p_2(t)$, and $p_3(t)$ are designed as simple narrow-band pulses at different frequencies. They are given by

$$p_m(t) = w(t)\sin(2\pi f_m t), \qquad 0 < t < T \tag{9}$$

for $m = [1, 2, 3]$, where f_m is the center frequency of the mth signal, and T is the pulse duration. $w(t)$ is a window designed to reduce the spectral leakages into the other bands. A window giving good spectral side-lobe suppression is the

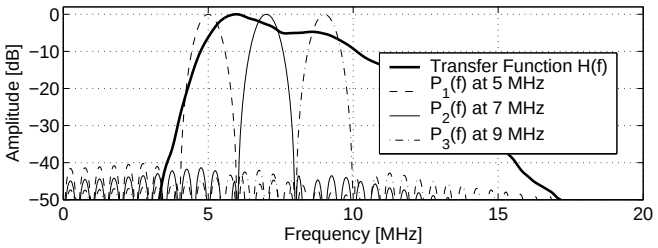

Fig. 2. The two-way system transfer function and the amplitude spectra of the three emitted pulses.

Hamming window

$$w(t) = 0.54 - 0.46\cos(\frac{2\pi t}{T}), \qquad 0 < t < T \tag{10}$$

which has spectral side-lobes below -40 dB. In the receiver the signals are then separated by filters matched to the emitted signals

$$h_m(t) = p_m(T - t), \qquad 0 < t < T \tag{11}$$

Other more advanced design methods could of course be used for designing the signals and filters. This will be considered in Section II-D. The number of pulses M, which can be emitted, is determined by the transducer bandwidth compared to the bandwidth of the signals $p_m(t)$. Fig. 2 shows the transfer function of a commercial linear array transducer (thick line), and the amplitude spectra of three signal $p_1(t)$, $p_2(t)$, and $p_3(t)$ using $f_m = [5, 7, 9]$ MHz and $T = 2$ μs (thin lines). The spectral leakage is below -40 dB for all bands.

The minimum detectable velocity is now limited by the lowest frequency band, centered at f_1,

$$v_{min} = \frac{c}{2}\frac{f_{prf}}{N f_1}, \tag{12}$$

and the maximum detectable velocity is limited by the highest frequency band f_M

$$v_{max} = \frac{c}{2}\frac{f_{prf}}{2f_M + B}. \tag{13}$$

The increased frame rate, thus, comes at the expense of a slightly decreased velocity range compared to a single narrow-band pulse. This will be further elaborated in Section V. Furthermore, the method requires M parallel beamformers, which is incorporated in most commercial high-end scanners at present, and a matched filtration of the channel RF-data. This will also be addressed in Section V.

D. Signal and filter design

To quantify the design of the signals $p_m(t)$ and the corresponding matched filters $h_m(t)$, the $p_2(t)$ signal is compared to a Parks-McClellan design [15] and least squares design [16] in Fig. 3. The left column shows the signals in the time domain, while the right column shows them in the frequency domain. The signal duration was maintained at $T = 2$ μs, the center frequency at $f_2 = 7$ MHz, and the maximum side-lobe level at -40 dB, while the -40 dB bandwidth was minimized. The signal given by (9) and the least squares design both had

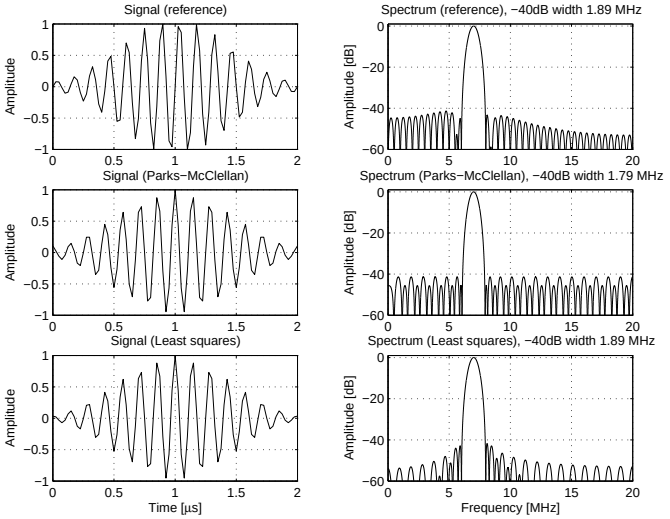

Fig. 3. A comparison of the signal $p_2(t)$ in (9) to a Parks-McClellan design and a least squares design. The left column shows the signals in the time domain, while the right column shows them in the frequency domain. The top row shows the signal $p_2(t)$, the middle row shows the Park-McClellan design, and the bottom row shows the least squares design.

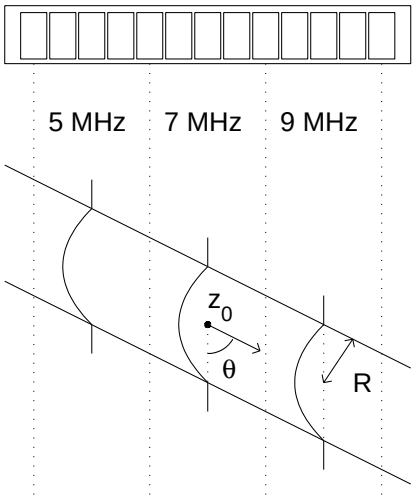

Fig. 4. Physical setup of the phantom experiment. The transducer is mounted at height $z = z_0$ over the tube center at an angle of $\theta = 60°$. The tube has radius R. The figure also shows the three regions of the CFM made at different frequency bands. Each region is sampled left to right and all regions are sampled simultaneously. The position of the three velocity profiles correspond to the profiles shown in Fig. 5.

a bandwidth of 1.89 MHz, while a slight improvement was attained using the Parks-MacClellan design, where a -40 dB bandwidth of 1.79 MHz was seen. This comes at the expense of increased far side-lobes compared to the reference. The signals given by (9) are therefore used in all the measurements presented in this paper.

III. Phantom experiments

A. Simultaneous sampling of multiple CFM lines

The method was tested in a recirculating flow rig, where a blood mimicking fluid was pumped at a constant velocity through a rubber tube submerged in a water tank. The tube had an internal radius of $R = 6$ mm. The fluid passed a 1 meter long straight metal tube with the same radius prior to entering the rubber tube and the Reynolds number was kept below 300, both to ensure a parabolic flow profile. The transducer was mounted in the water tank with the transducer surface $z_0 = 33.5$ mm above the tube center and with a $\theta = 60°$ angle between the beam axis and the flow direction. The axial component of the velocity $v_z(z)$ at the center axis of the transducer was assumed to be parabolic and centered at $z = z_0$. It is given by

$$v_z(z) = \left(1 - \frac{(z - z_0)^2}{(R/\sin\theta)^2}\right) v_0 \cos\theta, \quad z_0 - \frac{R}{\sin\theta} < z < z_0 + \frac{R}{\sin\theta}, \tag{14}$$

where $v_0 = 0.1$ m/s is the peak velocity along the flow direction. The physical setup of the phantom experiment is shown in Fig. 4, which also shows the definition of the depth z_0, the tube radius R, and the beam-to-flow angle θ.

The data acquisition was performed using a 128 element linear array transducer and the RASMUS multi-channel sampling system [17]. This system can emit arbitrary waveforms on 128 elements, and sample 64 transducer elements in real-time. To acquire data from all 128 elements, the emission is repeated and multiplexing is used. This effectively halves the frame rate. The three signals shown in Fig. 2 were used and the parameters for the experiment are given in Table I.

The acquired data were processed as described in Section II. 17 repetitions of the entire sequence were processed, yielding 17 full color flow maps. The velocity profiles at the center line of each of the three regions (see Fig. 4) were extracted and the mean and standard deviation over the repetitions were found. These are shown in Fig. 5 along with the expected velocity profile given by (14).

Fig. 5 reveals a slightly higher standard deviation in the lower frequency bands. The standard deviations of the velocity estimates are averaged over the tube diameter and are given in Table II as percent of the theoretical peak velocity of $v_0 = 0.1$ m/s. The increase in standard deviation, although present, is not as large as predicted by (5). For this phantom experiment performed in water a quite good signal-to-noise ratio is attained, and no frequency dependent attenuation is present. The increased standard deviation at lower frequency bands is therefore qualitatively in accordance with (5), which is derived assuming no noise.

B. Multi-Frequency Quadroplex imaging

At present, triplex imaging is only possible at very low frame-rates due to the switching between acquisition of CFM data and spectrogram data. The proposed method can be used to solve this problem. By acquiring data for the CFM in one frequency band and simultaneously acquiring the spectrogram data in another frequency band, this switching is no longer

TABLE I

PARAMETERS USED FOR THE PHANTOM EXPERIMENT.

Parameter	Value
Transducer type	Linear array
Number of transducer elements	128
Transducer element pitch	0.26 mm
Transducer element height	4 mm
Elevation focus	15 mm
Transfer function	See Fig. 2
Transmit focus depth	28.7 mm
Number of transmit bands, M	3
Center frequencies, f_1, f_2, and f_3	5, 7, and 9 MHz
Pulse duration, T	2 μs
Amplitude tapering	Hamming window
Number of emit. elements / band	22
Transmit apodization	Tukey window
Number of receiving elements	128 (2x64 through multiplexing)
Receive apodization	Hanning window (over 64 elem. cnt. around the current image line)
Sampling frequency, f_s	40 MHz
Pulse repetition frequency, f_{prf}	1.65 kHz (3.3 kHz incl. multiplex)
Number of shots per estimate, N	32 (64 incl. multiplexing)
Clutter filtering	Subtracting mean of N signals
Number of CFM lines created	33
Inter-line spacing	0.52 mm
Repetitions of entire sequence	17
Internal tube radius	6 mm
Depth to tube center	33.5 mm
Peak velocity	0.1 m/s
Flow angle θ (w.r.t. depth axis)	60°

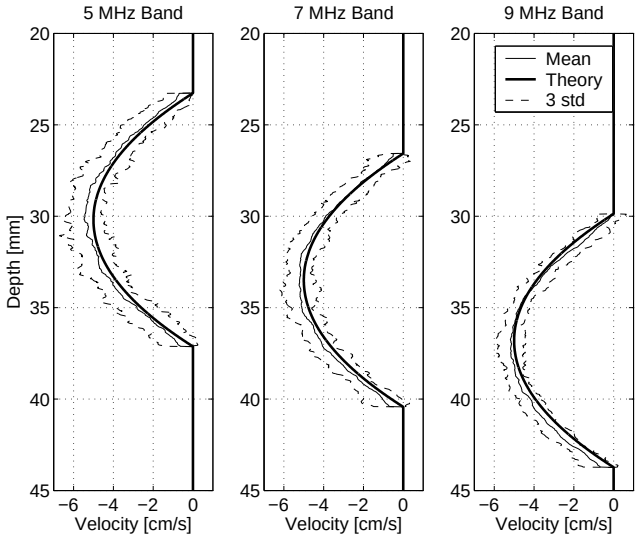

Fig. 5. Three resulting velocity profiles made at different frequency bands. The plot shows the expected velocity profile (thick line), the average of 17 profiles (thin line), and three times the standard deviation of the 17 profiles (dashed line).

TABLE II

THE AVERAGE STANDARD DEVIATION OF THE VELOCITY ESTIMATES MADE AT DIFFERENT FREQUENCY BANDS. THE STANDARD DEVIATIONS ARE GIVEN IN % OF THE TRUE PEAK VELOCITY $v_0 = 0.1$ M/S.

Frequency band	Mean Standard Deviation
5 MHz	3.1 %
7 MHz	2.5 %
9 MHz	2.2 %
Total	2.6 %

needed. If all three bands shown in Fig. 2 are used, a CFM can be created while data from two range gates are simultaneously acquired. This yields a MFQ image. Fig. 6 shows a MFQ image made in the flow rig described in Section III-A. The CFM in the top plot was made from the 5 MHz band using $N = 16$ repetitions per line (32 including multiplexing), while the leftmost spectrogram was made using the 7 MHz band, and the rightmost spectrogram using the 9 MHz band. The transmit focus was set at 30 mm, a peak velocity of $v_0 = 15$ cm/s was used and the pulse repetition frequency was set at $f_{prf} = 1.2$ kHz. The remaining parameters were set as given in Table I. The spectrograms in Fig. 6 were made in a 1 mm range gate using $N_s = 64$ hamming weighted pulse repetition samples per estimate. The processing was done as described in Section II-B. The expected axial peak velocity was $v_z = v_0 \cos(\theta) = 7.5$ cm/s.

IV. IN-VIVO EXPERIMENTS

A. Simultaneous sampling of multiple CFM lines

The method was also tested for *in-vivo* applications. Approximately 1.5 seconds of data from the common carotid artery of a healthy 31-year-old male were acquired. The parameters of Table I was used except the depth of focus was set at 15 mm, and the pulse repetition frequency f_{prf} was set at 12 kHz (24 kHz including multiplexing), giving a maximum detectable velocity of $v_{max} = 0.46$ m/s. The emitted signals were those shown in Fig. 2 and the different narrow band signals were used in regions as shown in Fig. 4. After acquisition of each flow data frame, a B-mode image was acquired in order to create complete color flow maps.

Fig. 7 shows a frame from diastole. No post-processing is applied to the velocity estimates. The flow has a parabolic tendency and no boundary effect is seen between the three regions operating at different center frequencies. A few erroneous estimates are seen in the highest frequency band (right part). Since a larger attenuation will be experienced for the higher frequency bands, this could be a result of decreased SNR.

Fig. 8 shows a frame from systole. Again, no distinct boundaries are seen but the highest frequency band seems to display a slightly degraded performance compared to the lower frequency bands. Nevertheless, due to the order of data acquisition, boundaries will be seen during acceleration. Fig. 9 shows a frame during the early systolic accelerating phase. Here the boundaries are clearly visible.

B. Multi-Frequency Quadroplex imaging

The MFQ imaging was also tested *in vivo* using a pulse repetition frequency of $f_{prf} = 12$ kHz (24 kHz including multiplexing) and a transmit focus depth of 15 mm. Two examples from the common carotid artery are shown in Fig. 10 and Fig. 11 during systole and diastole, respectively. Also here, the CFM data are acquired using the 5 MHz band, while the leftmost spectrogram is made using the 7 MHz band, and the rightmost using the 9 MHz band. The emission of the spectrogram waveforms is slightly delayed in time as described in Section II-C. Thereby the same transducer element can be

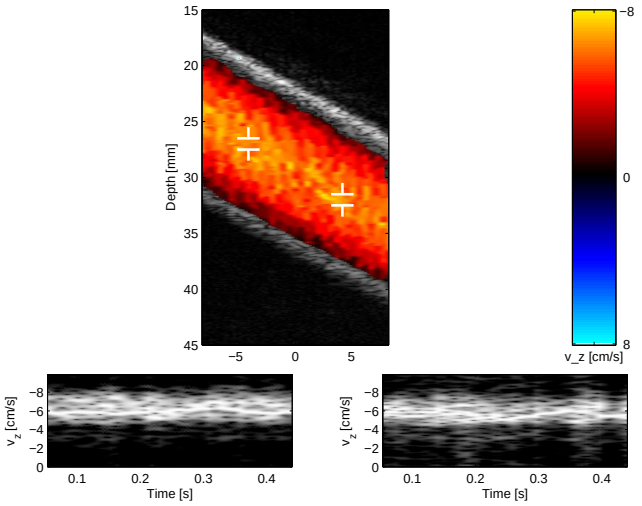

Fig. 6. Multi-Frequency Quadroplex image from the flow rig. The upper image shows the color flow map using the 5 MHz band, the left spectral Doppler shows the 7 MHz band using the leftmost range gate, and the right spectral Doppler shows the 9 MHz band using the rightmost range gate.

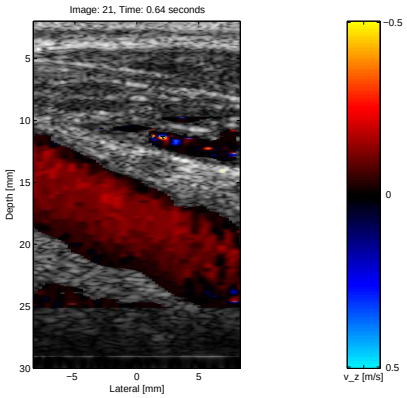

Fig. 7. Color flow map of the common carotid artery at diastole, made using the proposed method.

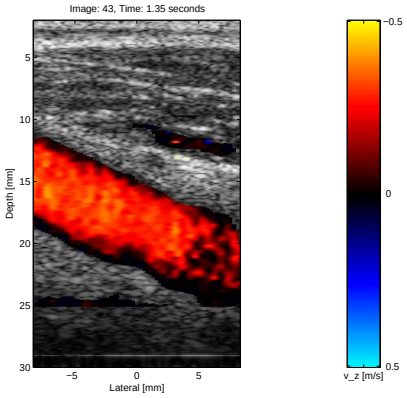

Fig. 8. Color flow map of the common carotid artery at systole, made using the proposed method.

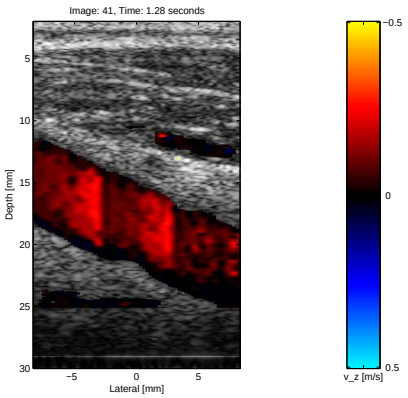

Fig. 9. Color flow map of the common carotid artery during acceleration, made using the proposed method.

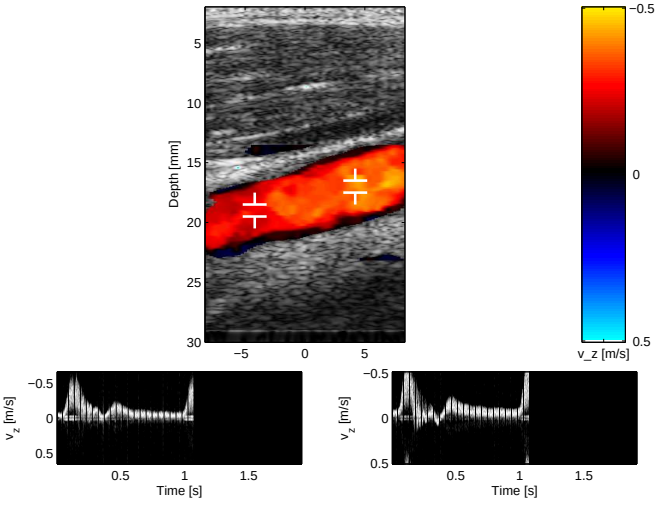

Fig. 10. Multi-Frequency Quadroplex image of the common carotid artery during systole. The upper image shows the color flow map using the 5 MHz band, the left spectral Doppler shows the 7 MHz band using the leftmost range gate, and the right spectral Doppler shows the 9 MHz band using the rightmost range gate.

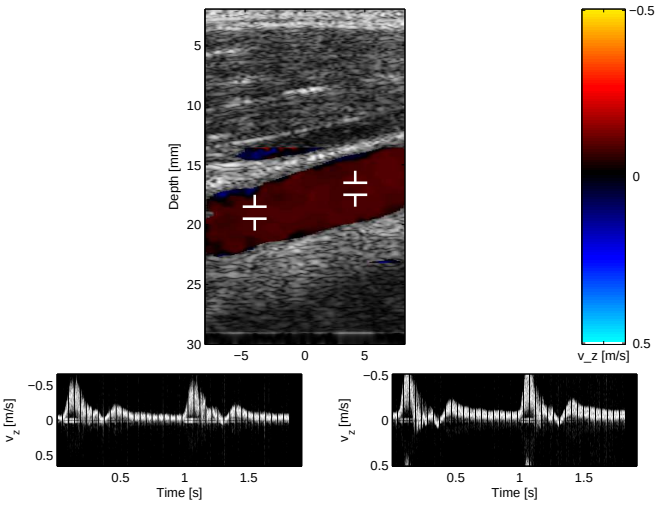

Fig. 11. Multi-Frequency Quadroplex image of the common carotid artery during diastole.

used for both emitting the CFM pulse (first, at 5 MHz) and the spectrogram pulse (second, at 7 or 9 MHz) at full amplitude range. The spectrogram data can therefore not be sampled at the very bottom of the image and the CFM data can not be sampled at the very top of the image. The ordering could of course be interchanged if desired. The CFM is composed of 33 lines, each sampled 16 times (32 including multiplexing), and the B-mode image is made from 65 emissions. This gives a frame rate of 21.4 Hz. Each spectrogram estimate was made from 64 lines using the method described in II-B. While the B-mode data was acquired (which happens 21.4 times each second), no spectrogram data are available. This is a result of the B-mode emissions using the entire transducer bandwidth. In Fig. 10, this is seen as gaps in the spectrogram. These gaps are not inherent for the proposed method, but are dependent on how the emissions are ordered. There are multiple ways of avoiding these gaps. One is to interleave the B-mode emissions and the flow data emissions, which decreases the effective pulse repetition frequency by a factor of 2. Another method was proposed by Kristoffersen and Angelsen [18], where a synthetic data segment was created using filtering of white noise by a filter generated from the spectrogram data. Finally, the power spectrum can be estimated through the Fourier transform of the autocorrelation, which can be estimated from sparse data sequences [19].

The MFQ imaging mode yields the possibility of studying the change in flow over an arterial stenosis by placing a range gate at both sides of the stenosis and monitoring the flow over time while still maintaining the CFM. An almost two second movie has been made from this data set where the MFQ is created at a frame rate of 21.4 Hz. If receive multiplexing was not needed (if all 128 receiving elements could be sampled simultaneously) a MFQ with a frame rate of 42.8 Hz would be possible for the current region of interest.

V. Discussion

The simultaneous sampling of multiple lines using different frequency bands was described in Section II-C assuming the use of three narrow-band signals. The number of bands used depends on both the available transducer bandwidth and the intensity limits set by the Food and Drug Administration. When simultaneously sampling M different frequency bands, the time spent on data acquisition will be $1/M$ times the time normally spent. But the method results in a number of side effects, which must be considered.

Firstly, the method requires an increase in hardware complexity. In order to beamform M lines at each emission, M parallel beamformers are needed, and the emission of multiple beams simultaneously in the transmitting front-end must be supported. Since most commercial high-end scanners at present have multiple parallel beamformers, the problem is already partly solved. Furthermore, the matched filters have to be applied directly to the sampled channel RF-data in order to separate the M signals. In other words, the method translates a physical problem related to the propagation speed of sound into a problem of increased processing complexity. While the speed of sound c is a constant, processing capability has historically increased exponentially.

Secondly, the performance of the velocity estimator is dependent on the center frequency of the narrow band as given by (5). This states that for the noiseless case, the variance decreases with $1/f_0^2$. The variance at lower bands will, thus, be larger than that at higher bands, assuming no noise. At the same time, the frequency dependent attenuation will lower the signal-to-noise ratio at higher frequency bands, which result in decreased performance of the autocorrelation estimator at higher frequency band. The two mechanisms essentially work against each other and, depending on the depth of investigation and the type of tissue, one band will show better performance than the other.

Thirdly, the range of velocities that can be estimated depends on the center frequency of the emitted pulse as given by (3) and (4). When using multiple frequency bands, the minimum detectable velocity will be determined by the lowest frequency band as given by (12), and the maximum detectable velocity will be given by the aliasing limit of the highest frequency band as in (13). This sets additional limits on the velocity range, and must be considered when choosing the number of frequency bands and designing the emitted signals. However, there is a way to work around this limitation. In commercial scanners a filter is often applied to the velocity estimates prior to display. This could for instance be a median filter to remove erroneous estimates. If the frequency bands are switched when the sub-apertures are slid (going from the left part to the right part of Fig. 1), consecutive CFM lines are made at different frequencies. By applying a median filter of lateral size M to the velocity estimates, erroneous estimates generated by a single frequency band could be removed. If we for instance consider the example of $M = 3$ frequency bands, it would not matter if the lowest frequency band drowns in clutter or there is aliasing in the highest frequency band. This also ensures homogenous appearance of the CFM in spite of the difference of performance in the various frequency bands.

The acceleration artifact seen in Fig. 9 was a result of the acquisition order chosen for the experiment, which can be seen in Fig. 1. The lines could be acquired in the usual order by overlapping the transmitting sub-apertures and transmitting the waveforms slightly delayed in time, as was described in Section II-C for the MFQ mode. The CFM could then not be made at the very top and the very bottom of the imaging area, but the acceleration artifact would not appear.

Fourthly, since multiple signals are emitted from the transducer simultaneously, special care must be taken to stay within the intensity limits set by the Food and Drug Administration [11]. In cases where the Spatial Peak Temporal Average intensity I_{SPTA} or the transducer surface temperature sets the limit of the system, it might be necessary to slightly reduce the transmit voltage, affecting the signal-to-noise ratio of the received signals and thereby the estimator performance.

The decrease in data acquisition time opens a window to various applications. As mentioned, deeper lying structures can be imaged at higher frame rates. Another possibility is to use $M-1$ frequency bands for $M-1$ simultaneous range gates for spectral Doppler while using one band for CFM data, as shown in Section IV-B. The authors have named this method Multi-Frequency Quadroplex imaging (MFQ) when using three fre-

quency bands. This can for instance be used for investigating the velocity distribution upstream and downstream from an arterial stenosis. Since the upstream and downstream velocities are measured simultaneously, this offers the possibility of deriving relative measures of for instance the degree of a stenosis. Furthermore, the use of multiple frequency bands can potentially be used for recognizing aliasing, due to the fact that different frequency bands will alias differently. Thereby aliasing could potentially be compensated for, resulting in larger velocity ranges of the estimator.

The parallel receive beamforming approach presented in [9] was restricted to beamforming closely spaced lines within the transmit beam width. The approach presented in this paper gives full flexibility of which lines are sampled, since the data acquired in different frequency bands are totally independent. However, the presented method, in contrast to the method in [9], can only be used for sampling within a narrow frequency band, and is therefore appropriate only for narrow-band applications such as velocity estimation, and not for instance for B-mode imaging. The method has its main advantages in applications such as MFQ imaging, where the data must be independent. Nevertheless, the two methods do not exclude each other. By combining the two methods and sampling K parallel receive lines within each of the M frequency bands, the data acquisition time will decrease by a factor of KM. At present, CFMs of three-dimensional volumes make use of ECG-gating for achieving a sufficient frame rate. The modality is thereby strictly speaking not real-time. By combining the two methods and decreasing the data acquisition time by a factor of KM, CFMs of three-dimensional volumes in real-time become feasible.

ACKNOWLEDGMENTS

This work was supported by grant 26-04-0024 from the Danish Science Foundation, by the Danish research council for Technology and Production grant 274-05-0327, and by B-K Medical A/S, Herlev, Denmark. MD Kristoffer Lindskov Hansen is acknowledged for performing the *in-vivo* data acquisition.

REFERENCES

[1] C. Kasai, K. Namekawa, A. Koyano, and R. Omoto. Real-time two-dimensional blood flow imaging using an autocorrelation technique. *IEEE Trans. Son. Ultrason.*, 32:458–463, 1985.

[2] J. A. Jensen. *Estimation of Blood Velocities Using Ultrasound: A Signal Processing Approach*. Cambridge University Press, New York, 1996.

[3] O. Bonnefous and P. Pesqué. Time domain formulation of pulse-Doppler ultrasound and blood velocity estimation by cross correlation. *Ultrason. Imaging*, 8:73–85, 1986.

[4] K. W. Ferrara and V. R. Algazi. A new wideband spread target maximum likelihood estimator for blood velocity estimation – Part I: Theory. *IEEE Trans. Ultrason., Ferroelec., Freq. Contr.*, 38:1–16, 1991a.

[5] L. S. Wilson. Description of broad-band pulsed Doppler ultrasound processing using the two-dimensional Fourier transform. *Ultrason. Imaging*, 13:301–315, 1991.

[6] H. Torp and K. Kristoffersen. Velocity matched spectrum analysis: A new method for suppressing velocity ambiguity in pulsed-wave doppler. *Ultrasound Med. Biol.*, 21(7):937–944, 1995.

[7] P. R. Phillips. Medical diagnostic ultrasound method and apparatus for improving doppler processing, United States patent 6179781, 2001.

[8] J. Udesen, F. Gran, and J. A. Jensen. A frequency splitting method for CFM imaging. In *Proc. IEEE Ultrason. Symp.*, pages 2019–2022, 2006.

[9] D. P. Shattuck, M. D. Weinshenker, S. W. Smith, and O. T. von Ramm. Explososcan: A parallel processing technique for high speed ultrasound imaging with linear phased arrays. *J. Acoust. Soc. Am.*, 75:1273–1282, 1984.

[10] J. W. Allison. *Parallel Doppler processing in ultrasonic flow imaging.* PhD thesis, Duke University, Durham, NC, 1987.

[11] FDA. Information for manufacturers seeking marketing clearance of diagnostic ultrasound systems and transducers. Technical report, Center for Devices and Radiological Health, United States Food and Drug Administration, 1997.

[12] F. Gran and J. A. Jensen. Frequency division transmission and synthetic aperture reconstruction. *IEEE Trans. Ultrason., Ferroelec., Freq. Contr.*, 53(5):900–911, 2006.

[13] F. Gran and J. A. Jensen. Directional velocity estimation using a spatio-temporal encoding technique based on frequency division for synthetic transmit aperture ultrasound. *IEEE Trans. Ultrason., Ferroelec., Freq. Contr.*, 53(7):1289–1299, 2006.

[14] T. Loupas, J. T. Powers, and R. W. Gill. An axial velocity estimator for ultrasound blood flow imaging, based on a full evaluation of the Doppler equation by means of a two-dimensional autocorrelation approach. *IEEE Trans. Ultrason., Ferroelec., Freq. Contr.*, 42:672–688, 1995.

[15] J. H. McClellan and T. W. Parksand L. R. Rabiner. A computer program for designing optimum fir linear phase digital filters. *IEEE Transactions on Audio and Electroacoustics*, AU-21, no. 6:506–526, 1973.

[16] John G. Proakis and Dimitris G. Manolakis. *Digital Signal Processing, Principles, Algorithms, and Applications*. Prentice Hall, Upper Saddle River, New Jersey, 3rd edition, 1996.

[17] J. A. Jensen, O. Holm, L. J. Jensen, H. Bendsen, S. I. Nikolov, B. G. Tomov, P. Munk, M. Hansen, K. Salomonsen, J. Hansen, K. Gormsen, H. M. Pedersen, and K. L. Gammelmark. Ultrasound research scanner for real-time synthetic aperture image acquisition. *IEEE Trans. Ultrason., Ferroelec., Freq. Contr.*, 52 (5):881–891, May 2005.

[18] K. Kristoffersen and B. A. J. Angelsen. A time-shared ultrasound Doppler measurement and 2-D imaging system. *IEEE Trans. Biomed. Eng.*, BME-35:285–295, 1988.

[19] J. A. Jensen. Spectral velocity estimation in ultrasound using sparse data sets. *J. Acoust. Soc. Am.*, vol 120(1):211–220, 2006.

A.4 Oddershede, N. and Løvstakken, L. and Torp, H. and Jensen, J. A., Estimating 2-D vector velocities using multi-dimensional spectrum analysis, *IEEE Transactions on Ultrasonic, Ferroelectrics, and Frequency Control, submitted for publication, November 2007.*

Estimating 2-D vector velocities using multi-dimensional spectrum analysis

Niels Oddershede[1], Lasse Løvstakken[2], Hans Torp[2], and Jørgen Arendt Jensen[1]
1) Center for Fast Ultrasound Imaging, Ørsted•DTU, Build. 349,
Technical University of Denmark, DK-2800 Lyngby, Denmark
2) Department of Circulation and Medical Imaging,
Norwegian University of Science and Technology, Trondheim, Norway

***Abstract*— Wilson (1991) presented a wide-band estimator for axial blood flow velocity estimation through the use of the two-dimensional Fourier transform. It was shown how a single velocity component was concentrated along a line in the two-dimensional Fourier space, where the slope was given by the axial velocity. This paper presents an expansion of this study. If data are sampled within a region, instead of along a line, a three-dimensional (3-D) data matrix is created along lateral space, axial space, and pulse repetitions. It is shown, that a single velocity component will be concentrated along a plane in the 3-D Fourier space, which is found through the 3-D Fourier transform of the data matrix, and that the plane is tilted according to the axial and lateral velocity components. Two estimators are derived for finding the plane in the 3-D Fourier space, where the integrated power spectrum is largest. The first uses the 3-D Fourier transform to find the power spectrum, while the second uses a minimum variance approach. Based on this plane, the axial and lateral velocity components are estimated. A number of phantom measurements, for flow-to-depth angles of 60, 75, and 90 degrees, were performed. The receive apodization was manipulated to create an oscillation in the lateral direction, and multiple parallel lines were beamformed simultaneously. The two estimators were then applied to the data. The axial velocity component was estimated with an average standard deviation below 2 % of the peak velocity, while the average standard deviation of the lateral velocity estimates was between 2.1 % and 16.4 %. The two estimators were also tested on *in-vivo* data from a transverse scan of the common carotid artery, showing the potential of the vector velocity estimation method under *in-vivo* conditions.**

I. Introduction

Blood flow velocity estimation in ultrasound systems is usually performed by repeating a number N_t of focused emissions along the same direction at the pulse repetition frequency f_{prf}. The received signal is sampled along the beam direction at a temporal sampling frequency of f_s, corresponding to a spatial sampling in depth of $2f_s/c$. A data matrix $s(z,t)$ can then be formed with N_z depth samples and N_t pulse repetition samples, also known as slow-time samples.

Numerous estimators have been proposed for finding the axial velocity component from this data matrix. Kasai and coworkers [1] proposed the autocorrelation estimator, where the average phase shift along pulse repetitions is found. This phase shift scales with the axial velocity. Bonnefous and Pesque proposed a cross-correlation estimator [2], where the consecutive columns of $s(z,t)$ are cross-correlated to find the spatial shift. This spatial shift relates to the axial velocity through the pulse repetition interval $T_{prf} = 1/f_{prf}$. Ferrara and Algazi [3], [4] proposed a maximum likelihood estimator, essentially using both the envelope information and the phase information in the estimator. Wilson [5] and Torp and Kristoffersen [6] proposed to find the axial velocity component through the two-dimensional Fourier transform of the matrix $s(z,t)$. If only a single velocity is present within the observation window, the two-dimensional power spectrum will peak along a line in the spectral domain. This line was denoted an iso-velocity line in [6]. The axial velocity can be estimated by finding the slope of this line [5]. Allam and coworkers [7], [8] proposed a frequency re-sampling method in the two-dimensional Fourier space which projects the wide-band Fourier components along the iso-velocity lines to multiple narrow-band signals at the same center frequency. Hereby, high resolution spectral estimators such as minimum variance (Capon) and MUSIC [9] can be used for finding the axial velocity component.

Numerous authors have extended these estimators to search for both the axial and the lateral velocity component. Fox [10] proposed using two crossing tilted beams, and finding the velocity along each beam. From these, the axial and lateral components could be found locally. Munk and Jensen [11], [12], [13] proposed a method for estimating both velocity vectors by creating a lateral oscillation through manipulation of the receive apodization. An extension of the autocorrelation estimator was derived for finding the velocity components [13]. A similar method entitled spatial quadrature was proposed by Anderson [14]. Trahey and coworkers [15] proposed a two-dimensional cross-correlation method, also known as speckle tracking, for finding the axial and lateral velocity components.

The purpose of this paper is to extend the estimator presented by Wilson [5] and Torp and Kristoffersen [6] to search for both the axial and the lateral component. If data are sampled in a region both axially and laterally over a number of repetitions, a three-dimensional signal matrix $s(x,z,t)$ can be created. It will be shown in Section II that for a single velocity, the three-dimensional power spectrum of $s(x,z,t)$ will be concentrated along a plane in the three-dimensional Fourier space, and in Section III, two estimators will be derived. The two velocity components are estimated by summing the power spectrum along the iso-velocity plane corresponding to all combinations of the possible lateral and axial velocity

components (v_x, v_z) and choosing the combination that yield the maximum sum. This essentially corresponds to using the Radon transform in the three-dimensional power spectral domain. The first estimator finds the power spectral components through a Fourier transform, while the second uses a minimum variance approach [16].

As will be shown in Section II, the power spectral components are limited not only by the iso-velocity plane, but also by the emitted waveform in one dimension and the transmit and receive apodization in another. To practically find this plane, the receive apodization is manipulated, as has previously been used by Munk and Jensen [11], [12], [13] and by Anderson [14] for 2-D vector velocity estimators. Hereby an oscillation along the lateral direction of the point spread function is created. Section IV describes how this oscillation is created, and why this helps the velocity estimation. Section V presents a simulation of the point spread function for the proposed imaging sequence, while Section VI presents a number of measurements performed in a flow rig phantom. An *in-vivo* example from the common carotid of a healthy male volunteer is presented in Section VII, while concluding remarks are given in Section VIII.

II. Three-dimensional Fourier transform of ultrasonic data

Most ultrasonic velocity estimation systems do numerous transmissions along the same direction, and a data matrix $s(z,t)$ can be formed, where z denotes depth and t slow time. Normally both variables are discrete.

Wilson showed [5] that if the flow has constant velocity within the limits of z, the 2-D fast Fourier transform $S(\zeta, f_d)$ of $s(z,t)$ will be concentrated along a line in the 2-D plane spanned by the spatial frequency ζ and the temporal frequency f_d, and that the slope of this line is proportional to the flow velocity.

Assuming we could sample within a plane instead of just a line, a three-dimensional data matrix $s(x,z,t)$ could be constructed, where x is lateral position, z is depth, and t is slow-time. Lets first assume the data are continuous in all dimensions and the observation time and space are infinitely long. The three-dimensional Fourier transform of this matrix is given by

$$\begin{aligned} F(\chi,\zeta,f_d) &= \int_{-\infty}^{\infty}\int_{-\infty}^{\infty}\int_{-\infty}^{\infty} s(x,z,t)\cdot \\ &\quad e^{-j2\pi\chi x}e^{-j2\pi\zeta z}e^{-j2\pi f_d t}dxdzdt, \end{aligned} \quad (1)$$

where χ is the spatial frequency along the lateral direction, ζ is the spatial frequency along the axial direction, and f_d is the slow-time frequency commonly known as the Doppler frequency.

Considering a constant velocity movement within the axial-lateral plane and disregarding the change in spatial impulse response, the three-dimensional data matrix $s(x,z,t)$ can be approximated by a two-dimensional function $s_0(x,z)$ moving within the plane with axial velocity v_z and lateral velocity v_x

$$s(x,z,t) = s_0(x - v_x t, z - v_z t). \quad (2)$$

The three-dimensional Fourier transform of $s(x,z,t)$, as given in (1), is then calculated as

$$\begin{aligned} F(\chi,\zeta,f_d) &= \int_{-\infty}^{\infty}\int_{-\infty}^{\infty}\int_{-\infty}^{\infty} s_0(x - v_x t, z - v_z t)\cdot \\ &\quad e^{-j2\pi\chi x}e^{-j2\pi\zeta z}e^{-j2\pi f_d t}dxdzdt \\ &= \int_{-\infty}^{\infty} S_0(\chi,\zeta)e^{-j2\pi\chi v_x t}e^{-j2\pi\zeta v_z t}e^{-j2\pi f_d t}dt \\ &= S_0(\chi,\zeta)\int_{-\infty}^{\infty} e^{-j2\pi(f_d + v_x\chi + v_z\zeta)t}dt \\ &= S_0(\chi,\zeta)\delta(f_d + v_x\chi + v_z\zeta), \end{aligned} \quad (3)$$

where $S_0(\chi,\zeta)$ is the two-dimensional Fourier transform of $s_0(x,z)$. This function is zero except for a plane intersecting the origo. This plane in the three-dimensional Fourier space spanned by (χ,ζ,f_d) satisfies

$$f_d = -v_x\chi - v_z\zeta. \quad (4)$$

The two-dimensional spectrum $S_0(\chi,\zeta)$ is assumed separable, so that

$$S_0(\chi,\zeta) = S_x(\chi)S_z(\zeta) \quad (5)$$

where $S_z(\zeta)$ is the spectrum of the emitted signal, peaking at $\zeta = \pm 2f_0/c$, where f_0 is the temporal center frequency of the emitted pulse, and $S_x(\chi)$ is the lateral spatial spectrum. This spectrum is the Fourier transform of the aperture smoothing function $W(\vec{k})$

$$S_x(\chi) = \int_{-\infty}^{\infty} W(\vec{k})e^{j2\pi\chi x}dx. \quad (6)$$

Assuming a linear array of $2M+1$ omnidirectional point sources, equally spaced at distance d, the aperture smoothing function in the focus point is given by [16]

$$W(\vec{k}) = \sum_{m=-M}^{M} w(m)e^{jk_x md}. \quad (7)$$

Here $w(m)$ is the apodization at the m'th transducer element and

$$k_x = -\frac{\omega_0}{c}\sin(\alpha) = -\frac{2\pi f_0}{c}\frac{x}{r} \approx -\frac{2\pi}{\lambda z}x, \quad (8)$$

and α is the angle from the aperture center axis to the point (x,z), r is the distance from the aperture center to (x,z), and the approximation $r \approx z$ is made assuming a small angle α. The lateral spectrum $S_x(\chi)$ can now be approximated by

$$\begin{aligned} S_x(\chi) &\approx \int_{-\infty}^{\infty}\left[\sum_{m=-M}^{M} w(m)e^{-j\frac{2\pi md}{\lambda z}x}\right]e^{j2\pi\chi x}dx \\ &= \sum_{m=-M}^{M} w(m)\int_{-\infty}^{\infty} e^{-j2\pi(\frac{md}{\lambda z}-\chi)x}dx \\ &= \sum_{m=-M}^{M} w(m)\delta(\chi - \frac{md}{\lambda z}). \end{aligned} \quad (9)$$

According to (9), the lateral spatial spectrum $S_x(\chi)$ will approximately be a scaled version of the apodization function $w(m)$, where the lateral spatial frequency axis scales with

depth z. According to the Nyquist sampling theorem, the lateral sampling at a certain depth z must therefore obey

$$\Delta x < \frac{\lambda z}{2Md}, \tag{10}$$

where Δx is the lateral sampling interval.

The assumptions of continuous data and infinitely long observation time and space made in deriving (3) are of course not satisfied in ultrasonic velocity estimation. Neither is the assumption of a constant velocity over the observation time and space. By limiting the observation space both laterally and axially by windowing the signal, a spectral broadening will occur in these dimensions and side-lobes will appear. The same goes for the limited observation time. Nevertheless, the three-dimensional spectral content of a constant velocity within the observation window will be concentrated along the plane indicated by (4).

The sampling along space and time will result in spectral repetitions at all multiples of the sampling frequency. The spatial sampling can relatively easy be set to avoid aliasing, while aliasing might occur along the temporal direction at high velocities. Aliasing in the three-dimensional power spectral domain will occur when f_d in (4) exceeds $f_{prf}/2$. Nevertheless, the estimators derived in the proceeding section are cyclic in nature, and aliasing in the temporal direction is not expected to cause difficulties.

III. 2-D VECTOR VELOCITY ESTIMATOR

In [5], [6], the axial velocity was estimated by summing the two-dimensional power spectrum (spanned by the axial frequency and the slow-time frequency) along iso-velocity lines, and choosing the velocity corresponding to the largest sum.

In the vector velocity estimation case, both the axial and lateral velocities are sought and according to (3) a constant velocity will give rise to non-zero values along a plane in the three-dimensional power spectral space. This indicates that the axial and lateral velocity components can be estimated by finding the plane satisfying (4), over which the sum of power spectral components is largest. The velocity components will then correspond to the angles with which the plane is tilted in the three-dimensional power spectral space. Two estimators for finding the spectral components along this plane are given. The first, given in Section III-A uses the periodogram (the magnitude squared of the Fourier coefficients), while the second, given in Section III-B uses a minimum variance spectral estimator.

A. Periodogram estimator

By assuming the velocity components v_x and v_z given, the Fourier components at the plane corresponding to these velocities are given by

$$\begin{aligned} F(\chi,\zeta|v_x,v_z) &= \int_{-\infty}^{\infty}\int_{-\infty}^{\infty}\int_{-\infty}^{\infty} s(x,z,t)\cdot \\ & e^{-j2\pi[\chi(x-v_xt)+\zeta(z-v_zt)]}dxdzdt \end{aligned} \tag{11}$$

which is found by inserting (4) into (1). The total power along this plane is found by integrating the magnitude squared of (11) over all spatial frequencies χ and ζ

$$P(v_x,v_z) = \int_{-\infty}^{\infty}\int_{-\infty}^{\infty} \left|F(\chi,\zeta|v_x,v_z)\right|^2 d\chi d\zeta. \tag{12}$$

Since data are sampled both spatially and temporally, the integrals become sums and the problem can be solved in matrix form. By ordering the three-dimensional signal matrix in a row vector $\mathbf{s}$ of length $N_xN_zN_t$, and defining the row vector

$$\begin{aligned} \mathbf{e}_i &= e^{j2\pi(\chi_i x+\zeta_i z+f_d t)} \\ &= e^{j2\pi(\chi_i(x-v_xt)+\zeta_i(z-v_zt))} \end{aligned} \tag{13}$$

for spatial frequencies χ_i and ζ_i, we have

$$F(\chi_i,\zeta_i|v_x,v_z) = \mathbf{e}_i^H\mathbf{s}, \tag{14}$$

where $(\cdot)^H$ denotes the complex conjugate transpose. By making a $\mathbf{e}_i$ vector for all I permutations of the spatial frequencies the total power along the plane given by velocities v_x and v_z is then found by

$$\begin{aligned} P(v_x,v_z) &= \sum_{i=0}^{I-1}\left|F(\chi_i,\zeta_i|v_x,v_z)\right|^2 \\ &= \sum_{i=0}^{I-1}\mathbf{e}_i^H\mathbf{s}(\mathbf{e}_i^H\mathbf{s})^H \\ &= \sum_{i=0}^{I-1}\mathbf{e}_i^H\mathbf{s}\mathbf{s}^H\mathbf{e}_i. \end{aligned} \tag{15}$$

In case the covariance matrix of the data $\mathbf{R} = E\{\mathbf{s}\mathbf{s}^H\}$ is known, where $E\{\cdot\}$ denotes the expectation value, the power spectral estimate of (15) can be found by

$$P(v_x,v_z) = \sum_{i=0}^{I-1}\mathbf{e}_i^H\mathbf{R}\mathbf{e}_i. \tag{16}$$

Estimation of the covariance matrix is considered in Section III-B. By doing the calculation in (16) for all combinations of v_x and v_z, the velocity components can be estimated by finding the velocities yielding the highest power along the plane

$$\hat{v}_x = \arg\max_{v_x} P(v_x,v_z) \tag{17}$$

$$\hat{v}_z = \arg\max_{v_z} P(v_x,v_z). \tag{18}$$

These discrete estimates can be further refined by interpolation of the $P(v_x,v_z)$ function.

B. Minimum variance estimator

The periodogram estimator suffers from poor spectral resolution when the observation window is limited [7], as is the case here. If the signal covariance matrix $\mathbf{R}$ is known, the power spectral component at lateral frequency χ_i and axial frequency ζ_i on the plane given by v_x and v_z can be found by a minimum variance estimator [16]

$$\left|F_{mv}(\chi_i,\zeta_i|v_x,v_z)\right|^2 = \frac{1}{\mathbf{e}_i^H\mathbf{R}^{-1}\mathbf{e}_i}, \tag{19}$$

where the covariance matrix is given by

$$\mathbf{R} = E\{\mathbf{s}\mathbf{s}^H\}. \tag{20}$$

$E\{\cdot\}$ denotes the expectation value and $\{\cdot\}^{-1}$ denotes the matrix inverse. Again, the estimates along the plane are summed to find the total power on the plane given by v_x and v_z. This can be found by

$$P_{mv}(v_x, v_z) = \sum_{i=0}^{I-1} \frac{1}{\mathbf{e}_i^H \mathbf{R}^{-1} \mathbf{e}_i}, \tag{21}$$

Since the data covariance matrix is not known, an estimate must be found. This can be done by dividing the data cube $s(x, z, t)$ of size $[N_x, N_z, N_t]$ into sub-cubes of size $[M_x, M_z, M_t]$. Hereby a total of $(N_x - M_x + 1)(N_z - M_z + 1)(N_t - M_t + 1)$ sub-cubes can be created. This is essentially a three-dimensional form of sub-array averaging used in some adaptive beamformers [9]. By organizing each data sub-cube in a row vector $\mathbf{s}_{mx,mz,mt}$, where mx, mz, and mt are indexes to the first sub-cube element, the covariance matrix of size $[M_x M_z M_t, M_x M_z M_t]$ can be estimated by

$$\hat{\mathbf{R}} = \sum_{mx=0}^{N_x - M_x} \sum_{mz=0}^{N_z - M_z} \sum_{mt=0}^{N_t - M_t} \mathbf{s}_{mx,mz,mt} \mathbf{s}_{mx,mz,mt}^H. \tag{22}$$

To ensure full rank of $\hat{\mathbf{R}}$, needed for finding the inverse, the inequality $(N_x - M_x + 1)(N_z - M_z + 1)(N_t - M_t + 1) \geq M_x M_z M_t$ must be satisfied. The sum along the plane in the power spectral domain can then be found from (21) by creating the vectors $\mathbf{e}_i$ according to the new data dimensions, and using the estimated covariance matrix $\hat{\mathbf{R}}$. Again, the lateral and axial velocity estimates are found by a search for the highest total power

$$\hat{v}_x = \arg\max_{v_x} P_{mv}(v_x, v_z) \tag{23}$$

$$\hat{v}_z = \arg\max_{v_z} P_{mv}(v_x, v_z). \tag{24}$$

IV. Measurement setup

The estimators derived in Section III search for the plane in the three-dimensional Fourier domain where the power is largest. From (3) and (5) it is apparent that both the spectral support of the emitted waveform and the apodization through (9) will limit the power spectral components along the plane. By using a rectangular or windowed apodization, the lateral spectrum $S_x(\chi)$ will be centered at $\chi = 0$. This means that only two clouds centered at $(\chi, \zeta) = (0, 2f_0/c)$ and $(0, -2f_0/c)$ will define the plane, and the lateral velocity component will be hard to estimate.

Nevertheless, by using the receive apodization shown in Fig. 1 (bottom), four clouds will define the plane though (5) and (3). Hereby both the axial and lateral velocities, corresponding to the slope of the plane in two directions, can be better estimated. Manipulation of the apodization function in this way has previously been used by Munk and Jensen [11], [12], [13] and by Anderson [14], using a different estimation scheme. As shown in [12], using an apodization function as that in Fig. 1 will create a lateral oscillation of the point spread function. In [13], normally focused beams were emitted, while

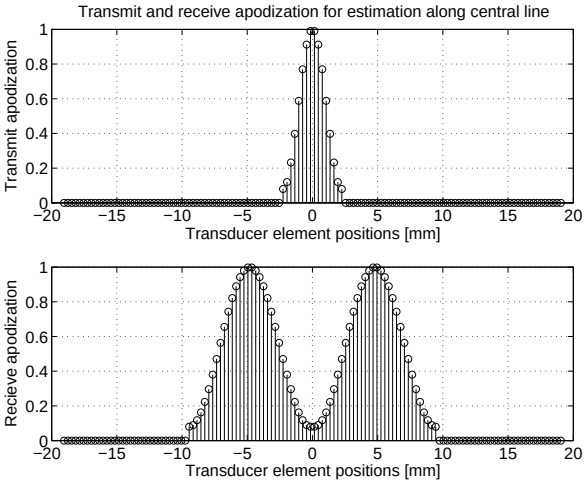

Fig. 1. The transmit (top) and receive (bottom) apodization used for central line. A narrow transmit apodization is used to create a broad beam, enabling parallel beamforming. Only 64 of the 128 elements are active while receiving, and the linear array is scanned in the usual way.

the receive apodization was two separated $sinc$ functions. Other receive apodization functions, such as two Hanning functions, two Hamming functions, two Blackman functions and two Gaussian functions have been tried [17]. Since the estimator derived in [13] is a narrow-band estimator, a trade-off between the bandwidth and the signal-to-noise ratio (SNR) existed, since using fewer elements for reception lowers the SNR. This trade-off is considered in [17].

According to (3) and (5), the plane in the three-dimensional Fourier space will be limited by the lateral and axial spectral support, $S_x(\chi)$ and $S_z(\zeta)$. The performance of the estimators derived in Section III will therefore expectedly increase as the bandwidth of $S_x(\chi)$ and $S_z(\zeta)$ is increased, essentially revealing more of the iso-velocity plane. A broad-band pulse is therefore emitted so that $S_z(\zeta)$ is only limited by the transfer function of the transducer and measurement system. Likewise, the lateral bandwidth is increased by increasing the width of the two separated receive apodization functions, furthermore ensuring good lateral resolution.

The transmit and receive apodization used in the measurements are shown in Fig. 1. The receive apodization consisting of two 32 element Hamming windows will create a broadband oscillation in the lateral direction of the point spread function at a lateral spatial center frequency of

$$\chi_0 = \frac{m_{max} d}{\lambda z} = \frac{16 \cdot 0.3\text{mm}}{0.296\text{mm} \cdot 20\text{mm}} = 811\text{m}^{-1}. \tag{25}$$

For comparison, the axial spatial center frequency is $\zeta_0 = 2f_0/c = 6752$ m^{-1}. The maximum lateral sampling distance at depth $z = 20$ mm is found through (10) to be

$$\Delta x < \frac{\lambda z}{2Md} = \frac{0.296\text{mm} \cdot 20\text{mm}}{2 \cdot 32 \cdot 0.3\text{mm}} = 308\mu\text{m} \tag{26}$$

The narrow transmit apodization consisting of a 16 element Hamming window is used to insure a broad focus, enabling the simultaneous sampling of multiple parallel lines used in the estimator. At every emission, $N_x = 7$ parallel lines around

the center of emission is beamformed at inter-line distance $\Delta x = 200$ μm using delay-and-sum beamforming [16]. The lines are beamformed at $f_s = 20$ MHz, corresponding to an axial sampling interval of 37 μm. For every point along the line, where the vector velocity is estimated, $N_z = 33$ samples along depth are used, corresponding to both a lateral and axial extent of 1.2 mm. $N_t = 32$ repetitions are made along the same direction. Table I summarizes the parameters used for the measurements.

TABLE I
PARAMETERS.

Transducer	
Transducer type	Linear array
Number of transducer elements	128
Transducer element pitch, d	0.3 mm
Transducer element kerf	0.035 mm
Transducer element height	5 mm
Elevation focus	20 mm
Center frequency, f_0	5 MHz
Speed of sound, c	1481 m/s
Wavelength, $\lambda = c/f_0$	0.296 mm
Transmission	
Excitation type	1.5 cycle sinusoid at f_0
Transmit apodization	16 element Hamming
Receive apodization	Two 32 element Hamming
Transmit focus	20 mm
Receive focus	Dynamic
Pulse repetition frequency, f_{prf}	1 kHz
Vessel	
Vessel radius, R	6 mm
Flow angles, θ	$60°$, $75°$ and $90°$
Depth of tube center, z_0	22, 24, and 19 mm, respect.
Peak velocity, v_0	10 cm/s
Processing	
Lateral sampling interval	0.2 mm
Axial sampling interval	0.037 mm
Number of points lateral, N_x	7
Number of points axial, N_z	33
Number of pulses per estimate,N_t	32
Size of region of interest, [lateral, axial]	$[1.2, 1.2]$ mm
Lateral samples in sub-cube, M_x	6
Axial samples in sub-cube, M_z	6
Temporal samples in sub-cube, M_t	12
Clutter filtering method	Mean subtraction
Number of freq. lateral, MV, N_χ	11
Number of freq. axial, MV, N_ζ	11
Number of frequency permutations, I	121
Velocity search range	-12 to 12 cm/s
Velocity search interval	0.5 cm/s

V. SIMULATION

A simulation was performed using the Field II simulation program [18], [19]. A single stationary scatterer was placed directly below the transducer at depth $z = 20$ mm and a single emission was performed from the center of the transducer using the transmit apodization given in Fig. 1. The data were beamformed using delay and sum beamforming with dynamic receive focus and using the two-Hamming receive apodization shown in Fig. 1. The parameters were set according to Table I.

The top plot of Fig. 2 shows the beamformed, envelope detected, and logarithmic compressed image of the single point on a 60 dB scale. The far side-lobes are around -50 dB. The middle plot of Fig. 2 shows a slice through the point spread function at $z = 20$ mm, prior to envelope detection and logarithmic compression. It shows a short oscillating pulse as would be expected [11], [12], [13], [14]. The bottom plot of Fig. 2 shows the Fourier transform of the lateral slice (solid line), which gives the lateral spectrum $S_x(\chi)$. The plot also shows the convolution of the transmit and receive apodization functions of Fig. 1 scaled according to (9).

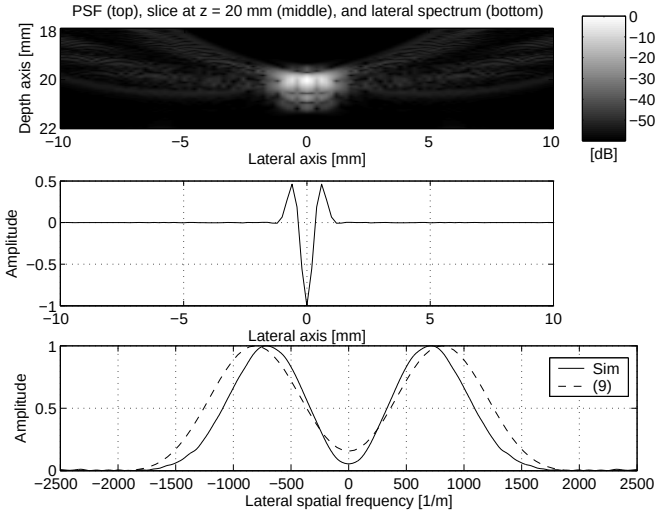

Fig. 2. Simulation. The top plot shows the envelope detected and logarithmic compressed point spread function beamformed from one emission using the spodization shown in Fig. 1. The middle plot shows a slice through the point spread function at depth $z = 20$ mm prior to envelope detection. The plot is shown on a linear scale. The bottom plot shows the Fourier transform of the middle plot yielding the lateral spatial spectrum $S_x(\chi)$ on a linear scale (solid). The bottom plot also shows the expected lateral spatial spectrum found by convolving the transmit and receive apodization and scaling according to (9).

A slight mismatch between the simulation and the theoretical lateral spectrum is revealed from the plot. The simulated spectrum peaks around $\chi = 700$ m^{-1}, while a peak is expected around $\chi = 800$ m^{-1}. The reason for this mismatch probably comes from the derivation of (9). This equation is derived assuming omnidirectional point sources, and the directivity of the individual transducer elements is not included. This directivity will effectively lower the apodization of the outermost transducer elements and therefore slightly lower the center frequency.

VI. PHANTOM MEASUREMENTS

A series of measurements was performed in a flow-rig phantom. A blood mimicking fluid was circulated at a constant velocity through a tube submerged in a water tank. A linear array transducer was fixed above the tube at a controlled angle. Three measurements were made with angles of $\theta = 60°$, $75°$, and $90°$ (transverse flow) between the transducer axis and the flow direction. The data were collected using our RASMUS experimental ultrasound scanner [20]. The parameters for the measurements are given by Table I.

The data were beamformed as described in Section IV and clutter filtering was performed by subtracting the average of $N_t = 32$ slow-time samples at each spatial position. Fig.

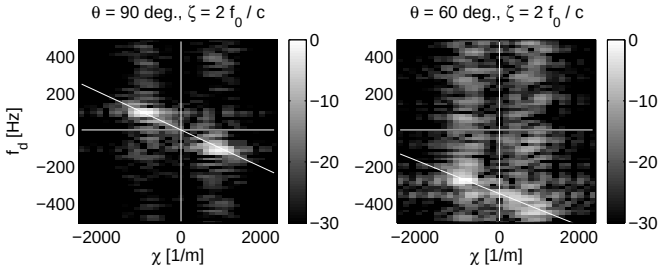

Fig. 3. Examples of power spectra at $\zeta = 2f_0/c$ on a dB scale. Data from phantom measurement at $\theta = 90°$ (left) and $\theta = 60°$ (right). A white line indicates $f_d = -v_x\chi - v_z\zeta$.

3 shows slices of the three-dimensional power spectrum at the axial center frequency $\zeta = 2f_0/c$. The left plot is for the $\theta = 90°$ experiment, and the right plot is for the $\theta = 60°$ experiment. In both plots, a white line indicating the intersection with the plane expected from (4) is also shown. Note that for $\theta = 60°$, the intersection of the plane and $\chi = 0$ is shifted according to $f_d = -2v_z f_0/c$, and that the slopes are different in the two plots due to the different lateral velocity components. Note also how the lateral spectral content resembles the apodization, as also seen in Fig. 1.

The two estimators derived in Section III were applied to the data from directly below the transducer. $N_{rep} = 18$ repetitions were made, creating 18 independent velocity profiles through the tube at each beam-to-flow angle. The average velocity profile over the N_{rep} repetitions was found

$$\bar{v}(z) = \frac{1}{N_{rep}} \sum_{i=0}^{N_{rep}-1} \hat{v}_i(z), \tag{27}$$

where $\hat{v}_i(z)$ is the i'th velocity profile at a certain beam-to-flow angle and using a certain estimator. Furthermore, the standard deviation profile was found by

$$std(z) = \frac{1}{N_{rep}-1} \sum_{i=0}^{N_{rep}-1} [\hat{v}_i(z) - \bar{v}(z)]^2. \tag{28}$$

The flow was assumed laminar with a parabolic flow profile, and the expected velocity profile is therefore given by

$$\begin{aligned} v_x(z) &= v_0 \left(1 - \left(\frac{(z-z_0)}{R/\sin(\theta)}\right)^2\right) \sin(\theta) \\ v_z(z) &= v_0 \left(1 - \left(\frac{(z-z_0)}{R/\sin(\theta)}\right)^2\right) \cos(\theta) \\ & \quad z_0 - \frac{R}{sin(\theta)} < z < z_0 + \frac{R}{sin(\theta)}, \end{aligned} \tag{29}$$

where z_0 is the depth of the vessel center. Fig. 4 through 6 give the results of the phantom measurements. The figures are organized as follows. The top left plot shows the lateral velocity estimates using the Periodogram estimator from Section III-A, while the top right plot shows the axial velocity estimates using the Periodogram estimator. The bottom left plot shows the lateral velocity estimates using the Minimum Variance estimator from Section III-B, while the bottom right plot shows the axial velocity estimates using the Minimum Variance estimator. In every plot the average velocity profile $\bar{v}(z)$ is shown (solid, thin line), the average profile ± 3 times the standard deviation $\bar{v}(z) \pm 3std(z)$ (dashed lines), and the expected profile from (29) (solid, thick line).

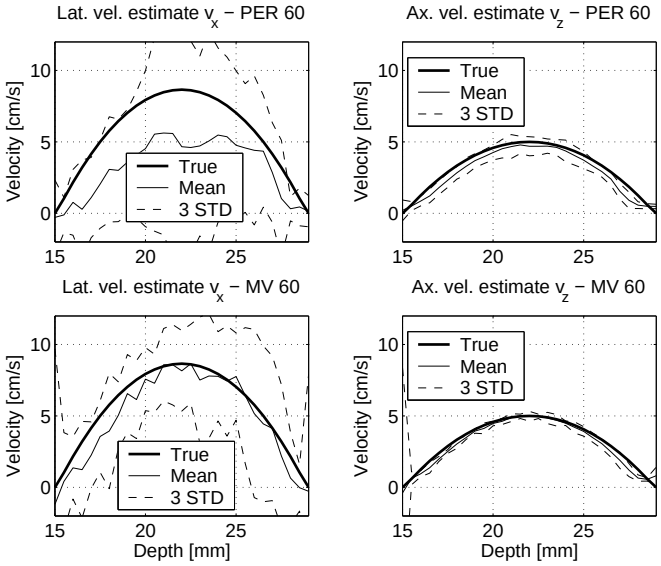

Fig. 4. Phantom measurement at a beam-to-flow angle of $\theta = 60°$. All plots gvie the expected profile (thick solid line), the average of 18 estimated profiles (thin solid line), and the average ± 3 times the standard deviation (dashed line). The top row gives the results from using the Periodogram estimator, while the bottom row gives the results from the Minimum Variance estimator. The left column is the lateral velocity estimates, while the right column is the axial velocity estimates.

Fig. 4 through 6 reveal a better performance in estimating the axial velocity component (right column) than in estimating the lateral velocity component (left column). Furthermore, there seems to be a tendency that both estimators perform better as the beam-to-flow angle approaches $\theta = 90°$.

To compare the estimators across the three beam-to-flow angles, two performance measures are defined. The first is the average standard deviation (ASD) defined as

$$ASD = \frac{\sqrt{\sum_{k=k_{min}}^{k_{max}} [std(k\Delta z)]^2}}{v_0} \cdot 100\%, \tag{30}$$

where k_{min} is the first estimate within the tube, k_{max} is the last estimate within the tube, and $\Delta z = 0.5$ mm is the axial distance between the velocity estimates. $v_0 = 10$ cm/s is the peak velocity of the flow. The second performance measure is the average bias (AB) defined as

$$AB = \frac{\sum_{k=k_{min}}^{k_{max}} \bar{v}(k\Delta z) - v_{exp}(k\Delta z)}{v_0} \cdot 100\%, \tag{31}$$

where $v_{exp}(z) = v_x(z)$ or $v_z(z)$ is the expected profile. Table II summarizes the performance measures for all three beam-to-flow angles and both velocity estimators.

The results from Table II have been plotted in Fig. 7. The top left plot shows the average standard deviation (ASD) of (30) for the lateral velocity estimates as a function of beam-to-flow angle. The results for the periodogram estimator is

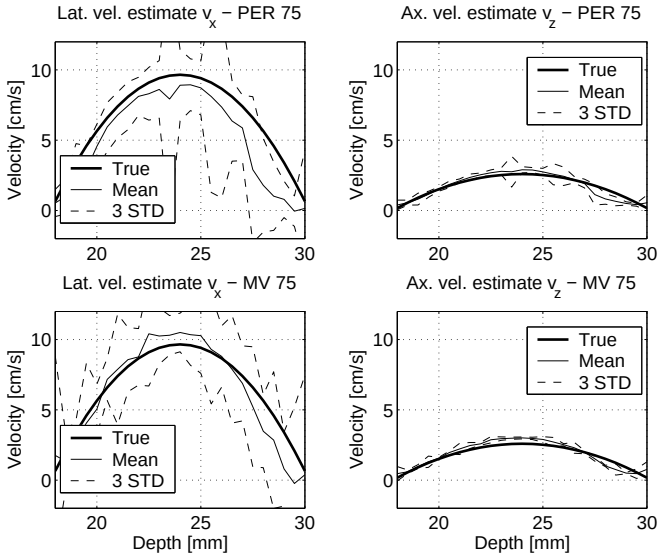

Fig. 5. Phantom measurement at a beam-to-flow angle of $\theta = 75°$. The plots are organized as in Fig. 4.

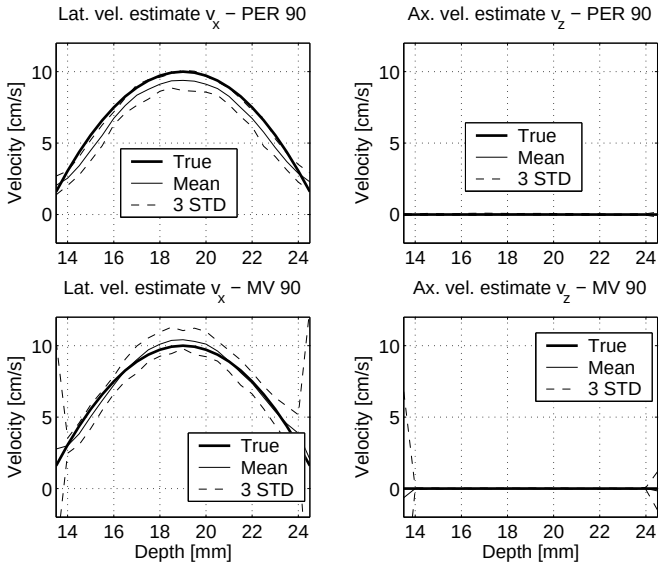

Fig. 6. Phantom measurement at a beam-to-flow angle of $\theta = 90°$. The plots are organized as in Fig. 4.

TABLE II

AVERAGE STANDARD DEVIATION (ASD) AND AVERAGE BIAS (AB) ACROSS PROFILE, GIVEN IN % OF PEAK VELOCITY $v_0 = 10$ CM/S. RESULTS ARE GIVEN FOR BOTH THE PERIODOGRAM ESTIMATOR (PER) AND THE MINIMUM VARIANCE ESTIMATOR (MV).

ASD				
Angle, θ	PER v_x	PER v_z	MV v_x	MV v_z
$60°$	16.4%	1.7%	14.2%	2.0%
$75°$	11.5%	1.1%	11.8%	0.7%
$90°$	2.1%	0.2%	9.4%	1.4%
AB				
Angle, θ	PER v_x	PER v_z	MV v_x	MV v_z
$60°$	-23.6%	-3.4%	-7.2%	-1.9%
$75°$	-14.1%	0.1%	-2.1%	1.4%
$90°$	-5.8%	0.1%	1.3%	-0.3%

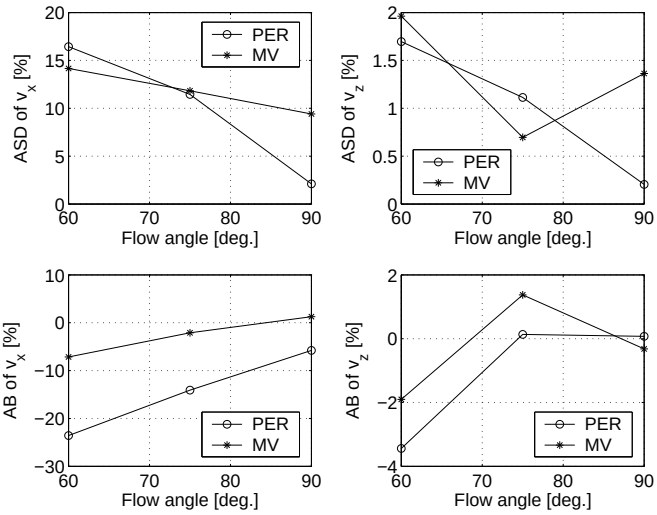

Fig. 7. Performance of the two estimators at different beam-to-flow angles, corresponding the Table II. The top row gives the average standard deviation (ASD) for the lateral velocity estimates (left) and the axial velocity estimates (right). The bottom row gives the average bias (AB) for the lateral velocity estimates (left) and the axial velocity estimates (right). The results using the periodogram estimator is marked by a circle, while the results from the Minimum Variance estimator is marked by a star.

marked by circles (○), while the results using the minimum variance estimator is marked by stars (*). The top right plot of Fig. 7 shows the average standard deviation (ASD) of the axial velocity estimates. The bottom left plot shows the average bias (AB) of (31) for the lateral velocity estimates, while the bottom right plot shows the average bias (AB) of the axial velocity estimates.

From Fig. 7 it becomes clear, that the axial velocity estimates show both lower standard deviation and lower bias than the lateral velocity estimates. The difference is on the order of a magnitude. Also, both the standard deviation and the bias drops as the beam-to-flow angle approaches $90°$ (transverse flow). The only exception is the average standard deviation (ASD) of the axial velocity estimates (top right plot) at $90°$ using the minimum variance estimator, which is higher than that at $75°$. Referring to the bottom left plot of Fig 6, the increased standard deviation in this particular case comes from the outermost part of the tube, where the flow is very low.

Comparing the two estimators in Fig. 7, the average standard deviation (ASD) does not differ significantly (top row of Fig. 7), except for the $\theta = 90°$ experiment, where the periodogram estimator experiences a lower ASD than the minimum variance estimator. Nevertheless, the average bias of the lateral velocity estimates (bottom left) is much larger for the periodogram estimator, than for the minimum variance estimator.

None of the two estimators from Section III therefore outperform the other, since the performance is dependent on the measurement situation and the performance measure chosen.

VII. IN-VIVO MEASUREMENT

An *in-vivo* measurement has been performed using the proposed method. The common carotid artery of a healthy

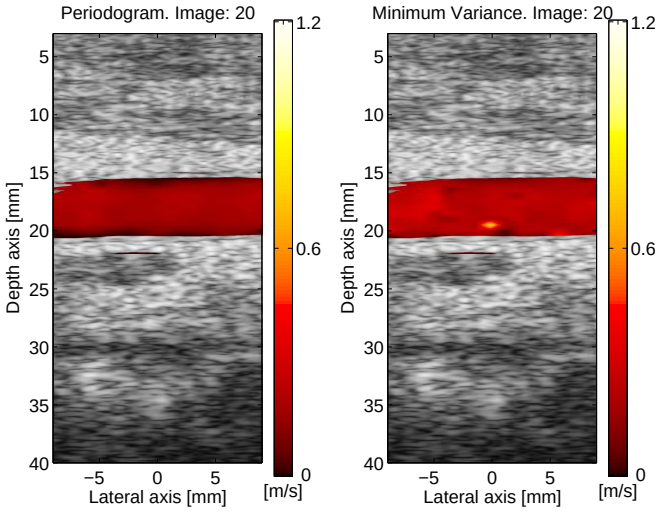

Fig. 8. Color flow map of the common carotid artery of a healthy male volunteer during diastole. The leftmost part shows the magnitude of the velocity estimates found using the periodogram estimator, while the rightmost part shows that using the minimum variance estimator.

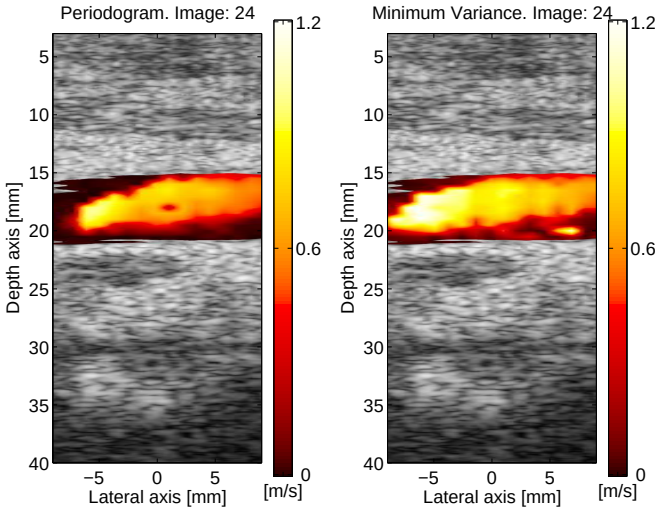

Fig. 9. Color flow map of the common carotid artery of a healthy male volunteer during systole. The leftmost part shows the magnitude of the velocity estimates found using the periodogram estimator, while the rightmost part shows that using the minimum variance estimator.

32-year-old male volunteer was scanned for 3 seconds using our RASMUS experimental ultrasound scanner [20] and the same linear array transducer as for the phantom measurements. The parameters were the same as in Table I, except the pulse repetition frequency was set at $f_{prf} = 6$ kHz. The vector velocities were estimated from 32 repeated emissions along 17 different lines, 1.2 mm apart. Along each line, the vector velocity was estimated at every 0.5 mm in depth. A B-mode image was created from the same data, using a single Hamming window as receive apodization. From the vector velocity estimates, the velocity magnitude $|\hat{v}| = \sqrt{\hat{v}_x^2 + \hat{v}_z^2}$ was found, and a color flow map (CFM) was created showing both the B-mode image at 40 dB dynamic range (black and white) and the velocity magnitude from 0 to 1.2 m/s (color). A CFM from the diastolic period is shown in Fig. 8. The left part of Fig. 8 shows the CFM created using the periodogram estimator from Section III-A, while the rightmost plot of Fig. 8 shows the CFM using the minimum variance estimator from Section III-B. Note that no post processing of the velocity estimates has been performed.

Fig. 8 confirms the tendency from the phantom measurements. A few false estimates are seen using the minimum variance estimator, corresponding to an increased standard deviation.

Fig. 9 shows a CFM of the common carotid artery during systole. The estimated velocities now peak around 1.1 m/s. In the leftmost part of the common carotid a few high velocity estimates are missing, especially using the periodogram estimator. Nevertheless, both estimators seem to perform well at a large velocity range under *in-vivo* conditions.

VIII. Conclusion

This paper has shown that when data are sampled in a rectangular spatial window over time, a single velocity component is concentrated along a plane in the three-dimensional power spectrum spanned by lateral, axial, and temporal frequencies. The plane will be tilted according to the lateral and axial velocity components. Two estimators were derived for finding the two velocity components, the first based on the periodogram and the second on minimum variance.

Both estimators were tested on measured phantom data for beam-to-flow angles of $60°$, $75°$, and $90°$. The axial velocity estimates showed a standard deviation and bias an order of magnitude below that of the lateral velocity estimates, and the performance of the vector velocity estimators was increased as the beam-to-flow angle approached $90°$.

An *in-vivo* transverse scan of the common carotid artery was performed, showing the potential of the method under *in-vivo* conditions.

Acknowledgement

This work was supported by grant 26-04-0024 from the Danish Science Foundation and by B-K Medical, Herlev, Denmark. The authors wish to thank MD Kristoffer Lindskov Hansen, University Hospital of Copenhagen, Denmark, for performing the *in-vivo* scan.

References

[1] C. Kasai, K. Namekawa, A. Koyano, and R. Omoto. Real-time two-dimensional blood flow imaging using an autocorrelation technique. *IEEE Trans. Son. Ultrason.*, 32:458–463, 1985.

[2] O. Bonnefous and P. Pesqué. Time domain formulation of pulse-Doppler ultrasound and blood velocity estimation by cross correlation. *Ultrason. Imaging*, 8:73–85, 1986.

[3] K. W. Ferrara and V. R. Algazi. A new wideband spread target maximum likelihood estimator for blood velocity estimation – Part I: Theory. *IEEE Trans. Ultrason., Ferroelec., Freq. Contr.*, 38:1–16, 1991a.

[4] K. W. Ferrara and V. R. Algazi. A new wideband spread target maximum likelihood estimator for blood velocity estimation – Part II: Evaluation of estimators with experimental data. *IEEE Trans. Ultrason., Ferroelec., Freq. Contr.*, 38:17–26, 1991b.

[5] L. S. Wilson. Description of broad-band pulsed Doppler ultrasound processing using the two-dimensional Fourier transform. *Ultrason. Imaging*, 13:301–315, 1991.

[6] H. Torp and K. Kristoffersen. Velocity matched spectrum analysis: A new method for suppressing velocity ambiguity in pulsed-wave doppler. *Ultrasound Med. Biol.*, 21(7):937–944, 1995.

[7] M. E. Allam and J. F. Greenleaf. Isomorphism between pulsed-wave doppler ultrasound and direction-of-arrival estimation - part i: Basic principles. *IEEE Trans. Ultrason., Ferroelec., Freq. Contr.*, 43:911–922, 1996.

[8] M. E. Allam, R. R. Kinnick, and J. F. Greenleaf. Isomorphism between pulsed-wave doppler ultrasound and direction-of-arrival estimation - part ii: Experimental results. *IEEE Trans. Ultrason., Ferroelec., Freq. Contr.*, 43:923–935, 1996.

[9] H. Krim and M. Viberg. Two decades of array signal processing research. *IEEE Signal Processing Magazine*, 13:67–94, July 1996.

[10] M. D. Fox. Multiple crossed-beam ultrasound Doppler velocimetry. *IEEE Trans. Son. Ultrason.*, SU-25:281–286, 1978.

[11] P. Munk. Estimation of the 2-D flow vector in ultrasonic imaging: a new approach. Master's thesis, Department of Information Technology, Technical University of Denmark, 1996.

[12] J. A. Jensen and P. Munk. A new method for estimation of velocity vectors. *IEEE Trans. Ultrason., Ferroelec., Freq. Contr.*, 45:837–851, 1998.

[13] J. A. Jensen. A new estimator for vector velocity estimation. *IEEE Trans. Ultrason., Ferroelec., Freq. Contr.*, 48(4):886–894, 2001.

[14] M. E. Anderson. Spatial quadrature: a novel technique for multi-dimensional velocity estimation. In *Proc. IEEE Ultrason. Symp.*, volume 45, pages 1233–1238, 1997.

[15] G. E. Trahey, J. W. Allison, and O. T. von Ramm. Angle independent ultrasonic detection of blood flow. *IEEE Trans. Biomed. Eng.*, BME-34:965–967, 1987.

[16] D. H. Johnson and D. E. Dudgeon. *Array signal processing. Concepts and techniques.* Prentice-Hall., Englewood Cliffs, New Jersey, 1993.

[17] J. Udesen and J. A. Jensen. Investigation of transverse oscillation method. *IEEE Trans. Ultrason., Ferroelec., Freq. Contr.*, 53:959–971, 2006.

[18] J. A. Jensen and N. B. Svendsen. Calculation of pressure fields from arbitrarily shaped, apodized, and excited ultrasound transducers. *IEEE Trans. Ultrason., Ferroelec., Freq. Contr.*, 39:262–267, 1992.

[19] J. A. Jensen. Field: A program for simulating ultrasound systems. *Med. Biol. Eng. Comp.*, 10th Nordic-Baltic Conference on Biomedical Imaging, Vol. 4, Supplement 1, Part 1:351–353, 1996b.

[20] J. A. Jensen, O. Holm, L. J. Jensen, H. Bendsen, S. I. Nikolov, B. G. Tomov, P. Munk, M. Hansen, K. Salomonsen, J. Hansen, K. Gormsen, H. M. Pedersen, and K. L. Gammelmark. Ultrasound research scanner for real-time synthetic aperture image acquisition. *IEEE Trans. Ultrason., Ferroelec., Freq. Contr.*, 52 (5):881–891, May 2005.

A.5 Oddershede, N. and Jensen, J. A.,
Experimental investigation of synthetic aperture flow angle estimation, ***Proceedings of SPIE Medical Imaging 2005, volume 5750, pp. 417-26.***

Experimental investigation of synthetic aperture flow angle estimation

Niels Oddershede and Jørgen Arendt Jensen

Center for Fast Ultrasound Imaging, Ørsted•DTU, Build. 348,
Technical University of Denmark, 2800 Kgs. Lyngby, Denmark

ABSTRACT

Currently synthetic aperture flow methods can find the correct velocity magnitude, when the flow direction is known. To make a fully automatic system, the direction should also be estimated. Such an approach has been suggested by Jensen (2004) based on a search of the highest cross-correlation as a function of velocity and angle. This paper presents an experimental investigation of this velocity angle estimation method based on a set of synthetic aperture flow data measured using our RASMUS experimental ultrasound system. The measurements are performed for flow angles of 60°, 75°, and 90° with respect to the axial direction, and for constant velocities with a peak of 0.1 m/s and 0.2 m/s. The implemented synthetic aperture imaging method uses virtual point sources in front of the transducer, and recursive imaging is used to increase the data rate. A 128 element linear array transducer is used for the experiments, and the emitted pulse is a 20μs chirp, linearly sweeping frequencies from approximately 3.5 to 10.5 MHz. The flow angle could be estimated with an average bias up to 5.0°, and a average standard deviation between 0.2° and 5.2°. Using the angle estimates, the velocity magnitudes were estimated with average standard deviations no higher than 6.5% relative to the peak velocity.

Keywords: Ultrasound, synthetic aperture, blood flow velocity, velocity angle estimation.

1. INTRODUCTION

Conventional ultrasound velocity estimation systems are limited to estimating velocities projected onto the direction of the emitted ultrasound beam, so that an angle-dependent fraction of the actual velocity magnitude is found. Furthermore, in cases where the direction of blood flow is perpendicular to the ultrasound beam, no velocity is found. A significant gain in diagnosis will probably be attained, if blood flow velocities could be estimated in any given direction.

To find the velocity vector within the imaging plane, various approaches have been investigated. For instance, introducing oscillations in the lateral direction have been tried,[2] estimating both the axial and lateral projection of the velocity.

Throughout the years, synthetic transmit aperture (STA) methods have been investigated for ultrasound imaging. STA imaging is done by emitting unfocused beams and receiving with a large aperture. Dynamic receive focussing is applied using time-of-flight considerations to calculate receive delays, and transmit focussing is done by summing data for a number of emissions using different transmitting elements. This method has the advantages of continuous availability of data, and the ability to beamform data along any direction.[3] It has previously been shown[4,5] that using STA imaging, the flow velocity magnitude can be estimated, provided the flow angle is known. This is done by cross-correlating lines beamformed along the direction of flow, finding the spatial movement within a time interval.

Jensen (2004) has shown that it is possible, using synthetic aperture flow, to find the blood flow velocity vector within the two-dimensional imaging plane, and the article furthermore presented a method for finding this vector. The method is based on a search for the highest cross-correlation as a function of angle, using that de-correlation will be lowest for the direction of flow. This paper presents an experimental investigation of this method under a number of measurement conditions.

Send correspondence to Niels Oddershede, E-mail: no@oersted.dtu.dk

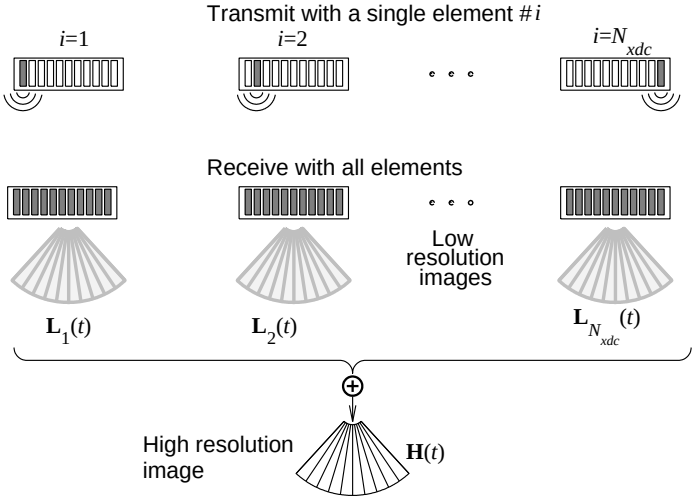

Figure 1. The principle of synthetic transmit aperture ultrasound imaging.[5] Every transmission is done by emitting with one transducer element and receiving with all. After every emission a low resolution image (LRI) is created. The emission is repeated for a number of different elements, and the resulting LRIs are summed to form a high resolution image.

2. METHOD

This section explains the principles of the implemented method. Section 2.1 concentrates on the imaging method, describing the excitation, emission sequence and other details, while Section 2.2 explains the method for determining the velocity angle.

2.1. Imaging method

In STA ultrasound the transmitting aperture emits an unfocused wave and receives with a large number of elements. This unfocused wave can be created by emitting with only one element as seen in Fig. 1. After every emission a low resolution image (LRI) can be created using delay-and-sum beamforming, where the delays are found by calculating the time of flight from the emitting element to the focus point and back to the receiving element. This image is focused only in receive, and a high resolution image (HRI) can be formed by emitting with different elements and summing the resulting LRIs.

In the method implemented, 16 transducer elements are used at every emission to create a virtual point source[6,7] in front of the transducer. This point acts as a source emitting higher energy spherical waves within a limited angular extend. The virtual point is located so that the f-number is 1/2, and 64 transducer elements are used in receive. The received echoes from a single transmission can be focused in arbitrary points[8] generating a LRI. The emission is repeated with the next 16 elements a total of eight times until all 128 transducer elements have been used. The 64 receiving elements are slided for each emission centered around the transmitting elements. The emission sequence used is sketched in Fig. 2 which also shows the positioning of the virtual point sources. After eight emissions highly focused directional signals can be made by summing the focused data from the last $N_t = 8$ transmissions

$$y_d(k,\theta) = \sum_{i=1}^{N_t} L_i(\vec{r}_p(k,\theta)), \tag{1}$$

where $\vec{r}_p(k,\theta)$ is a vector of focus points on a line having an angle θ with respect to the axial direction, and $L_i(\vec{r}_p(k,\theta))$ is the received data for emission i focused along the line. Using recursive imaging[9] a new high resolution line can be made after every emission, simply by adding focused data from the new transmission and subtracting that N_t emissions earlier.

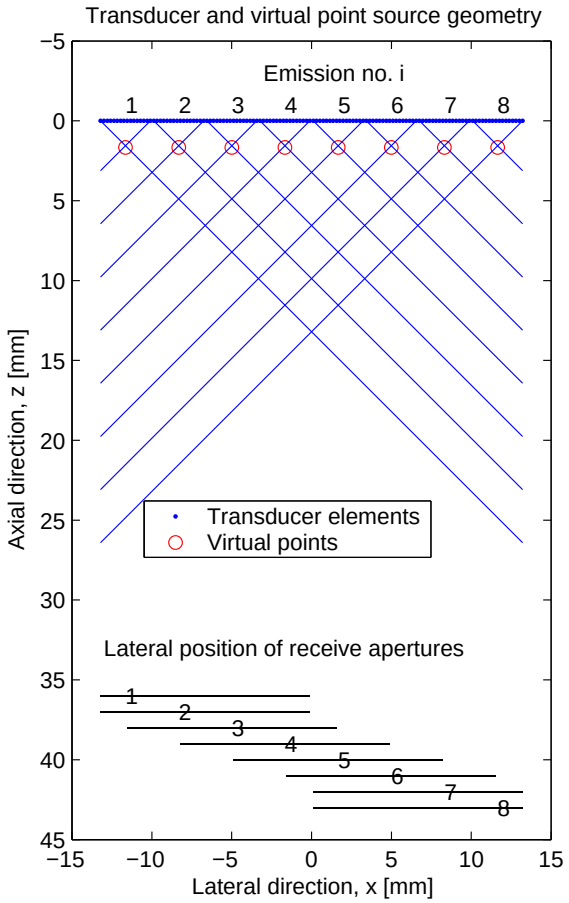

Figure 2: Emission sequence and the geometry of the transducer and virtual points.

The excitation used is a $20\mu s$ chirp, linearly sweeping frequencies from approximately 3.5 to 10.5 MHz. It is amplitude weighted by a Tukey window of a 10% duration.[10] RF sampling is done at a frequency of 40 MHz, and the pulse repetition frequency is set to 3 kHz. Prior to beamforming, a compression filter consisting of the time inverse chirp, amplitude weighted by a Chebychev window with 70 dB relative sidelobe attenuation, is applied. When the velocity angle has been found as described in Section 2.2, the velocity magnitude is determined using the cross-correlation method.[4]

2.2. Velocity angle determination

The received RF data are beamformed along lines having different angles θ_m compared to the axial direction, but all centered in the same point where the velocity angle is to be estimated. Stationary echo cancelling is done on these beamformed data by subtracting the mean of $N_s = 15$ former high resolution images made using the same emissions sequence. This can be expressed as

$$\hat{y}_d^{(n)}(k,\theta_m) = y_d^{(n)}(k,\theta_m) - \frac{1}{N_s}\sum_{i=0}^{N_s-1} y_d^{(n-iN_t)}(k,\theta_m), \tag{2}$$

where $y_d^{(n)}(k,\theta_m)$ is the directional signal at angle θ_m focused after emission n, and $N_t = 8$ is the number of emissions used to create one high resolution image. Cross correlating two echo cancelled high resolution images

over $N_k + 1$ samples, both images acquired using the same emission sequence, gives[8]

$$R_{n-N_t,n}(l,\theta_m) = \frac{1}{N_k+1} \sum_{k=-N_k/2}^{N_k/2} \hat{y}_d^{(n-N_t)}(k,\theta_m)\hat{y}_d^{(n)}(k+l,\theta_m). \tag{3}$$

Using the fact that the cross-correlation between the high resolution images will be largest when beamformed at the actual angle of flow, the angle can be found. At all other angles de-correlation will occur. First the correlation peaks at all angles are found and normalized by the signal power

$$\rho_{n-N_t,n}(\theta_m) = \frac{\max(R_{n-N_t,n}(l,\theta_m))}{\sqrt{R_{n-N_t,n-N_t}(0,\theta_m)R_{n,n}(0,\theta_m)}}, \tag{4}$$

where $\max(R_{n-N_t,n}(l,\theta_m))$ is the maximum value of the cross-correlation function at an angle θ_m, and the denominator is the signal power for the same angle. Assuming the angle of flow does not change significantly over N_c emissions, the average normalized cross-correlation function can be found over this period of time yielding

$$\rho_{av}(\theta_m) = \frac{1}{N_c} \sum_{i=-N_c+1}^{0} \rho_{n-N_t-i,n-i}(\theta_m). \tag{5}$$

In the present implementation the averaging is done over $N_c = 121$ emissions which corresponds to a little more than 40 ms of data for a pulse repetition frequency of $f_{prf} = 3$ kHz. Finding where $\rho_{av}(\theta_m)$ is largest yields the blood flow angle:

$$\theta = \arg\max_{\theta_m} \rho_{av}(\theta_m). \tag{6}$$

To minimize computational time, RF data are beamformed for every $\triangle\theta = 5°$ covering half a circle. This means that $\theta_m = 0, 5, 10, ..., 180°$, which gives the angle estimate θ a poor resolution. The angle found is therefore interpolated by a parabolic approximation[11]

$$\theta_{int} = \theta - \frac{\rho_{av}(\theta+1) - \rho_{av}(\theta-1)}{2(\rho_{av}(\theta+1) - 2\rho_{av}(\theta) + \rho_{av}(\theta-1))}\triangle\theta, \tag{7}$$

where θ is the angle found by (6), $\triangle\theta$ is the angular spacing and θ_{int} gives the interpolated angle.

3. MEASUREMENTS

The measurements are done in a circulating flow rig consisting of a variable speed gear pump (Model 75211-15, made by Cole-Parmer Instrument Company, IL, US) circulating a blood mimicking fluid (made by Danish Phantom Service, Jyllinge, Denmark) within tubes. The fluid consists of water, glycerol, orgasol, Trition x-100, NaBenzoat, and K_2EDTA diluted 10 to 1 with demineralised water. Its viscosity has been measured by an Oswald capillary viscometer to be $2.6 \cdot 10^{-3}$ kg/(m·s). After more than 1 m straight steel tubing with an internal radius of 6.4 mm, the flow enters a tube made of a heat shrinking material having an internal radius of 6.725 mm. In this material the propagation speed of sound has been measured to 1463 m/s, which is close to that seen in water, and its characteristic acoustic impedance is around $1.3 \cdot 10^6$ kg/(m^2·s). The heat shrinking tube is lowered into a water tank. A linear array transducer BK-8804 (made by B-K Medical, Herlev, Denmark) is fixated within the water tank, at a fixed angle relative to the flow direction, using a steel holding device. The tube and fixation device can be seen in Fig. 3.

The measurements are all made using our RASMUS multi-channel sampling system.[12] This system has 128 transmit channels, and can sample 64 channels simultaneously at 40 MHz with 12 bits precision. Imaging is performed as described in Section 2.1. The linear array BK-8804 transducer, which has a center frequency of $f_0 = 7$ MHz, is used. Although this is a 192 element transducer, only the center 128 elements are used due to limitations of the hardware.

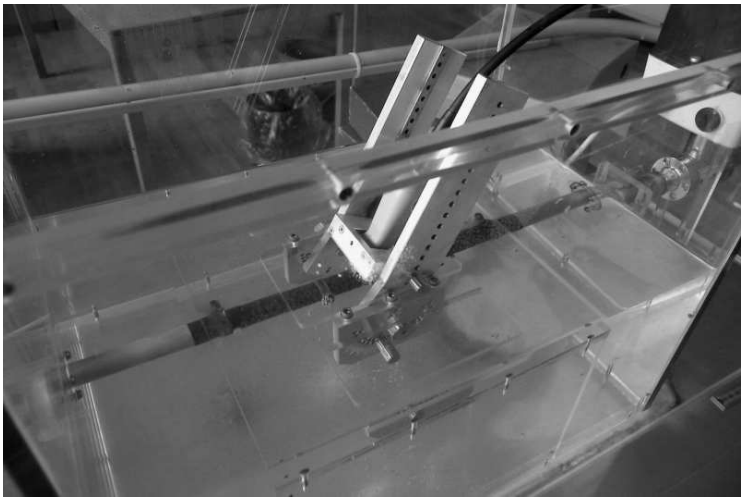

Figure 3. The experimental setup is a transducer fixated within a water tank at a certain angle with respect to a tube. Through the tube a blood mimicking fluid is pumped at a constant velocity.

The measurement is repeated for flow angles of $\theta_{true} = 60°$, 75°, and 90° relative to the axial direction, and for peak velocities around $v_0 = 0.1$ m/s and 0.2 m/s. For each measurement, one second of real-time data is acquired and stored for off-line processing. The velocity profile is assumed parabolic due to a Reynolds number below 2000.[13]

The angle of flow is estimated at a number of points equally spaced by 1 mm in a profile across the tube. For every point, data are beamformed for different angles $\theta_m = 0, 5, 10, ..., 180°$ with respect to the axial direction, yielding the focus points

$$\vec{r}_p(k, \theta_m) = [\Delta r \cdot k \cdot \sin(\theta_m),\ 0,\ \Delta r \cdot k \cdot \cos(\theta_m) + p_z], \tag{8}$$

where $\Delta r = \lambda/20$ is the spatial sampling interval, given the wavelength $\lambda = \frac{c}{f_0} = 0.21$ mm, k takes integer values from -200 to 200, and $p = [0, 0, p_z]$ is the point along the profile where the velocity is estimated. The lines are all 20λ long corresponding to 4.2 mm. After beamformation stationary echo cancelling is done as in (2), and the direction of flow is estimated for positions across the tube profile.

4. RESULTS

This section presents the results from applying the angle determination method to the measured data. All profiles are made at lines following the axial direction, centered at the transducer center, and the direction of flow is estimated for every 1 mm depth. 42.7 ms of data, corresponding to 128 emissions are used to make each angle profile. Figure 4 shows the estimated angles for the $\theta_{true} = 60°$ experiments. The leftmost plots show 10 individual angle profiles made at different time instances, whereas the rightmost plots show the average angle profiles ±3 times the standard deviation. The top row is for a peak velocity of $v_0 = 0.1$ m/s, and the bottom row for $v_0 = 0.2$ m/s. The borders of the tube are marked by vertical lines. It can be seen that well inside the tube none of the angle estimates differ more than ±5° from the average angle estimate, being 56.7° and 57.2° for peak velocities of $v_0 = 0.1$ m/s and $v_0 = 0.2$ m/s, respectively. Compared to $\theta_{true} = 60°$ the angles are determined with a bias, averaged over the tube profile, of $-3.3°$ and $-2.8°$ for peak velocities of $v_0 = 0.1$ m/s and $v_0 = 0.2$ m/s, respectively. The average standard deviation of all angle estimates within the tube are 1.9° and 1.3° for the two different peak velocities. Fig. 5 shows the angle estimates for the $\theta_{true} = 75°$ experiment. Again the top row is for the $v_0 = 0.1$ m/s experiment, and the bottom row for $v_0 = 0.2$ m/s. In both experiments, false angle estimates are seen close to the tube border, and for the $v_0 = 0.2$ m/s experiment, 7 false estimates (defined as being more than ±5° from the mean) are seen close to the vessel center. These all

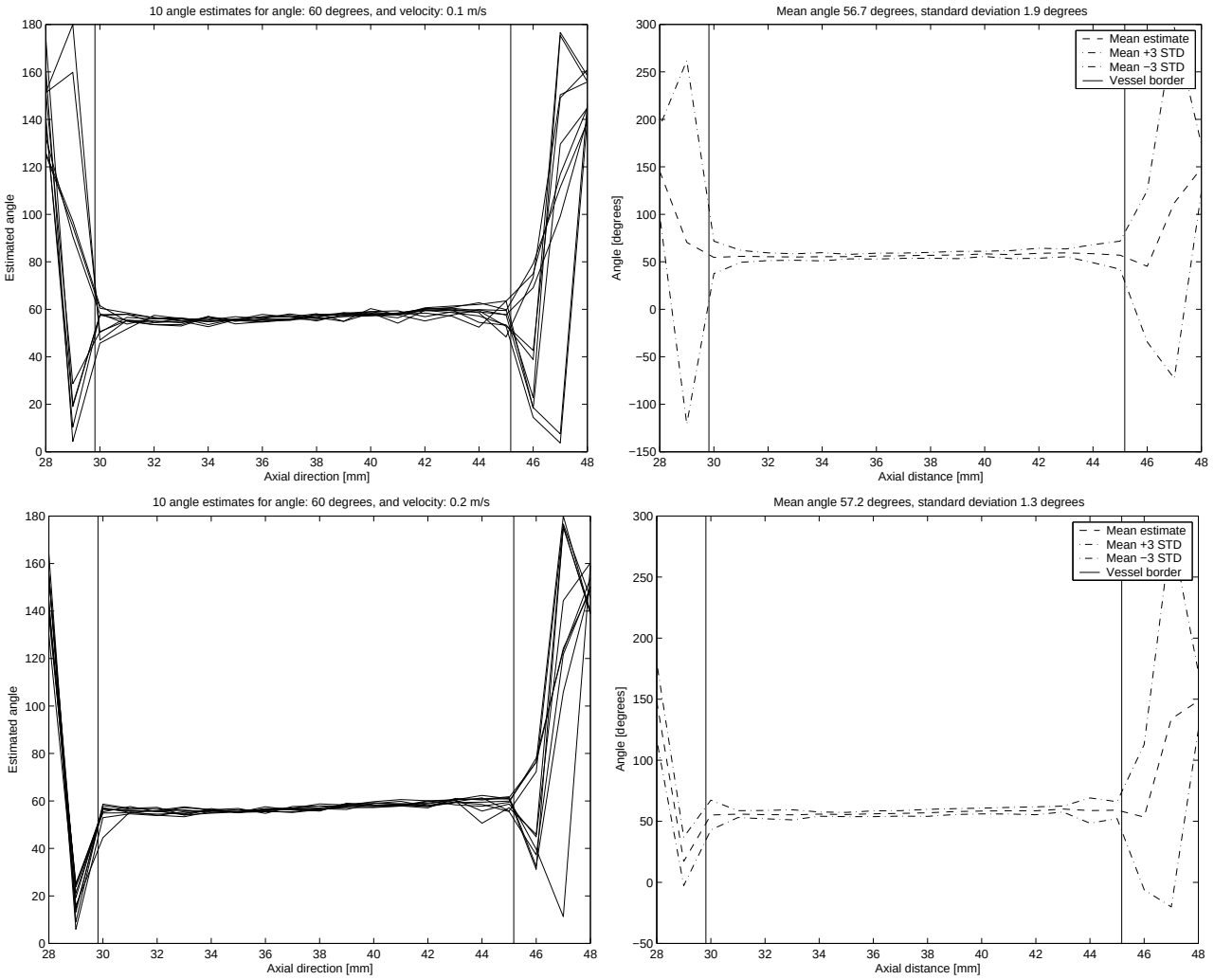

Figure 4. Estimated velocity angles for the $\theta_{true} = 60°$ experiment. The top row show results for $v_0 = 0.1$ m/s and the bottom row for $v_0 = 0.2$ m/s. In the leftmost plots one line is shown for each of 10 independent estimates, and in the rightmost plots the average estimates ± 3 times the standard deviation is shown. The tube borders are marked by vertical lines.

estimate the angle $\approx 85°$. Within the tube the average angle estimated is $70.0°$ and $71.1°$ for peak velocities of $v_0 = 0.1$ m/s and $v_0 = 0.2$ m/s, respectively. The mean biases are $-5.0°$ and $-3.9°$, and the average standard deviation across the profiles are $4.6°$ and $5.2°$. Angle estimates for the $\theta_{true} = 90°$ experiment are shown in Fig. 6. As before, $v_0 = 0.1$ m/s for the top plots, and $v_0 = 0.2$ m/s for the bottom plots. Here no estimates within the vessel differ more than $\pm 5°$ from the average angle estimate, and the flow angle was estimated with a bias of $0.4°$ for $v_0 = 0.1$ m/s, and $-0.2°$ for $v_0 = 0.2$ m/s. The average standard deviation across the profile was $1.1°$ and $0.2°$, respectively.

The performance of the angle estimation method for the 6 different experiments, measured by the angle bias and the average standard deviation of angle estimates across the profile, is shown in Table 1. The results from the $\theta_{true} = 75°$ experiments are inferior to those seen for the $\theta_{true} = 60°$ and $\theta_{true} = 90°$ experiments. The reason for this can be found in a 10 times lower front-end amplification used for the $\theta_{true} = 75°$ experiments, resulting in a lower signal-to-noise ratio. This makes direct comparison of these results unfair, although it shows the method

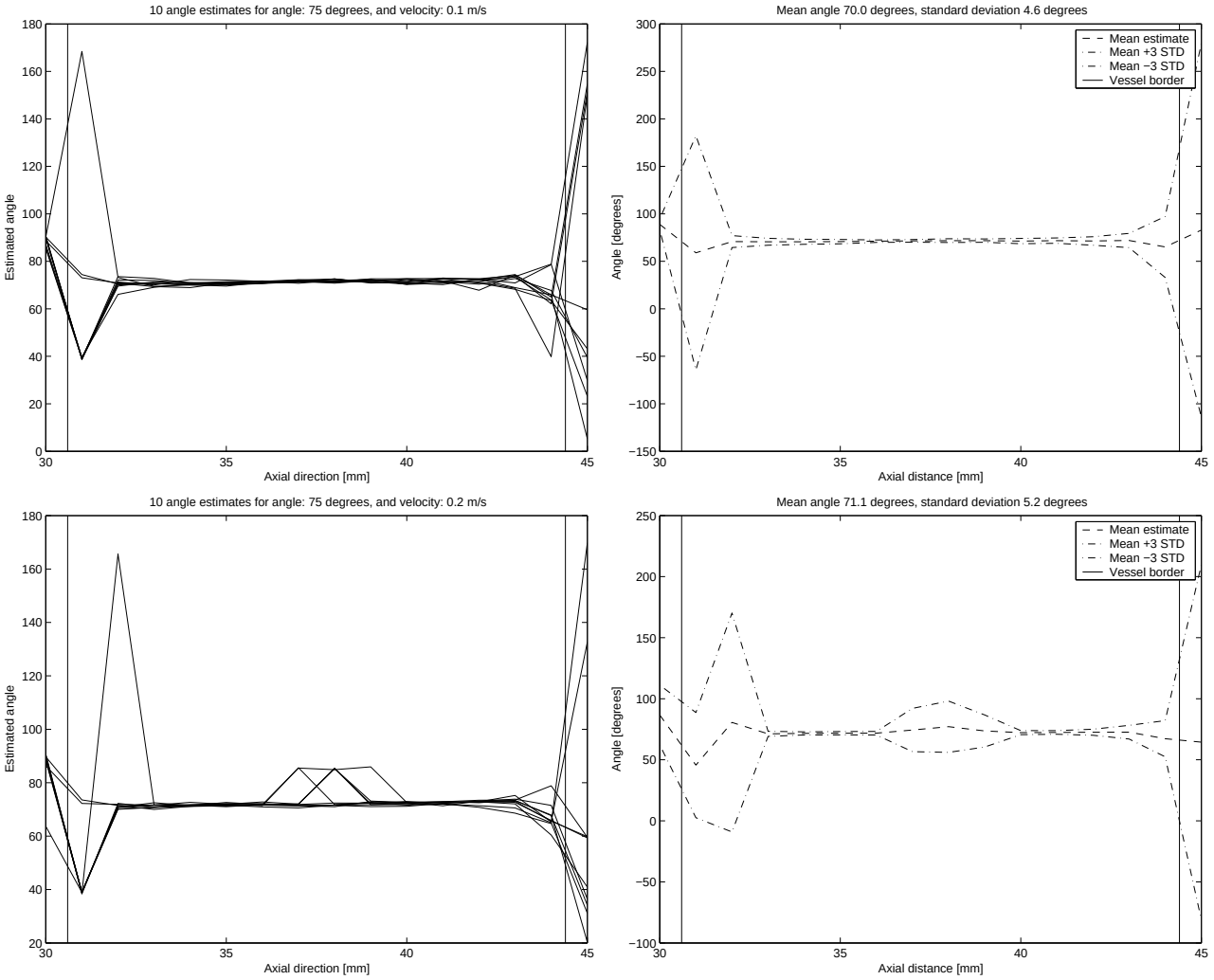

Figure 5. Estimated velocity angles for the $\theta_{true} = 75^\circ$ experiment. The top row show results for $v_0 = 0.1$ m/s and the bottom row for $v_0 = 0.2$ m/s. In the leftmost plots one line is shown for each of 10 independent estimates, and in the rightmost plots the average estimates ± 3 times the standard deviation is shown. The tube borders are marked by vertical lines.

Table 1: Average angle estimate and average standard deviation of angle estimates across profile.

True Angle [°]	Peak Velocity [m/s]	Mean angle [°]	Angle bias [°]	Standard deviation [°]
60	0.1	56.7	−3.3	1.9
60	0.2	57.2	−2.8	1.3
75	0.1	70.0	−5.0	4.6
75	0.2	71.1	−3.9	5.2
90	0.1	90.4	+0.4	1.1
90	0.2	89.8	−0.2	0.2

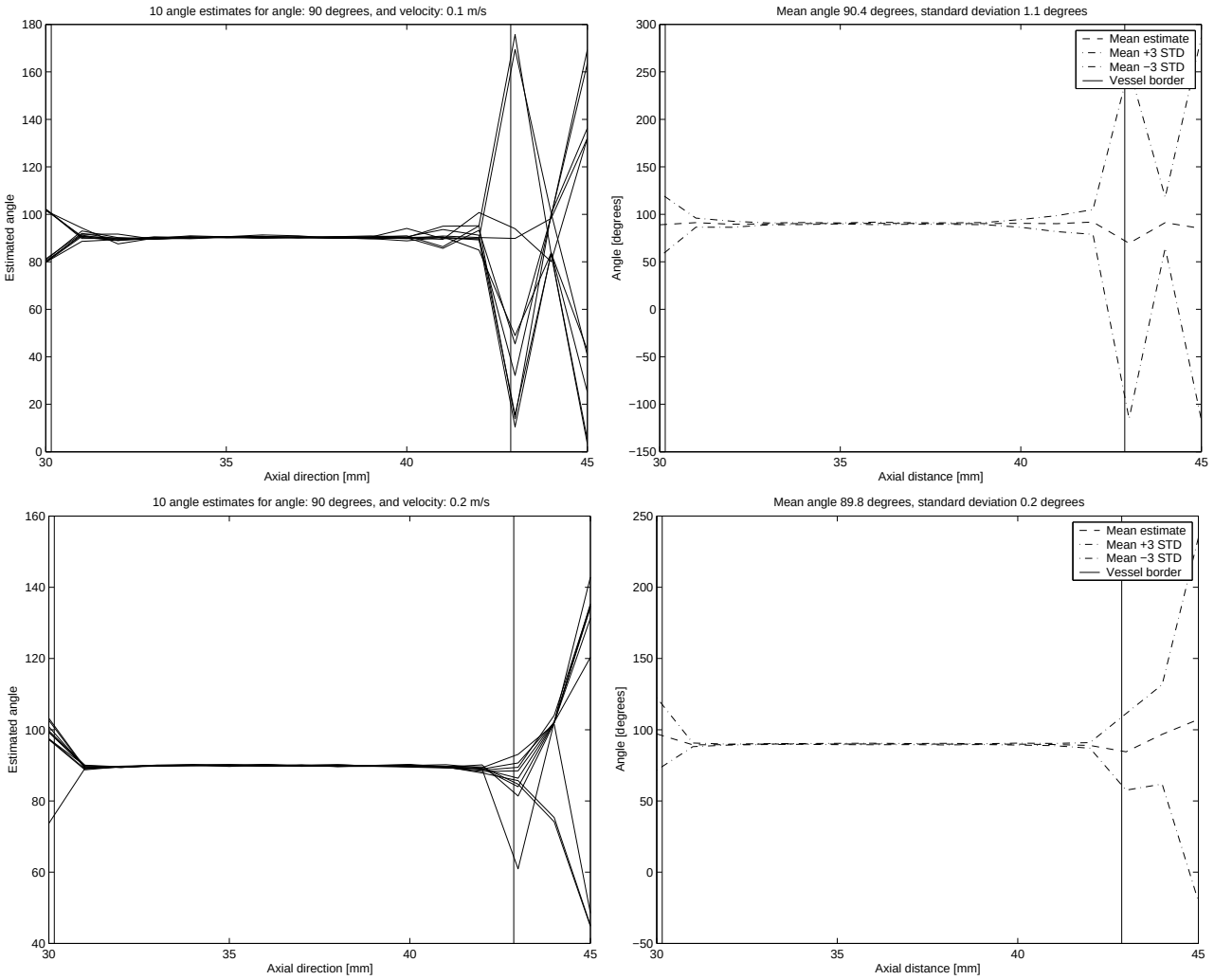

Figure 6. Estimated velocity angles for the $\theta_{true} = 90°$ experiment. The top row show results for $v_0 = 0.1$ m/s and the bottom row for $v_0 = 0.2$ m/s. In the leftmost plots one line is shown for each of 10 independent estimates, and in the rightmost plots the average estimates ± 3 times the standard deviation is shown. The tube borders are marked by vertical lines.

dependency on a good signal-to-noise ratio. Slightly better results are seen for the $\theta_{true} = 90°$ experiments than for the $\theta_{true} = 60°$ experiments. Furthermore there seems to be a tendency for better results when $v_0 = 0.2$ m/s, probably due to a larger de-correlation at wrong angles.

The estimated flow angles were used for velocity magnitude estimation,[14] which is done using the cross-correlation between two high resolution lines made using the same emission sequence. The cross-correlation functions are averaged over $N_c = 121$ emissions and the lag of maximum correlation is found. This spatial movement is divided by elapsed time to yield the velocity magnitude. Figure 7 shows velocity profiles for the six different experiments where the velocity magnitudes are estimated along the directions found by (7). Here the average of 10 independent profiles ± 3 times the standard deviation is compared to the true profile. The average standard deviation of the velocity magnitude estimates are between 1.2% and 6.5% of the peak velocity, where the maximum is found for the $\theta_{true} = 75°$ experiments.

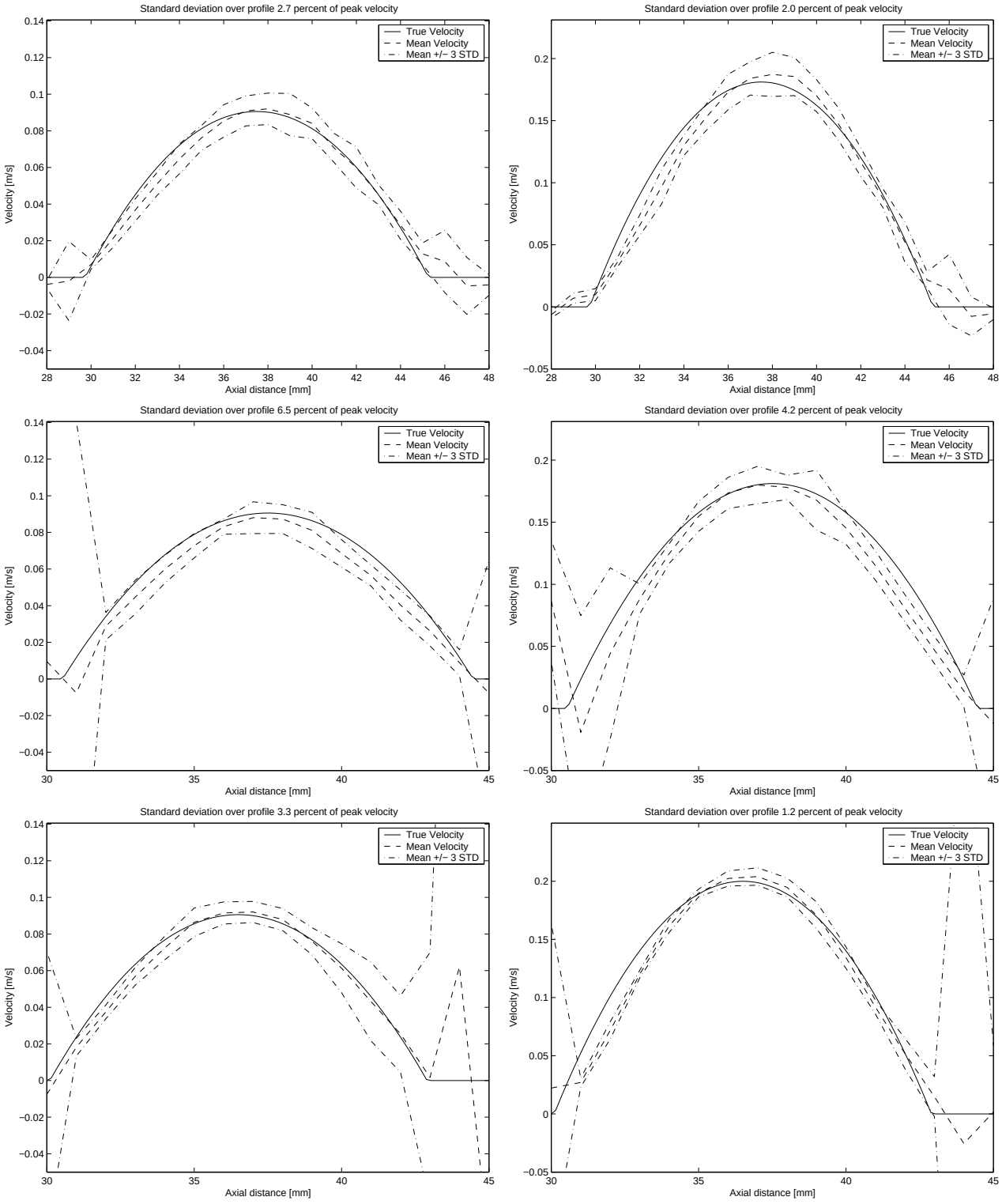

Figure 7. Average velocity profiles ± 3 times the standard deviation for the six experiments, compared to the true velocity profile. The top row shows the velocity profiles for the $\theta_{true} = 60^\circ$ experiments, middle row is for $\theta_{true} = 75^\circ$, and bottom row is for $\theta_{true} = 90^\circ$. The velocity magnitudes are estimated along the directions found by (7).

5. CONCLUSION

The described method for angle determination in synthetic aperture flow imaging was tested on a series of measurements, having different directions of flow and different velocity magnitudes. Angles of 60°, 75°, and 90° and peak velocities of 0.1 and 0.2 m/s were used. Angles were estimated with average biases no higher than 5.0° and average standard deviation between 0.2° and 5.2°. The highest both bias and standard deviation was seen for the 75° experiment, probably due to a lower signal-to-noise ratio than seen in the other experiments. Using the estimated angles, the velocity magnitude was estimated across the tube profiles. These were found with a average standard deviation within the tube of 1.2% to 6.5% relative to peak velocity.

REFERENCES

1. J. A. Jensen, "Velocity vector estimation in synthetic aperture flow and B-mode imaging," in *IEEE International Symposium on Biomedical imaging from nano to macro*, pp. 32–35, 2004.
2. J. A. Jensen and P. Munk, "A new method for estimation of velocity vectors," *IEEE Trans. Ultrason., Ferroelec., Freq. Contr.* **45**, pp. 837–851, 1998.
3. M. Karaman, P. C. Li, and M. O'Donnell, "Synthetic aperture imaging for small scale systems," *IEEE Trans. Ultrason., Ferroelec., Freq. Contr.* **42**, pp. 429–442, 1995.
4. J. A. Jensen and S. I. Nikolov, "Transverse flow imaging using synthetic aperture directional beamforming," in *Proc. IEEE Ultrason. Symp.*, pp. 1488–1492, 2002.
5. S. I. Nikolov and J. A. Jensen, "In-vivo synthetic aperture flow imaging in medical ultrasound," *IEEE Trans. Ultrason., Ferroelec., Freq. Contr.* , pp. 848–856, 2003.
6. M. H. Bae, M. K. Jeong, T. K. Song, and Y. B. Ahn, "Experimental study of transmit synthetic focusing combined with receive dynamic focusing in B-mode ultrasound imaging systems," in *Proc. IEEE Ultrason. Symp.*, pp. 1261–1264, 1999.
7. S. I. Nikolov and J. A. Jensen, "Comparison between different encoding schemes for synthetic aperture imaging," in *Proc. SPIE - Progress in biomedical optics and imaging*, **3**, pp. 1–12, 2002.
8. J. A. Jensen and S. I. Nikolov, "Directional synthetic aperture flow imaging," *IEEE Trans. Ultrason., Ferroelec., Freq. Contr.* , pp. 1107–1118, 2004.
9. S. I. Nikolov, K. Gammelmark, and J. A. Jensen, "Recursive ultrasound imaging," in *Proc. IEEE Ultrason. Symp.*, **2**, pp. 1621–1625, 1999.
10. T. Misaridis, *Ultrasound imaging using coded signals.* PhD thesis, Ørsted•DTU, Technical University of Denmark, Lyngby, Denmark, 2001.
11. S. G. Foster, *A pulsed ultrasonic flowmeter employing time domain methods.* PhD thesis, Dept. Elec. Eng., University of Illinois, Urbana, Ill., 1985.
12. J. A. Jensen, O. Holm, L. J. Jensen, H. Bendsen, H. M. Pedersen, K. Salomonsen, J. Hansen, and S. Nikolov, "Experimental ultrasound system for real-time synthetic imaging," in *Proc. IEEE Ultrason. Symp.*, **2**, pp. 1595–1599, 1999.
13. D. J. Acheson, *Elementary Fluid Dynamics*, Clarendon Press, Oxford, 1990.
14. S. I. Nikolov and J. A. Jensen, "Velocity estimation using synthetic aperture imaging," in *Proc. IEEE Ultrason. Symp.*, pp. 1409–1412, 2001.

A.6 Oddershede, N. and Jensen, J. A.,
Synthetic aperture flow angle estimation on in-vivo data from the common carotid, ***Proceedings of IEEE Ultrasonics Symposium 2005, pp. 1331-34.***

Synthetic aperture flow angle estimation on in-vivo data from the carotid artery

Niels Oddershede and Jørgen Arendt Jensen
Center for Fast Ultrasound Imaging, Ørsted•DTU, Build. 349,
Technical University of Denmark, DK-2800 Lyngby, Denmark

Abstract— **In conventional ultrasound velocity estimation systems only the velocity projected onto the direction of the steered ultrasound beam is found. It has previously been shown how true blood flow velocity magnitudes can be found using synthetic transmit aperture imaging. The method is based on cross-correlation between lines beamformed along the flow direction. This method assumes the direction of flow is known.**

Jensen (2004) presented a method for estimating the direction of flow [1]. The angle determination method is based on a search for the maximum normalized cross-correlation as a function of angle. It assumes the largest correlation is seen for the angle of flow. Previously, this method has only been validated using data from a circulating flow rig. This paper presents an In-Vivo investigation of the method.

Real time data covering 2.2 seconds of the carotid artery of a healthy 30-year old male volunteer is acquired and then processed off-line using a large computer cluster.

Data are acquired using our RASMUS experimental ultrasound scanner and a 128 element 6.2 MHz linear array transducer. A 20 μs chirp was used during emission and virtual transmit sources were created behind the transducer using 11 transmitting elements. Data from 8 transmissions with each 64 receiving elements are beamformed and coherently summed to create high resolution lines at different angles for a set of points within the region of flow. The pulse repetition frequency was set to 10 kHz.

The direction of flow is estimated using the above mentioned method. It is compared to the flow angle of 106° with respect to the axial direction, determined visually from the B-mode image. For a point in the center of the common carotid artery, 76 % of the flow angle estimates over the 2.2 seconds were within $\pm 10^\circ$ of the visually determined flow angle. The standard deviation of these estimates was below 2.7°.

Full color flow maps from different parts of the cardiac cycle are presented, including vector arrows indicating both estimated flow direction and velocity magnitude.

I. Introduction

Conventional velocity estimation systems are based on emitting a number of focused pulses in the same direction and finding either the spatial shift [2] or the change in phase [3] between emissions. To make a full color flow map this process must be repeated for a number of lines, and a different sequence is used to make a B-mode image, limiting the frame rate of the system.

Both methods have the severe limitation of only estimating a projection of the actual velocity onto the direction of the steered ultrasound beam. Therefore no velocity is estimated when the flow is perpendicular to the emitted ultrasound beam. In a clinical environment this is often solved by tilting the transducer, which might result in poor contact between the transducer and skin surface, or pressure might be applied to the vessel under investigation and change the flow.

In 2004 Pedersen et. al. showed that the use of synthetic aperture ultrasound imaging techniques can potentially improve the diagnostic value of ultrasound imaging [4]. Significant increase in both penetration depth and image quality was seen compared to conventional ultrasound imaging. In synthetic aperture imaging, data from the whole imaging area is sampled simultaneously, giving a frame rate equal to the pulse repetition frequency [5].

A method for velocity estimation using synthetic aperture imaging was presented in [6] and validated on both phantom measurements and in-vivo data. The method was based on cross-correlating lines beamformed along the flow direction. The flow direction was here determined visually from the B-mode images.

To make a fully autonomous velocity estimation system, a method for automatically detecting the direction of flow was needed. In 2004 Jensen presented a method for automatically determining the angle of flow within the imaging plane [1]. The method was based on finding the angle of maximum normalized cross-correlation. The method was validated using data from a circulating flow rig at flow angles of 60° and 90° relative to the axial direction.

In this paper, the angle determination method is applied to a set of in-vivo data from the common carotid artery of a 30-year-old healthy male, and full 2-D vector velocity images are shown from different parts of the cardiac cycle.

II. Theory

Synthetic transmit aperture imaging is based on emitting a spherical wave from either one or a collection of transducer elements [7], [8]. Echoes are received using all transducer elements and focused dynamically, creating a low resolution image. The process is repeated using K different sets of transmitting elements, and the resulting low resolution images are summed to form a high resolution image, yielding dynamic focus in both transmit and receive. Using recursive imaging methods [5], a high resolution image can be created after every emission.

Due to this continuous availability of data and the dynamic focus in both transmit and receive, data can be beamformed along any direction at a very high data rate. This is used for determining the flow direction and velocity.

For every point $\vec{p_0}$ where the velocity direction and magnitude is estimated, a number of lines $\vec{p_\theta}(n)$ are beamformed through the point at different angles

$$\vec{p_\theta}(n) = \vec{p_0} + \Delta x[\sin\theta, 0, \cos\theta](n - \frac{N}{2}), \quad (1)$$

where $n = [0, 1, ..., N]$, $\theta = [0, \Delta\theta, 2\Delta\theta, ..., 180°]$ are the angles with respect to the beam axis z, and Δx is the spatial sampling distance. Figure 1 shows one of the lines through $\vec{p_0}$. The lines are beamformed by delaying the received signals from each of the receiving elements according to the time of flight and summing over all Q receiving elements and all K emissions in the emission sequence

$$h_{l,\theta}(n) = \sum_{k=0}^{K-1} \sum_{q=0}^{Q-1} r_{l-k,q}\left(t_{k,q}(\vec{p_\theta}(n))\right), \quad (2)$$

where $r_{l,q}(t)$ is the signal received at element q at emission l, $h_{l,\theta}(n)$ is the l:th high resolution line at angle θ, and $t_{k,q}(\vec{p_\theta}(n))$ is the time of flight from the virtual source k to the point $\vec{p_\theta}(n)$ and back to receiving element q given by

$$t_{k,q}(\vec{p_\theta}(n)) = \frac{\|\vec{p_\theta}(n) - \vec{r}_{xmt,k}\| + \|\vec{r}_{rcv,q} - \vec{p_\theta}(n)\|}{c}, \quad (3)$$

where $\vec{r}_{xmt,k}$ is the position of virtual source k [9], $\vec{r}_{rcv,q}$ is the position of receiving element q, and c is the speed of sound. As indicated by Figure 1, the emitted wave can only be assumed spherical within a limited angular extend. When beamforming $h_{l,\theta}(n)$ only data where $\vec{p_0}$ is within this angular extend is used. For all other emissions $r_{l,q}(t)$ is set to zero.

The flow direction is found by searching for the angle of maximum normalized cross-correlation [1]. The normalized cross-correlation between two high-resolution lines acquired using the same emission sequence is given by

$$\rho_l(m,\theta) = \frac{\sum_{n=0}^{N} hc_{l,\theta}(n) hc_{l+K,\theta}(n+m)}{\sqrt{\sum_{n=0}^{N} hc_{l,\theta}^2(n) \sum_{n=0}^{N} hc_{l+K,\theta}^2(n)}}, \quad (4)$$

where $hc_{l,\theta}(n)$ is the high resolution line after stationary echo cancelling, and K is the number of emissions in the emission sequence. The stationary echo cancelling is done using a linear regression filter [10] over high resolution lines made using the same emission sequence. L cross-correlations are averaged

$$\rho_{av}(m,\theta) = \frac{1}{L} \sum_{l=0}^{L-1} \rho_l(m,\theta), \quad (5)$$

and the maximum cross-correlation at each angle is found

$$\rho(\theta) = \max\left(\rho_{av}(m,\theta)\right). \quad (6)$$

The flow direction is then found as the angle where ρ peaks

$$\theta_d = \arg\max_\theta \rho(\theta). \quad (7)$$

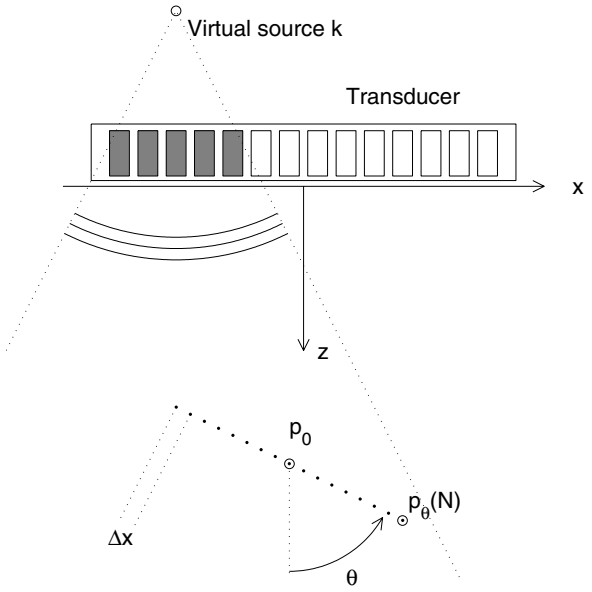

Fig. 1. A number of elements emit a wave which is approximately spherical within a limited angular extend as if it originated from virtual source k. One of the lines beamformed through $\vec{p_0}$ is indicated along with the angle θ and the spatial sampling interval Δx

The discrete angle estimate θ_d is interpolated using a parabolic approximation given by [11]

$$\hat{\theta} = \theta_d - \frac{\rho(\theta_d + 1) - \rho(\theta_d - 1)}{2(\rho(\theta_d + 1) - 2\rho(\theta_d) + \rho(\theta_d - 1))}\Delta\theta, \quad (8)$$

where $\Delta\theta$ is the angular sampling interval. The flow velocity along the estimated direction is then found by repeating the beamforming along $\hat{\theta}$ and finding the lag of maximum correlation

$$m_d = \arg\max_m \rho_{av}(m, \hat{\theta}). \quad (9)$$

This lag can be interpolated using (8) to yield $\hat{m}$. The velocity magnitude along $\hat{\theta}$ is then found by

$$|\vec{v}| = \frac{\hat{m}\Delta x f_{prf}}{K}, \quad (10)$$

where f_{prf} is the pulse repetition frequency. By applying prior knowledge of the expected velocity range, the search range can be limited by only evaluating the cross correlation function (4) in lags corresponding to the expected velocity range.

III. Results

2.2 seconds of real-time in-vivo data of the common carotid artery of a healthy 30-year-old male volunteer was acquired using our RASMUS multichannel sampling system [12] and a 128 element linear array transducer. The scanning was done by an experienced sonographer. Data processing was performed off-line on a large computer cluster. The parameters used for data acquisition and processing are outlined in Table I.

Due to hardware limitations only 64 elements of the full 128 element array was used at reception. The receiving sub-aperture was slid at each emission to be centered around the emitting sub-aperture.

The excitation waveform was a 20 μs chirp linearly sweeping frequencies from 3 to 8 MHz, amplitude tapered by a 10% Tukey window. The received signals were compressed using a mismatch compression filter, which was the time-inverse chirp tapered by a Chebyshev window with 70 % relative side-lobe attenuation [13].

TABLE I

PARAMETERS USED FOR THE EXPERIMENT

Transducer type	Linear array
Number of transducer elements	128
Transducer element pitch	0.3 mm
Transducer element kerf	0.035 mm
Transducer element height	5 mm
Elevation focus	20 mm
Center frequency, f_0	6.2 MHz
Wavelength, $\lambda = c/f_0$	0.25 mm
Excitation type	20 μs tapered chirp
Frequencies swept	$\sim$ 3 - 8 MHz
Number of emitting elements	11
Number of receiving elements, Q	64, centered at em.
Number of emissions in sequence, K	8
Number of virtual sources, $(= K)$	8
Virtual source positions	[x, 0, -17.55] mm
Pulse repetition frequency, f_{prf}	10 kHz
Points in line, $N + 1$	401
Spatial sampling interval, Δx	$\lambda/20 = 12.5\mu$m
Line length	$20\lambda = 5$ mm
Angular sampling interval, $\Delta\theta$	5°
Stationary echo cancelling method	Linear regression
Number of correlations averaged, L	113
Velocity search range	-1.5 to 1.5 m/s

Data was processed in blocks of 128 emissions corresponding to 12.8 ms of data. For every data block the flow angle was estimated as described in Section II for a 1 mm grid of points ranging from 16 to 31 mm depth and -10 to 10 mm lateral. The velocity magnitude was estimated along the angle found for each individual point. The estimation process for each point was therefore mutually independent.

B-mode images were simply made by beamforming high resolution lines along the axial direction followed by envelope detection and logarithmic compression. All B-mode images are shown in 30 dB dynamic range only. The reason for the low B-mode image quality compared to that of [4] is found in the sparse emission sequence used for flow estimation. A solution could be to make interleaved emission sequences of both B-mode and flow emissions.

Full 2-D vector flow images were made by combining B-mode images with both colors indicating velocity magnitude and vector arrows showing the estimated flow direction and velocity magnitude. Velocity estimates were displayed when the energy of $hc_{l,\theta}(n)$ was above a certain fraction of the energy of $h_{l,\theta}(n)$.

Figure 2 shows a synthetic aperture vector flow image made at mid-diastole. Both the common carotid artery and a cross-section of the jugular vein is seen. The base of each

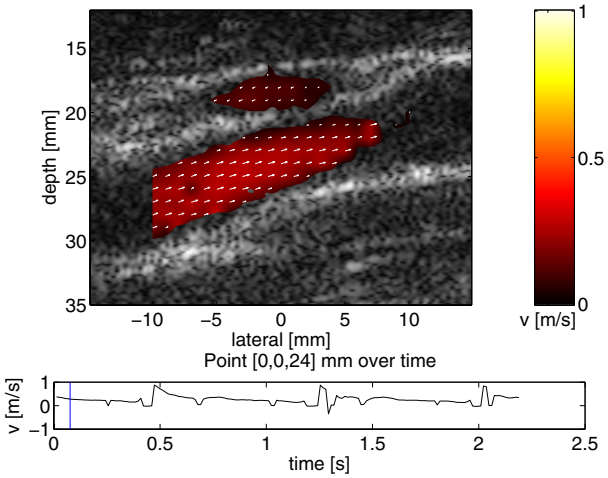

Fig. 2. Synthetic aperture vector flow image of the common carotid artery and jugular vein at mid-diastole.

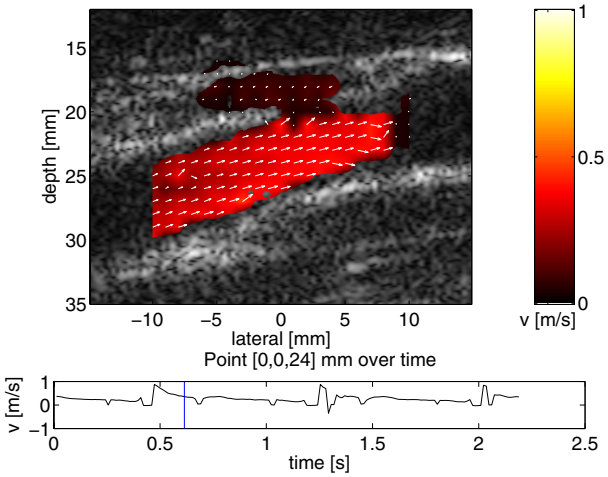

Fig. 3. Synthetic aperture vector flow image of the common carotid artery and jugular vein at end systole.

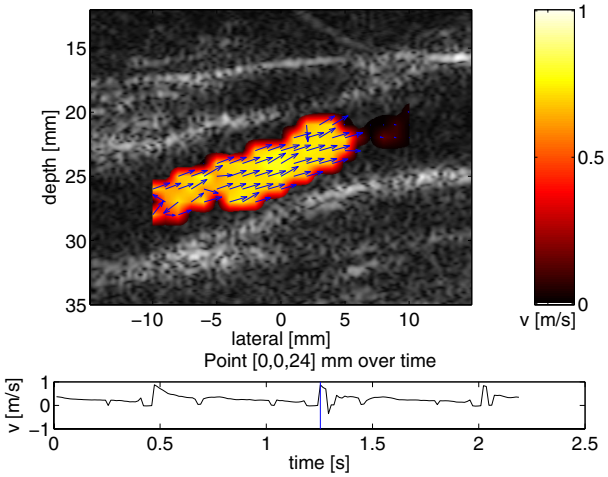

Fig. 4. Synthetic aperture vector flow image of the common carotid artery and jugular vein at peak systole.

vector arrow shows the point p_0 of estimation, and the vector direction and length indicates the flow angle and magnitude, respectively. The bottom plot indicates the velocity at point [0,0,24] mm over the entire 2.2 seconds of data, and the vertical bar indicates the time of the current frame. The peak systoles occur around time $t = 0.5$, 1.3, and 2.0 seconds.

A vector flow image made at end systole is shown in Figure 3. The increased velocity is indicated both by a lighter color, and by the increased length of the vector arrows. A slight discrimination problem between tissue and blood is seen at the border between the carotid artery and the jugular vein.

Figure 4 shows a vector flow image made at peak systole. Dark velocity vectors are used for better visualization. In the vessel center the majority of the angle estimates are within the expected range, but close to the vessel border the performance is poor. This is mainly due to problems of suppressing the large vessel border movements during the systolic phase.

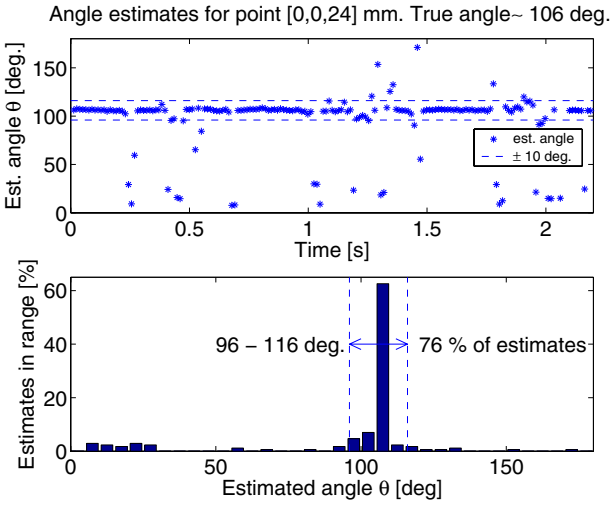

Fig. 5. The top plot show the individual angle estimates for a point in the center of the common carotid artery [0,0,24] mm over time. The bottom plot shows a histogram of the flow angle estimates, indicating that 76% of the estimates are within $\pm 10^\circ$ of the flow angle of 106° visually determined from the B-mode image.

The top plot of Figure 5 shows the estimated angles for a point in the center of the common carotid artery over time. The majority of the estimates are centered around $\theta = 106^\circ$ which corresponds to the flow angle visually determined from the B-mode image (see Figure 2). The bottom plot shows a histogram of the angle estimates, where 76% of the 171 estimates are within the range of $106^\circ \pm 10^\circ$ which is considered adequate for finding the velocity magnitude. These estimates within the $\pm 10^\circ$ range have a standard deviation below 2.7°. 69% of the estimates are within the range of $106^\circ \pm 5^\circ$. There seems to be a tendency for an increasing number of false estimates around time $t = 0.5$, 1.3, and 2.0 seconds where the peak systoles are found. Furthermore, it is noticed that the majority of the erroneous estimates are close to perpendicular to the flow direction, indicating that the suppression of the high amplitude tissue signal by the stationary echo cancelling filter is not optimal. This can potentially be solved by applying more advanced stationary echo cancelling filters.

IV. Conclusion

In this paper a synthetic aperture 2-D vector velocity estimation method is applied to in-vivo data from the human common carotid artery. Full color flow maps including 2-D vectors showing the flow direction are presented from both the diastolic and systolic phase. For a point in the vessel center the flow angle is estimated over time and 76% of the estimates were within $\pm 10^\circ$ of the flow direction visually determined from the B-mode image.

Acknowledgment

This work was supported by grant 26-04-0024 from the Danish Science Foundation and by B-K Medical A/S, Herlev, Denmark.

A thank you goes to Michael Bachmann Nielsen and Kristina Rue Nielsen, both from the Department of Radiology, Section of Ultrasound, Rigshospitalet, Denmark, for performing the clinical scanning.

References

[1] J. A. Jensen. Velocity vector estimation in synthetic aperture flow and B-mode imaging. In *IEEE International Symposium on Biomedical imaging from nano to macro*, pages 32–35, 2004.

[2] O. Bonnefous and P. Pesqué. Time domain formulation of pulse-Doppler ultrasound and blood velocity estimation by cross correlation. *Ultrason. Imaging*, 8:73–85, 1986.

[3] C. Kasai, K. Namekawa, A. Koyano, and R. Omoto. Real-time two-dimensional blood flow imaging using an autocorrelation technique. *IEEE Trans. Son. Ultrason.*, 32:458–463, 1985.

[4] M. H. Pedersen, K. L. Gammelmark, and J. A. Jensen. Preliminary in-vivo evaluation of convex array synthetic aperture imaging. In *Proc. SPIE - Progress in biomedical optics and imaging*, pages 33–43, 2004.

[5] S. I. Nikolov, K. Gammelmark, and J. A. Jensen. Recursive ultrasound imaging. In *Proc. IEEE Ultrason. Symp.*, volume 2, pages 1621–1625, 1999.

[6] J. A. Jensen and S. I. Nikolov. Transverse flow imaging using synthetic aperture directional beamforming. In *Proc. IEEE Ultrason. Symp.*, pages 1488–1492, 2002.

[7] M. Karaman, P. C. Li, and M. O'Donnell. Synthetic aperture imaging for small scale systems. *IEEE Trans. Ultrason., Ferroelec., Freq. Contr.*, 42:429–442, 1995.

[8] G. R. Lockwood, J. R. Talman, and S. S. Brunke. Real-time 3-D ultrasound imaging using sparse synthetic aperture beamforming. *IEEE Trans. Ultrason., Ferroelec., Freq. Contr.*, 45:980–988, 1998.

[9] S. I. Nikolov and J. A. Jensen. Virtual ultrasound sources in high-resolution ultrasound imaging. In *Proc. SPIE - Progress in biomedical optics and imaging*, volume 3, pages 395–405, 2002.

[10] A. P. G Hoeks, J. J. W. van de Vorst, A. Dabekaussen, P. J. Brands, and R. S. Reneman. An efficient algorithm to remove low frequency Doppler signal in digital Doppler systems. *Ultrason. Imaging*, 13:135–145, 1991a.

[11] S. G. Foster. *A pulsed ultrasonic flowmeter employing time domain methods*. PhD thesis, Dept. Elec. Eng., University of Illinois, Urbana, Ill., 1985.

[12] J. A. Jensen, O. Holm, L. J. Jensen, H. Bendsen, S. I. Nikolov, B. G. Tomov, P. Munk, M. Hansen, K. Salomonsen, J. Hansen, K. Gormsen, H. M. Pedersen, and K. L. Gammelmark. Ultrasound research scanner for real-time synthetic aperture image acquisition. *IEEE Trans. Ultrason., Ferroelec., Freq. Contr.*, 52 (5), May 2005.

[13] T. Misaridis. *Ultrasound imaging using coded signals*. PhD thesis, Ørsted•DTU, Technical University of Denmark, Lyngby, Denmark, 2001.

A.7 Oddershede, N. and Jensen, J. A.,
Motion compensated beamforming in synthetic aperture vector flow imaging, *Proceedings of IEEE Ultrasonics Symposium 2006, pp. 2027-31.*

Motion compensated beamforming in synthetic aperture vector flow imaging

Niels Oddershede and Jørgen Arendt Jensen
Center for Fast Ultrasound Imaging, Ørsted•DTU, Build. 349,
Technical University of Denmark, DK-2800 Lyngby, Denmark

Abstract— **In synthetic aperture imaging the beamformed data from a number of emissions are summed to create dynamic focusing in transmit. This makes the method susceptible to motion, which is especially the case for the synthetic aperture flow estimation method, where large movements are expected. In this paper, these motion effects are considered.**

A number of Field II simulations of a single scatterer moving at different velocities are performed both for axial and lateral velocities from 0 to 1 m/s. Data are simulated at a pulse repetition frequency of 5 kHz. The signal-to-noise ratio (SNR) of the beamformed response from the scatterer at all velocities is compared to that of a stationary scatterer. For lateral movement, the SNR drops almost linearly with velocity to -4 dB at 1 m/s, while for axial movement the SNR drop is largest, when the scatterer moves a quarter of a wavelength between emissions. Here the SNR is -10 dB compared to the stationary scatterer.

A 2D motion compensation method for synthetic aperture vector flow imaging is proposed, where the former vector velocity estimate is used for compensating the beamforming of new data. This method is tested on data from an experimental flow rig acquired using our RASMUS experimental ultrasound scanner and a 5.5 MHz linear array transducer. A 11.25 μs non-linear chirp is used as excitation and the data from 128 emissions is used for estimating the flow direction and magnitude at a profile across the tube.

The measurement was conducted at a flow angle of 60° with respect to the axial direction and a peak velocity of 0.1 m/s sampled at a pulse repetition frequency of 1 kHz. The mean bias across the profile was -8.4 % with respect to the peak velocity and the mean standard deviation was 12.2 % prior to compensation. When the proposed compensation was applied a mean bias of -3.6 % and a mean standard deviation of 2.8 % was seen.

I. Introduction

Synthetic transmit aperture (STA) imaging is susceptible to motion artifacts due to the summation of a number of low resolution images created at different time instances. This results in incoherent summation and degradation of both resolution, contrast, and signal-to-noise ratio (SNR). The purpose of this paper is to implement and test a beamforming approach for synthetic aperture vector flow imaging which compensates for 2-D motion.

The effects of tissue motion in synthetic aperture ultrasound have been studied by various authors [1], [2], [3], [4], [5]. Trahey and Nock investigated motion effects in a synthetic receive aperture system in [1] and showed that motion along the axial direction has a far larger effect on the resolution than lateral movement. Also, it was argued that the problem increases with the length of the emission sequence and the center frequency. A 1-D motion compensation method based on axial cross-correlation of low resolution images (LRIs) was proposed. Hazard and Lockwood [3] tested motion effects in a STA system with 3 emissions in the emission sequence. They showed that axial movement on the order of 3% of the wavelength between emissions had only little effect on the resolution and virtually no effect on the contrast, whereas a 10 times larger movement resulted in both a slight shift and widening of the main-lobe and a reduced contrast.

A method for blood flow velocity estimation using STA was presented in [6]. Here data were beamformed along the axial direction and a cross-correlation estimator was used. The STA velocity estimator of [7] was based on cross-correlation of lines beamformed along the flow, assuming the direction of flow is known.

A method for estimating the direction of flow was presented in [8] based on a search for the highest normalized cross-correlation as a function of angle. By finding both the in-plane flow direction and magnitude, 2-D velocity vectors can be displayed for in principle all image points. The synthetic aperture velocity estimation method as presented in [8] is shortly described in Section II. In these methods the resolution and contrast degradation due to the motion of blood are neglected resulting in a smearing of the point spread function and a decrease in SNR.

In [9] a 2-D motion compensation method for STA B-mode imaging was presented. The method used an interleaved sequence consisting of both a long STA sequence for making high resolution B-mode images and a short STA sequence for motion estimation. The cross-correlation estimator of [8] was used on the short sequence to find the tissue motion in two dimensions, and a compensation was made from the estimated tissue motion, when beamforming the B-mode image from the long sequence.

In this paper the motion compensation method presented in [9] is used in flow estimation. Here only a short sequence is used for both blood velocity estimation and motion compensation. The previous 2-D velocity vector estimate is used for compensating for the motion of the blood in the initial beamforming of the following high resolution lines. This method is described in Section III, simulated in Section IV, and tested on flow phantom data in Section V.

II. Synthetic aperture velocity estimation

This section describes how the STA velocity estimation method presented in [8] is performed. Due to the dynamic

1051-0117/06/$20.00 ©2006 IEEE

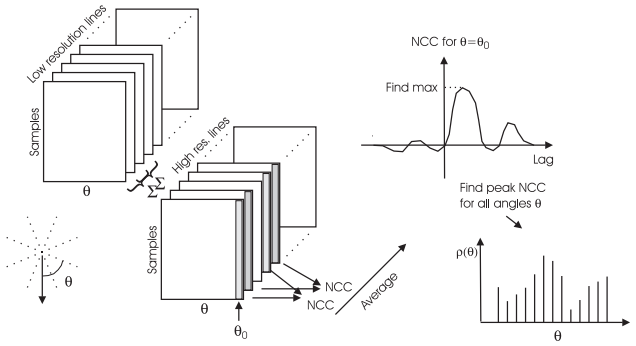

Fig. 1. The synthetic aperture vector flow imaging algorithm. Lines are beamformed in a star-shape as shown in the lower left corner. Low resolution lines are coherently summed to create high resolution lines. After stationary echo cancelling these are cross-correlated and averaged, and the flow angle is estimated as the angle of maximum normalized cross-correlation. The velocity magnitude is found as the cross-correlation peak along this direction.

focus in both transmit and receive, data can be beamformed in every point [7]. This is used for determining the flow direction and velocity.

For every point $\vec{p_0}$, where the velocity direction and magnitude is estimated, a number of lines $\vec{p}(n,\theta)$ are beamformed through the point at different angles

$$\vec{p}(n,\theta) = \vec{p_0} + \Delta x[\sin\theta, 0, \cos\theta](n - \frac{N}{2}), \quad (1)$$

where $n = [0, 1, ..., N]$ is the sample index of the lines, $\theta = [0, \Delta\theta, 2\Delta\theta, ..., 180°]$ are the angles with respect to the beam axis z, and Δx is the spatial sampling distance. Notice, a 3-D right-hand cartesian coordinate system is used where x follows the lateral direction, y the elevation direction, and z the axial, while the origo is placed at the center of the transducer surface. The lines in (1) create a star-shape through the point $\vec{p_0}$ as shown in the bottom left of Fig. 1. The low resolution lines are beamformed by delaying the received signals from each of the receiving elements according to the time of flight and summing over all Q receiving elements as

$$l_k(n,\theta) = \sum_{q=0}^{Q-1} r_{k,q}(t_{k,q}(\vec{p}(n,\theta))) \quad (2)$$

where $r_{k,q}(t)$ is the signal received at element q at emission k and $t_{k,q}(\vec{p}(n,\theta))$ is the time of flight from the virtual source used at emission k to the point $\vec{p}(n,\theta)$ and back to receiving element q given by

$$t_{k,q}(\vec{p}(n,\theta)) = \frac{\|\vec{p}(n,\theta) - \vec{r}_{xmt,k}\| + \|\vec{r}_{rcv,q} - \vec{p}(n,\theta)\|}{c}, \quad (3)$$

where $\vec{r}_{xmt,k}$ is the position of the virtual source used at emission k, $\vec{r}_{rcv,q}$ is the position of receiving element q, and c is the speed of sound. The high resolution lines are formed by summing K consecutive low resolution lines, where K is the number of emissions in the emission sequence, as

$$h_k(n,\theta) = \sum_{k'=0}^{K-1} l_{k+k'}(n,\theta). \quad (4)$$

The flow direction is found by searching for the angle of maximum normalized cross-correlation (NCC) [8]. The NCC between two high-resolution lines acquired using the same emission sequence is given by

$$\rho_k(m,\theta) = \frac{\sum_{n=0}^{N} hc_k(n,\theta) hc_{k+K}(n+m,\theta)}{\sqrt{\sum_{n=0}^{N} hc_k^2(n,\theta) \sum_{n=0}^{N} hc_{k+K}^2(n,\theta)}}, \quad (5)$$

where $hc_k(n,\theta)$ is the high resolution line after stationary echo cancelling, and K is the number of emissions in the emission sequence. The stationary echo cancelling is done using a linear regression filter [10] over high resolution lines made using the same emission sequence. L cross-correlations are averaged

$$\rho_{av}(m,\theta) = \frac{1}{L} \sum_{k=0}^{L-1} \rho_k(m,\theta), \quad (6)$$

and the maximum cross-correlation at each angle is found

$$\rho(\theta) = \max(\rho_{av}(m,\theta)). \quad (7)$$

The flow direction is then found as the angle where ρ has its maximum

$$\theta_d = \arg\max_{\theta} \rho(\theta). \quad (8)$$

The discrete angle estimate θ_d is interpolated using a parabolic approximation given by [11]

$$\hat{\theta} = \theta_d - \frac{\rho(\theta_d + \Delta\theta) - \rho(\theta_d - \Delta\theta)}{2(\rho(\theta_d + \Delta\theta) - 2\rho(\theta_d) + \rho(\theta_d - \Delta\theta))} \Delta\theta, \quad (9)$$

where $\Delta\theta$ is the angular sampling interval. The flow velocity along the estimated direction is then found by repeating the beamforming along $\hat{\theta}$ and finding the lag of maximum correlation

$$m_d = \arg\max_{m} \rho_{av}(m,\hat{\theta}). \quad (10)$$

This lag can be interpolated using parabolic interpolation to yield $\hat{m}$. The velocity magnitude along $\hat{\theta}$ is then found by

$$\hat{v}_{\hat{\theta}} = \frac{\hat{m}\Delta x f_{prf}}{K}, \quad (11)$$

where f_{prf} is the pulse repetition frequency. By applying prior knowledge of the expected velocity range, the search range can be limited by only evaluating the cross correlation function (5) in lags corresponding to the expected velocity range.

III. Velocity estimation with motion compensation

To sum low resolution lines (LRLs) in phase during movement, a compensation can be made for the current velocity during beamformation. In a velocity estimation system the velocity is of course not known in advantage, but by assuming a constant velocity, the velocity vector estimate from the latest time instance $\vec{v}_{est}$ can be used as a compensation for creating the next high resolution lines (HRLs). The assumption of constant velocity is rarely fulfilled in-vivo but due to the continuous availability of data in STA and the recursive

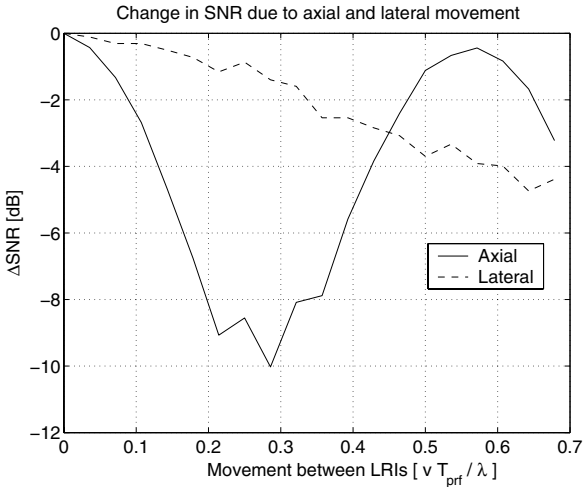

Fig. 2. The change in SNR due to axial and lateral motion. Found by simulation using a non-linear chirp sweeping frequencies from 3.7 to 7.3 MHz.

formation of HRLs, the velocity can be closely tracked. The motion compensated HRLs are formed as

$$h_k(n,\theta) = \sum_{k'=0}^{K-1}\sum_{q=0}^{Q-1} r_{k+k',q}(t_{k+k',q}(\vec{p}(n,\theta) + k'\vec{v}_{est}/f_{prf})), \tag{12}$$

where $\vec{v}_{est} = \hat{v}_{\hat{\theta}}[\sin(\hat{\theta}), 0, \cos(\hat{\theta})]$ is the latest velocity vector estimate and f_{prf} is the pulse repetition frequency. The motion effect will be fully compensated for if $\vec{v}_{est}$ equals the true velocity. Cross-correlating two high-resolution lines K emissions apart will still expectedly peak at the lag corresponding to the blood velocity. Even if an erroneous velocity estimate is used for the compensation, the point spread function of a single scatterer is simply smeared, which was already the case prior to compensation.

IV. Simulations

A number of simulations were performed using Field II [12], [13]. Here a single scatterer, initially located at depth $z = 30$ mm and below the aperture center $x = 0$ mm, is moving along the axial direction, while $K = 8$ low resolution images (LRIs) are acquired. The high resolution image (HRI) is created by summing the LRIs. The SNR of the HRI is then compared to the SNR of the HRI assuming no motion. The simulation was repeated for velocities of $v' = 0, 5, 10, ..., 95$ cm/s corresponding to movement of up to 0.68λ between each LRI, where $\lambda = c/f_0$ is the wavelength. The excitation waveform was an 11.25 μs non-linear chirp designed using a frequency sampling method [14]. The parameters used in the simulation are given in Table I.

For each of the simulations the change in SNR due to movement ΔSNR is found as

$$\Delta SNR = 10\log_{10}\left(\frac{E_{v=v'}}{E_{v=0}}\right) \tag{13}$$

TABLE I

Parameters used for simulation and measurement.

Transducer	
Transducer type	Linear array
Number of transducer elements	128
Transducer element pitch	0.3 mm
Transducer element kerf	0.035 mm
Transducer element height	5 mm
Elevation focus	20 mm
Center frequency, f_0	5.5 MHz
Wavelength, $\lambda = c/f_0$	0.28 mm
STA transmission	
Excitation type	11.25 μs non-linear chirp [14]
Frequencies swept	$\sim$ 3.5 - 7.5 MHz
Number of emitting elements	11
Number of receiving elements, Q	64, centered at emission
Number of emissions in sequence, K	8
Number of virtual sources, $(= K)$	8
Virtual source positions	$[x_{vs}, 0, -2.5]$ mm
Pulse repetition frequency, f_{prf}	5 kHz (sim.) and 1 kHz (meas.)
Simulation, Inter-LRI movement	
Velocities simulated, v'	$0, 5, 10, ..., 95$ cm/s
Corresponding inter-LRI movement	$0, ..., 0.68\lambda$
Measurement, Flow rig setup	
Tube radius, R	6 mm
Flow angles, θ	60° and 90°
Depth of tube center, z_0	34.5 mm (60°), 39.5 mm (90°)
Peak velocity, v_0	0.1 m/s
Measurement, STA processing	
Points in line, $N + 1$	401
Spatial sampling interval, Δx	12.5μm
Line length	5 mm
Angular sampling interval, $\Delta\theta$	5°
Stationary echo cancelling method	Linear regression [10]
Number of correlations averaged, L	113
Velocity search range	-1 to 1 m/s

where $E_{v=v'}$ is the total energy of the 2-D HRI point spread function when the point moves at velocity v'. The HRI point spread function is found from -20 mm to 20 mm lateral and 20 mm to 40 mm axial for every 40 μm. This calculation of the point spread function energy assumes that the noise power is the same in both cases. ΔSNR is plotted in Fig. 2 as a function of the movement between LRIs given by vT_{prf}/λ, where T_{prf} is the pulse repetition period. The same simulation is repeated for lateral movement at the same velocities. The resulting ΔSNR is plotted in Fig. 2 with a dashed line. The SNR during axial movement is significantly deteriorated at an inter-LRI movement of $\sim 0.25\lambda$, whereas the SNR at $\sim 0.5\lambda$ is comparable to that of a stationary scatterer.

From these simulations the lateral contrast at different velocities can also be extracted. This has been done, and the resulting plot is shown in Fig. 3 for purely axial motion. The results show the same tendency as [3]. For small velocities the contrast is almost unchanged, but for axial motion of $v' = 0.35$ m/s in Fig. 3, corresponding to 0.25λ, the lateral side-lobes are up almost 20 dB compared to the stationary case. This is the worst case where the received echoes are 180° out of phase, and looking at Fig. 2 also close to where the SNR is lowest. At higher axial velocities both contrast and SNR is better.

The motion compensation method is applied to the single point simulation data. Fig. 4 shows the lateral side-lobe

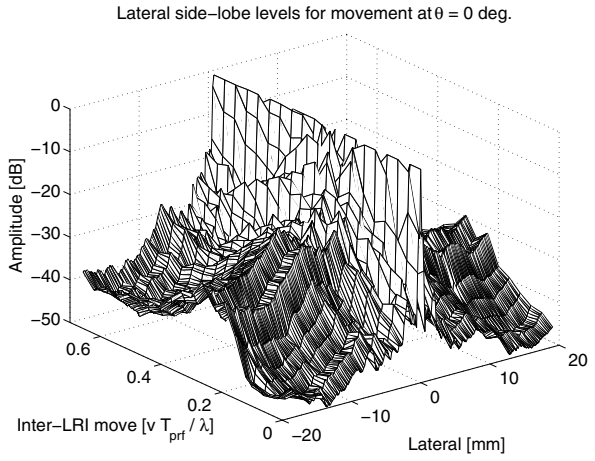

Fig. 3. Lateral side-lobe structure at different purely axial velocities. A ~ 20 dB increase in side-lobes is seen around $v = 0.35$ m/s corresponding to a movement of 0.25λ between LRIs.

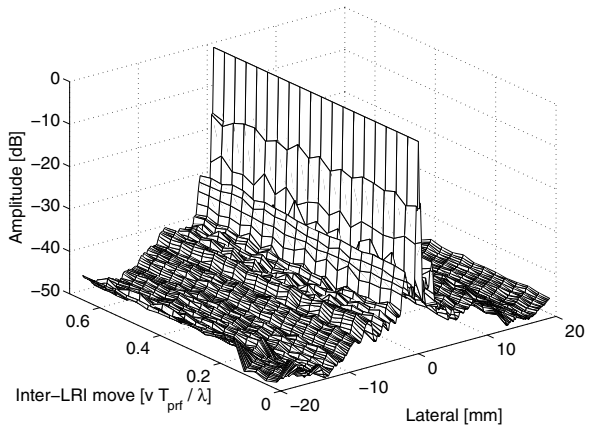

Fig. 4. Lateral side-lobe structure at different purely axial velocities when the motion is compensated in beamforming.

structure for the compensated simulations for purely axial motion. This can be compared to Fig. 3. After compensation almost no increase in side-lobe levels due to the motion is seen. This demonstrates the potential for the motion compensation.

V. Phantom experiments

A number of experiments were conducted using a flow rig phantom where blood mimicking fluid was circulated through tubes. A linear array transducer was fixed at a certain height z_0 above the tubing and at a certain angle θ with respect to the flow. The flow was constant over time, and the flow velocity profile was assumed parabolic. The velocity directly below the transducer center as a function of depth z is then

$$v(z) = v_0 \left(1 - \left(\frac{(z - z_0)\sin(\theta)}{R} \right)^2 \right), |z - z_0| < \frac{R}{\sin(\theta)}, \tag{14}$$

where R is the vessel radius. Data were acquired using our RASMUS ultrasound multichannel sampling system [15] and processed as described in Section II. Various parameters for the data acquisition and processing are given in Table I.

Measurements were made for flow angles of $\theta = 60^\circ$ and 90° and for pulse repetition frequencies of $f_{prf} = 5$ kHz and 1 kHz. This corresponds to a peak movement of $\sim 7\%$ and 35% of λ between emissions with the peak velocity $v_0 = 0.1$ m/s and $\lambda = 0.28$ mm. Lowering the f_{prf} is equivalent to increasing the velocity.

Velocity directions and magnitudes were estimated along a profile through the tube at 20 uncorrelated time instances, and the estimated velocities were compared to the expected velocity profile given by (14). The resulting angle and velocity estimates for the $f_{prf} = 1$ kHz and $\theta = 60^\circ$ experiment are shown in Fig. 5, which also show the average profiles ± 3 times the standard deviation. A number of false angle estimates is seen mainly between 35 and 40 mm depth, resulting in too low velocity estimates.

The compensation method given by (12) is applied to the data prior to velocity estimation. Here the previous estimate of the vector velocity is used to compensate for the inter-LRI movement while beamforming. The resulting profiles are plotted in Fig. 6, where the majority of the false estimates are no longer present.

The average bias $\bar{B}_v$ and average standard deviation $\bar{\sigma}_v$ of the 20 estimated velocity profiles are used as a measure for the performance of the velocity estimation method. These are given by

$$\bar{B}_v = \frac{1}{v_0(z_2 - z_1)} \sum_{z=z_1}^{z_2} (\bar{v}(z) - v(z))$$

$$\bar{\sigma}_v = \frac{1}{v_0(z_2 - z_1)} \sum_{z=z_1}^{z_2} \sqrt{\frac{1}{20} \sum_{i=1}^{20} (\hat{v}_i(z) - \bar{v}(z))^2},$$

where $z_1 = z_0 - R/\sin\theta$ and $z_2 = z_0 + R/\sin\theta$ are the tube edges, $\hat{v}_i(z)$ is the i^{th} velocity estimate at depth z, $v(z)$ is the true velocity at depth z as defined by (14), and $\bar{v}(z) = \sum_{i=1}^{20} \hat{v}_i(z)/20$ is the average estimate at depth z. These quantities are calculated for the four experiments and are given in Table II.

TABLE II

Average bias and standard deviation of vector velocity estimates in % of peak velocity v_0 for profile made with and without compensation.

Angle	f_{prf}	Bias	Std	Bias, comp	Std, comp
60°	5 kHz	-3.1%	3.7%	-2.8%	3.7%
60°	1 kHz	-8.4%	12.2%	-3.6%	2.8%
90°	5 kHz	-0.1%	5.6%	0.5%	5.6%
90°	1 kHz	-50.8%	30.1%	-38.5%	20.3%

Table II shows a significant decrease in both average bias and average standard deviation for the measurement at $\theta = 60^\circ$ and $f_{prf} = 1$ kHz, and a moderate decrease for the $\theta = 90^\circ$ and $f_{prf} = 1$ kHz experiment. Only small changes are seen for

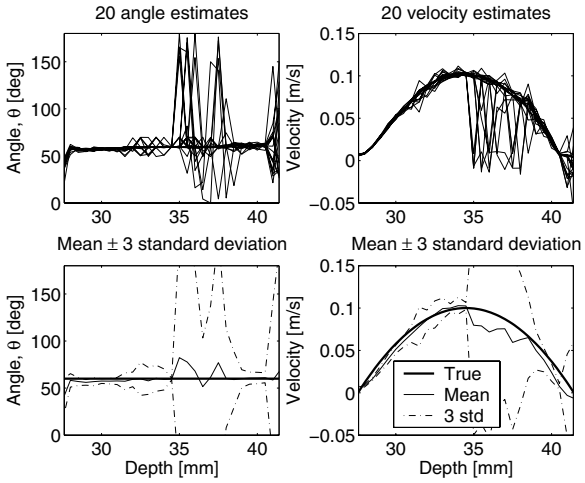

Fig. 5. Angle (left column) and velocity (right column) estimates for flow phantom experiments when no motion compensation is applied. The figure show 20 independent estimates (top) and the average and 3 times the standard deviation compared to the true values (bottom). The data are from the $\theta = 60°$ and $f_{prf} = 1$ kHz experiment.

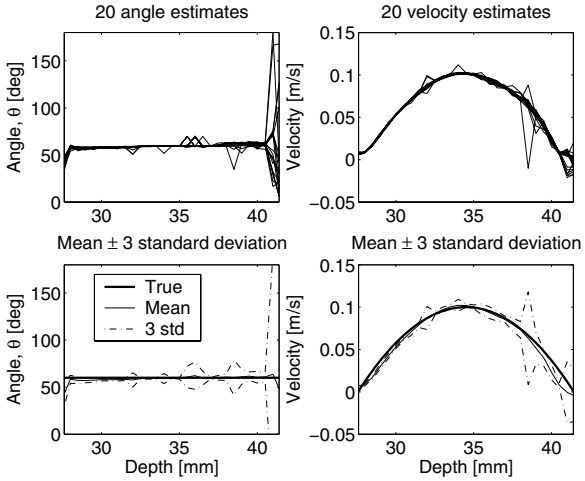

Fig. 6. Angle (left column) and velocity (right column) estimates for flow phantom experiments when the proposed motion compensation is applied. The figure show 20 independent estimates (top) and the average and 3 times the standard deviation compared to the true values (bottom). The data are from the $\theta = 60°$ and $f_{prf} = 1$ kHz experiment.

the other measurements. This indicates that the compensation method can decrease the number of false peaks when only a limited number of false peaks are present, and that the motion compensation has the largest effect at angles where the center frequency of the LRLs are highest.

VI. Conclusion

A 2-D motion compensated beamforming for synthetic aperture vector flow imaging was presented, where the former velocity estimate was used in the beamforming of new data.

Simulations showed a large drop in signal-to-noise ratio and significantly increased lateral side-lobes when the axial inter-LRI movement was around a quarter of a wavelength. The side-lobe increase was almost completely removed when the motion compensated beamforming was applied.

Flow phantom experiments of constant flow showed increased performance using the motion compensated beamforming on data where large movement is present. The method is yet to be tested on accelerating flow.

Acknowledgement

This work was supported by grant 26-04-0024 from the Danish Science Foundation and by B-K Medical A/S, Herlev, Denmark.

References

[1] G. E. Trahey and L. F. Nock. Synthetic receive aperture imaging with phase correction for motion and for tissue inhomogenities - part II: effects of and correction for motion. *IEEE Trans. Ultrason., Ferroelec., Freq. Contr.*, 39:496–501, 1992.

[2] M. Karaman, H. Ş. Bilge, and M. O'Donnell. Adaptive multi-element synthetic aperture imaging with motion and phase aberation correction. *IEEE Trans. Ultrason., Ferroelec., Freq. Contr.*, 42:1077–1087, 1998.

[3] C. R. Hazard and G. R. Lockwood. Effects of motion artifacts on a synthetic aperture beamformer for real-time 3D ultrasound. In *Proc. IEEE Ultrason. Symp.*, pages 1221–1224, 1999.

[4] J. S. Jeong, J. S. Hwang, M. H. Bae, and T. K. Song. Effects and limitations of motion compensation in synthetic aperture techniques. In *Proc. IEEE Ultrason. Symp.*, pages 1759 –1762, 2000.

[5] S. I. Nikolov and J. A. Jensen. K-space model of motion artifacts in synthetic transmit aperture ultrasound imaging. In *Proc. IEEE Ultrason. Symp.*, pages 1824–1828, 2003.

[6] S. I. Nikolov and J. A. Jensen. Velocity estimation using synthetic aperture imaging. In *Proc. IEEE Ultrason. Symp.*, pages 1409–1412, 2001.

[7] S. I. Nikolov and J. A. Jensen. In-vivo synthetic aperture flow imaging in medical ultrasound. *IEEE Trans. Ultrason., Ferroelec., Freq. Contr.*, pages 848–856, 2003.

[8] J. A. Jensen. Velocity vector estimation in synthetic aperture flow and B-mode imaging. In *IEEE International Symposium on Biomedical imaging from nano to macro*, pages 32–35, 2004.

[9] K. L. Gammelmark and J. A. Jensen. Duplex synthetic aperture imaging with tissue motion compensation. In *Proc. IEEE Ultrason. Symp.*, pages 1569–1573, 2003.

[10] A. P. G Hoeks, J. J. W. van de Vorst, A. Dabekaussen, P. J. Brands, and R. S. Reneman. An efficient algorithm to remove low frequency Doppler signal in digital Doppler systems. *Ultrason. Imaging*, 13:135–145, 1991a.

[11] S. G. Foster. *A pulsed ultrasonic flowmeter employing time domain methods*. PhD thesis, Dept. Elec. Eng., University of Illinois, Urbana, Ill., 1985.

[12] J. A. Jensen and N. B. Svendsen. Calculation of pressure fields from arbitrarily shaped, apodized, and excited ultrasound transducers. *IEEE Trans. Ultrason., Ferroelec., Freq. Contr.*, 39:262–267, 1992.

[13] J. A. Jensen. Field: A program for simulating ultrasound systems. *Med. Biol. Eng. Comp.*, 10th Nordic-Baltic Conference on Biomedical Imaging, Vol. 4, Supplement 1, Part 1:351–353, 1996b.

[14] F. Gran and J. A. Jensen. Designing waveforms for temporal encoding using a frequency sampling method. *IEEE Trans. Ultrason., Ferroelec., Freq. Contr.*, Submitted, 2006.

[15] J. A. Jensen, O. Holm, L. J. Jensen, H. Bendsen, S. I. Nikolov, B. G. Tomov, P. Munk, M. Hansen, K. Salomonsen, J. Hansen, K. Gormsen, H. M. Pedersen, and K. L. Gammelmark. Ultrasound research scanner for real-time synthetic aperture image acquisition. *IEEE Trans. Ultrason., Ferroelec., Freq. Contr.*, 52 (5), May 2005.

A.8 Oddershede, N. and Hansen, K. L. and Nielsen, M. B. and Jensen, J. A.,
In-vivo examples of synthetic aperture vector flow imaging, *Proceedings of SPIE Medical Imaging 2007, volume 6513.*

In-vivo examples of synthetic aperture vector flow imaging

Niels Oddershede[1], Kristoffer Lindskov Hansen[1,2], Michael Bachmann Nielsen[2], and Jørgen Arendt Jensen[1]

1) Center for Fast Ultrasound Imaging, Ørsted•DTU, Build. 348, Technical University of Denmark, DK-2800 Kgs. Lyngby, Denmark

2) University Hospital of Copenhagen, Rigshospitalet Blegdamsvej 9, DK-2100 Copenhagen, Denmark

ABSTRACT

The majority of the commercial ultrasound scanners feature blood flow velocity estimation based on the autocorrelation method, yielding estimates of the axial velocity component only. For studying complex flow patterns like arterial bifurcations or venous confluences, 2-D vector velocity estimates would be needed. Synthetic aperture vector flow imaging could potentially provide this. The purpose of this paper is to test the synthetic aperture vector flow imaging method on challenging in-vivo data. Two synthetic aperture in-vivo data sets are acquired using a commercial linear array transducer and our RASMUS experimental ultrasound scanner. The first data set covers the femoral artery and the confluence of the femoral and saphenous vein of a healthy 26-year-old male volunteer. The second shows the carotid bifurcation of a healthy 32-year-old male volunteer. Both 2 second long data sets are processed, and movies of full vector flow images are generated. This paper presents still frames from different time instances of these movies. The movie from the femoral data tracks the accelerating velocity in the femoral artery during systole and a backwards flow at the end of the systole. A complex flow pattern is seen at the junction of the femoral and saphenous vein. The movie of the carotid bifurcation shows high velocities close to the separating wall between the internal and external carotid, and a vortex tendency at the outermost wall. The volume flow through the femoral artery is extracted from the velocity estimates of the femoral data set by assuming the artery is rotational symmetric. An average volume flow just above 500 ml/min was found for the 26-year-old volunteer. This is in agreement with values found in literature.

1. INTRODUCTION

During a couple of decades, ultrasound scanners featuring blood flow velocity estimation have been commercially available. The majority of these have been based on the autocorrelation method[1] giving robust velocity estimates and full color flow maps at a limited frame rate. The velocity estimated by the auto-correlation method is the axial component of the actual velocity and no information about flow direction or lateral velocity are acquired. Although adequate for many applications, this method yields only limited insight into the complex flow patterns at arterial bifurcations and venous confluences. To study these patterns, 2-D vector velocity estimates at a high frame rate would be needed over a certain spatial extent. Synthetic aperture vector flow imaging can potentially provide this.

Velocity estimation using synthetic aperture imaging was first presented in 2001.[2,3] Here data were beamformed along the axial direction and a cross-correlation estimator[4] was used to estimate the axial projection of the velocity. Later,[5] beamforming along the flow direction was presented, which assumed the direction of flow was known in advance. In 2004 a method for estimating the flow direction was presented,[6] based on a search for the maximum normalized cross-correlation as a function of angle. Full 2-D vector flow images can be created for each point in the image by first estimating the local flow direction and then finding the velocity magnitude along this direction. Only a single in-vivo example of synthetic aperture vector flow imaging, where both the blood flow direction and velocity magnitude was automatically estimated, has been presented until now.[7]

The purpose of this paper is to test the synthetic aperture vector flow imaging method in challenging in-vivo situations. The first example is data from the femoral artery, featuring large acceleration and reverse flow, and a confluence of the femoral vein and the saphenous vein. The second example is the carotid bifurcation, where complex flow patterns are expected[8] and a somewhat large tissue movement is found.

Send correspondence to Niels Oddershede, E-mail: no@oersted.dtu.dk

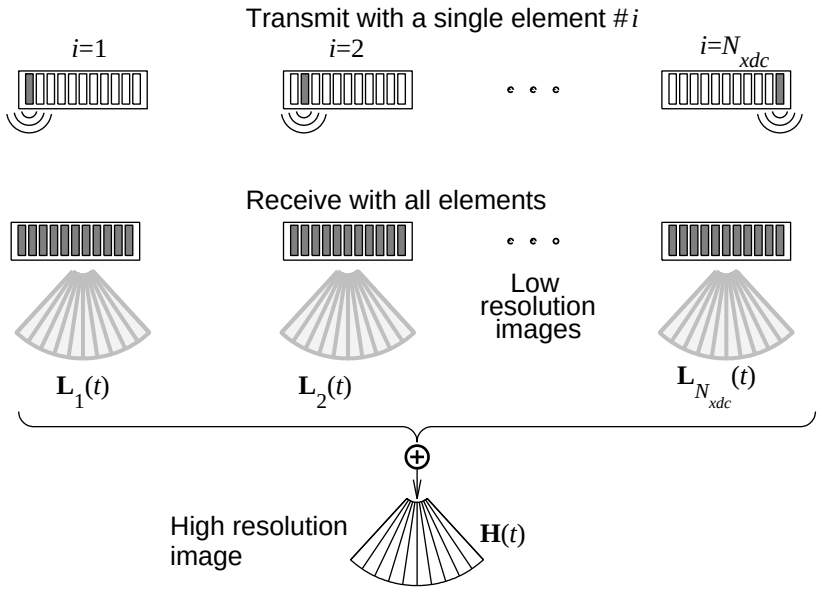

Figure 1. Synthetic transmit aperture imaging. A single transducer element i emits an approximately spherical wave and the echoes are received on all elements. A low resolution image $L_i(t)$ is created by dynamic receive focus. The process is repeated for all N_{xdc} elements and each time a low resolution image is created. A high resolution image $H(t)$ is created by summing all N_{xdc} low resolution images. (Figure from[3]).

2. THEORY

2.1. Synthetic transmit aperture imaging

Synthetic aperture imaging was originally developed for radar imaging[9] where a broad-beam radar was mounted on a moving platform, typically an airplane or a satellite. Increased resolution and contrast was then attained from reconstructing the image from numerous emissions, synthesizing a larger aperture. A lot of research has been done on implementing various versions of synthetic aperture imaging in ultrasound systems. One of these versions is synthetic transmit aperture imaging, defined by Chiao and coworkers[10] as a synthetic aperture imaging method, where only the transmit location change.

Fig. 1 demonstrates the synthetic transmit aperture imaging method. A single transducer element i emits an approximately spherical wave and all transducer elements receive the reflected echoes. A low resolution image (LRI) is formed using dynamic receive focusing according to the time of flight. The term "low resolution image" refers to the image being focused only in the receiving stage. The process is repeated by sequentially emitting from different transducer elements and each time, a new low resolution image is formed. Finally the low resolution images are summed to form a high resolution image (HRI), which is dynamically focused in both the transmitting and receiving stage.

By using only a single element during transmission, the signal-to-noise ratio (SNR) is significantly affected. Therefore a collection of consecutive transducer elements are used during transmission to create a spherical wave. The spherical wave approximation will be valid only within a certain angular extent called the opening angle.[11] Transmit delays are calculated to emulate a virtual source[12,13] behind the aperture, and data are then beamformed as if the wave emanated from this virtual source. The low resolution image is given by

$$\mathbf{L}_i(\vec{r}_p) = \sum_{j=1}^{N_{xdc}} w(j, \vec{r}_i, \vec{r}_p) s_{ij} \left(\frac{|\vec{r}_p - \vec{r}_i| + |\vec{r}_j - \vec{r}_p|}{c} \right), \tag{1}$$

where $s_{ij}(t)$ is the received signal at element j, when the emission emanated from the i'th virtual source. $\vec{r}_p$ is the position of the beamformed point, $\vec{r}_j$ the position of receiving element j, and $\vec{r}_i$ the position of the virtual

source used at emission i. N_{xdc} is the number of transducer elements and c is the speed of sound. The receive apodization $w(j, \vec{r}_i, \vec{r}_p)$, which depend on the point of emission and the position of the beamformed point, is chosen so that only points located within the opening angle of the virtual source are beamformed at each emission. The high resolution image is given by

$$\mathbf{H}(\vec{r}_p) = \sum_{i=1}^{N} \mathbf{L}_i(\vec{r}_p) \tag{2}$$

where N is the number of virtual sources, and therefore the number of emissions used for each high resolution image. Notice that any point $\vec{r}_p$ within the opening angle of the virtual source can be fully focused, and the beamforming is therefore not restricted to be along straight lines.[3]

After the first HRI is created, new HRIs can be created by recursively adding the newest LRI and subtracting the oldest,[14] but motion during data acquisition will affect the HRIs differently so that only $\mathbf{H}_{i+N}$ and $\mathbf{H}_i$ will experience the same motion effects.[2] As indicated in (2), the number of emissions N can be chosen lower than the number of transducer elements N_{xdc} resulting in a sparse sampling of the transmitting aperture. Hereby the time between similar HRIs is decreased, but the contrast and SNR will also be affected.

2.2. Interleaving of flow sequence and B-mode sequence

To create full vector color flow maps, both vector velocity estimates and B-mode images are needed. For the synthetic aperture vector flow estimation method described in the proceeding subsection, a sparse emission sequence of around $N = 8$ emissions is needed. Hereby a sufficient temporal sampling is attained, while the SNR and contrast is acceptable (lateral sidelobes at ~ -35 dB). Nevertheless, this contrast is too poor for the B-mode images. Two different emission sequences are therefore interleaved,[15] a sparse sequence for velocity estimation with $N = 8$ virtual sources equally spread across the aperture, and a full sequence of $N = 118$ emissions covering all possible positions for 11 consecutive elements on a 128 element linear array transducer.

The order of emissions can be chosen in various ways depending on the desired frame rate for the two sequences, and the two data sets presented in this work are in fact acquired in different ways. For the femoral data set, the two sequences are interleaved 1-to-1, meaning that every even emission is a B-mode emission and every odd emission is a flow emission. The effective pulse repetition frequency for the high resolution flow data is $f_{eff} = f_{prf}/16$, where f_{prf} is the pulse repetition frequency of the data acquisition system. A B-mode image can be created after 236 emissions.

For the carotid data set, the sequences are interleaved 8-to-1, meaning that after every 8 flow emissions, 1 B-mode emission is carried out. This results in an effective pulse repetition frequency for the flow sequence of $f_{eff} = f_{prf}/9$, while a B-mode image can be created after 1062 emissions.

2.3. Flow estimation

In synthetic transmit aperture imaging, image points can be beamformed within any grid desired. This is used for the vector velocity estimation.[6] For every point $\vec{r}_p$, where the vector velocity is estimated, a number of lines $\vec{p}_p(m, \theta)$ are beamformed through the point at different angles θ

$$\vec{p}_p(m, \theta) = \vec{r}_p + \Delta r[\sin\theta, 0, \cos\theta](m - \frac{M}{2}) \tag{3}$$

where $m = [0, 1, ..., M]$ is the sample index along the line, $\theta = [0, \Delta\theta, 2\Delta\theta, ..., 180°]$ is the angle between the beamformed line and the axial direction z, and Δr is the spatial sampling distance. Notice that a three-dimensional cartesian coordinate system is used, where x follows the lateral direction, y the elevation direction, and z the axial direction. The coordinate system is centered at the center of the transducer surface. The points defined by $\vec{p}_p(m, \theta)$ create a star shape, and the received echoes $s_{ij}(t)$ are beamformed along the lines defined by $\vec{p}_p(m, \theta)$ to form high resolution lines (HRLs)

$$h_k(m, \theta) = \sum_{i=k}^{k+N-1} \sum_{j=1}^{N_{xdc}} w(j, \vec{r}_i, \vec{r}_p) s_{ij} \left(\frac{|\vec{p}_p(m, \theta) - \vec{r}_i)| + |\vec{r}_j - \vec{p}_p(m, \theta)|}{c} \right). \tag{4}$$

Fundamental to this estimation method is the assumption that the beamformed lines along the flow direction after clutter rejection will have a larger normalized correlation than lines at other directions. The normalized cross-correlation of the HRLs after clutter filtering is given by

$$\rho_k(l,\theta) = \frac{\sum_{m=0}^{M} hc_k(m,\theta) hc_{k+N}(m+l,\theta)}{\sqrt{\sum_{m=0}^{M} hc_k^2(m,\theta) \sum_{m=0}^{M} hc_{k+N}^2(m,\theta)}}, \tag{5}$$

where $hc_k(m,\theta)$ is the k'th HRL after clutter filtering at angle θ. Notice that only lines N emissions apart are correlated. These will, as mentioned, experience similar motion effects. All cross correlation functions within a certain number of emissions K are averaged to yield a more robust estimate

$$\bar{\rho}(l,\theta) = \frac{1}{K} \sum_{k=1}^{K} \rho_k(l,\theta). \tag{6}$$

The number of emissions K over which the averaging is performed is limited by an assumption of quasi-stationary velocity. The maximum average normalized correlation at each angle is extracted

$$\rho(\theta) = \max(\bar{\rho}(l,\theta)), \tag{7}$$

and the angle is estimated as the angle yielding the largest correlation

$$\theta_d = \arg\max_{\theta} \rho(\theta). \tag{8}$$

This estimate is quantized in steps of $\Delta\theta$ and a parabolic interpolation[16] is performed to increase accuracy

$$\widehat{\theta} = \theta_d - \frac{\rho(\theta_d + \Delta\theta) - \rho(\theta_d - \Delta\theta)}{2(\rho(\theta_d + \Delta\theta) - 2\rho(\theta_d) + \rho(\theta_d - \Delta\theta))} \Delta\theta. \tag{9}$$

After acquiring the angle estimate $\widehat{\theta}$, the beamforming is repeated along $\widehat{\theta}$ and the lag of maximum normalized cross-correlation, averaged over the K emissions, is found

$$l_d = \arg\max_{l} \bar{\rho}(l,\widehat{\theta}). \tag{10}$$

The quantized lag interpolated using parabolic interpolation to yield $\widehat{l}$, and the velocity is given by

$$\widehat{v}_{\widehat{\theta}} = \widehat{l} \Delta r f_{eff} \tag{11}$$

where f_{eff} is the effective pulse repetition frequency, which depends on the emission sequence and how the B-mode sequence and the flow sequence are interleaved. When both the flow angle $\widehat{\theta}$ and magnitude $\widehat{v}_{\widehat{\theta}}$ are estimated in a grid covering the region of interest, a full color flow map is created by color coding the velocity magnitudes, and vector arrows are added to indicate the flow direction and magnitude.

2.4. Clutter filtering

Prior to cross-correlating the beamformed high-resolution lines (HRLs), quasi-stationary echoes from surrounding tissue must be removed. Numerous methods for clutter filtering have been suggested in the literature for the conventional velocity estimation methods, including high-pass FIR (finite impulse response) filtering, IIR (infinite impulse response) filters with various initializations,[17] polynomial regression,[18] and various adaptive methods.[19] The different methods each have their advantages and disadvantages with respect to transition band width and algorithm complexity. Common to all methods is the assumption that only a limited packet size (number of pulse repetitions) are available.

This limitation is relaxed in synthetic aperture vector flow imaging due to the continuous availability of data for the entire region of interest. This comes at the cost of a lowered effective pulse repetition frequency, but enables the use of much longer FIR filters or IIR filters without initialization.

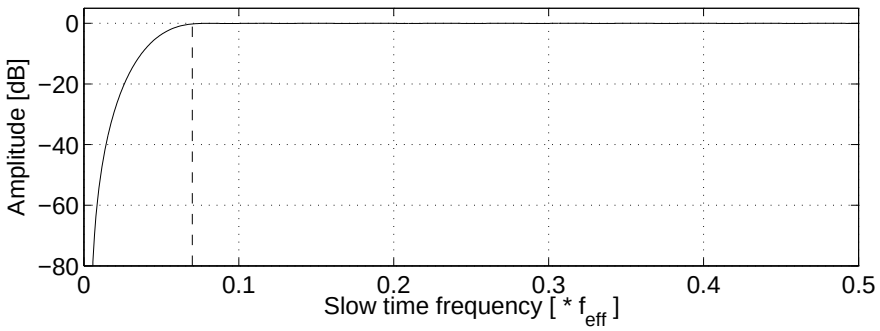

Figure 2. FIR linear phase high-pass filter used for clutter filtering of the carotid data.

Nevertheless, another problem arises when estimating 2D velocity vectors. For velocities of the same magnitude, axial and lateral motion will result in different slow time frequencies. An axial motion of velocity v_z results in a slow-time frequency centered at $f_d = 2v_z f_0/c$, where the spectrum resembles a scaled version of the excitation spectrum (convolved with the system transfer function). f_0 is the center frequency of the emitted waveform. A lateral motion of velocity v_x results in a slow-time frequency centered at 0 Hz, where the spectrum resembles a scaled version of the effective aperture function. Any clutter filter will therefore also eliminate a portion of the lateral motion signal.[20]

A compromise must therefore be made when choosing the clutter filter cut-off frequency depending on the expected velocity range, the effective pulse repetition frequency etc. For the femoral data set a linear regression filter over 14 HRLs is used, whereas a 48 tap linear phase FIR filter is used for the carotid data set. The FIR filter was designed using the Parks-McClellan algorithm[21] and the filter transfer function is shown in Figure 2. The pass-band start around $f_p = 0.07 f_{eff}$ as indicated by the dashed line, which for the parameters used (see Table 1) corresponds to an axial velocity of 2 cm/s. The carotid wall rarely moves at a velocity higher than this.[22]

3. DATA ACQUISITION

Two sets of in-vivo data have been acquired from healthy male volunteers of age 26 and 32. The scans were performed using a 128 element linear array transducer and our RASMUS experimental ultrasound scanner,[23] and both scans were 2 seconds long. Two synthetic aperture emission sequences were interleaved as described in Section 2.2, one for creating the B-mode image and one for estimating flow. The B-mode sequence was 118 emissions long, stepping 1 pitch per emission, while the flow sequence was a sparse sequence of eight emissions spread across the aperture. Data acquisition was performed with a pulse repetition frequency of $f_{prf} = 10$ kHz for the femoral data set, and $f_{prf} = 21$ kHz for the carotid data set. Emissions were defocused and a 11.25 μs non-linear chirp[24] was used for the femoral data set while a 2-cycle sinusoidal burst was used for the carotid data set, and the RF-data at the 64 elements closest to the point of emission were sampled. All processing was performed off-line on a computer cluster.

A number of lines were beamformed at different angles through every point where the 2-D velocity is estimated, and a clutter filter was applied. Cross-correlation was performed along all angles, and the flow angle estimate was chosen as the angle of maximum normalized cross-correlation.[6] The blood flow velocity magnitude along this direction was found as the lag of maximum correlation divided by elapsed time.

The vector velocity was estimated in a 1 mm grid covering the whole region of interest. For the femoral data set, data from 118 emissions of each sequence was used for making one full vector flow image, resulting in a frame rate of 42.4 frames per second, while data from 944 flow-emissions and 118 B-emissions were used in the carotid data set resulting in a frame rate of 19.7 frames per second. The parameters used for the two data sets are given in Table 1.

Table 1. Parameters.

Transducer parameters	Femoral data set	Carotid data set
Transducer type	Linear array	Linear array
Number of transducer elements	128	128
Transducer element pitch	0.3 mm	0.3 mm
Transducer element kerf	0.035 mm	0.035 mm
Transducer element height	5 mm	5 mm
Elevation focus	20 mm	20 mm
Center frequency, f_0	6.2 MHz	6.2 MHz
Wavelength, $\lambda = c/f_0$	0.25 mm	0.25 mm
Transmission parameters		
Excitation type	11.25 μs non-linear chirp[24]	2 cycles at f_0, Hanning tapering
Frequencies swept	$\sim$ 3.5 - 7.5 MHz	-
Number of emitting elements	11	16
Number of receiving elements, Q	64, centered at emission	64, centered at emission
Number of emissions in sequence, K	8	8
Number of virtual sources, $(= K)$	8	8
Virtual source positions, $\vec{r}_i$	$[x_{vs}, 0, -2.5]$ mm	$[x_{vs}, 0, -3.4]$ mm
Pulse repetition frequency, f_{prf}	10 kHz	21 kHz
Effective PRF for flow, f_{eff}	625 Hz	2.33 kHz
Processing parameters		
Points in line, $M + 1$	401	401
Spatial sampling interval, Δr	12.5μm	12.5μm
Line length	5 mm	5 mm
Angular sampling interval, $\Delta\theta$	5°	5°
Stationary echo cancelling method	Linear regression[18]	48 tap FIR filter
Number of correlations averaged, L	103	425
Velocity search range	-1.5 to 1.5 m/s	-1.5 to 1.5 m/s

Movies are made from the 2 times 2 seconds of data presenting full vector flow images where a color coding shows the velocity magnitude and vector arrows show both flow direction and magnitude. The result section presents still frames from these movies.

The volume flow in the femoral artery is estimated by re-sampling the velocity estimates in a profile through the vessel and assuming the artery is rotational symmetric. The average volume flow is compared with average volume flows of the femoral artery found in the literature.

4. RESULTS

In this section some preliminary processing results of the two data sets are shown. Fig. 3 shows a frame from the femoral data set at the time of peak systole. The color coding show the estimated velocity magnitude while the vector arrows show both local estimated flow direction and flow magnitude. The femoral artery is seen in the top of the image, while the confluence of the femoral vein and the saphenous vein is seen below. In Fig. 3 an approximately parabolic flow is seen in the femoral artery, and the reverse arterial flow is clearly seen in Fig. 4. Fig. 5 shows a frame during diastole where the arterial flow has decreased, while an increase in venous flow velocity is seen.

The volume flow in the femoral artery is estimated over time from the acquired vector velocity estimates. The estimates are re-sampled to fit a grid following 8 mm along the artery and the projection along the artery found visually from the B-mode image is extracted. By assuming the artery is rotationally symmetric, the volume flow over time is found by averaging the projection of the estimates along the 8 mm of the flow direction. Fig. 6 shows the estimated volume flow in the femoral artery. The volume flow over time is plotted and the average

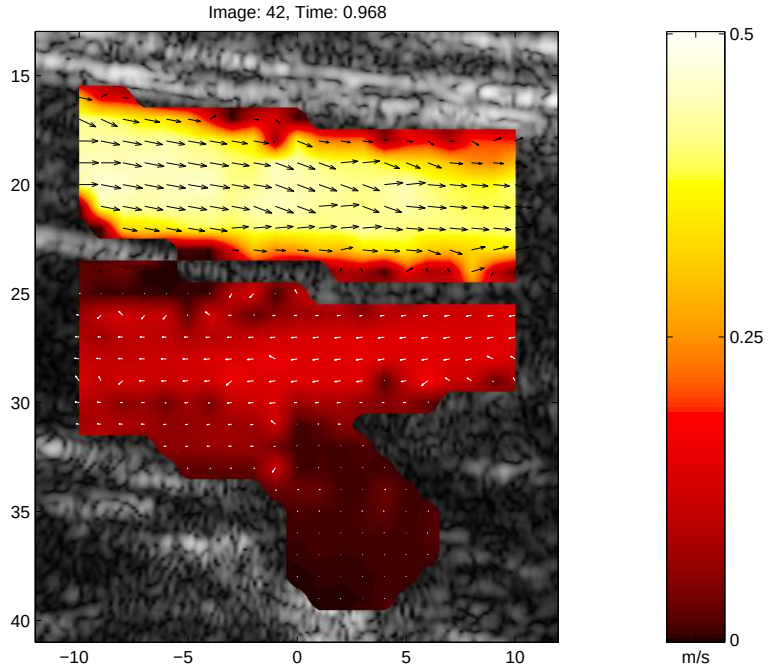

Figure 3. Single frame from the femoral data set at the time of peak systole. The color coding show the estimated velocity magnitude while the vector arrows show both local estimated flow direction and flow magnitude. Notice, the color of the vector arrows have been changed to black to visualize the flow direction in the artery.

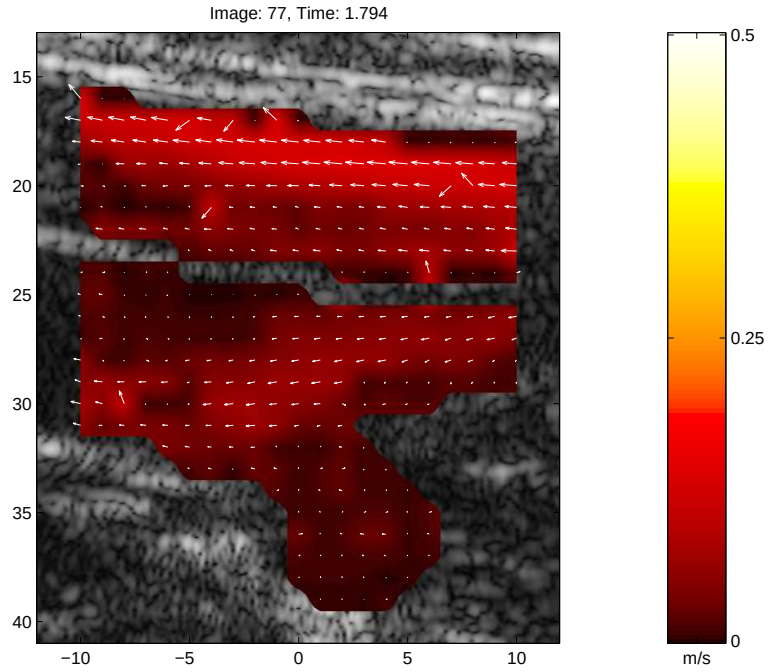

Figure 4. Single frame from the femoral data set at the time of reverse arterial flow. Notice, the arterial and venous flow are in the same direction. The color coding show the estimated velocity magnitude while the vector arrows show both local estimated flow direction and flow magnitude.

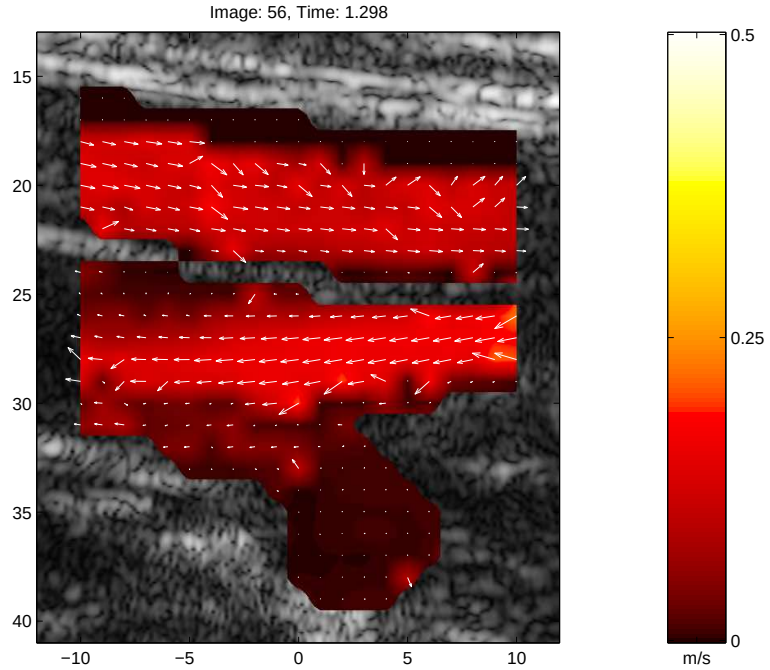

Figure 5. Single frame from the femoral data set at diastole. The color coding show the estimated velocity magnitude while the vector arrows show both local estimated flow direction and flow magnitude.

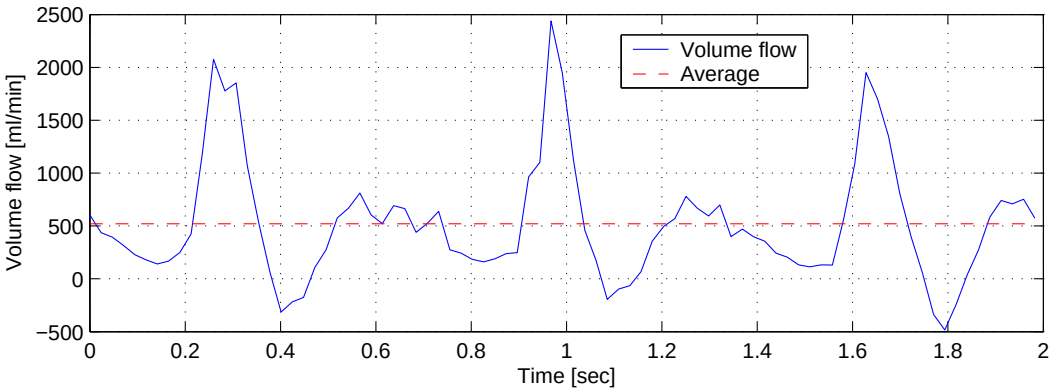

Figure 6. The estimated volume flow in the femoral artery.

volume flow over the entire data set is found and plotted as the dashed line. An average volume flow just above 500 ml/min is found.

A magnetic resonance imaging study found in literature[25] showed a femoral artery average volume flow of 411 ml/min for 25 healthy male subjects between 26 and 80 years of age. A statistically significant tendency for decreased volume flow in the femoral artery as a function of age was found. The volume flow estimated from the present femoral data, thus, seems plausible.

Fig. 7 shows data from the carotid bifurcation during systoly. The flow profiles in both the internal and external carotid arteries are highly skewed. Notice the high velocity magnitudes at the separating wall, peaking around 1 m/s, and the vortex tendency in the carotid bulb. These findings agree qualitatively with MRI measurements and numerical simulations found in the literature.[8]

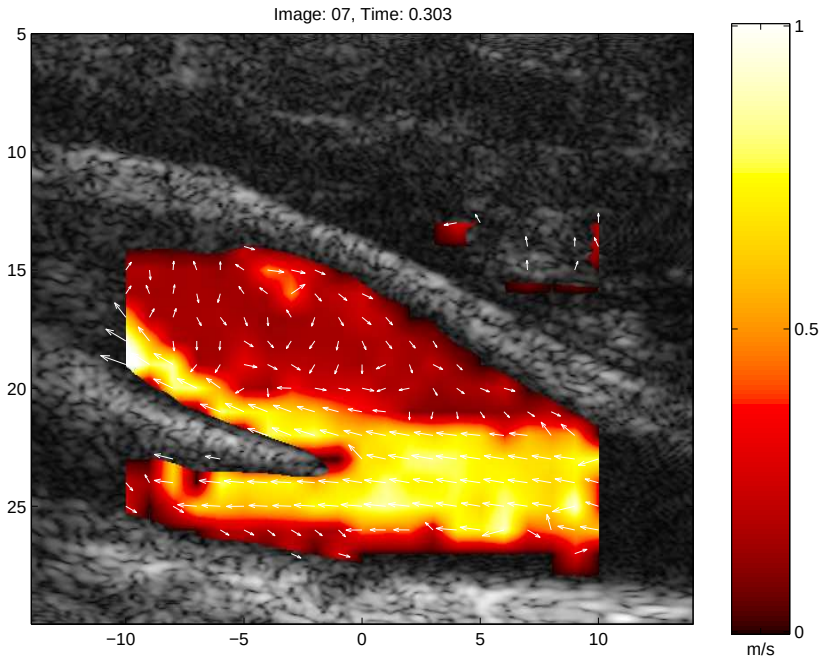

Figure 7. Single frame from the carotid data set at systole. The color coding show the estimated velocity magnitude while the vector arrows show both local estimated flow direction and flow magnitude.

5. CONCLUSION

Two challenging sets of in-vivo data have been acquired using synthetic aperture ultrasound. The first data set was from the femoral artery and the confluence of the femoral and saphenous vein. The second shows the carotid bifurcation.

Vector velocities have been estimated and full vector flow movies generated. Single frames from different time instances of these have been presented, and the volume flow in the femoral artery was estimated. A average volume flow during the 2 seconds of just above 500 ml/min was found.

Although a number of presumably false estimates are seen in the movie frames, interesting flow patterns are revealed, which would not be readily visible in conventional color flow imaging. These patterns could potentially be useful in future clinical work, when considering diagnosis and treatment of e.g. atherosclerosis, thrombo-embolic disease, and evaluation of transplants and cardiac flow dynamics.

ACKNOWLEDGMENTS

This work was supported by grant 26-04-0024 from the Danish Science Foundation and by B-K Medical A/S, Herlev, Denmark.

REFERENCES

1. C. Kasai, K. Namekawa, A. Koyano, and R. Omoto, "Real-time two-dimensional blood flow imaging using an autocorrelation technique," *IEEE Trans. Son. Ultrason.* **32**, pp. 458–463, 1985.
2. S. I. Nikolov and J. A. Jensen, "Velocity estimation using synthetic aperture imaging," in *Proc. IEEE Ultrason. Symp.*, pp. 1409–1412, 2001.
3. S. I. Nikolov and J. A. Jensen, "In-vivo synthetic aperture flow imaging in medical ultrasound," *IEEE Trans. Ultrason., Ferroelec., Freq. Contr.* , pp. 848–856, 2003.

4. O. Bonnefous, P. Pesqué, and X. Bernard, "A new velocity estimator for color flow mapping," in *Proc. IEEE Ultrason. Symp.*, pp. 855–860, 1986.
5. J. A. Jensen and S. I. Nikolov, "Directional synthetic aperture flow imaging," *IEEE Trans. Ultrason., Ferroelec., Freq. Contr.* , pp. 1107–1118, 2004.
6. J. A. Jensen, "Velocity vector estimation in synthetic aperture flow and B-mode imaging," in *IEEE International Symposium on Biomedical imaging from nano to macro*, pp. 32–35, 2004.
7. N. Oddershede and J. A. Jensen, "Synthetic aperture flow angle estimation on in-vivo data from the carotid artery," in *Proc. IEEE Ultrason. Symp.*, pp. 1331–1334, 2005.
8. R. Botnar, G. Rappitsch, M. B. Scheidegger, D. Liepsch, K. Perktold, and P. Boesiger, "Hemodynamics in the carotid artery bifurcation: a comparison between numerical simulations and in vitro MRI measurements," *J. Biomech.* **33**, pp. 137–144, 2000.
9. M. Soumekh, *Synthetic aperture radar. Signal processing with MATLAB algorithms*, John Wiley & Sons, Inc., New York, 1999.
10. R. Y. Chiao, L. J. Thomas, and S. D. Silverstein, "Sparse array imaging with spatially-encoded transmits," in *Proc. IEEE Ultrason. Symp.*, pp. 1679–1682, 1997.
11. S. I. Nikolov and J. A. Jensen, "Virtual ultrasound sources in high-resolution ultrasound imaging," in *Proc. SPIE - Progress in biomedical optics and imaging*, **3**, pp. 395–405, 2002.
12. M. Karaman, P. C. Li, and M. O'Donnell, "Synthetic aperture imaging for small scale systems," *IEEE Trans. Ultrason., Ferroelec., Freq. Contr.* **42**, pp. 429–442, 1995.
13. G. R. Lockwood, J. R. Talman, and S. S. Brunke, "Real-time 3-D ultrasound imaging using sparse synthetic aperture beamforming," *IEEE Trans. Ultrason., Ferroelec., Freq. Contr.* **45**, pp. 980–988, 1998.
14. S. I. Nikolov, K. Gammelmark, and J. A. Jensen, "Recursive ultrasound imaging," in *Proc. IEEE Ultrason. Symp.*, **2**, pp. 1621–1625, 1999.
15. K. L. Gammelmark and J. A. Jensen, "Duplex synthetic aperture imaging with tissue motion compensation," in *Proc. IEEE Ultrason. Symp.*, pp. 1569–1573, 2003.
16. S. G. Foster, *A pulsed ultrasonic flowmeter employing time domain methods.* PhD thesis, Dept. Elec. Eng., University of Illinois, Urbana, Ill., 1985.
17. A. P. Kadi and T. Loupas, "On the performance of regression and step-initialized IIR clutter filters for color Doppler systems in diagnostic medical ultrasound," *IEEE Trans. Ultrason., Ferroelec., Freq. Contr.* **42**, pp. 927–937, 1995.
18. A. P. G. Hoeks, J. J. W. van de Vorst, A. Dabekaussen, P. J. Brands, and R. S. Reneman, "An efficient algorithm to remove low frequency Doppler signal in digital Doppler systems," *Ultrason. Imaging* **13**, pp. 135–145, 1991a.
19. S. Bjærum, K. Kristoffersen, and H. Torp, "Clutter filters adapted to tissue motion in ultrasound color flow imaging," *IEEE Trans. Ultrason., Ferroelec., Freq. Contr.* **49**, pp. 693–704, June 2002.
20. B. H. Friemel, L. N. Bohs, K. R. Nightingale, and G. E. Trahey, "Wall filtering challenges in two-dimensional vector velocity estimation," *Proc. IEEE Ultrason. Symp.* **2**, pp. 1031–1034, 1993.
21. J. H. McClellan, T. W. Parks, and L. R. Rabiner, "A computer program for designing optimum fir linear phase digital filters," *IEEE Transactions on Audio and Electroacoustics* **AU-21, no. 6**, pp. 506–526, 1973.
22. A. Schmidt-Trucksass, D. Grathwohl, A. Schmid, R. Boragk, C. Upmeier, J. Keul, and M. Huonker, "Assessment of carotid wall motion and stiffness with tissue doppler imaging," *Ultrasound Med. Biol.* **24**, pp. 639–646, May 1998.
23. J. A. Jensen, O. Holm, L. J. Jensen, H. Bendsen, S. I. Nikolov, B. G. Tomov, P. Munk, M. Hansen, K. Salomonsen, J. Hansen, K. Gormsen, H. M. Pedersen, and K. L. Gammelmark, "Ultrasound research scanner for real-time synthetic aperture image acquisition," *IEEE Trans. Ultrason., Ferroelec., Freq. Contr.* **52 (5)**, pp. 881–891, May 2005.
24. F. Gran and J. A. Jensen, "Designing waveforms for temporal encoding using a frequency sampling method," *IEEE Trans. Ultrason., Ferroelec., Freq. Contr.* **Submitted**, 2006.
25. W. M. Klein, L. W. Bartels, L. Bax, Y. van der Graaf, and W. P. T. M. Mali, "Magnetic resonance imaging measurement of blood flow in the peripheral arteries in healthy subjects," *Journal of Vascular Surgery* **38**, pp. 1060–1066, 2003.

A.9 Oddershede, N. and Gran, F. and Jensen, J. A.,
Multi-frequency encoding for rapid color flow and quadroplex imaging, *Proceedings of IEEE Ultrasonics Symposium 2007, accepted for publication.*

Multi-frequency encoding for rapid color flow and quadroplex imaging

Niels Oddershede, Fredrik Gran, and Jørgen Arendt Jensen
Center for Fast Ultrasound Imaging, Ørsted•DTU, Build. 348,
Technical University of Denmark, DK-2800 Kgs. Lyngby, Denmark

***Abstract*— Ultrasonic color flow maps are made by estimating the velocities line by line over the region of interest. For each velocity estimate, multiple repetitions are needed. This sets a limit on the frame rate, which becomes increasingly severe when imaging deeper lying structures or when simultaneously acquiring spectrogram data for triplex imaging.**

This paper proposes a method for decreasing the data acquisition time by simultaneously sampling multiple lines at different spatial positions for the color flow map using narrow band signals with disjoint spectral support. The signals are separated in the receiver by filters matched to the emitted waveforms and the autocorrelation estimator is applied. Alternatively, one spectral band can be used for creating a color flow map, while data for a number of spectrograms are acquired simultaneously. Using three disjoint spectral bands, this will result in a multi-frequency quadroplex imaging mode featuring a color flow map and two spectrograms at the same frame rate as a normal color flow map. The method is presented, various side-effects are considered, and the method is tested on data from a re-circulating flow phantom where a constant parabolic flow with a peak of 0.1 m/s is generated with a flow angle of 60 degrees. A commercial linear array transducer is used and data are sampled using our RASMUS multi-channel sampling system. An *in-vivo* multi-frequency quadroplex movie of the common carotid artery of a healthy male volunteer was created.

The flow phantom measurements gave a mean standard deviation across the flow profile of 3.1%, 2.5%, and 2.1% of the peak velocity for bands at 5 MHz, 7 MHz, and 9 MHz, respectively. The *in-vivo* multi-frequency quadroplex movie showed the color flow map, and the two independent spectrograms at different spatial positions. This enables studying the flow over an arterial stenosis by simultaneously acquiring spectrograms on both sides of the stenosis, while maintaining the color flow map. A frame rate of 21.4 frames per second was achieved in this *in-vivo* experiment.

I. Introduction

Since the introduction of the autocorrelation estimator for ultrasonic blood flow imaging by Kasai et. al. [1] in the mid-eighties, it has been possible to create full color flow maps (CFM) in real time. The method is robust and fairly simple to implement. The velocities are estimated line by line over the region of interest, and for each line, repeated transmissions are needed. The performance of the estimator is closely linked to the number of repetitions used to form the estimate [2]. An inherent trade-off between frame rate and performance therefore exist. When imaging deep structures like the heart, this might severely affect either the performance or the frame rate. Also, in the triplex imaging mode, where both CFM data and a spectrogram are shown, the time for data acquisition must be divided between multiple sets of data, increasing the significance of this problem even further.

The autocorrelation estimator essentially assumes a narrow-band signal, and the variance of the velocity estimates decreases as the bandwidth is decreased [2]. Therefore a long sinusoidal narrow-band pulse is used for CFM. Nevertheless, ultrasound transducers are often designed fairly wide-band to ensure a good resolution in B-mode images. Using only a narrow frequency band for collecting CFM data does not exploit the available bandwidth efficiently.

This paper proposes a method for significantly decreasing the time spent on data collection for CFM by simultaneously sampling multiple lines using different frequency bands. The signals are then separated in the receiver by a simple filtering operation and the autocorrelation estimator is applied. The number of frequency bands M depends on the available transducer bandwidth and the intensity limits set by the Food and Drug Administration [3]. The total time spent on CFM data acquisition will decrease by a factor of M, potentially increasing the frame rate with a factor of M. Alternatively, the proposed method can be used for simultaneously acquiring CFM data and spectrogram data for triplex imaging. This paper will demonstrate how data for an extension of triplex imaging, namely Multi-Frequency Quadroplex imaging (MFQ) featuring two independent spectrograms and a CFM, can be acquired during the time normally spent on acquiring a CFM.

Parallel receive beamforming has previously been proposed for decreasing the time spent on data acquisition for B-mode images [4] and for blood flow estimation [5]. Here a broadly focused transmit beam is emitted, and multiple receive beams are generated simultaneously by steering the beams in slightly different directions. While the parallel receive beamforming presented in [4] is limited to sample closely spaced lines within the transmitted beam, the proposed method provides a larger flexibility in where data is sampled, for instance enabling MFQ imaging. Ultimately, the two methods could be combined, introducing the possibility of making real-time CFMs of 3D volumes without ECG-gating.

II. Theory

A. Autocorrelation estimator

The autocorrelation method for ultrasonic blood flow imaging was first introduced by Kasai et. al. [1]. Narrow-band pulses are repeatedly emitted along the same direction, and the received rf data are Hilbert transformed to give the in-phase and quadrature components. This results in a complex matrix $y(l, i)$, where i is the transmission number and l is the sample

index along the rf line corresponding to depth $d_l = \frac{c}{2f_s}l$. The axial velocity at a given depth can be estimated as [1]

$$v_z = -\frac{cf_{prf}}{4\pi f_0}\arctan\left(\frac{\Im\{R(1)\}}{\Re\{R(1)\}}\right), \quad (1)$$

where c is the speed of sound, f_{prf} is the pulse repetition frequency, f_0 is the center frequency of the emitted narrow-band signal, $\Re\{\cdot\}$ and $\Im\{\cdot\}$ denotes the real and imaginary parts, and $R(1)$ is the complex auto-correlation function of $y(l,i)$ at lag 1, evaluated at a certain depth corresponding to $l = L_d$. This autocorrelation function can be estimated by

$$\hat{R}(1) = \frac{1}{(N-1)N_l}\sum_{l=0}^{N_l-1}\sum_{i=0}^{N-2} y(l+L_d,i)y^*(l+L_d,i+1), \quad (2)$$

which includes an averaging over N_l rf samples. This has been shown to lower the variance of the estimated autocorrelation function, and thereby increase the accuracy of the velocity estimate [6].

By demanding that a whole period of the signal must be observed to distinguish the flow signal from that of a stationary structure, the minimum detectable velocity of an autocorrelation estimator is given by [2]

$$v_{min} = \frac{c}{2}\frac{f_{prf}}{Nf_0}. \quad (3)$$

This is a quite conservative demand, and v_{min} is not considered a rigid limit. According to the Nyquist sampling theorem, the maximum detectable velocity of an autocorrelation estimator is [2]

$$v_{max} = \frac{c}{2}\frac{f_{prf}}{2f_0+B}, \quad (4)$$

where B is the bandwidth of the emitted signal. The variance of the velocity estimate assuming a constant velocity, and under the assumption that no noise is present, can be approximated by [2]

$$\sigma_v^2 = \frac{c}{4\pi^2 f_0^2}\frac{f_{prf}}{T}|v_z|, \quad (5)$$

where T is the duration of the emitted pulse. Both the velocity range and the performance of the estimator are therefore dependent on the center frequency f_0.

B. Spectral velocity estimation

A spectrogram displays variation of the spectral content of the slow-time signal over time, hereby yielding a direct measure of the axial velocity of the moving blood. It can be estimated from the complex signal matrix $y(l,i)$ when the number of observations is sufficiently high. At a certain time instance $t = k/f_{prf}$, the power spectrum over pulse repetitions is estimated from N_s pulse repetitions and averaged over a number of rf samples N_l, which is known as the range gate. The segment size N_s is chosen low enough to capture the frequency variations over time and high enough to give an acceptable spectral resolution. A window $w(i)$ is often applied

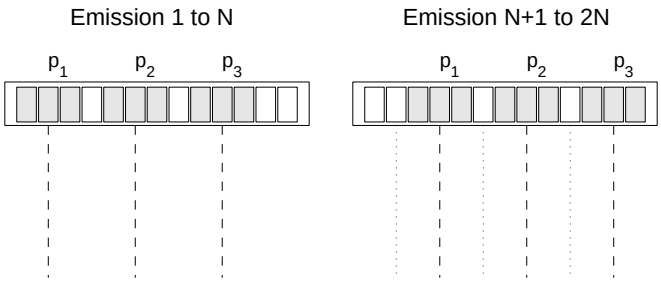

Fig. 1. The basic principle of the proposed method. Three different pulses $p_1(t)$, $p_2(t)$, and $p_3(t)$ are emitted N times and the received signals are separated in the receiver to simultaneously create three lines of the color flow map. The position of the transmitting sub-apertures are shifted and new lines are created.

to the data prior to the Fourier transform. The estimated power spectral density is given by

$$\hat{P}_y(f_p,k) = \frac{1}{N_l}\frac{1}{N_s}\sum_{l=0}^{N_l-1}\left|\sum_{i=0}^{N_s-1} w(i)y(l+L_d,i+k)e^{-j2\pi f_p i/f_{prf}}\right|^2. \quad (6)$$

For a certain depth, corresponding to rf index L_d, $\hat{P}_y(f_p,k)$ is a function of frequency f_p and time given by pulse repetition number k. Using a Hamming window given by

$$w(i) = 0.54 - 0.46\cos\left(\frac{2\pi i}{N-1}\right), \quad i = 0,1,...,N-1 \quad (7)$$

will lower the spectral side-lobes, coming from the limited observation time, to approximately -40 dB.

C. Spatial encoding using frequency division

The proposed method aims at increasing the frame rate of color flow mapping by simultaneously sampling data for multiple lines in the CFM. Fig. 1 (left) shows a linear array transducer simultaneously emitting $M = 3$ different pulses $p_1(t)$, $p_2(t)$, and $p_3(t)$ using different sub-apertures. Assuming the signals can be separated in the receiver, three different lines can be beamformed after each emission. The emission is repeated N times at a given pulse repetition frequency f_{prf} and three lines in the CFM are created using the autocorrelation estimator [1]. The transmitting sub-apertures are slid across the aperture and the emissions are repeated until data for the entire CFM is collected. The time used for collecting data will in this example only be a third of that normally used.

Alternatively, the CFM data can be acquired as is usually done, using one narrow band signal $p_1(t)$. Simultaneously, data for two spectrograms can be acquired using the signals $p_2(t)$ and $p_3(t)$. These signals are repeatedly emitted from the same sub-apertures, continuously sampling along the same lines. Hereby a CFM and two spectrograms are acquired simultaneously yielding an expansion of triplex imaging named Multi-Frequency Quadroplex imaging (MFQ). The data acquisition time will equal that normally spent on acquiring a CFM. At some point, a transducer element will be required to emit both

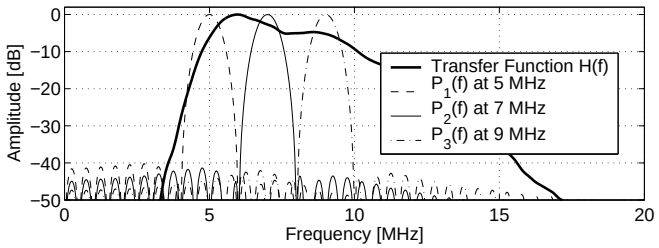

Fig. 2. The two-way system transfer function and the amplitude spectra of the three emitted pulses.

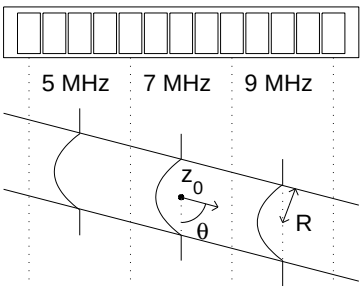

Fig. 3. Physical setup of the phantom experiment. The transducer is mounted at height $z = z_0$ over the tube center at an angle of $\theta = 60°$. The tube has radius R. The figure also shows the three regions of the CFM made at different frequency bands. Each region is sampled left to right and all regions are sampled simultaneously. The position of the three velocity profiles correspond to the profiles shown in Fig. 4.

a delayed version of $p_1(t)$ and for instance $p_2(t)$. To use the entire amplitude range while emitting each signal, $p_2(t)$ and $p_3(t)$ are delayed so that they are emitted later than $p_1(t)$.

The emitted signals $p_m(t)$ are designed as simple narrow-band pulses at different frequencies. They are given by

$$p_m(t) = w(t)\sin(2\pi f_m t), \qquad 0 < t < T \tag{8}$$

for $m = [1, 2, 3]$, where f_m is the center frequency of the mth signal, and T is the pulse duration. $w(t)$ is a window designed to reduce the spectral leakages into the other bands. A Hamming window, which has spectral side-lobes below -40 dB, is used. The signals are then separated in the receiver by filters matched to the emitted signals, $h_m(t) = p_m(T-t), 0 < t < T$. The number of pulses M, which can be emitted, is determined by the transducer bandwidth compared to the bandwidth of the signals $p_m(t)$. Fig. 2 shows the transfer function of a commercial linear array transducer (thick line), and the amplitude spectra of three signals in (8) using $f_m = [5, 7, 9]$ MHz and $T = 2$ μs (thin lines). The spectral leakage is below -40 dB for all bands.

The minimum detectable velocity is now limited by the lowest frequency band centered at f_1 through (3), and the maximum detectable velocity is limited by the highest frequency band f_M through (4). The increased frame rate, thus, comes at the expense of a slightly decreased velocity range compared to a single narrow-band pulse. Furthermore, the method requires M parallel beamformers, which is incorporated in most commercial high-end scanners at present, and a matched filtration of the channel RF-data.

III. Simultaneous sampling of multiple CFM lines

The method was tested in a re-circulating flow rig, where a blood mimicking fluid was pumped at a constant velocity through a rubber tube submerged in a water tank. The physical setup of the phantom experiment is shown in Fig. 3, which also show the definition of the tube depth $z_0 = 33.5$ mm, the tube radius $R = 6$ mm, and the beam-to-flow angle $\theta = 60°$. The peak velocity was $v_0 = 0.1$ m/s.

The data acquisition was performed using a 128 element linear array transducer and the RASMUS multi-channel sampling system [7]. This system can emit arbitrary waveforms on 128 elements, and sample 64 transducer elements in real-time. To acquire data from all 128 elements, the emission is repeated and multiplexing is used. This effectively halves the frame rate. The three signals shown in Fig. 2 were used and the parameters for the experiment are given in Table I.

TABLE I

Parameters used for the phantom experiment.

Parameter	Value
Transducer type	Linear array
Number of transducer elements	128
Transducer element pitch	0.26 mm
Transducer element height	4 mm
Elevation focus	15 mm
Transfer function	See Fig. 2
Transmit focus depth	28.7 mm
Number of transmit bands	3
Center frequencies, f_1, f_2, and f_3	5, 7, and 9 MHz
Pulse duration, T	2 μs
Amplitude tapering	Hamming window
Number of emit. elements / band	22
Transmit apodization	Tukey window
Number of receiving elements	128 (2x64 through multiplexing)
Receive apodization	Hanning window (over 64 elem. cnt. around the current image line)
Sampling frequency, f_s	40 MHz
Pulse repetition frequency, f_{prf}	1.65 kHz (3.3 kHz incl. multiplex)
Number of shots per estimate, N	32 (64 incl. multiplexing)
Clutter filtering	Subtracting mean of N signals
Number of CFM lines created	33
Inter-line spacing	0.52 mm

The acquired data was processed as described in Section II. 17 repetitions of the entire sequence was processed, yielding 17 full color flow maps. The velocity profiles at the center line of each of the three regions (see Fig. 3) were extracted and the mean and standard deviation over the repetitions were found. These are shown in Fig. 4 along with the expected parabolic velocity profile.

Fig. 4 reveals a slightly higher standard deviation in the lower frequency bands. The standard deviations of the velocity estimates are averaged over the tube diameter yielding 3.1, 2.5, and 2.2 % of the theoretical peak velocity $v_0 = 0.1$ m/s for the 5 MHz, 7 MHz, and 9 MHz bands, respectively. The increase in standard deviation, although present, is not as large as predicted by (5). For this phantom experiment performed

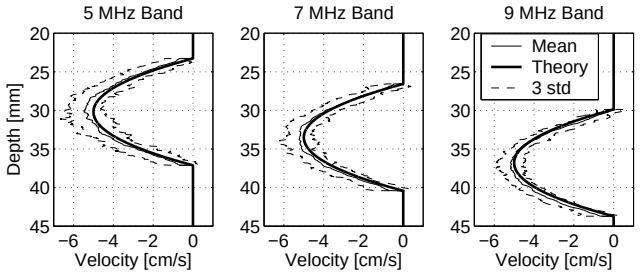

Fig. 4. Three resulting velocity profiles made at different frequency bands. The plot shows the expected velocity profile (thick line), the average of 17 profiles (thin line), and three times the standard deviation of the 17 profiles (dashed line).

in water a quite good signal-to-noise ratio is attained, and no frequency dependent attenuation is present. The increased standard deviation at lower frequency bands is therefore qualitatively in accordance with (5), which is derived assuming no noise.

IV. Multi-Frequency Quadroplex imaging

At present, triplex imaging is only possible at very low frame-rates due to the switching between acquisition of CFM data and spectrogram data. The proposed method can be used to solve this problem, and further to do MFQ imaging as described in Section II-C. The MFQ imaging was tested *in vivo* using a pulse repetition frequency of $f_{prf} = 12$ kHz (24 kHz including multiplexing) and a transmit focus depth of 15 mm. The remaining parameters were set as described in Table I. An examples from the common carotid artery of a healthy male volunteer is shown in Fig. 5. The CFM is made using the 5 MHz band and is composed of 33 lines, each sampled 16 times (32 including multiplexing), and the B-mode image is made from 65 emissions. The leftmost spectrogram was made using the 7 MHz band and the rightmost using the 9 MHz band. Each spectrogram estimate was made from 64 lines using the method described in II-B. The frame rate was 21.4 Hz. While the B-mode data was acquired (which happens 21.4 times each second), no spectrogram data are available. This is a result of the B-mode emissions using the entire transducer bandwidth. In Fig. 5, this is seen as gaps in the spectrogram. These gaps are not inherent for the proposed method, but are dependent on how the emissions are ordered, and there are multiple ways of avoiding these gaps [8], [2], [9].

V. Conclusion

A data acquisition method for simultaneously sampling multiple lines using different narrow frequency bands has been presented. The method can be used for increasing the frame rate of CFMs or for MFQ imaging, featuring a CFM and two independent spectrograms. The MFQ imaging mode yields the possibility of studying the change in flow over an arterial stenosis by placing a range gate at both sides of the stenosis and monitoring the flow over time, while still maintaining the CFM.

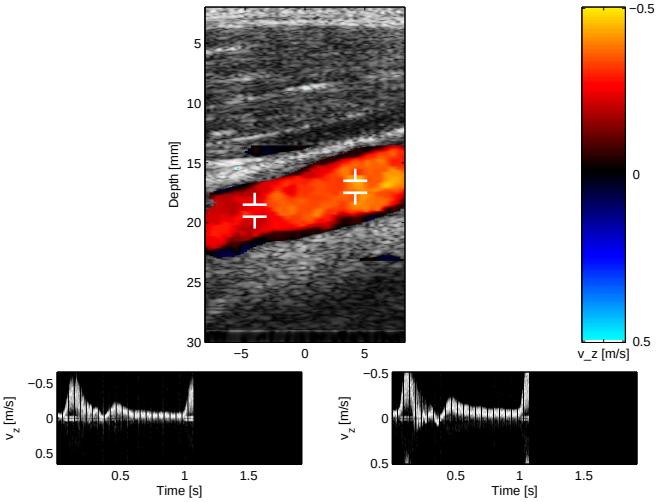

Fig. 5. Multi-Frequency Quadroplex image of the common carotid artery during systole. The upper image shows the color flow map using the 5 MHz band, the left spectral Doppler shows the 7 MHz band using the leftmost range gate, and the right spectral Doppler shows the 9 MHz band using the rightmost range gate.

Acknowledgments

This work was supported by grant 26-04-0024 from the Danish Science Foundation, by the Danish research council for Technology and Production grant 274-05-0327, and by B-K Medical, Herlev, Denmark. MD Kristoffer Lindskov Hansen is thanked for performing the *in-vivo* data acquisition.

References

[1] C. Kasai, K. Namekawa, A. Koyano, and R. Omoto. Real-time two-dimensional blood flow imaging using an autocorrelation technique. *IEEE Trans. Son. Ultrason.*, 32:458–463, 1985.

[2] J. A. Jensen. *Estimation of Blood Velocities Using Ultrasound: A Signal Processing Approach.* Cambridge University Press, New York, 1996.

[3] FDA. Information for manufacturers seeking marketing clearance of diagnostic ultrasound systems and transducers. Technical report, Center for Devices and Radiological Health, United States Food and Drug Administration, 1997.

[4] D. P. Shattuck, M. D. Weinshenker, S. W. Smith, and O. T. von Ramm. Explososcan: A parallel processing technique for high speed ultrasound imaging with linear phased arrays. *J. Acoust. Soc. Am.*, 75:1273–1282, 1984.

[5] J. W. Allison. *Parallel Doppler processing in ultrasonic flow imaging.* PhD thesis, Duke University, Durham, NC, 1987.

[6] T. Loupas, J. T. Powers, and R. W. Gill. An axial velocity estimator for ultrasound blood flow imaging, based on a full evaluation of the Doppler equation by means of a two-dimensional autocorrelation approach. *IEEE Trans. Ultrason., Ferroelec., Freq. Contr.*, 42:672–688, 1995.

[7] J. A. Jensen, O. Holm, L. J. Jensen, H. Bendsen, S. I. Nikolov, B. G. Tomov, P. Munk, M. Hansen, K. Salomonsen, J. Hansen, K. Gormsen, H. M. Pedersen, and K. L. Gammelmark. Ultrasound research scanner for real-time synthetic aperture image acquisition. *IEEE Trans. Ultrason., Ferroelec., Freq. Contr.*, 52 (5):881–891, May 2005.

[8] K. Kristoffersen and B. A. J. Angelsen. A time-shared ultrasound Doppler measurement and 2-D imaging system. *IEEE Trans. Biomed. Eng.*, BME-35:285–295, 1988.

[9] J. A. Jensen. Spectral velocity estimation in ultrasound using sparse data sets. *J. Acoust. Soc. Am.*, vol 120(1):211–220, 2006.

A.10 Oddershede, N. and Løvstakken, L. and Torp, H. and Jensen, J. A., Multi-dimensional spectrum analysis for 2-D vector velocity estimation, *Proceedings of IEEE Ultrasonics Symposium 2007, accepted for publication.*

Multi-dimensional spectrum analysis for 2-D vector velocity estimation

Niels Oddershede[1], Lasse Løvstakken[2], Hans Torp[2], and Jørgen Arendt Jensen[1]
1) Center for Fast Ultrasound Imaging, Ørsted•DTU, Build. 349,
Technical University of Denmark, DK-2800 Lyngby, Denmark
2) Department of Circulation and Medical Imaging,
Norwegian University of Science and Technology, Trondheim, Norway

***Abstract*— Wilson (1991) presented a wide-band estimator for axial blood flow velocity estimation through the use of the two-dimensional (2-D) Fourier transform. It was shown how a single velocity component was concentrated along a line in the 2-D Fourier space, where the slope was given by the axial velocity. This paper presents an expansion of this study. If data are sampled within a region, instead of along a line, a three-dimensional (3-D) data matrix is created along lateral space, axial space, and pulse repetitions. It is shown, that a single velocity component will be concentrated along a plane in the 3-D Fourier space, which is found through the 3-D Fourier transform of the data matrix, and that the plane is tilted according to the axial and lateral velocity components.**

Two estimators are derived for finding the plane in the 3-D Fourier space, where the integrated power spectrum is largest. The first uses the 3-D Fourier transform to find the power spectrum, while the second uses a minimum variance approach. Based on this plane, the axial and lateral velocity components are estimated. A number of phantom flow measurements, for flow-to-beam angles of 60, 75, and 90 degrees, were performed to test the estimator. The data were collected using our RASMUS experimental ultrasound scanner and a 128 element commercial linear array transducer. The receive apodization function was manipulated, creating an oscillation in the lateral direction, and multiple parallel lines were beamformed simultaneously. The two estimators were then applied to the data. Finally, an *in-vivo* scan of the common carotid artery was performed.

The average standard deviation was found across the phantom tube, for both the axial and the lateral velocity estimate. Twenty independent estimates were made for each positions. The average standard deviation of the lateral velocity estimates ranged from 16.4 % to 2.1 %, relative to the peak velocity, while the average standard deviation of the axial velocity ranged from 2.0 % to 0.2 %. Both estimators performed best for flow-to-beam angles of 90 degrees. The *in-vivo* scan showed the potential of the method, yielding an estimate of the velocity magnitude independent of vessel orientation.

I. Introduction

Blood flow velocity estimation in ultrasound systems is usually performed by repeating a number N_t of focused emissions along the same direction at the pulse repetition frequency f_{prf}. The received signal is sampled along the beam direction at a temporal sampling frequency of f_s, corresponding to a spatial sampling in depth of $2f_s/c$, where c is the speed of sound. A data matrix $s(z,t)$ can then be formed with N_z depth samples and N_t pulse repetition samples, also known as slow-time samples.

Numerous estimators have been proposed for finding the axial velocity component from this data matrix. Kasai and coworkers [1] proposed the autocorrelation estimator, where the axial velocity is found through the average phase shift along pulse repetitions. Bonnefous and Pesque proposed a cross-correlation estimator [2], where the consecutive columns of $s(z,t)$ are cross-correlated to find the spatial shift and thus the velocity. Ferrara and Algazi [3] proposed a maximum likelihood estimator, essentially using both the envelope information and the phase information in the estimator. Wilson [4] and Torp and Kristoffersen [5] proposed to find the axial velocity component through the 2-D Fourier transform of the matrix $s(z,t)$. If only a single velocity is present within the observation window, the 2-D power spectrum will peak along a line in the spectral domain. This line was denoted an iso-velocity line in [5]. The axial velocity can be estimated by finding the slope of this line [4].

The purpose of this paper is to extend the estimator presented by Wilson [4] and Torp and Kristoffersen [5] to search for both the axial and the lateral component. If data are sampled in a region both axially and laterally over a number of repetitions, a 3-D signal matrix $s(x,z,t)$ can be created. It will be shown that for a single velocity, the 3-D power spectrum of $s(x,z,t)$ will be concentrated along a plane in the 3-D Fourier space, and two estimators will be derived. The two velocity components are estimated by summing the power spectrum along the iso-velocity plane corresponding to all combinations of the possible lateral and axial velocity components (v_x, v_z) and choosing the combination that yield the maximum sum. The first estimator finds the power spectral components through a Fourier transform, while the second uses a minimum variance approach [6].

II. Three-dimensional Fourier transform of ultrasonic data

Most ultrasonic velocity estimation systems do numerous transmissions along the same direction, and a data matrix $s(z,t)$ can be formed, where z denotes depth and t slow time. Normally both variables are discrete. Wilson showed [4] that if the flow has constant velocity within the limits of z, the 2-D fast Fourier transform $S(\zeta, f_d)$ of $s(z,t)$ will be concentrated along a line in the 2-D plane spanned by the spatial frequency

ζ and the temporal frequency f_d, and that the slope of this line is proportional to the flow velocity.

Assuming we could sample within a plane instead of just a line, a 3-D data matrix $s(x, z, t)$ could be constructed, where x is lateral position, z is depth, and t is slow time. Lets first assume the data are continuous in all dimensions and the observation time and space are infinitely long. The 3-D Fourier transform of this matrix is given by

$$F(\chi, \zeta, f_d) = \int_{-\infty}^{\infty}\int_{-\infty}^{\infty}\int_{-\infty}^{\infty} s(x, z, t) \cdot e^{-j2\pi\chi x} e^{-j2\pi\zeta z} e^{-j2\pi f_d t} dx dz dt, \quad (1)$$

where χ is the spatial frequency along the lateral direction, ζ is the spatial frequency along the axial direction, and f_d is the slow-time frequency commonly known as the Doppler frequency.

Considering a constant velocity movement within the axial-lateral plane and disregarding the change in spatial impulse response, the 3-D data matrix $s(x, z, t)$ can be approximated by a 2-D function $s_0(x, z)$ moving within the plane with axial velocity v_z and lateral velocity v_x

$$s(x, z, t) = s_0(x - v_x t, z - v_z t). \quad (2)$$

The 3-D Fourier transform of $s(x, z, t)$, as given in (1), is then

$$\begin{aligned} F(\chi, \zeta, f_d) &= \int_{-\infty}^{\infty}\int_{-\infty}^{\infty}\int_{-\infty}^{\infty} s_0(x - v_x t, z - v_z t) \cdot \\ &\quad e^{-j2\pi\chi x} e^{-j2\pi\zeta z} e^{-j2\pi f_d t} dx dz dt \\ &= \int_{-\infty}^{\infty} S_0(\chi, \zeta) e^{-j2\pi\chi v_x t} e^{-j2\pi\zeta v_z t} e^{-j2\pi f_d t} dt \\ &= S_0(\chi, \zeta) \int_{-\infty}^{\infty} e^{-j2\pi(f_d + v_x\chi + v_z\zeta)t} dt \\ &= S_0(\chi, \zeta)\delta(f_d + v_x\chi + v_z\zeta), \end{aligned} \quad (3)$$

where $S_0(\chi, \zeta)$ is the 2-D Fourier transform of $s_0(x, z)$. The function in (3) is zero except for a plane intersecting origo. This plane in the 3-D Fourier space spanned by (χ, ζ, f_d) satisfies

$$f_d = -v_x\chi - v_z\zeta. \quad (4)$$

The 2-D spectrum $S_0(\chi, \zeta)$ is assumed separable, so that

$$S_0(\chi, \zeta) = S_x(\chi) S_z(\zeta) \quad (5)$$

where $S_z(\zeta)$ is the spectrum of the emitted signal, peaking at $\zeta = \pm 2f_0/c$, where f_0 is the temporal center frequency of the emitted pulse, and $S_x(\chi)$ is the lateral spatial spectrum. By assuming a linear array of $2M + 1$ omnidirectional point sources, equally spaced at distance d, the lateral spectrum can be approximated by a scaled version of the apodization function [6]

$$S_x(\chi) = \sum_{m=-M}^{M} w(m)\delta(\chi - \frac{md}{\lambda z}), \quad (6)$$

where $w(m)$ is the apodization function, and $\lambda = c/f_0$ is the axial wavelength. According to the Nyquist sampling theorem, the lateral sampling interval Δx at a certain depth z must therefore obey

$$\Delta x < \frac{\lambda z}{2Md}, \quad (7)$$

The assumptions of continuous data, infinitely long observation time and space, and constant velocity made in deriving (3) are of course not satisfied in ultrasonic velocity estimation. By limiting the observation space both laterally and axially by windowing the signal, a spectral broadening will occur in these dimensions and side-lobes will appear. The same goes for the limited observation time. Nevertheless, the three-dimensional spectral content of an almost constant velocity within the observation window will mainly be concentrated along the plane indicated by (4). The sampling along space and time will result in spectral repetitions at all multiples of the sampling frequency. The spatial sampling can relatively easy be set to avoid aliasing, while aliasing might occur along the temporal direction at high velocities. Aliasing in the 3-D power spectral domain will occur when f_d in (4) exceeds $f_{prf}/2$.

III. 2-D VECTOR VELOCITY ESTIMATOR

In [4], [5], the axial velocity was estimated by summing the 2-D power spectrum along iso-velocity lines, and choosing the velocity corresponding to the largest sum. In the vector velocity estimation case, both the axial and lateral velocities are sought and according to (3) a constant velocity will give rise to non-zero values along a plane in the 3-D power spectral space. The axial and lateral velocity components can be estimated by finding the plane satisfying (4), over which the sum of power spectral components is largest. The velocity components will then correspond to the angles with which the plane is tilted in the 3-D power spectral space.

A. Periodogram estimator

By assuming the velocity components v_x and v_z given, the Fourier components at the plane corresponding to these velocities are given by

$$F(\chi, \zeta | v_x, v_z) = \int_{-\infty}^{\infty}\int_{-\infty}^{\infty}\int_{-\infty}^{\infty} s(x, z, t) \cdot e^{-j2\pi[\chi(x - v_x t) + \zeta(z - v_z t)]} dx dz dt \quad (8)$$

which is found by inserting (4) into (1). The total power along this plane is found by integrating the magnitude squared of (8) over all spatial frequencies χ and ζ

$$P(v_x, v_z) = \int_{-\infty}^{\infty}\int_{-\infty}^{\infty} |F(\chi, \zeta | v_x, v_z)|^2 \, d\chi d\zeta. \quad (9)$$

Since data are sampled both spatially and temporally, the integrals become sums and the problem can be solved in matrix form. By ordering the 3-D signal matrix in a row vector $\mathbf{s}$ of length $N_x N_z N_t$, and defining the row vector

$$\mathbf{e}_i = e^{j2\pi(\chi_i(x - v_x t) + \zeta_i(z - v_z t))} \quad (10)$$

for spatial frequencies χ_i and ζ_i, we have

$$F(\chi_i, \zeta_i | v_x, v_z) = \mathbf{e}_i^H \mathbf{s}, \quad (11)$$

where $(\cdot)^H$ denotes the complex conjugate transpose. By making a $\mathbf{e}_i$ vector for all I permutations of the spatial frequencies, the total power along the plane given by velocities v_x and v_z is found by

$$\begin{aligned} P(v_x, v_z) &= \sum_{i=0}^{I-1} |F(\chi_i, \zeta_i | v_x, v_z)|^2 \\ &= \sum_{i=0}^{I-1} \mathbf{e}_i^H \mathbf{s} (\mathbf{e}_i^H \mathbf{s})^H = \sum_{i=0}^{I-1} \mathbf{e}_i^H \mathbf{R} \mathbf{e}_i. \end{aligned} \quad (12)$$

where $\mathbf{R} = E\{\mathbf{s}\mathbf{s}^H\}$ is the covariance matrix of the data, and $E\{\cdot\}$ denotes the expectation value. Estimation of the covariance matrix is considered in Section III-B. By doing the calculation in (12) for all combinations of v_x and v_z, the velocity components can be estimated by finding the velocities yielding the highest power along the plane

$$\hat{v}_x = \arg\max_{v_x} P(v_x, v_z) \quad (13)$$

$$\hat{v}_z = \arg\max_{v_z} P(v_x, v_z). \quad (14)$$

These discrete estimates can be further refined by interpolation of the $P(v_x, v_z)$ function.

B. Minimum variance estimator

The periodogram estimator suffers from poor spectral resolution when the observation window is limited [6], as is the case here. If the signal covariance matrix $\mathbf{R}$ is known, the power spectral component at lateral frequency χ_i and axial frequency ζ_i on the plane given by v_x and v_z can be found by a minimum variance estimator [6]

$$|F_{mv}(\chi_i, \zeta_i | v_x, v_z)|^2 = \frac{1}{\mathbf{e}_i^H \mathbf{R}^{-1} \mathbf{e}_i}, \quad (15)$$

where $\{\cdot\}^{-1}$ denotes the matrix inverse. Again, the estimates along the plane are summed to find the total power on the plane given by v_x and v_z. This can be found by

$$P_{mv}(v_x, v_z) = \sum_{i=0}^{I-1} \frac{1}{\mathbf{e}_i^H \mathbf{R}^{-1} \mathbf{e}_i}, \quad (16)$$

Since the data covariance matrix is not known, an estimate must be found. This can be done by dividing the data cube $s(x, z, t)$ of size $[N_x, N_z, N_t]$ into sub-cubes of size $[M_x, M_z, M_t]$. Hereby a total of $(N_x - M_x + 1)(N_z - M_z + 1)(N_t - M_t + 1)$ sub-cubes can be created. This is essentially a three-dimensional form of sub-array averaging used in some adaptive beamformers [7]. By organizing each data sub-cube in a row vector $\mathbf{s}_{mx,mz,mt}$, where mx, mz, and mt are indexes to the first sub-cube element, the covariance matrix of size $[M_x M_z M_t, M_x M_z M_t]$ can be estimated by

$$\hat{\mathbf{R}} = \sum_{mx=0}^{N_x - M_x} \sum_{mz=0}^{N_z - M_z} \sum_{mt=0}^{N_t - M_t} \mathbf{s}_{mx,mz,mt} \mathbf{s}_{mx,mz,mt}^H. \quad (17)$$

To ensure full rank of $\hat{\mathbf{R}}$, needed for finding the inverse, the inequality $(N_x - M_x + 1)(N_z - M_z + 1)(N_t - M_t + 1) \geq M_x M_z M_t$ must be satisfied. The sum along the plane in the power spectral domain can then be found from (16) by creating the vectors $\mathbf{e}_i$ according to the new data dimensions, and using the estimated covariance matrix $\hat{\mathbf{R}}$. Again, the lateral and axial velocity estimates are found by a search for the highest total power as in (13) and (14).

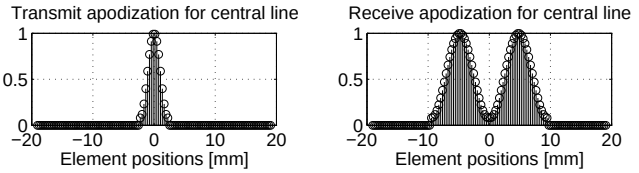

Fig. 1. Transmit and receive apodization used for central line. A narrow transmit apodization is used to create a broad beam, enabling parallel beamforming. The receive apodization creates a short broadband oscillation in the lateral direction of the point spread function.

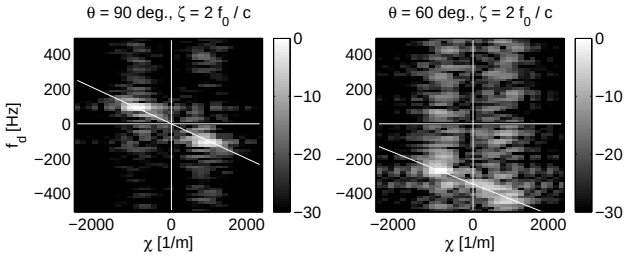

Fig. 2. Examples of power spectra at $\zeta = 2f_0/c$ on a dB scale. Data from phantom measurements at $\theta = 90°$ (left) and $\theta = 60°$ (right). A white line indicates $f_d = -v_x\chi - v_z\zeta$.

IV. Measurements

The estimators derived in Section III search for the plane in the 3-D Fourier domain where the power is largest, but through (3) and (5) the power is limited in the ζ-direction by the spectrum of the emitted wave, and in the χ-direction by the apodization through (6). If a rectangular or normally windowed apodization is used, the lateral spectrum $S_x(\chi)$ will be centered at $\chi = 0$. But by using the receive apodization shown in Fig. 1, which will create an oscillation in the lateral direction of the point spread function [8], [9], [10], the plane will intersect four clouds in the 3-D spectral domain instead of two. This is expected to increase the lateral estimator performance.

A series of measurements was performed in a flow-rig phantom. A blood mimicking fluid was circulated at a constant velocity through a tube submerged in a water tank. A linear array transducer was fixed above the tube at a controlled angle. Three measurements were made with angles of $\theta = 60°$, $75°$, and $90°$ (transverse flow) between the transducer axis and the flow direction. The data were collected using our RASMUS experimental ultrasound scanner [11]. The parameters for the measurements are given by Table I. At every emission, $N_x = 7$ parallel lines around the center of emission are beamformed at inter-line distance $\Delta x = 200$ μm using delay-and-sum beamforming [6]. The lines are beamformed at $f_s = 20$ MHz,

corresponding to an axial sampling interval of 37 μm. For every point along the line, where the vector velocity is estimated, $N_z = 33$ samples along depth are used, corresponding to both a lateral and axial extent of 1.2 mm. $N_t = 32$ repetitions are made along the same direction. Clutter filtering was performed by subtracting the average of $N_t = 32$ slow-time samples at each spatial position. The spectra of the data at $\zeta = 2f_0/c$ are shown in Fig. 2 for the $\theta = 90°$ (left) and $\theta = 60°$ (right) measurement. Also shown is the line corresponding to (4).

TABLE I
PARAMETERS.

Transducer	
Transducer type	Linear array
Number of transducer elements	128
Transducer element pitch, d	0.3 mm
Transducer element kerf	0.035 mm
Transducer element height	5 mm
Elevation focus	20 mm
Center frequency, f_0	5 MHz
Speed of sound, c	1481 m/s
Wavelength, $\lambda = c/f_0$	0.296 mm
Transmission	
Excitation type	1.5 cycle sinusoid at f_0
Transmit apodization	16 element Hamming
Receive apodization	Two 32 element Hamming
Transmit focus	20 mm
Receive focus	Dynamic
Pulse repetition frequency, f_{prf}	1 kHz
Phantom vessel	
Vessel radius, R	6 mm
Flow angles, θ	$60°$, $75°$ and $90°$
Depth of tube center, z_0	22, 24, and 19 mm, respect.
Peak velocity, v_0	10 cm/s
Processing	
Lateral sampling interval	0.2 mm
Axial sampling interval	0.037 mm
Number of points lateral, N_x	7
Number of points axial, N_z	33
Number of pulses per estimate,N_t	32
Size of region of interest, [lateral, axial]	$[1.2, 1.2]$ mm
Lateral samples in sub-cube, M_x	6
Axial samples in sub-cube, M_z	6
Temporal samples in sub-cube, M_t	12
Clutter filtering method	Mean subtraction
Number of freq. lateral, MV, N_χ	11
Number of freq. axial, MV, N_ζ	11
Number of frequency permutations, I	121
Velocity search range	-12 to 12 cm/s
Velocity search interval	0.5 cm/s

The two estimators were applied. $N_{rep} = 18$ repetitions were made, creating 18 independent velocity profiles through the tube at each beam-to-flow angle. The average velocity profile and the standard deviation profile was found. Fig. 3 gives the results of the phantom measurement at $\theta = 75°$, showing the average profile (solid, thin line), the average plus/minus three times the standard deviation profile (dashed lines), and the expected profile (solid, thick line). The top left plot shows the lateral velocity estimates using the Periodogram estimator, while the top right plot shows the axial velocity estimates using the Periodogram estimator. The bottom left plot shows the lateral velocity estimates using the Minimum Variance estimator, while the bottom right plot shows the axial velocity estimates using the Minimum Variance estimator.

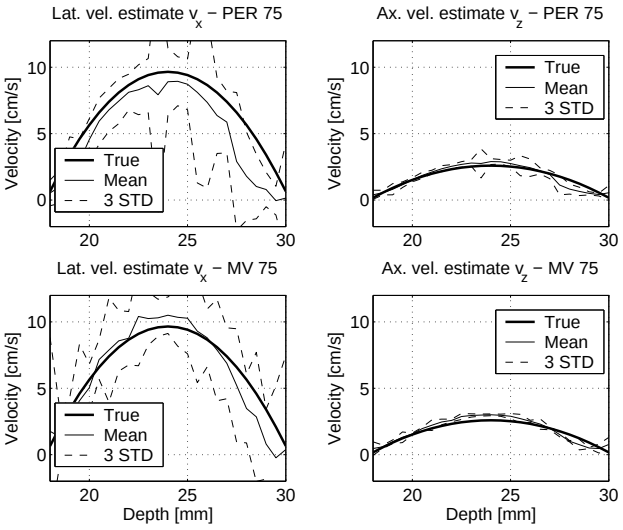

Fig. 3. Phantom measurement at a beam-to-flow angle of $\theta = 75°$. All plots give the expected profile (thick solid line), the average of 18 estimated profiles (thin solid line), and the average ± 3 times the standard deviation (dashed line). The top row gives the results from using the Periodogram estimator, while the bottom row gives the results from the Minimum Variance estimator. The left column is the lateral velocity estimates, while the right column is the axial velocity estimates.

Fig. 3 reveals a better performance in estimating the axial velocity component (right column) than the lateral velocity component (left column). To compare the estimators across the three beam-to-flow angles, the variance and bias was averaged across the profile. Tab. II and Fig. 4 summarize the standard deviation and bias for all three beam-to-flow angles and both velocity estimators.

TABLE II
AVERAGE STANDARD DEVIATION (ASD) AND AVERAGE BIAS (AB) ACROSS PROFILE, GIVEN IN % OF PEAK VELOCITY $v_0 = 10$ CM/S. RESULTS ARE GIVEN FOR BOTH THE PERIODOGRAM ESTIMATOR (PER) AND THE MINIMUM VARIANCE ESTIMATOR (MV).

ASD				
Angle, θ	PER v_x	PER v_z	MV v_x	MV v_z
$60°$	16.4%	1.7%	14.2%	2.0%
$75°$	11.5%	1.1%	11.8%	0.7%
$90°$	2.1%	0.2%	9.4%	1.4%
AB				
Angle, θ	PER v_x	PER v_z	MV v_x	MV v_z
$60°$	-23.6%	-3.4%	-7.2%	-1.9%
$75°$	-14.1%	0.1%	-2.1%	1.4%
$90°$	-5.8%	0.1%	1.3%	-0.3%

Comparing the two estimators, the average standard deviation (ASD) does not differ significantly, except for the $\theta = 90°$ experiment, where the periodogram estimator experiences a lower ASD than the minimum variance estimator. Nevertheless, the average bias of the lateral velocity estimates (bottom left) is much larger for the periodogram estimator, than for the minimum variance estimator. None of the two estimators therefore outperform the other in all cases.

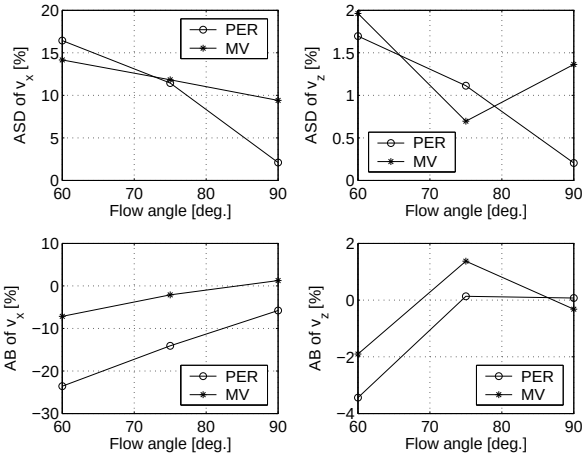

Fig. 4. Performance of the two estimators at different beam-to-flow angles, results from Table II. The top row gives the average standard deviation (ASD) for the lateral velocity estimates (left) and the axial velocity estimates (right). The bottom row gives the average bias (AB) for the lateral velocity estimates (left) and the axial velocity estimates (right). The results using the periodogram estimator is marked by a circle, while the results from the Minimum Variance estimator is marked by a star.

V. In-vivo measurement

An *in-vivo* measurement has been performed using the proposed method. The common carotid artery of a healthy 32-year-old male volunteer was scanned for 3 seconds using our RASMUS experimental ultrasound scanner [11]. The parameters were the same as in Table I, except the pulse repetition frequency was set at $f_{prf} = 6$ kHz. The vector velocities were estimated from 32 repeated emissions along 17 different lines, 1.2 mm apart. Along each line, the vector velocity was estimated at every 0.5 mm in depth. A B-mode image was created from the same data, using a single Hamming window as receive apodization. From the vector velocity estimates, the velocity magnitude $|\hat{v}| = \sqrt{\hat{v}_x^2 + \hat{v}_z^2}$ was found, and a color flow map (CFM) was created showing both the B-mode image at 40 dB dynamic range (black and white) and the velocity magnitude from 0 to 1.2 m/s (color). A CFM from the diastolic period is shown in Fig. 5. The left part of Fig. 5 shows the CFM created using the periodogram estimator from Section III-A, while the rightmost plot of Fig. 5 shows the CFM using the minimum variance estimator from Section III-B. Note that no post processing of the velocity estimates has been performed.

VI. Conclusion

This paper has shown that when data are sampled in a rectangular spatial window over time, a single velocity component is concentrated along a plane in the three-dimensional power spectrum spanned by lateral, axial, and temporal frequencies. The plane will be tilted according to the lateral and axial velocity components. Two estimators were derived for finding the two velocity components, the first based on the periodogram and the second on minimum variance. Both estimators were tested on measured phantom data for beam-to-flow angles of $60°$, $75°$, and $90°$. The axial velocity estimates showed a standard deviation and bias an order of magnitude below that of the lateral velocity estimates, and the performance of the vector velocity estimators was increased as the beam-to-flow angle approached $90°$. An *in-vivo* transverse scan of the common carotid artery was performed, showing the potential of the method under *in-vivo* conditions.

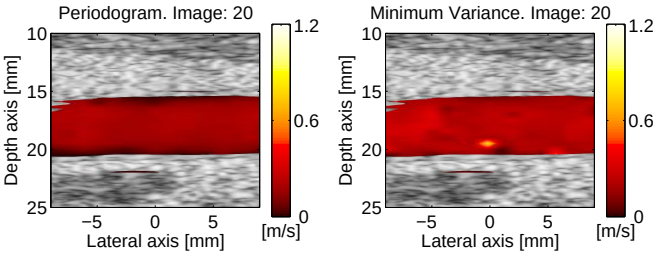

Fig. 5. Color flow map of the common carotid artery of a healthy male volunteer during diastole. The leftmost part shows the magnitude of the velocity estimates found using the periodogram estimator, while the rightmost part shows that using the minimum variance estimator.

Acknowledgement

This work was supported by grant 26-04-0024 from the Danish Science Foundation and by B-K Medical, Herlev, Denmark. The authors wish to thank MD Kristoffer Lindskov Hansen, University Hospital of Copenhagen, Denmark, for performing the *in-vivo* scan.

References

[1] C. Kasai, K. Namekawa, A. Koyano, and R. Omoto. Real-time two-dimensional blood flow imaging using an autocorrelation technique. *IEEE Trans. Son. Ultrason.*, 32:458–463, 1985.

[2] O. Bonnefous and P. Pesqué. Time domain formulation of pulse-Doppler ultrasound and blood velocity estimation by cross correlation. *Ultrason. Imaging*, 8:73–85, 1986.

[3] K. W. Ferrara and V. R. Algazi. A new wideband spread target maximum likelihood estimator for blood velocity estimation – Part I: Theory. *IEEE Trans. Ultrason., Ferroelec., Freq. Contr.*, 38:1–16, 1991a.

[4] L. S. Wilson. Description of broad-band pulsed Doppler ultrasound processing using the two-dimensional Fourier transform. *Ultrason. Imaging*, 13:301–315, 1991.

[5] H. Torp and K. Kristoffersen. Velocity matched spectrum analysis: A new method for suppressing velocity ambiguity in pulsed-wave doppler. *Ultrasound Med. Biol.*, 21(7):937–944, 1995.

[6] D. H. Johnson and D. E. Dudgeon. *Array signal processing. Concepts and techniques.* Prentice-Hall., Englewood Cliffs, New Jersey, 1993.

[7] H. Krim and M. Viberg. Two decades of array signal processing research. *IEEE Signal Processing Magazine*, 13:67–94, July 1996.

[8] J. A. Jensen and P. Munk. A new method for estimation of velocity vectors. *IEEE Trans. Ultrason., Ferroelec., Freq. Contr.*, 45:837–851, 1998.

[9] M. E. Anderson. Spatial quadrature: a novel technique for multi-dimensional velocity estimation. In *Proc. IEEE Ultrason. Symp.*, volume 45, pages 1233–1238, 1997.

[10] J. A. Jensen. A new estimator for vector velocity estimation. *IEEE Trans. Ultrason., Ferroelec., Freq. Contr.*, 48(4):886–894, 2001.

[11] J. A. Jensen, O. Holm, L. J. Jensen, H. Bendsen, S. I. Nikolov, B. G. Tomov, P. Munk, M. Hansen, K. Salomonsen, J. Hansen, K. Gormsen, H. M. Pedersen, and K. L. Gammelmark. Ultrasound research scanner for real-time synthetic aperture image acquisition. *IEEE Trans. Ultrason., Ferroelec., Freq. Contr.*, 52 (5):881–891, May 2005.